Novel Superconducting States in Hybrid Devices

Zur Erlangung des akademischen Grades eines
DOKTORS DER NATURWISSENSCHAFTEN
von der Fakultät für Physik des
Karlsruher Instituts für Technologie

genehmigte

DISSERTATION

von

Dipl.-Phys. Roland Georg Grein

aus Heidelberg
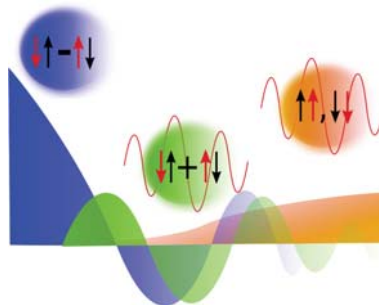
Tag der mündlichen Prüfung: 3.2.2012

Hauptreferent: **Prof. Dr. Matthias Eschrig**
Korreferent: **Prof. Dr. Gerd Schön**

"This furnishes us with an evident explanation of the great superiority in certitude of Arithmetic and Geometry to other sciences. The former alone deal with an object so pure and uncomplicated, that they need make no assumptions at all which experience renders uncertain, but wholly consist in the rational deduction of consequences. They are on that account much the easiest and clearest of all, and possess an object such as we require, for in them it is scarce humanly possible for anyone to err except by inadvertence. And yet we should not be surprised to find that plenty of people of their own accord prefer to apply their intelligence to other studies, or to Philosophy. The reason for this is that every person permits himself the liberty of making guesses in the matter of an obscure subject with more confidence than in one which is clear, and that it is much easier to have some vague notion about any subject, no matter what, than to arrive at the real truth about a single question however simple that may be."

René Decartes
Rules for the Direction of the Mind[1]

---

[1] Translated by Elizabeth S. Haldane and G. R. T. Ross in "Philosophical Works of Decartes", Cambridge University Press, 1911

Contents

Preface

This thesis covers most of my research activity on superconducting heterostructures conducted between 2008 and 2011 at the Institute for Theoretical Solid State Physics, Karlsruhe Institute of Technology, and the Department of Physics, Royal Holloway, University of London. The common physical theme of all topics discussed here is the superconducting proximity effect, i.e., the penetration of superconducting order into a non-superconducting state that comes about if a material – usually a metal – is brought into contact with a superconductor. This phenomenon has been investigated for decades already [30] and is intimately related to prominent physical effects, like Josephson currents or Andreev reflection.

More recently, the idea that the superconducting proximity effect may allow for 'engineering' superconducting states that so far eluded observation in bulk systems stimulated renewed research efforts in this field [38]. Generally, one may say that this requires a normal state[a] which is not commensurate with the order of conventional superconductivity, i.e. singlet s-wave pairing. Typically, this implies breaking spin-rotation symmetry – which is readily achieved with magnetic fields, exchange interactions, or spin-orbit coupling. Regarding applications, such proximity induced superconducting phases offer exciting prospects in the context of spintronics and (topological) quantum computation [38, 93].

We study two examples of such normal states here: ferromagnetic conductors and the two-dimensional helical metal realised at the surface of three-dimensional topological insulators. Since these systems do not only differ fundamentally in their phenomenology and potential applications, but also in terms of the theoretical methods that we invoke to study them, the thesis is split into two largely independent parts.

The first part treats the triplet proximity effect in superconductor-ferromagnet heterostructures. The current interest in these devices was triggered by the discovery of so-called 0-π oscillations in Josephson-junctions where the non-superconducting interlayer is a weakly ferromagnetic alloy [104]. The term 0-π oscillation refers to the fact that the current-phase relation switches periodically between $\sin(\Delta\chi)$ and $\sin(\Delta\chi + \pi)$ as a function of junction length and temperature [18]. This can be understood as an effect of the ferromagnetic exchange field. The Cooper-pairs of a conventional superconductor consist of electrons with opposite spin and momentum. When they tunnel into a ferromagnetic material, this symmetry cannot be upheld, as the momenta of conduction electrons at the Fermi-level are now different for electrons with opposite spin-orientation. Consequently, the proximity induced pairing correlations acquire a finite centre of mass momentum, leading to their oscillation on a scale set by the exchange field. This is directly analogous to the FFLO-state, where this effect is caused by a magnetic field [18]. Ferromagnetic π-junctions were recently incorporated in superconducting Qubits [43], which may allow to reduce their cell size and make them less susceptible to noise.[b]

---

[a]The term 'normal state' is nothing but a shorthand for 'non-superconducting state' here.

[b]See Ref. [43] and references therein.

However, the exchange field does not only lead to oscillations of the pair wave function, it is also detrimental to the proximity effect and reduces its decay length [30, 55]. This loss of particle-hole coherence is associated to the wave vector mismatch between spin-up and -down states. It was therefore widely believed that the proximity effect in ferromagnetic materials whose exchange energy is of the order of the Fermi-energy should be suppressed on the inter-atomic length scale. In 2001, a first proposal for circumventing this suppression was put forward by Bergeret et al. [10]. It relies on converting the pairing correlations of the superconductor, whose spin wave function is singlet, to correlations between electrons with the same spin. Obviously, these are not affected by the exchange field. This initial idea entailed a lot of theoretical activity in the following years and a supercurrent carried by such triplet correlations was eventually confirmed by Keizer et al. in 2006, using junctions with half metallic CrO_2 [67]. Since CrO_2 is fully (or almost fully) spin-polarised, and since the length of the junctions was of the order of 100 nm, this Josephson coupling must have been carried by spin-polarised Cooper-pairs, i.e. a long range triplet proximity effect. This was the first instance of a fully spin-polarised Josephson current. A large number of experiments on this effect followed since 2010, an incomplete overview is provided in chapter 1 of this thesis. This development may pave the way for a marriage between superconducting circuits and spintronics [38]. For instance, theory predicts that both the critical current and the current-phase relation of these junctions may be controllable by magnetic fields, and this was partly confirmed in experiment already [71].

In this general context, the present work is devoted to the application of a particular theoretical method in non-equilibrium superconductivity, the *quasiclassical Green's function technique* [114], to such systems. This theory was pioneered by Eilenberger [33] and Larkin and Ovchinnikov [76]. It can be considered as an extension of Landau's Fermi-liquid theory [75] to superconductors [36]. However, while Landau argued that the distribution function of a Fermi-liquid is sufficient to describe its transport properties, this is no true for the superconducting state. The condensate of conventional superconductors consists of Cooper-pairs and its elementary excitations are described by superpositions of particle-like and hole-like states in a thin shell around the Fermi-energy [8, 113]. The quasiclassical theory of superconductivity accounts for this order by describing the particle-hole and spin degrees of freedom as quantum mechanical, while real space coordinates and momentum enter as classical parameters [114]. This turns out to be sufficient if the problem one wishes to consider abides a separation of energy scales. The 'low' energy scale is set by the superconducting gap, and the 'high' energy scale by the Fermi-energy. Translated to length scales, this implies that we can describe variations of the system on the scale of the superconducting coherence length, while variations on the interatomic scale – which are usually irrelevant – are integrated out [114]. Consequently, this technique figures among the most efficient approaches to dealing with inhomogeneous and non-equilibrium problems in superconductivity.

It goes without saying that this is only true as long as the assumptions underlying the quasiclassical approximation are well-founded for the problem at hand. As a matter of fact, ferromagnets pose a problem in this respect. Until recently, only 'small' exchange fields comparable to the superconducting gap could be treated consistently [52, 53]. A generalisation of the boundary conditions for the quasiclassical Green's function near interfaces and surfaces worked out by Eschrig [37] then allowed for considering another limit, i.e. exchange fields of the order of the Fermi-energy. This is the relevant case for ferromagnets like Co, Ni, Fe and of course half metallic compounds like CrO_2.

The novelty of the results presented in this thesis relies fundamentally on this innovation. On the one hand, I discuss the triplet proximity effect in strongly polarised ferromagnets and in particular the Josephson effect related to it. Most experimental prove of induced triplet correlations in such structures available so far relies on the observation of supercur-

rents. While the half metallic case was analysed before using QC theory [39, 40], I show that the presence of a second spin-band has important consequences for the current-phase relation and the critical current and may even lead to a novel effect – the presence of a spin-supercurrent in a superconductor-ferromagnet bilayer. In recent experiments, junctions with an anti-ferromagnetic domain structure were investigated [68, 70]. My study of this problem shows that backscattering at the domain boundaries leads to an additional suppression of the supercurrent, and I find a 0-π switching of the current-phase relation as a function of the number of domains. In relation to a recent result of Chung et al. [22], I briefly comment on the triplet proximity effect induced by an interface whose spin-activity is caused by Rashba spin-orbit coupling, finding that $p_x \pm ip_y$-superconductivity with opposite chirality is induced in the two spin-bands.

Secondly, I present an investigation of point-contact spectra which have become a popular experimental tool for obtaining the spin-polarisation of ferromagnets. The theory put forward here is an extension of earlier theoretical models [28, 83] that accounts for spin-active scattering at the interface and the Fermi-surface geometry of the adjacent materials. I show that previous theories are contained as limiting cases in this formalism. I also investigate simple microscopic models to understand the origin of the scattering effects which are believed to drive the singlet-triplet conversion. It was shown previously [46, 142] that spin-active scattering leads to interface bound states and resonant Andreev scattering at SC/FM contacts. I show that these effects may help to understand point-contact spectra of (Ga,Mn)As, even though they are not directly observable due to temperature smearing. A first direct observation of such bound state signatures in conductance signals was very recently reported by Hübler et al. [61], who investigated Al/Fe tunnel junctions. Moreover, I discuss how this theory allows to reconcile point-contact spectra of CrO_2 with its alleged complete spin-polarisation.

Regarding technicalities, I discuss the boundary conditions put forward by Eschrig [37] and their diagrammatic representation in detail. A set of diagrammatic rules is proposed which may be helpful for the interpretation of theoretical results obtained with this formalism.

In the second part, I present a numerical study of a problem that attracted a lot of attention in the last two years – the proximity effect in surface states of topological insulators. Prior to their discovery in 2007 [72], topological insulators had been predicted theoretically [64, 14] as a special type of band insulator whose band structure topology implies the existence of topologically protected edge states at surfaces and interfaces. This idea was first applied to ' two-dimensional' materials, e.g. graphene [65] and semiconductor quantum wells [13]. It was argued that this state can be understood as the time-reversal invariant analogue of the Quantum Hall state, where the role of the magnetic field is – in a sense – taken over by spin-orbit coupling [13]. The quantum well proposal turned out to work, the existence of edge states was confirmed in transport measurements [72]. A little later, it was realised that this state has a three-dimensional analogue [90]. The first material predicted and confirmed to be such a three-dimensional topological insulator was $Bi_{1-x}Sb_x$ [124, 58]. Bi_2Se_3 [137, 59], Bi_2Te_3 [21] followed a little later. In these cases, surface states were identified by ARPES-measurements, being the predestined tool for studying surface electronic structure. The surface states of these 3D materials form a two-dimensional, helical metal with a Dirac cone dispersion around the Γ-point [56]. The term 'helical' refers to the special spin-structure of these states. For every wave vector $\mathbf{k} = (k_x, k_y)$, there is exactly one state at energy ϵ, i.e., there is no spin-degeneracy – a situation referred to as spin-momentum locking [56]. The states at $\mathbf{k}$ and $-\mathbf{k}$ have opposite spin-orientation, which implies that the spin winds around the Fermi-surface of the surface states. In fact, the low-energy Hamiltonian describing this dispersion is the same as that of graphene, just that σ now refers to real spin instead of pseudo-spin [56]. It was then theorised by Fu and Kane [47], that an instance of the $p_x + ip_y$-superconductor can be created

in these states if a pair-potential is induced by means of the superconducting proximity effect. This would have important implications, since this type of superconductor hosts Majorana-fermion excitations at vortex-cores or line junctions [47].[a] While these particles so far eluded observation in the realm of high-energy physics, there is a growing number of low dimensional condensed matter systems that are conjectured to host quasiparticle excitations of the Majorana-type. These quasiparticles would obey non-abelian statistics and are hence relevant to the field of topological quantum computation [93].

The experimental study of the proximity effect in topological insulators is, however, only just beginning [140, 106]. Thus, rather than exploring further consequences of the Fu-Kane proposal, I decided to investigate the validity of their phenomenological model. To this end, I employ a finite differences discretisation of a topological insulator-superconductor heterostructure, where the interface is modelled by a transfer-Hamiltonian. The dispersion is then calculated with a recursive Green's function technique. In agreement with earlier studies of this problem [108, 121, 74], I find that the Fu-Kane model is a reasonable approximation if the coupling between the two materials is small to intermediate. This obviously implies that the induced gap in the surface states will be smaller than the superconducting gap of the bulk superconductor. The validity of the Fu-Kane model can in this case be understood in terms of McMillan's theory of the proximity effect [85] – the pair-potential in the surface state is identified with an effective self-energy that accounts for the presence of the superconductor [108]. To recover the Fu-Kane model, one must, however, assume the energy and momentum independence of this self-energy, which turns out to be a bad approximation if the coupling is strong.

While this basic understanding was established before [108], the numerical method employed here is a powerful tool for material specific calculations [122], and will certainly be useful for future studies of transport in superconducting nanostructures involving topological insulators.

The results discussed in this thesis were all obtained in collaboration with other scientists. Regarding my personal contributions, modelling and calculations for the Josephson effect and point-contact spectra were carried out by me, with the exception of the numerical calculations for the smooth potential model (chapter 4), implemented by Georgo Metalidis, and the model for the spin-orbit coupled barrier (chapter 6), worked out by Tomas Löfwander. As far as the comparison to experimental results is concerned, the data on (Ga,Mn)As was taken by Samanta Piano and BTK fits are due to her as well. I did the theoretical modelling and fitting of the data with our theory. The accompanying calculations with the Kane-model were carried out by Karel Výborný. The calculations done for fitting the CrO_2 spectra are entirely due to Tomas Löfwander; I still discuss them here, since this is a very nice application of our general theory. Unpublished calculations and those which I present in the second part of the thesis were all done by me. In all cases, theoretical modelling and interpretation was done in close collaboration with the respective scientists and in particular my advisor, Matthias Eschrig.

Lastly, the quotation which I chose to prelude this thesis may seem unfitting to some, since condensed matter theory hardly lives up to the standards of mathematical rigour that Descartes proposed in his *regulae ad directionem ingenii*. As Descartes admitted himself, this is necessarily true for an science aspiring to describe and understand the material world, rather than contenting itself with formal logics. Thus, the words of Albert Einstein: *"As far as the laws of mathematics refer to reality, they are not certain; and as far as they are certain, they do not refer to reality."*,[b] do better justice to theoretical physics

---

[a]Majorana-fermions are fermionic particles with the property of being their own anti-particle. They were proposed by Ettore Majorana, who found that such particles are a solution of the Dirac-equation [133].

[b]Albert Einstein in "Geometry and Experience", January 27, 1921

in this respect. Still, I stumbled across this quotation during my first year at university in one of my undergraduate textbooks,[a] and they remained a source of motivation to me ever since.

Roland Grein, January 2012

---

[a]"Lehrbuch der Analysis, Teil 1", Harro Heuser, Teubner, 15th edition, 2003

List of Publications

Parts of the work discussed in this thesis have already been published, specifically:[a]

- *"Spin-Dependent Cooper Pair Phase and Pure Spin Supercurrents in Strongly Polarized Ferromagnets"*
  R. Grein, M. Eschrig, G. Metalidis, and G. Schön, Phys. Rev. Lett. **102**, 227005 (2009) – is covered in chapters 3 and 6,

- *"Theory of superconductor-ferromagnet point-contact spectra: The case of strong spin polarization"*
  R. Grein, T. Löfwander, G. Metalidis, and M. Eschrig, Phys. Rev. B **81**, 094508 (2010) Editors' Suggestion – is covered in chapters 3, 4, 5 and the appendix,

- *"Spin polarization of (Ga,Mn)As measured by Andreev spectroscopy: The role of spin-active scattering"*
  S. Piano, R. Grein, C. J. Mellor, K. Výborný, R. Campion, M. Wang, M. Eschrig, and B. L. Gallagher, Phys. Rev. B **83**, 081305(R) (2011) – is covered in chapter 5,

- *"Is CrO2 Fully Spin Polarized? Analysis of Andreev Spectra and Excess Current"*
  T. Löfwander, R. Grein, M. Eschrig, Phys. Rev. Lett. **105**, 207001 (2010) – is covered in chapter 5,

- *"A Numerical Study of the Superconducting Proximity Effect in Topological Surface States"*
  R. Grein, J. Michelsen, and M. Eschrig, arXiv:1111.0445 (2011), submitted to J. Phys.: Conf. Ser. – is covered in chapters 8 and 10.

Further publications not covered here are:

- *"Nonlocal conductance via overlapping Andreev bound states in ferromagnet-superconductor heterostructures "*
  G. Metalidis, M. Eschrig, R. Grein, and G. Schön, Phys. Rev. B **82**, 180305(R) (2010),

- *"Signature of odd-frequency pairing correlations induced by a magnetic interface"*
  J. Linder, A. Sudø, T. Yokoyama, R. Grein, and M. Eschrig, Phys. Rev. B **81**, 214504 (2010) Editors' Suggestion,

- *"Electronic dispersion anomalies in the iron pnictide superconductor $Ba_{1-x}K_xFe_2As_2$"*
  Andreas Heimes, R. Grein, Matthias Eschrig, Phys. Rev. Lett. **106**, 047003 (2011).

---

[a]Some parts of this work were also discussed in the diploma thesis of the author, albeit in a less mature way [51].

Acknowledgements

Part I.

On the Triplet Proximity Effect in Superconductor-Ferromagnet Heterostructures

1. Superconductor-Ferromagnet Heterostructures

The basic phenomenon behind the physical effects observed in superconducting nanostructures is the so-called proximity effect [30]. It can quite generally be understood as the penetration of one ordered state of matter into another – a situation which is typically realised at interfaces between materials with different ground states. In the particular case of singlet, s-wave superconductivity and ferromagnetism – which we shall be concerned with here – this situation becomes even more interesting, since these states are mutually exclusive [18, 11]. A singlet superconductor pairs electrons with opposite spin orientation, while the ferromagnetic states favours the alignment of electron spins. How this fundamental contradiction can be overcome and the interpenetration of such states of matter achieved has been subject to intense research activity over the past decade [38]. It turned out that novel types of superconducting pairing, which remain unobserved in bulk-systems, arise at such interfaces, resulting in a rich phenomenology of physical effects. Thus, these devices are not only interesting in terms of functionality, but also from a fundamental point of view.

This chapter is supposed to provide a general introduction to this topic and review some of the very recent experimental results in this area. As such, it hopefully constitutes a convincing motivation for the theoretical questions which are at the heart of this part of the thesis.

1.1. Symmetry Classification of Pairing Correlations

In this section, we shortly explain why the symmetrisation postulate, being the basis of many-body quantum mechanics, enforces a symmetry constraint for pairing correlations, and how this fact can be used to chart all possible types of pairing. On that basis, we then discuss the pairing correlations induced by the proximity effect at superconductor-ferromagnet interfaces.

The model Hamiltonian used by Bardeen, Cooper and Schrieffer to give a first microscopic explanation of superconductivity [8] has the following general structure in real space [2]:

$$\mathcal{H} = \mathcal{H}_0 + \mathcal{H}_{\text{int}}, \tag{1.1}$$

$$\mathcal{H}_{\text{int}} = \int d^3x \int d^3\mu \sum_{\alpha,\beta,\gamma,\eta} V_{\alpha,\beta,\gamma,\eta}(4,3,2,1)\Psi_\alpha^\dagger(4)\Psi_\beta^\dagger(3)\Psi_\gamma(2)\Psi_\eta(1),$$

where $\mathcal{H}_0$ is the single-particle Hamiltonian and $\mathcal{H}_{\text{int}}$ describes the pairing interaction. Moreover, $\mu \in \{1, 2, 3, 4\} : \mu = \mathbf{x}_\mu$ and $d^3\mu = \prod_\mu d^3 x_\mu$. In standard BCS-theory we have [2]:

$$V_{\alpha,\beta,\gamma,\eta}(4, 3, 2, 1) = \lambda \delta_{\beta\gamma} \delta_{\alpha\eta} \prod_{\mu=1}^{4} \bar{\delta}^3(\mathbf{x}_\mu - \mathbf{x}), \tag{1.2}$$

where $\lambda < 0$ is a constant and $\bar{\delta}^3$ is defined by [2]:

$$\bar{\delta}^3(\mathbf{x}) = \frac{1}{(2\pi)^3} \int d^3 p \; \theta_{\mathbf{p}} e^{i\mathbf{p}\vec{x}} \quad \theta_{\mathbf{p}} = \begin{cases} 1 & |\epsilon(\mathbf{p}) - E_{\text{F}}| < \epsilon_c \\ 0 & |\epsilon(\mathbf{p}) - E_{\text{F}}| > \epsilon_c \end{cases}. \tag{1.3}$$

Here, E_{F} is the Fermi-energy of the system's normal state, $\epsilon(\mathbf{p})$ the single-particle dispersion, and ϵ_c an energy cut-off of the interaction, usually assumed to be the Debye-frequency. The solution of this problem, pioneered by BCS, is based on a mean-field approximation which results in a Hamiltonian that is second order in field-operators. To this effect, one considers the expectation values

$$\langle \Psi_\gamma(2)\Psi_\eta(1)\rangle, \quad \langle \Psi_\alpha^\dagger(4)\Psi_\beta^\dagger(3)\rangle \tag{1.4}$$

with respect to the equilibrium state of the system and defines the superconducting order parameter as:

$$\Delta_{\alpha,\beta}(4, 3) = \int d^3 x_2 d^3 x_1 \sum_{\gamma,\eta} V_{\alpha,\beta,\gamma,\eta}(4, 3, 2, 1)\langle \Psi_\gamma(2)\Psi_\eta(1)\rangle. \tag{1.5}$$

Thus, within this mean-field treatment, the superconducting state can be characterised by correlation functions of the form:

$$f_{\alpha,\beta}(\mathbf{x}, \mathbf{x}', t, t') = \langle \Psi_\alpha(\mathbf{x}, t)\Psi_\beta(\mathbf{x}', t')\rangle, \tag{1.6}$$

$$\tilde{f}_{\alpha,\beta}(\mathbf{x}, \mathbf{x}', t, t') = \langle \Psi_\alpha^\dagger(\mathbf{x}, t)\Psi_\beta^\dagger(\mathbf{x}', t')\rangle, \tag{1.7}$$

if we transform to the Heisenberg-picture. These so-called *pairing correlations* are only non-zero in the superconducting state, and the symmetry classification of superconducting states amounts to classifying the possible symmetries of these functions under particle-exchange [42]. The basic ingredients of this classification are (a) the symmetrisation postulate (or Pauli principle), implying that fermionic field-operators anti-commute and (b) the fact that the field-operators entering these functions are of the same type and that an exchange of field-operators is thus formally identical to an exchange of coordinates. Such correlation functions enter any Green's function formalism describing the superconducting state as *anomalous* Green's functions. Their specific definition depends on the Green's function formalism in question and may be different from the one chosen above.[a] Their fundamental structure, however, is always the same and the argumentation laid out in the following thus holds irrespective of these technical details.

The equilibrium state of a translationally invariant system does not depend on the 'centre of mass' coordinates in time and space, i.e. $\mathbf{R} = (\mathbf{x} + \mathbf{x}')/2$ and $T = (t + t')/2$. These coordinates are also invariant under the exchange $\mathbf{x} \leftrightarrow \mathbf{x}'$, $t \leftrightarrow t'$, while the corresponding relative coordinates change sign. Usually, one then considers the Fourier-transform of

---

[a]If the time coordinates introduced here are understood to reside on the Keldysh contour, f is identical to the Keldysh part F^{K} of the Gor'kov Green's function up to a constant factor (cf. Ref. [102]). In equilibrium, it is more convenient to discuss this argument in terms of Matsubara correlation functions [42].
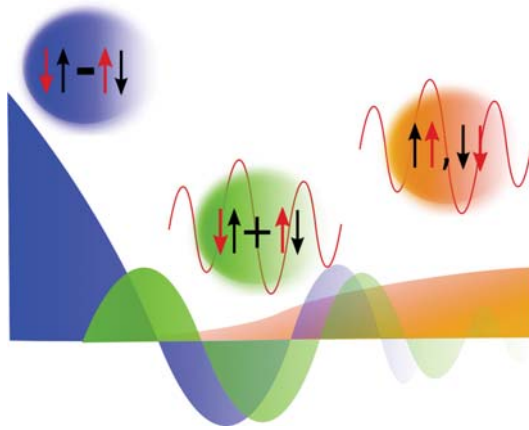
Figure 1.1. – Sketch of the singlet, s-wave (blue) and odd-frequency $S_z = \pm 1$ (orange) and $S_z = 0$ (green) correlations present at superconductor/ferromagnet interfaces as a function of the spatial coordinate.

the correlation functions with respect to the relative time and space coordinate, i.e. $\mathbf{r} = \mathbf{x} - \mathbf{x}' \mapsto \mathbf{p}$, $\bar{t} = t - t' \mapsto \omega$. This eventually results in the symmetry constraint [42]:

$$f_{\alpha,\beta}(\mathbf{p}, \omega) = -f_{\beta,\alpha}(-\mathbf{p}, -\omega), \tag{1.8}$$

which one may use to classify the possible pairing correlations. Relation (1.8) can be reformulated as [42, 40]:

$$\left(\text{momentum} = \begin{Bmatrix} \text{even} \\ \text{odd} \end{Bmatrix} \right) \times \left(\text{frequency} = \begin{Bmatrix} \text{even} \\ \text{odd} \end{Bmatrix} \right) \times \left(\text{spin} = \begin{Bmatrix} \text{even} \\ \text{odd} \end{Bmatrix} \right) = \text{odd}, \tag{1.9}$$

to obtain the classification scheme. Conventional superconductivity is even in momentum and frequency but odd in spin. The same holds for cuprate superconductors [129] and is at least very likely in a large number of the recently discovered iron-based superconductors [84, 82]. Triplet-superconducting states which are odd in momentum can for instance be found in superfluid He^3 [130].[a]

This scheme cannot only be used to classify superconducting bulk-states. At interfaces between superconducting and non-superconducting materials, pairing correlations will be induced in the normal region by means of the proximity effect and those in the superconductor will be modified. The latter is sometimes referred to as 'inverse' proximity effect. Far away from the interface, the pairing correlations drop to zero in the normal region and recover their bulk value inside the superconductor (SC). If the non-superconducting material breaks additional symmetries compared to the superconductor, it is to be expected that pairing correlations belonging to symmetry classes different from that of the SC bulk-state are induced. A ferromagnet breaks spin-rotation symmetry. Thus, correlation breaking spin-rotation symmetry, i.e. triplet amplitudes, are to be expected. Since triplet amplitudes are even in spin, they have to be odd in either momentum or frequency. Generally, both cases may occur [40]. If, however, impurity scattering is strong, correlations that are odd in momentum will be suppressed [10, 40]. Thus, the proximity effect will be dominated by odd-frequency triplet correlations unless the nanostructure is in the ballistic limit.

A further sub-classification can be applied to these triplet amplitudes [40]. Recall that f is a matrix in spin-space. We call its diagonal entries, $f_{\uparrow,\uparrow}$ and $f_{\downarrow,\downarrow}$, equal-spin triplet, or

---

[a]In the case of bulk-superconductors, the classification refers to Δ rather than to the f-functions.

$S_z = \pm 1$ amplitudes. We may also use the corresponding two-particle spin-wave functions $|\uparrow\uparrow\rangle$, $|\downarrow\downarrow\rangle$ to denote them. The amplitude $(f_{\uparrow,\downarrow} + f_{\downarrow,\uparrow})/2$ is the opposite-spin triplet, or $S_z = 0$ component, and we may write $|\uparrow\downarrow\rangle + |\downarrow\uparrow\rangle$ to refer to it. $(f_{\uparrow,\downarrow} - f_{\downarrow,\uparrow})/2$ is the usual singlet ($|\uparrow\downarrow\rangle - |\downarrow\uparrow\rangle$) amplitude. The reason for this distinction is that the ferromagnetic exchange field is as detrimental to the $|\uparrow\downarrow\rangle + |\downarrow\uparrow\rangle$-correlations as to the singlet ones. The equal spin correlations, on the other hand, are insensitive to the exchange field and are thus also called 'long range' [10, 39].

This situation is sketched in Fig. 1.1, illustrating qualitatively the behaviour of the relevant symmetry components at an SC/FM interface. The singlet s-wave correlations of the bulk superconductor show an oscillating decay into the ferromagnetic region, while $S_z = 0$ and $S_z = \pm 1$ triplet components are induced. The first meet the same fate as the original singlet correlations, since they still pair electrons with opposite spin. The $S_z = \pm 1$ correlations, on the other hand, can penetrate the ferromagnet on the scale of the normal metal coherence length.

The suppression of all $S_z = 0$ components is a consequence of the fact that the paired electrons no longer have the same magnitude of momentum due to the exchange field. Another way to put it is that the correlations acquire a finite centre of mass momentum. They hence decay on the scale of the magnetic coherence length $\xi_J = \hbar/(p_\uparrow - p_\downarrow)$ in the clean limit and this situation also leads to their oscillating behaviour [18]. The $S_z = 0$ proximity effect was first observed in 2001 by Ryazanov et al. [104]. Obviously, finding any sizeable effect arising from the $S_z = 0$ amplitude requires a relatively weak exchange field. This can be realised in ferromagnetic alloys. For example, Ryazanov et al. used $Cu_x Ni_{1-x}$ with $x \approx 0.5$ in their experiment [104].

Most natural ferromagnets, however, have an exchange field which is of the order of the Fermi-energy, implying that all $S_z = 0$ components are suppressed on the interatomic length scale [39]. Consequently, the question under which circumstances the $S_z = \pm 1$ amplitudes can be induced at an SC/FM interface arose, and a first answer was provided by Bergeret and coworkers [10]. As it is this $S_z = \pm 1$ proximity effect that we are interested in here, the question how these correlations come about will be addressed in the next section.

1.2. Singlet-Triplet Conversion through Interface Scattering

So far, we only provided a vague symmetry argument as a motivation for the creation of triplet amplitudes and what makes the creation of a $S_z = \pm 1$ proximity effect more complicated than the $S_z = 0$ case is unclear as of now. We shall see in a second that a homogeneous exchange field in the FM-region can only induce the $S_z = 0$ component. However, as opposed to singlet correlations, this component is no longer invariant under rotations in spin-space [40]. Hence, other components of the triplet-subspace can be created by introducing an inhomogeneous exchange field. This idea was first investigated by Bergeret et al. [10] in terms of domain wall at the SC/FM-interface whose magnetisation direction varies continuously over the width of the wall.

In a ferromagnet where the exchange field is of the order of the Fermi-energy, this domain wall would have to be atomically thin, i.e. the rotation must be abrupt. Otherwise, the $S_z = 0$ components would decay to zero before the conversion becomes effective [39]. This lead Eschrig et al. [39] to consider a different take on the problem. An atomically thin domain wall would effectively be part of the interface and, consequently, the conversion must happen directly in the interface region. Treating the interface within a scattering formalism, they then showed that equal-spin triplet correlations arise from a combination of two scattering effects, namely spin-mixing and spin-flip scattering. This is the conversion mechanism relevant to this thesis and we shall discuss it in detail here.

These are certainly not the only theoretical approaches to this problem. In fact, a huge number of proposals have been put forward and investigated using various techniques, but we refrain from giving a complete account of the theoretical developments in this area. A very recent overview over both experimental and theoretical advances is provided in Ref. [38], while Ref. [11] is a more comprehensive but also older review.

Spin-mixing effect

The 'spin-mixing effect' quite simply means that electron with different spin-orientation acquire different scattering phases upon scattering at a ferromagnetic surface or interface. Simple calculations show that this effect is ubiquitous for any spin-dependent scattering potential. The difference of scattering phases $\vartheta(\mathbf{k}) = \varphi_\uparrow(\mathbf{k}) - \varphi_\downarrow(\mathbf{k})$, which usually depends on the wave vector of the incident particles is called *spin-mixing angle* [39] here, but is also called spin-dependent interface phase shift (SDIPS) in the literature (see Ref. [25], for instance). Chapter 4 is devoted to an investigation of this mixing angle in different models of the interface region.

A simple hand-waiving calculation shows how the $S_z = 0$ triplet component is induced by these scattering phases [39]. We consider the wave function of a conventional Cooper-pair:

$$|\mathbf{k}\uparrow, -\mathbf{k}\downarrow\rangle - |\mathbf{k}\downarrow, -\mathbf{k}\uparrow\rangle. \tag{1.10}$$

Upon scattering, the single particle wave functions acquire a scattering phase according to their spin [39]:[a]

$$|-\mathbf{k}\uparrow\rangle = |\mathbf{k}\uparrow\rangle e^{i\varphi_\uparrow(\mathbf{k})}, \quad |-\mathbf{k}\downarrow\rangle = |\mathbf{k}\downarrow\rangle e^{i\varphi_\downarrow(\mathbf{k})}. \tag{1.11}$$

This implies that the Cooper-pair wave function transforms to [39]:

$$|\mathbf{k}\uparrow, -\mathbf{k}\downarrow\rangle e^{i(\varphi_\uparrow(\mathbf{k})-\varphi_\downarrow(\mathbf{k}))} - |\mathbf{k}\downarrow, -\mathbf{k}\uparrow\rangle e^{-i(\varphi_\uparrow(\mathbf{k})-\varphi_\downarrow(\mathbf{k}))}, \tag{1.12}$$

upon scattering at the interface, which we may rewrite as:

$$\cos\vartheta(\mathbf{k}) \cdot (|\mathbf{k}\uparrow, -\mathbf{k}\downarrow\rangle - |\mathbf{k}\downarrow, -\mathbf{k}\uparrow\rangle) + i\cdot\sin\vartheta(\mathbf{k}) \cdot (|\mathbf{k}\uparrow, -\mathbf{k}\downarrow\rangle + |\mathbf{k}\downarrow, -\mathbf{k}\uparrow\rangle). \tag{1.13}$$

Hence, we see that a $S_z = 0$ triplet component proportional to $\sin\vartheta(\mathbf{k})$ is induced. The spin-independent scattering phase $\varphi(\mathbf{k}) = [\varphi_\uparrow(\mathbf{k}) + \varphi_\downarrow(\mathbf{k})]/2$ is irrelevant.

Spin-flip scattering

As argued above, an additional spin-quantisation axis must enter the game to rotate parts of the $S_z = 0$ component into the required $S_z = \pm 1$ correlations. This is achieved by considering a spin-dependent interface potential whose quantisation axis is misaligned with respect to the ferromagnet. This misalignment is characterised by two spherical angles, α and φ, as shown in Fig. 1.2. The most obvious physical model that springs to mind is a canted ferromagnetic domain [40], but other mechanisms, like an interface with spin-orbit coupling [41], are also possible. The latter case, in which the misalignment angles become $\mathbf{k}$-dependent, has attracted attention very recently in the ongoing hunt for topological superconductors [22].

For now, we shall leave it at that. A thorough investigation of models for interface scattering is presented in chapter 4.

---

[a]The notation is somewhat sloppy here. If the interface is translationally invariant, scattering conserves parallel momentum, i.e., $\mathbf{k} = (\mathbf{k}_{||}, k_z) \to (\mathbf{k}_{||}, -k_z)$. If the scattering phases are the same for $\mathbf{k}_{||}$ and $-\mathbf{k}_{||}$, which is generically true if the scattering potential is not $\mathbf{k}$-dependent, the relations stated in this equation hold.
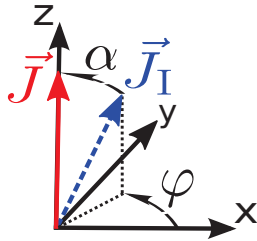
Figure 1.2. – The spherical angles characterising the misalignment of the interface spin-quantisation axis with respect to the magnetisation of the ferromagnetic bulk.

1.3. The Long Range Triplet Proximity Effect in Experiment

So far, the experimental verifications of a proximity effect due to the long range $S_z = \pm 1$ components are mostly based on the Josephson effect. The general argumentation is that if a Josephson current is measured across a SC/FM/SC junction with a FM-interlayer whose thickness exceeds the magnetic coherence length ξ_J, the superconducting correlations carrying this Josephson-current must be of the $S_z = \pm 1$ type. In this sense, the evidence is indirect but – in our opinion – certainly conclusive.

The Keizer-experiment

The first article reporting such a Josephson-current was published by Keizer and coworkers in 2006 [67]. Their setup consisted of two NbTiN-electrodes deposited on a layer of CrO_2, a half-metallic, i.e. a fully or almost fully spin-polarised, ferromagnet [23]. The CrO_2 film was grown on a TiO_2 substrate. Their data shows a Josephson current across junctions which are more than half a micron long.

In a half metal, where the minority spin band is completely absent, the conversion from singlet to triplet correlations must happen in the interface region, as outlined above. CrO_2 is metastable and rapidly oxidises at the surface to Cr_2O_3 [67]. Keizer et al. claim that they were able to remove this oxidised layer when creating the contacts to the superconducting electrodes. In any case, spin-active scattering must be induced at the contact, possibly by canted magnetic moments – an assumption which is supported by the fact that the observed critical currents show substantial variations between different samples. This may indicate that the interfaces, which form spontaneously, vary in their effectiveness of singlet-triplet conversion [67].

In the presence of a magnetic field H, the relatively poor Fraunhofer pattern shows a hysteresis loop as a function of the magnitude of the magnetic field, which an be understood from the magnetic anisotropy of the sample. The magnetisation M also implies an offset of the magnetic field B, resulting in a minimum of the Fraunhofer pattern at $H = 0$.

What is even more remarkable is that the critical current was shown to depend on the orientation of the magnetisation, which can be considered further evidence for the theoretical picture promoted here.

Only two months after the publication of this work, Sosnin et al. [118] reported a long range proximity effect in an Al/Ho junction. Ho becomes ferromagnetic below 21 K with a conical magnetisation structure, i.e. the magnetisation rotates along the c-axis of the crystal, thus providing an inhomogeneous magnetisation texture and thereby realising the original idea of Bergeret et al. [38]. In their Andreev interferometer device, they observed resistance oscillations as a function of the introduced magnetic flux up to Ho-layer lengths of 150nm, which exceeds the penetration depth of $S_z = 0$ correlations by far.

The year of triplet supercurrents

After the tantalising discoveries of Keizer et al. and Sosnin et al., the race was on for further confirmations of these effects. After several years of failed attempts, and the first jokes being made about the Keizer-experiment entering the annals of irreproducible experiments, 2010 proved to be the year of triplet supercurrents. Several groups confirmed the observation of long range supercurrents through strongly spin-polarised ferromagnets using different approaches and materials, all sharing the common idea that an inhomogeneous magnetisation must somehow be introduced at the SC/FM-contacts.

Anwar et al. [4] confirmed the Keizer-experiment on CrO_2, using both a different superconductor (amorphous $Mo_{70}Ge_{30}$) and a different substrate (Al_2O_3), but failed to reproduce a Josephson-coupling with TiO_2 as substrate. The current densities they found are considerably smaller than those of the Keizer-experiment and a Fraunhofer pattern was not observed. Hence, although the evidence for a supercurrent is clear, the riddle of the proximity effect in CrO_2 is still not solved. An important point in this respect seems to be that there is no direct control over the interfaces which must provide the conversion mechanism.

Khaire et al. [68, 69] overcame this problem by creating a complex multilayer structure where spin-active interfaces are introduced artificially. The interfaces consist of ferromagnetic alloys (either PdNi or CuNi) separated by Cu buffer layers from the central, strongly spin-polarised part of the device, which is made of Co. A major innovation was the additional introduction of an antiferromagnetic Ru-layer sandwiched between two extended layers of Co, enforcing an antiparallel magnetisation direction of the Co layers and thereby cancelling their intrinsic magnetic field. This resulted in a very clear Fraunhofer pattern whose quality exceeds that of the Keizer-experiment by far. Khaire and coworkers then showed that the effectiveness of singlet-triplet conversion can be controlled by the thickness of the alloy layers and they observed a crossover from the singlet-Josephson effect, which is rapidly suppressed as a function of the Co-layer thickness, to the triplet one, which showed no sign of decay for the junction lengths considered in Ref. [68] (up to 28nm) and a slow decay in their follow-up work [69] (up to 50nm). The origin of the inhomogeneous magnetisation structure was attributed to the domain wall structure of the weakly ferromagnetic alloys due to their out-of-plane magnetisation anisotropy. In their later work [69], they achieved even better results with pure Ni, which, according to them, has an in-plane magnetisation in Ni/Co layered structures and larger domain sizes than the alloys. This supports the picture that the relevant magnetisation misalignment is the one between the interface layer and the central Co part and not the one between different domains of the interface. This group also managed to enhance the effect even more by maximising the misalignment of the Ni layers with the help of a magnetic field [71]. Khaire et al. argue that their experiment is best described by the model of Houzet and Buzdin [57], who considered a ferromagnetic trilayer sandwiched between superconducting electrodes, but that the diffusive limit discussed in this work is not applicable to their samples [69].

Robinson et al. [103] used the holmium idea to create an inhomogeneous magnetisation profile in a Josephson junction whose central part was also made of Co. They did not use the ruthenium trick to obtain nice Fraunhofer patterns, but found a non-monotonic dependence of the critical current on the Ho thickness. This can, according to them, be attributed to a maximisation of the magnetisation inhomogeneity for Ho thicknesses that correspond to half complete windings of the magnetisation direction. They found a slow decay of the critical current for Co layers of up to about 16nm, which means that the junctions were shorter than those of Khaire et al., but still long enough to rule out a Josephson coupling carried by $S_z = 0$ correlations.

Evidence for a triplet Josephson current in the Heusler compound Cu_2MnAl was found

by Sprungmann et al. [120]. In this case, the conversion mechanism was attributed to a spin-glass phase forming at the contacts.

The longest Co-junction to show a supercurrent, no less than 600nm long, was reported by Wang et al. [132], who measured a Josephson current through a Co nanowire with tungsten forming the superconducting electrodes. How the conversion comes about is unclear in this case.

All in all, it is fair to say that the basic theoretical concepts behind the conjectured long range triplet proximity effect worked out over the past 10 years have been confirmed by these experimental results, which, on the other hand, certainly also raise a number of new questions deserving theoretical investigation.

In this context, the present thesis describes how the triplet Josephson effect can be described consistently with quasiclassical theory if the exchange field is of the order of the Fermi-energy. We investigate the critical current in the presence of domain wall structures and show that exotic current-phase relations may arise in high-transparency junctions. We argue that the latter may even imply the existence of a spin Josephson effect in junctions with only one SC-electrode.

1.4. Measuring the Spin-Polarisation

We now turn to another problem in the context of superconducting heterostructures, namely inferring the spin-polarisation of a ferromagnet from the differential conductance of a superconductor-ferromagnet point contact.

The basic idea was first proposed by de Jong and Beenakker [28], as a simple extension of the Blonder-Tinkham-Klapwijk theory [15] of transport across superconductor-normal metal contacts. The superconducting density of states has a gap at the Fermi energy which renders charge transport carried by single-particle excitations impossible unless the applied voltage exceeds the gap-energy.[a] The only process that contributes to transport at these energies is Andreev[b] reflection. In this case, a Cooper pair is created in the superconductor as a quasiparticle tunnels into it and a hole is coherently reflected into the non-superconducting metal. In the case of a conventional superconductor, the singlet symmetry of the Cooper-pair wave function requires that the reflected hole excitation has opposite spin with respect to the incident electron.[c]

Now, if the non-superconducting metal is spin-polarised, i.e. the density of states at the Fermi-level is different for spin-up and spin-down electrons, this process is naturally suppressed, since incoming spin-up particles have a reduced chance to find a spin-down partner for the Andreev process, as illustrated in Fig. 1.3. De Jong and Beenakker formulated a minimal model that accounts for this effect. They solved the BdG-equation with a step function switching between the pair-potential of the superconductor and the exchange field of the ferromagnet at the interface. This model thereby introduces wave vector mismatches at the interface which reduce transmission. These are neglected in BTK-theory, but inevitably present at such a contact. The first experiments using this idea to infer the spin-polarisation of ferromagnetic materials were carried out by Soulen et al. [119] and Upadhyay et al. [127]. For fitting their data, Soulen et al. used a model based on the idea of de Jong and Beenakker which neglects the wave vector mismatches. They write

---

[a]More precisely, this is true at $T = 0$.

[b]More precisely: Andreev-Saint-James reflection, as explained in Ref. [29]. We opt for the shorter, even though unjust terminology here.

[c]For reasons that will become clear later on, we define the spin of a hole excitation as the spin of the unoccupied state it is associated to.
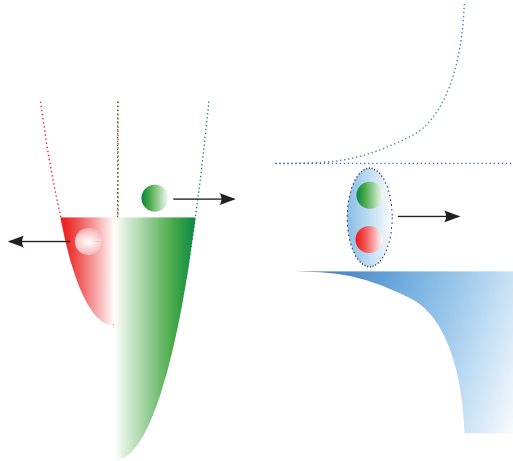
Figure 1.3. – The process of Andreev reflection at a superconductor-ferromagnet contact. In the ferromagnet (left), the DOS of spin-down quasiparticles (red) is reduced compared to that of spin-up quasiparticles. The superconductor (right) has an energy gap in the single-particle density of states. The injection of a pair into the superconducting condensate requires the coherent transmission of a spin-up and a spin-down quasiparticle into the superconductor. This implies the coherent reflection of a hole excitation in the down-band, as an up-quasiparticle transmits from the ferromagnet into the superconductor. Figure adapted from Ref. [119].

the conductance of the point-contact as a sum of two contributions [119]:

$$G(V) = (1 - P_C)G_{\text{BTK}}(V) + P_C G_H(V), \tag{1.14}$$

where $G_{\text{BTK}}(V)$ is the BTK-conductance formula for a superconductor-normal metal contact and P_C the so-called transport spin-polarisation [119]:

$$P_C = \frac{N_{\text{F}\uparrow}v_{\text{F}\uparrow} - N_{\text{F}\downarrow}v_{\text{F}\downarrow}}{N_{\text{F}\uparrow}v_{\text{F}\uparrow} + N_{\text{F}\downarrow}v_{\text{F}\downarrow}}. \tag{1.15}$$

The conductance G_H corresponds to the spin-up transport channels for which no spin-down partner exists, i.e. $G_H = 0$ for $|eV| < \Delta$. To obtain an expression for G_H, Soulen et al. use the BTK result again and simply put the contribution of Andreev reflection to zero. Subsequently, they renormalise the remaining contributions to ensure charge conservation [119]. The exact fitting formulas used by Upadhyay et al. are not clear from their publication, but were apparently obtained along similar lines as those published later by Mazin et al. [83]. In both cases, one ends up with a fitting formula that has only two parameters, the interface barrier parameter Z and the transport spin-polarisation P_C. The latter is then 'measured' by fitting the spectra to this formula. A formula for G_H obtained from a rigorous calculation, used as well for experimental fitting (see Refs. [135, 138], for instance), was later given by Mazin et al. [83]. This work did, however, not remedy the other shortcomings of the Soulen fitting formula, i.e. the neglect of wave vector mismatches and, more generally, the channel or **k**-dependence of all parameters characterising the contact, as well as further effects related to the spin-activity of such a magnetic interface.

In this thesis, we propose a generalised theory for the conductance of such a point-contact, taking into account the Fermi-surface geometry at the contact and the presence of spin-active scattering potentials. Although our results are obtained from a quasiclassical description, we find that they reproduce Mazin's formulas, which were obtained within a 'full quantum' formalism, exactly in the appropriate limiting case [53]. Moreover, we discuss applications of our model to experimental results on (Ga,Mn)As [98], one of the most important ferromagnetic semiconductors, and CrO_2 [81], which attracted a lot of attention in the context of triplet supercurrents.

2. Quasiclassical Theory of Superconductivity

In this chapter, we give a brief account of the Quasiclassical Theory of Superconductivity and in particular its application to heterostructures. This theory exploits a natural separation of energy scales and thereto related length scales which exists in most conventional superconductors.[a]

This situation is fully analogous to the one we encounter in a normal Fermi-liquid. The latter was first discussed by Landau [75], his fundamental insight being that the Fermi-liquid emerges from a gas of non-interacting Fermions as the interaction is adiabatically turned on and that there is a bijective map between the final states of the Fermi-liquid and the original particles of the gas [75, 24]. This is a direct consequence of the fact that fermionic particles are subject to the Pauli principle. The ground state of the Fermi-gas is a sphere of occupied states in k-space whose surface is called Fermi-surface. At finite temperatures, this surface is 'washed out' on a width proportional to T. Any scattering due to interactions between the particles is suppressed by a factor T^2 [75] in this thin layer around the Fermi-surface, as a result of their fermionic nature. This guarantees, according to Landau, the adiabatic evolution of the ground state as the interactions are turned on. As we know, there is a number of many-electron systems which do not self-organise as Fermi-liquids, i.e., this reasoning is only true for a certain range of interactions and particle densities. The Fermi-energy of such a liquid, i.e. the kinetic energy of electrons at the Fermi-surface, is usually very large compared to temperature, implying that the scattering rate of states in the Fermi-shell is strongly suppressed. Consequently, these states have quasi-infinite lifetime and were therefore called quasiparticles by Landau. The quasiparticles have renormalised properties due to the interactions but can be considered as effectively non-interacting. It follows from the above that only particles in this thin shell around the Fermi-surface can participate in any response of the system to external perturbations. To describe the dynamics of a Fermi-liquid, it is therefore sufficient to devise a theory which only takes into account these states. The quasiparticle states themselves are 'robust' against perturbations on the energy scale set by temperature. Thus, only changes in the distribution function of quasiparticles must be accounted for, which leads to a Boltzmann-type transport equation [75].

---

[a]In the following 'historical' outline, original articles are in some cases cited together with a secondary source that we obtained the information from. A more extensive list of original references is provided in Ref. [37], on which this overview is loosely based.

In most conventional superconductors, the superconducting energy gap is roughly 2-3 orders of magnitude smaller than the Fermi-energy of the superconductor in the normal state. Hence, the superconducting order is equally confined to this thin shell around the Fermi-surface and one is led to expect that a theory similar to Landau's Fermi-liquid theory can be put forward. An important difference is, however, that the quasiparticles of the superconductor in vicinity to the Fermi-surface are not the 'robust' quasiparticles of the normal Fermi-liquid, but rather linear superpositions of pairs of such states. In BCS-theory, the operators that create quasiparticles from the ground state read [113]:

$$\gamma^\dagger_{\mathbf{k}\uparrow} = u_{\mathbf{k}}c^\dagger_{\mathbf{k}\uparrow} - v_{\mathbf{k}}c_{-\mathbf{k}\downarrow}, \quad \gamma^\dagger_{-\mathbf{k}\downarrow} = u_{\mathbf{k}}c^\dagger_{-\mathbf{k}\downarrow} + v_{\mathbf{k}}c_{\mathbf{k}\uparrow}, \tag{2.1}$$

where $c_{\mathbf{k}\sigma}, c^\dagger_{\mathbf{k}\sigma}$ annihilate and create single particle excitations in the normal state and $v_{\mathbf{k}}, u_{\mathbf{k}}$ are scalar factors. This implies a coherent superposition of particle-like and hole-like states. The ground state of the superconductor, i.e. the condensate, is described on the same footing [113]:

$$|\Psi_0\rangle = \prod_{\mathbf{k}}(u_{\mathbf{k}} + v_{\mathbf{k}}c^\dagger_{\mathbf{k}\uparrow}c^\dagger_{-\mathbf{k}\downarrow})|0\rangle. \tag{2.2}$$

As far as this superposition is concerned, the states are susceptible to change on the small energy scale. Consequently, a kinetic equation for the distribution function is no longer sufficient. The corresponding quasiclassical theory must explicitly take into account this particle-hole degree of freedom and describe *"the coupled dynamics of both the quasiparticle states and their occupation"* [36].

The Quasiclassical Theory of Superconductivity discussed here makes explicit use of this separation of energy and length scales by integrating out the fast oscillations of the Nambu-Gor'kov Green's function on the scale of the Fermi-wavelength λ_{F}, retaining only an envelop function which varies on the scale of the superconducting coherence length $\xi_0 = \hbar|\mathbf{v}_{\mathrm{F}}|/2\pi k_{\mathrm{B}}T_{\mathrm{c}}$ [37]. This derivation was first carried out by Eilenberger and Larkin and Ovchinnikov [33, 76, 37] for equilibrium Green's functions and later generalised to non-equilibrium situations by Eliashberg, Larkin and Ovchinnikov and Schmid and Schön [34, 77, 109, 115, 37]. A mathematically more rigorous derivation was eventually given by Shelankov [115]. The properties of the system which are determined at the high energy and short wavelength scale, like the Fermi-surface geometry for example, enter the quasiclassical theory as phenomenological parameters. The resulting formalism provides an excellent description of systems whose parameters vary in time and space on a scale set by the 'low energy', i.e., on lengths comparable to the coherence length ξ_0 and times of order $\hbar/\Delta$ [37].

If one is concerned with heterostructures containing abrupt interfaces between different materials, the quasiclassical approach is bound to fail in the interface regions, where the system's properties vary rapidly on the interatomic scale, while being fully sufficient away from the interfaces (see Fig. 2.1). This led to the idea that quasiclassical propagators in the 'asymptotic' regions may be matched with a set of boundary conditions that have to be obtained from a microscopic description of the interface region. A first set of such boundary conditions was derived independently by Zaitsev [139, 89], Shelankov[a] [117, 37] and Kieselmann [89]. These were, however, restricted to interfaces between superconductors and normal metals and did not account for spin-dependent scattering. A generalisation accounting fully for spin-dependent scattering was later obtained by Millis et al. [89]. Such boundary conditions are in line with the general philosophy of quasiclassical theory. Relevant properties of the system which cannot be described within the theory itself enter

---

[a]These boundary conditions were, however, derived for the envelop functions of the wave function formalism.
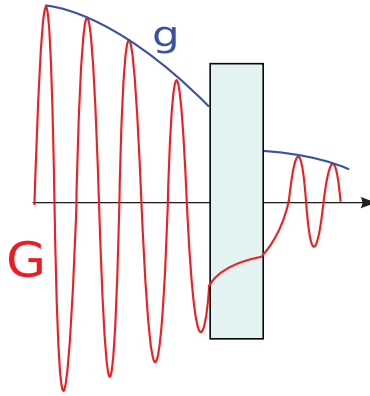
Figure 2.1. – The quasiclassical Green's function g can be understood as the envelop function of the microscopic Green's function G. It is not defined in an interface region where the system's properties vary rapidly. The envelop function is generally discontinuous across the interface. Figure from Ref. [51].

as phenomenological parameters. In this case, the parameters describe the scattering of quasiparticles at the interface and come in the form of a scattering matrix which must be assumed or calculated independently.

While these boundary conditions in principle allowed for describing heterostructures in quasiclassical theory, they are rather cumbersome and difficult to handle, since they are non-linear and admit unphysical solutions which need to be ruled out [36]. The fundamental problem is that solving the equation of motion for the quasiclassical Green's function and its accompanying normalisation condition is a boundary value rather than an initial value problem [37]. In other words, there is no obvious separation of 'incoming' and 'outgoing' solution with respect to the scatterer. This problem could eventually be overcome by introducing a particular parameterisation of the quasiclassical Green's function. These parameters obey transport equations which fall into the class of Riccati differential equations and were hence dubbed Riccati parameters [111, 112, 36]. They automatically guarantee the correct normalisation of the quasiclassical Green's function and, most importantly, transform the boundary value problem into initial value problems for the Riccati transport equations, thereby simplifying numerical calculations considerably [36]. In particular, the boundary conditions can be formulated as a system of linear equations [37] and thereby acquire a more transparent and tractable form.

The Riccati parameterisation was developed for the equilibrium case by Schopohl and Maki [111, 112], while the generalisation to Keldysh Green's functions and thus to non-equilibrium situations is due to Eschrig [35, 36]. A first set of boundary conditions for the Riccati parameters was obtained by Eschrig [36] and Shelankov and Osana [116]. They were, however, restrained to non-magnetic interfaces. After a number of generalisations [142, 46], a fully general solution of the scattering problem in quasiclassical theory was eventually presented by Eschrig [37] and it is this latest formulation that we shall employ here.

It should also be noted that other than incorporating interfaces and surfaces by a scattering matrix and boundary conditions into quasiclassical theory, one may also start from a transfer-Hamiltonian and treat the scatterer as a perturbation that directly enters the quasiclassical equation of motion [26, 37].

We would also like to emphasise that the Riccati parameterisation has merits which go beyond the undoubtful numerical advantages it provides. The Riccati equations in question are partial differential equations whose solutions can be assembled by integrating them

along straight lines, and they always have a definite stable direction of integration along those lines [36]. This allows us to think of Riccati parameters as quasiparticles moving along straight trajectories, although they do not, in an immediate sense, correspond to physical quasiparticles. On this basis, a diagrammatic representation of transport and scattering processes was developed by Löfwander, Zhao and Sauls [143, 144, 37] and extended by Eschrig [37], which simplifies the physical interpretation of results obtained from this theory considerably. Some applications of this will be discussed in the next chapter.

A full account of the development of quasiclassical methods for superconductors and their applications, spanning more than 50 years by now [49, 37], could fill a book of its own, which so far nobody found the time to write. An extensive review of the method in the context of its application to superfluid He^3 was given by Serene and Rainer [114], a thorough discussion of the Riccati formulation and its boundary conditions is provided in the seminal articles of Eschrig [36, 37]. The important diffusive limit of quasiclassical theory [128], is reviewed in Ref. [9], and the latest formulation of the boundary conditions for the diffusive case can be found in Ref. [25].

In what follows, we set up all the formalities needed to tackle the problems we shall be concerned with. This presentation will be rather sketchy as it constitutes no original work of the author. We choose to use the notation introduced by Eschrig [36, 37] and also the diagrammatic representation of Ref. [37].

2.1. The Quasiclassical Green's Function and its Equation of Motion

The starting point for the derivation of the quasiclassical Green's function is the Nambu-Gor'kov Green's function [113], being the Green's function formalism that directly corresponds to the BCS mean-field Hamiltonian. We use Keldysh's technique [102], which allows us to consider non-equilibrium phenomena.

The quasiclassical Green's function is formally obtained from the integration [114]:

$$\check{g}(\mathbf{p}_{\mathrm{F}}, \mathbf{R}, \varepsilon, t) = \frac{1}{a(\mathbf{p}_{\mathrm{F}})} \int \mathrm{d}\xi_p \hat{\tau}_3 \check{G}(\mathbf{p}, \mathbf{R}, \varepsilon, t), \qquad (2.3)$$

where $a(p_{\mathrm{F}})$ is a Landau renormalisation parameter and $\check{G}$ is the Nambu-Gor'kov Green's function. A check denotes a matrix in Keldysh-space and a hat a matrix in Nambu-Gor'kov space, i.e., the particle-hole degree of freedom. Specifically, we have:

$$\check{G}(x', x, t', t) = \begin{pmatrix} \hat{G}^{\mathrm{R}} & \hat{G}^{\mathrm{K}} \\ 0 & \hat{G}^{\mathrm{A}} \end{pmatrix}, \ \hat{G}^{\mathrm{R,A,K}} = \begin{pmatrix} G & F \\ -\tilde{F} & -\tilde{G} \end{pmatrix}^{\mathrm{R,A,K}}, \qquad (2.4)$$

from which $\check{G}(\mathbf{p}, \mathbf{R}, \varepsilon, t)$ is obtained by a transformation to relative and centre of mass coordinates and subsequent Fourier-transformations $\mathbf{r} \mapsto \mathbf{p}$ and $t \mapsto \varepsilon$. The matrices $\hat{\tau}_i$, $i = 1, 2, 3$, denote the Pauli matrices acting on particle-hole space, while σ_i are the Pauli-matrices acting on spin-space. The integration over momentum ($\xi_p = \mathbf{v}_{\mathrm{F}} \cdot (\mathbf{p} - \mathbf{p}_{\mathrm{F}})$) results in the elimination of the fast oscillations of $\check{G}$ on the scale of k_{F}. The off-diagonal elements of $\hat{G}^{\mathrm{R,A,K}}$ are the anomalous correlation functions describing pairing correlations. The resulting quasiclassical Green's function is generally a function of the spatial coordinate $\mathbf{R}$, the momentum $\mathbf{p}_{\mathrm{F}}$, which lies on the Fermi-surface, energy ε and time t [114]. While the Fourier-transformation of the spatial coordinate is mandatory to carry out the ξ_p-integration, the transformation of the time coordinate is not; and in fact, for a number of non-equilibrium problems it is advantageous to keep t, t' as parameters or Fourier-transform them individually.

The equation of motion for the quasiclassical Green's function is obtained from the Dyson-equation of the Nambu-Gor'kov Green's function. This involves a gradient expansion of the momentum operator, taking the difference between the Dyson-equation and its adjoint and carrying out the ξ_p-integration [114, 115]. The result is Eilenberger's equation:

$$i\hbar \mathbf{v}_{\mathrm{F}} \cdot \nabla_{\mathbf{R}} \check{g} + [\varepsilon \hat{\tau}_3 - \check{\Delta} - \check{h}, \check{g}]_{\otimes} = \check{0}. \tag{2.5}$$

Here, $\check{\Delta}$ denotes self-energies which are off-diagonal in particle-hole space, typically the order-parameter, and $\check{h}$ contains the diagonal components. These self-energies arise due to the mean-field treatment of interactions and impurity scattering, external fields can also be absorbed in these terms. $[\bullet, \bullet]_{\otimes}$ denotes a commutator with respect to the product $\otimes$, which combines a matrix product in Nambu-Gor'kov space with a convolution over internal time variables [114]. For our purposes, it reduces to the matrix product. The subtraction trick involved in the derivation of this equation results in a non-uniqueness of its solutions. It must hence be supplemented by a normalisation condition [114]:

$$\check{g} \otimes \check{g} = -\check{1}\pi^2. \tag{2.6}$$

The quasiclassical equation of motion is also complemented by a set of self-consistency relations arising from the mean-field treatment of superconducting pairing (BCS-theory) and other interactions (Landau parameters) [114]. The self-consistency relation for the superconducting order parameter reads [114]:

$$\Delta^{\mathrm{R}}(\mathbf{p}_{\mathrm{F}}, \mathbf{R}, t) = \int \frac{d\varepsilon}{4i\pi} \left\langle V(\mathbf{p}_{\mathrm{F}}, \mathbf{p}'_{\mathrm{F}}) f^{\mathrm{K}}(\mathbf{p}'_{\mathrm{F}}, \mathbf{R}, \varepsilon, t) \right\rangle_{p'_{\mathrm{F}}}. \tag{2.7}$$

The pairing interaction $V(\mathbf{p}_{\mathrm{F}}, \mathbf{p}'_{\mathrm{F}})$ is a constant for singlet, s-wave pairing and the energy integral runs over the interval $[-\epsilon_c, \epsilon_c]$.[a] $\langle \bullet \rangle_{p_{\mathrm{F}}}$ is the Fermi-surface average defined as [36]:

$$\langle \bullet \rangle_{p_{\mathrm{F}}} = \frac{1}{N_{\mathrm{F}}} \int_{FS} \frac{\mathrm{d}^2 p_{\mathrm{F}}}{(2\pi\hbar)^3 |\mathbf{v}_{\mathrm{F}}(\mathbf{p}_{\mathrm{F}})|} \, (\bullet) \,, \tag{2.8}$$

where N_{F} is the normal state density of states at the Fermi-level:

$$N_{\mathrm{F}} = \int_{FS} \frac{\mathrm{d}^2 p_{\mathrm{F}}}{(2\pi\hbar)^3 |\mathbf{v}_{\mathrm{F}}(\mathbf{p}_{\mathrm{F}})|}. \tag{2.9}$$

Apart from the boundary conditions, which we will only discuss in their latest formulation, this establishes the quasiclassical theory of superconductivity as a self-contained formalism. Eq. (2.3), while representing the connection to the microscopic theory, is irrelevant for the application of the method.

The physical observables relevant to us are the local density of states and the current density, which we obtain from [37]:

$$\frac{N(\mathbf{R}, \varepsilon, t)}{N_{\mathrm{F}}} = -\frac{1}{2\pi} \mathrm{Im} \left(\mathrm{Tr} \, \left\langle g^{\mathrm{R}}(\mathbf{p}_{\mathrm{F}}, \mathbf{R}, \varepsilon, t) \right\rangle \right) \tag{2.10}$$

and

$$\mathbf{j}(\mathbf{R}, t) = e N_{\mathrm{F}} \int \frac{\mathrm{d}\varepsilon}{8\pi i} \mathrm{Tr} \left\langle \mathbf{v}_{\mathrm{F}}(\mathbf{p}_{\mathrm{F}}) \hat{\tau}_3 \hat{g}^{\mathrm{K}}(\mathbf{p}_{\mathrm{F}}, \mathbf{R}, \varepsilon, t) \right\rangle. \tag{2.11}$$

The sign of the electronic charge is defined as $e = -|e|$.

---

[a]Note also that this is a matrix equation, and that $V(\mathbf{p}_{\mathrm{F}}, \mathbf{p}'_{\mathrm{F}}) = V_0$ automatically projects out the spin-singlet part of f^{K} under the energy integral and momentum average.

2.2. Riccati Parameterisation

We now turn to the Riccati parameterisation which eliminates the normalisation condition and allows us to solve the Eilenberger-equation by solving a set of initial value problems. We only state it here and refer the reader to Refs. [36, 37] for its derivation.

The Riccati parameterisation introduces 6 amplitudes. $\gamma^{R,A}$ and $\tilde{\gamma}^{R,A}$ are coherence functions describing the quasiparticle states and x^K and $\tilde{x}^K$ are distribution functions describing their occupation [36]. This already is an advantage over the usual Keldysh formulation of quasiclassical theory, where such a separation does not exist. The quasiclassical Green's function reads in terms of these parameters [37]:

$$\hat{g}^{R,A} = \mp 2\pi i \begin{pmatrix} \mathcal{G} & \mathcal{F} \\ -\tilde{\mathcal{F}} & -\tilde{\mathcal{G}} \end{pmatrix}^{R,A} \pm i\pi\hat{\tau}_3, \qquad (2.12)$$

$$\hat{g}^K = -2\pi i \begin{pmatrix} \mathcal{G} & \mathcal{F} \\ -\tilde{\mathcal{F}} & -\tilde{\mathcal{G}} \end{pmatrix}^R \begin{pmatrix} x^K & 0 \\ 0 & \tilde{x}^K \end{pmatrix} \begin{pmatrix} \mathcal{G} & \mathcal{F} \\ -\tilde{\mathcal{F}} & -\tilde{\mathcal{G}} \end{pmatrix}^A.$$

with $\mathcal{G} = (1 - \gamma\tilde{\gamma})^{-1}$, $\tilde{\mathcal{G}} = (1 - \tilde{\gamma}\gamma)^{-1}$, and $\mathcal{F} = \mathcal{G}\gamma$, $\tilde{\mathcal{F}} = \tilde{\mathcal{G}}\tilde{\gamma}$, and upper/lower signs hold for retarded/advanced quantities.

Symmetry Relations

A number of symmetry relations hold for the Riccati amplitudes, and we will make excessive use of them in the following chapters. The Nambu-Gor'kov or, equivalently, the Bogoliubov-de-Gennes description of superconductivity introduces a redundancy of information, expressing itself in a particle-hole symmetry of all quantities in the quasiclassical formalism [36]:

$$\tilde{Q}(\mathbf{p_F}, \mathbf{R}, z, t) = Q(-\mathbf{p_F}, \mathbf{R}, -z^*, t)^*, \qquad (2.13)$$

where $z = \varepsilon \pm i0^+$ for retarded/advanced quantities and real for Keldysh functions. Moreover, the following symmetries hold for the Riccati amplitudes [36]:

$$\gamma^A = (\tilde{\gamma}^R)^\dagger, \quad x^K = (x^K)^\dagger, \qquad (2.14)$$

from which follows that if we know for instance γ^R and x^K, all other components can be obtained from these relations. While (2.13) is general, the symmetry relations for self-energies in Keldysh-space are different from (2.14) [37]:

$$\Delta^A = -(\tilde{\Delta}^R)^\dagger \quad \Delta^K = (\tilde{\Delta}^K)^\dagger \quad \Sigma^A = (\Sigma^R)^\dagger \quad \Sigma^K = -(\Sigma^K)^\dagger. \qquad (2.15)$$

Transport Equations

With

$$\hat{\Delta}^{R,A} = \begin{pmatrix} 0 & \Delta^{R,A} \\ \tilde{\Delta}^{R,A} & 0 \end{pmatrix}, \quad \hat{h}^{R,A} = \begin{pmatrix} \Sigma^{R,A} & 0 \\ 0 & \tilde{\Sigma}^{R,A} \end{pmatrix}, \qquad (2.16)$$

$$\hat{\Delta}^K = \begin{pmatrix} 0 & \Delta^K \\ -\tilde{\Delta}^K & 0 \end{pmatrix}, \quad \hat{h}^K = \begin{pmatrix} \Sigma^K & 0 \\ 0 & -\tilde{\Sigma}^K \end{pmatrix},$$

the transport equations read [36]:

$$i\hbar\mathbf{v_F}\nabla\gamma^{R,A} + 2\varepsilon\gamma^{R,A} = \gamma^{R,A}\tilde{\Delta}^{R,A}\gamma^{R,A} + \Sigma^{R,A}\gamma^{R,A} - \gamma^{R,A}\tilde{\Sigma}^{R,A} - \Delta^{R,A},$$

$$i\hbar\mathbf{v_F}\nabla\tilde{\gamma}^{R,A} - 2\varepsilon\tilde{\gamma}^{R,A} = \tilde{\gamma}^{R,A}\Delta^{R,A}\tilde{\gamma}^{R,A} + \tilde{\Sigma}^{R,A}\tilde{\gamma}^{R,A} - \tilde{\gamma}^{R,A}\Sigma^{R,A} - \tilde{\Delta}^{R,A}, \qquad (2.17)$$

for the coherence functions and

$$
\begin{aligned}
& i\hbar\mathbf{v}_{\mathrm{F}}\nabla x^{\mathrm{K}} + i\hbar\partial_t x^{\mathrm{K}} - (\gamma^{\mathrm{R}}\tilde{\Delta}^{\mathrm{R}} + \Sigma^{\mathrm{R}})x^{\mathrm{K}} - x^{\mathrm{K}}(\Delta^{\mathrm{A}}\tilde{\gamma}^{\mathrm{A}} - \Sigma^{\mathrm{A}}) \\
& = -\gamma^{\mathrm{R}}\tilde{\Sigma}^{\mathrm{K}}\tilde{\gamma}^{\mathrm{A}} + \Delta^{\mathrm{K}}\tilde{\gamma}^{\mathrm{A}} + \gamma^{\mathrm{R}}\tilde{\Delta}^{\mathrm{K}} - \Sigma^{\mathrm{K}}, \\
& i\hbar\mathbf{v}_{\mathrm{F}}\nabla \tilde{x}^{\mathrm{K}} - i\hbar\partial_t \tilde{x}^{\mathrm{K}} - (\tilde{\gamma}^{\mathrm{R}}\Delta^{\mathrm{R}} + \tilde{\Sigma}^{\mathrm{R}})\tilde{x}^{\mathrm{K}} - \tilde{x}^{\mathrm{K}}(\tilde{\Delta}^{\mathrm{A}}\gamma^{\mathrm{A}} - \tilde{\Sigma}^{\mathrm{A}}) \\
& = -\tilde{\gamma}^{\mathrm{R}}\Sigma^{\mathrm{K}}\gamma^{\mathrm{A}} + \tilde{\Delta}^{\mathrm{K}}\gamma^{\mathrm{A}} + \tilde{\gamma}^{\mathrm{R}}\Delta^{\mathrm{K}} - \tilde{\Sigma}^{\mathrm{K}},
\end{aligned}
\tag{2.18}
$$

for the distribution functions [36]. We omitted the convolution product $\otimes$ here, which has to be taken whenever self-energies or Riccati amplitudes are multiplied [36]. Note that (2.17) is independent of the distribution functions and should hence be solved first. Equations (2.18) contain the coupling between quasiparticle states and their occupation. These are the kinetic equations which reduce to Boltzmann-type equations if the coherence functions are zero.[a]

In the homogeneous equilibrium state, the solutions of equation (2.17) are [37]:

$$
\gamma^{\mathrm{R,A}}_{\mathrm{h,eq}} = - \left[(\mathcal{E} \pm i\sqrt{-\Delta\tilde{\Delta} - \mathcal{E}^2})^{-1} \cdot \Delta \right]^{\mathrm{R,A}}
\tag{2.19}
$$

if $\mathcal{E}^{\mathrm{R,A}} = \varepsilon - [(\Sigma - \tilde{\Sigma})/2]^{\mathrm{R,A}}$ and $[\Delta\tilde{\Delta}]^{\mathrm{R,A}}$ are both diagonal and if $\gamma^{\mathrm{R,A}}$ and $\tilde{\Sigma}^{\mathrm{R,A}}$ commute. If they anti-commute, the definition of $\mathcal{E}^{\mathrm{R,A}}$ changes to $\mathcal{E}^{\mathrm{R,A}} = \varepsilon - [(\Sigma + \tilde{\Sigma})/2]^{\mathrm{R,A}}$, a case one is concerned with when considering a magnetic field.

For the distribution functions, the solution is [37]:

$$
x_{\mathrm{h,eq}} = (1 - \gamma^{\mathrm{R}}\tilde{\gamma}^{\mathrm{A}})\tanh\left(\frac{\varepsilon}{2k_B T}\right).
\tag{2.20}
$$

Generally, the solutions of these partial differential equations are obtained by solving them along their characteristics, which are straight lines in real space, starting from some initial value [36]. Their direction for any value of $\mathbf{p}_{\mathrm{F}}$ is given by the Fermi-velocity $\mathbf{v}_{\mathrm{F}}(\mathbf{p}_{\mathrm{F}})$. I.e., we have $\mathbf{R} = \hat{v}_{\mathrm{F}} \cdot x + \mathbf{c}$. So $i\hbar\mathbf{v}_{\mathrm{F}}\nabla Q(\mathbf{R})$ becomes $i\hbar|\mathbf{v}_{\mathrm{F}}|\partial_x Q(\hat{v}_{\mathrm{F}} \cdot x + \mathbf{c})$ and hence an ordinary differential equation (ODE). For a given value of $\mathbf{p}_{\mathrm{F}}$ on the Fermi-surface, the orientation along which the integration of this ODE is stable is identical for γ^R, $\tilde{\gamma}^A$, x^K and γ^A, $\tilde{\gamma}^R$, $\tilde{x}^K$ respectively, but opposite for these two groups [36].

In this sense, one can understand the Riccati amplitudes, which are in principle fields over real space, as 'particles' traveling along straight trajectories with a definite group velocity.

When considering a scattering problem, i.e., a region in which the quasiclassical description breaks down, these trajectories, which are only meaningful away from the scattering region, will get 'mixed' [36, 37]. The above discussed properties of the Riccati amplitudes now allow us to separate them in 'incoming' and 'outgoing' quantities with respect to the scatterer that are related by a set of boundary conditions [36, 37].

2.3. Boundary Conditions for Riccati-Amplitudes and Diagrammatic Representation

We now present the boundary conditions for Riccati amplitudes at the interface to a scattering region. Following Eschrig's notation [36], the separation of incoming and outgoing quantities we alluded to is made explicit by writing small case letters for incoming amplitudes and capital letters for outgoing ones. The phenomenological parameters entering

---

[a]Apart from the kinetic term, the equations for $x^{\mathrm{K}}, \tilde{x}^{\mathrm{K}}$ are identical to the usual quantum kinetic equation if the coherence functions are zero. For comparison, see equation (11.68) of Ref. [3], *p. 726*.

these boundary conditions are contained in the normal state scattering matrix of the scatterer [37, 89]. Indices $k = (p, \alpha)$ denote transport channels, i.e., they combine momentum p and band indices α. $-k$ implies $-k = (-p, \alpha)$. Generically, Riccati amplitudes are matrices in spin-space; if, however, a band is not spin-degenerate, they are scalar. The boundary conditions fully cover this case, which turns out to be important when modelling strongly spin-polarised ferromagnets in quasiclassical theory.

We also discuss the diagrammatic representation introduced in Ref. [37] in this context, as it provides an intuitive understanding of the boundary conditions. To this effect, we first consider the quantities $\mathcal{G}, \mathcal{F}, \tilde{\mathcal{G}}, \tilde{\mathcal{F}}$ introduced in (2.12). They can be expanded in a geometric series in γ and $\tilde{\gamma}$ pairs as shown in Fig. 2.2. γ and $\tilde{\gamma}$ encode the coherence between particle-like and hole-like states and can be seen as a *"local probability amplitude"* for a hole-to-particle (γ) or particle-to-hole transformation ($\tilde{\gamma}$) with the same momentum [37]. It is important to fully understand these elementary diagrams. They have two legs pointing in opposite directions. These legs represent quasi-particles (red) or -holes (blue) and their propagation direction. Thus γ and $\tilde{\gamma}$ represent conversions between quasi-particles and quasi-holes[a] with the same momentum and opposite group velocity, but they also have a group velocity associated to *themselves*, which, for a given value of momentum, is opposite for γ and $\tilde{\gamma}$. The quantities $\mathcal{F}$ and $\tilde{\mathcal{F}}$, forming the anomalous part of the Green's function, represent coherence functions in which the elementary particle-hole conversions are summed to infinite order. The quantities $\mathcal{G}$ and $\tilde{\mathcal{G}}$ describe quasi-particle and -hole excitations which are renormalised by particle-hole coherence [37]. Their representation is straight-forward to infer from their definition. Considering the same problem at the scatterer, we observe that the normal-state scattering matrix S of the scatterer connects quasiparticle states with incoming group velocity to states with outgoing group velocity. We are dealing with retarded/advanced and particle/hole quantities. The corresponding scattering matrices are related by the following symmetries [37]:

$$S^{\mathrm{R}}_{kk'} = [S^{\mathrm{A}}_{k'k}]^\dagger, \quad \tilde{S}^{\mathrm{R}}_{kk'} = [\tilde{S}^{\mathrm{A}}_{k'k}]^\dagger, \quad \tilde{S}^{\mathrm{R,A}}_{kk'} = [S^{\mathrm{R,A}}_{-k'-k}]^T. \tag{2.21}$$

A possible time or energy dependence is neglected here, as the properties of the S-matrix are usually determined on the 'high-energy' scale. The formalism would, however, also cover the case of such a dependence. Irrespective of which scattering states are connected by the S-matrix, a scattering event will always invert the group velocity of the quasi-particle from 'incoming' to 'outgoing' with respect to the scatterer, without changing its particle/hole character [37]. This is reflected in the elementary diagrammatic representation of scattering events shown in Fig. 2.3.

We are now interested in the outgoing quantities $\mathcal{F}^{\mathrm{R}}$ and $\mathcal{G}^{\mathrm{R}}$ at the scatterer as functions of the incoming coherence amplitudes γ_k and $\tilde{\gamma}_k$.[b] For $\mathcal{F}^{\mathrm{R}}$, this implies to find all possible paths contributing to the hole-particle conversion amplitude of an incoming hole to an outgoing particle. Since the scatterer will mix transport channels, we must also specify between which channels this conversion is to take place, i.e., $\mathcal{F}^{\mathrm{R}}_{kk'}$ acquires two band indices. The elementary hole-particle conversions appearing in the paths that contribute to this quantity must be the incoming ones. Their legs can, however, only be matched with those of the desired amplitude, if their group velocity is inverted by means of an elementary scattering event. This leads to the leading order in path length, or 'elementary',

---

[a] We use both 'quasiparticle' and 'quasi-particle'. The first term is supposed to refer to the general concept of quasiparticles introduced by Landau, while the latter is used when we want to distinguish particle-like from hole-like quasiparticle excitations.

[b] Note that γ_k and $\tilde{\gamma}_k$ have opposite momentum here, since their propagation direction is the same (pointing towards the scatterer).
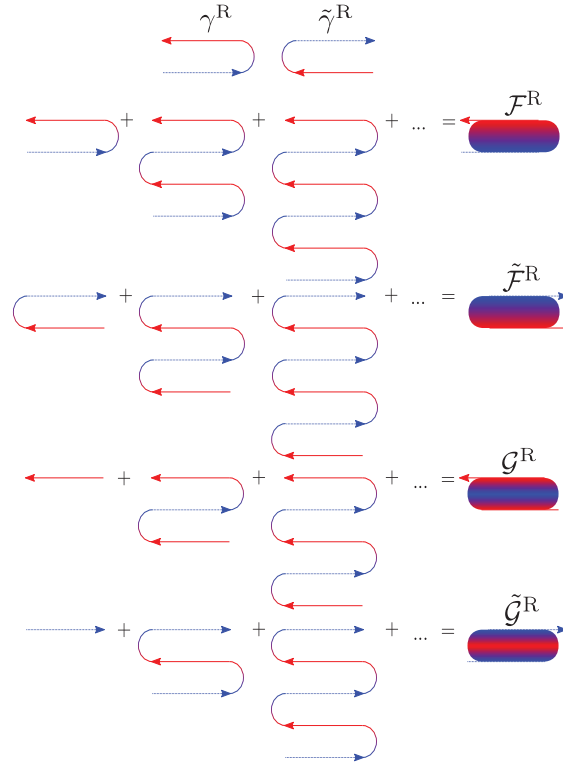
Figure 2.2. – Diagrammatic representation of the retarded coherence functions and the corresponding quantities $\mathcal{G}, \mathcal{F}, \tilde{\mathcal{G}}, \tilde{\mathcal{F}}$. For advanced amplitudes, the propagation direction of all lines must to be inverted with respect to the retarded ones. Figure adapted from Ref. [37].

contributions to $\mathcal{F}^{\mathrm{R}}_{kk'}$ [37]:

$$[\gamma'_{kk'}]^{\mathrm{R}} = \left[\sum_{k''} S_{kk''} \gamma_{k''} \tilde{S}_{k''k'} \right]^{\mathrm{R}}, \tag{2.22}$$

where a sum is taken over all possible channels. The diagrammatic representation is shown at the top of Fig. 2.3. Its hole-like leg is pointing towards the scatterer, and its particle-like leg way from it. This particle-like leg may now undergo another particle-hole conversion by means of the incoming amplitude $\tilde{\gamma}_k$. This will invert the group velocity and send the quasiparticle back to the scatterer. Consequently, the amplitude $\mathcal{F}^{\mathrm{R}}_{kk'}$ can – again – be written as an expansion in an infinite number of quasiparticle paths, and the same is true for $\mathcal{G}^{\mathrm{R}}_{kk'}$, as depicted in Fig. 2.3. The sum over these paths can be written in an implicit form as [37]:

$$\mathcal{F}^{\mathrm{R}}_{kk'} = \left[\gamma'_{kk'} + \sum_{k''} \mathcal{F}_{kk''} \tilde{\gamma}_{k''} \gamma'_{k''k'} \right]^{\mathrm{R}}. \tag{2.23}$$

Likewise, we obtain an expression for $\mathcal{G}^{\mathrm{R}}_{kk'}$ [37]:

$$\mathcal{G}^{\mathrm{R}}_{kk'} = [1 + \mathcal{F}_{kk'} \tilde{\gamma}_{k'}]^{\mathrm{R}}. \tag{2.24}$$

Now, what we are actually interested in are the outgoing coherence functions Γ^{R}_k, $\tilde{\Gamma}^{\mathrm{R}}_k$. These can be obtained from the definition of the Green's function. Note that if the group velocity $\mathbf{v}_{\mathrm{F}}(\mathbf{p}_{\mathrm{F}})$ points away from the scatterer, the amplitude γ^{R} entering $\hat{g}^{\mathrm{R}}(\mathbf{p}_{\mathrm{F}})$ is an outgoing one, while $\tilde{\gamma}^{\mathrm{R}}$ is incoming, $\hat{g}^{\mathrm{R}}(\mathbf{p}_{\mathrm{F}}) = \hat{g}^{\mathrm{R}}(\Gamma^{\mathrm{R}}, \tilde{\gamma}^{\mathrm{R}})$ [37]. We hence obtain Γ^{R} from
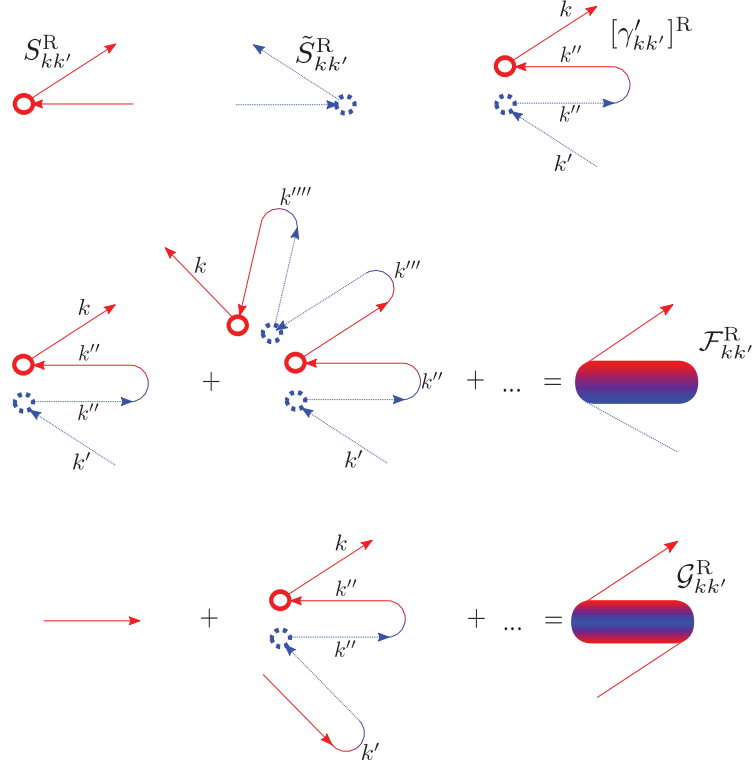
Figure 2.3. – Diagrammatic representation elementary scattering events (top-left), the elementary contributions to the outgoing coherence functions (top-right) and the diagrammatic expansion of the outgoing amplitudes $\mathcal{G}, \mathcal{F}$ at the scatterer. Figure adapted from Ref. [37].

the relation [37]:

$$\mathcal{F}^{\mathrm{R}}_{kk} = \mathcal{G}^{\mathrm{R}}_{kk}\Gamma^{\mathrm{R}}_{k} \Rightarrow \Gamma^{\mathrm{R}}_{k} = [\mathcal{G}^{-1}_{kk}\mathcal{F}_{kk}]^{\mathrm{R}}. \tag{2.25}$$

The logic here is that the fundamental quantities are in fact $\mathcal{G}_{kk'}$ and $\mathcal{F}_{kk'}$, for which we obtained the outgoing solutions from the sum-over-scattering-paths reasoning. The coherence amplitudes Γ_k, that enter the Riccati formalism, are then calculated from them. Obviously, the outgoing coherence functions are not connected to the amplitudes $\mathcal{F}_{kk'}$, $\mathcal{G}_{kk'}$ with $k \neq k'$. This is because they describe coherence between quasi-particles and quasi-holes with different momenta on the Fermi-sphere in the same band or even in different bands. This coherence is lost on the interatomic scale and does hence not enter the quasiclassical formalism [37]. Such contributions enter only indirectly through the boundary conditions. By generalising (2.25) as [37]:

$$\mathcal{F}^{\mathrm{R}}_{kk'} = \mathcal{G}^{\mathrm{R}}_{kk}\Gamma^{\mathrm{R}}_{k \leftarrow k'}, \tag{2.26}$$

we can directly write implicit equations for the outgoing coherence functions [37]:

$$\Gamma^{\mathrm{R}}_{k \leftarrow k'} = \left[\gamma'_{kk'} + \sum_{k'' \neq k} \Gamma_{k \leftarrow k''}\tilde{\gamma}_{k''}\gamma'_{k''k'} \right]^{\mathrm{R}}, \tag{2.27}$$

with $\Gamma^{\mathrm{R}}_{k} = \Gamma^{\mathrm{R}}_{k \leftarrow k}$.

The boundary conditions for the hole-like coherence functions are obtained analogously [37]:

$$\tilde{\Gamma}^{\mathrm{R}}_{k \leftarrow k'} = \left[\tilde{\gamma}'_{kk'} + \sum_{k'' \neq k} \tilde{\Gamma}_{k \leftarrow k''}\gamma_{k''}\tilde{\gamma}'_{k''k'} \right]^{\mathrm{R}}, \tag{2.28}$$
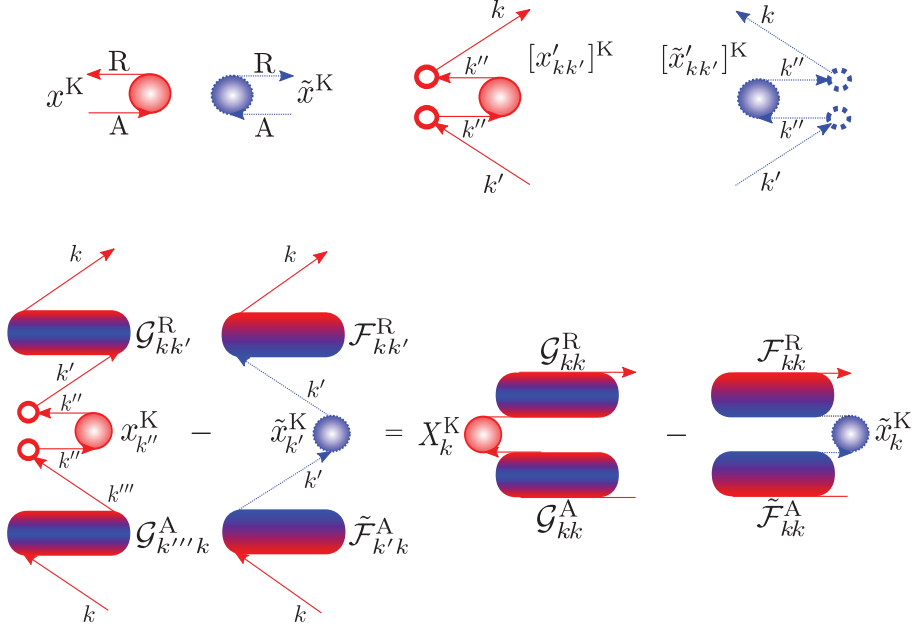
Figure 2.4. – Diagrammatic representation of the distribution functions x^K and $\tilde{x}^K$ and the distribution functions renormalised by elementary scattering events $[x'_{kk'}]^K$, $[\tilde{x}'_{kk'}]^K$. The lower figure depicts the identity used to obtain X^K. Figure adapted from Ref. [37].

while for advanced amplitudes, the direction of time is inverted, resulting in [37]:

$$\Gamma^A_{k\to k'} = \left[\gamma'_{kk'} + \sum_{k\neq k''} \gamma'_{k'k''}\tilde{\gamma}_{k''}\Gamma_{k''\to k'} \right]^A, \quad \tilde{\Gamma}^A_{k\to k'} = \left[\tilde{\gamma}'_{kk'} + \sum_{k\neq k''} \tilde{\gamma}'_{k'k''}\gamma_{k''}\tilde{\Gamma}_{k''\to k'} \right]^A.$$

$$(2.29)$$

We now turn to the boundary conditions for the outgoing distribution functions X^K and $\tilde{X}^K$. We observe that the distribution functions are connected to retarded coherence amplitudes on the left and advanced ones to the right in $\hat{g}^K$. This is reflected in their diagrammatic representation (see Fig. 2.4), they have one retarded and one advanced leg with the same quasiparticle character and, consequently, opposite group velocity [37]. Again, we introduce an elementary renormalisation of the distribution functions by scattering [37]:

$$[x'_{kk'}]^K = \sum_{k''} S^R_{kk''} x^K_{k''} S^A_{k''k'}, \quad [\tilde{x}'_{kk'}]^K = \sum_{k''} \tilde{S}^R_{kk''} \tilde{x}^K_{k''} \tilde{S}^A_{k''k'}.$$

$$(2.30)$$

We then obtain X^K by inspecting the Keldysh-Green's function for $\mathbf{v}_F(\mathbf{p}_F)$ pointing away from the scatterer [37]. In this case [37]:

$$\hat{g}^K_k(\mathbf{p}_{Fk}) = \hat{g}^K_k(\Gamma^R_k, \tilde{\gamma}^R_k, \gamma^A_k, \tilde{\Gamma}^A_k, X^K_k, \tilde{x}^K_k),$$

$$(2.31)$$

and we infer from equation (2.12) for the upper left entry of $\hat{g}^K$ [37]:

$$\mathcal{G}^R_{kk} X^K_k \mathcal{G}^A_{kk} - \mathcal{F}^R_{kk} \tilde{x}^K_k \tilde{\mathcal{F}}^A_{kk},$$

$$(2.32)$$

which is the quantity depicted on the right side of the identity in Fig. 2.4. This corresponds to the effective outgoing particle-distribution function which couples the bare distribution functions X^K and $\tilde{x}^K$ with the coherence amplitudes. The same quantity is obtained by

directly coupling the incoming bare distribution functions to the scatterer and the coherence functions [37]. For the bare incoming particle distribution function x^{K}, this involves a scattering first, so that the legs have the right group velocity. The renormalisation of the legs pointing away from the scatterer due to the coherence amplitudes and scattering is given by $\mathcal{G}_{kk'}^{\mathrm{R,A}}$ as discussed above. This gives the first term on the left side of the identity. The second term is due to the hole-like distribution function, whose legs already have the right group-velocity but most still undergo a hole-particle conversion to contribute to the particle distribution. The corresponding renormalisation is given by $\mathcal{F}_{kk'}^{\mathrm{R}}$ for the retarded and $\tilde{\mathcal{F}}_{kk'}^{\mathrm{A}}$ for the advanced branch. This gives us the identity [37]:

$$\sum_{k'k''} \mathcal{G}_{kk'}^{\mathrm{R}}[x'_{k'k''}]^{K}\mathcal{G}_{k''k}^{\mathrm{A}} - \mathcal{F}_{kk'}^{\mathrm{R}}\tilde{x}_{k'}^{\mathrm{K}}\tilde{\mathcal{F}}_{k'k}^{\mathrm{A}} = \mathcal{G}_{kk}^{\mathrm{R}}X_k^{\mathrm{K}}\mathcal{G}_{kk}^{\mathrm{A}} - \mathcal{F}_{kk}^{\mathrm{R}}\tilde{x}_k^{\mathrm{K}}\tilde{\mathcal{F}}_{kk}^{\mathrm{A}} \tag{2.33}$$

The identity can now be solved to give an expression for X^{K}, which we state here directly in terms of the amplitudes $\Gamma_{k \leftrightarrows k'}$ [37]:

$$X_k^{\mathrm{K}} = \sum_{k'k''}[\delta_{kk'} + \bar{\Gamma}_{k \leftarrow k'}\tilde{\gamma}_{k'}]^{\mathrm{R}}[x'_{k'k''}]^{\mathrm{K}}[\gamma_{k''}\tilde{\bar{\Gamma}}_{k'' \to k} + \delta_{k''k}]^{\mathrm{A}} - \bar{\Gamma}_{k \leftarrow k'}^{\mathrm{R}}\tilde{x}_{k'}^{\mathrm{K}}\tilde{\bar{\Gamma}}_{k' \to k}^{\mathrm{A}}, \tag{2.34}$$

where $\bar{\Gamma}_{k \leftrightarrows k'} = \Gamma_{k \leftrightarrows k'} - \delta_{kk'}\Gamma_k$.

The argumentation for the outgoing hole distribution function is again analogous and yields [37]:

$$\tilde{X}_k^{\mathrm{K}} = \sum_{k'k''}[\delta_{kk'} + \tilde{\bar{\Gamma}}_{k \leftarrow k'}\gamma'_k]^{\mathrm{R}}[\tilde{x}'_{k'k''}]^{\mathrm{K}}[\tilde{\gamma}_{k''}\bar{\Gamma}_{k'' \to k} + \delta_{k''k}]^{\mathrm{A}} - \tilde{\bar{\Gamma}}_{k \leftarrow k'}^{\mathrm{R}}x_{k'}^{\mathrm{K}}\bar{\Gamma}_{k' \to k}^{\mathrm{A}}. \tag{2.35}$$

This establishes the boundary conditions and completes our discussion of the Riccati technique. We tried to put an emphasis on the logics behind the diagrammatic representation and on how the boundary conditions can be understood in this context. As far as the technical aspects are concerned, the original article of Eschrig is certainly more comprehensive [37]. For brevity, we drop the Keldysh-index of the distribution functions in the following chapters.

2.4. Diagrammatic Rules

In the following, we state a set of diagrammatic rules which can be used to construct the solutions of the boundary conditions for Riccati amplitudes in terms of their diagrammatic representation. Note that only the boundary conditions for the coherence amplitudes require a solution in the sense that an algebraic elimination must be carried out to obtain explicit expressions for all $\Gamma_{k \leftrightarrows k'}$-amplitudes. Once these are known, the solutions for the distribution functions can simply be written down. The rules for these coherence amplitudes are straight-forward to construct based on the insight that: *"The diagrammatic representation of these equations is the same as for the functions $\mathcal{F}^{\mathrm{R,A}}$ and $\tilde{\mathcal{F}}^{\mathrm{R,A}}$, with the modification that in all internal sums the direction k of the final state that is scattered into is excluded."*, M. Eschrig, PRB 80, 134511-8 (2009).

This leads us to the following set of rules:

1. For the outgoing coherence function in question, draw the corresponding incoming and outgoing particle or hole line.

2. Draw all possible paths connecting these incoming and outgoing lines through elementary scattering events and particle-hole or hole-particle conversions via the incoming coherence functions. An elementary scattering event will change the character of the path from incoming to outgoing, an elementary particle-hole or hole-particle conversion from outgoing to incoming. Only incoming paths can be scattered and only outgoing ones can undergo conversion.
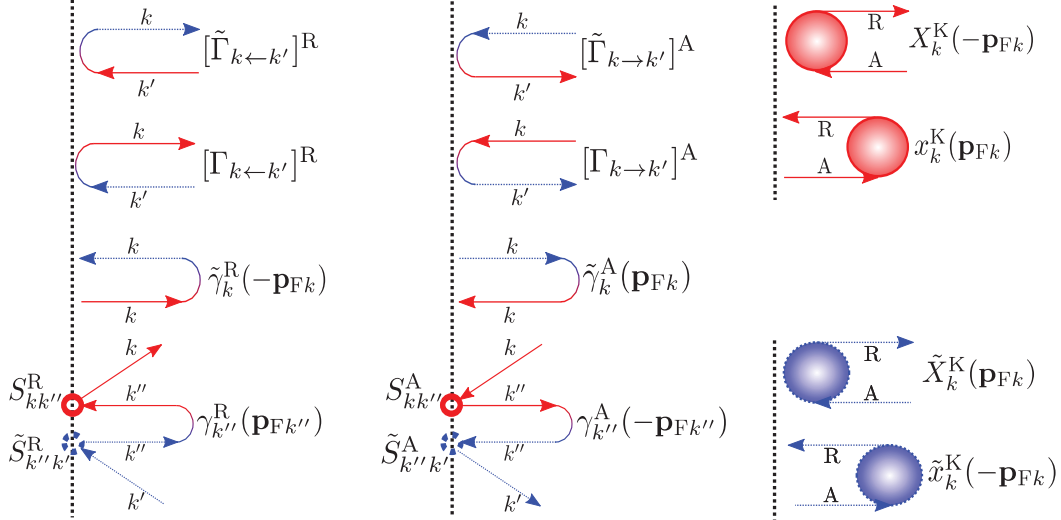
Figure 2.5. – Relevant elementary diagrams at the scatterer (dashed line). Legs pointing towards the scatterer are incoming, legs pointing away from it are outgoing. The momentum direction of the respective amplitudes are stated explicitly, $\mathbf{p}_{\mathrm{F}k}$ is pointing towards the scatterer. As for the $\Gamma_{k \leftrightarrows k'}$ amplitudes, a momentum direction is only defined for $k = k'$, and we have, for completeness, $-\mathbf{p}_{\mathrm{F}k}$ for Γ_k^{R} and $\tilde{\Gamma}_k^{\mathrm{A}}$ and $\mathbf{p}_{\mathrm{F}k}$ for $\tilde{\Gamma}_k^{\mathrm{R}}$ and Γ_k^{A}.

3. Reject all paths where the final outgoing line appears at an intermediate step.

4. For a given path, write out the corresponding scattering matrices and coherence amplitudes from right to left.

5. Take the sum over all paths.

For advanced amplitudes, rule 4 changes to 'left to right'. If one thinks about the diagrammatic representation of the $\mathcal{F}$-functions, all of these rules save the third are very obvious. Rule 3 takes care of the forbidden scattering into the final state. In Fig. 2.5, we give a summary of the leg-orientations of the relevant amplitudes at the scatterer.

On that basis, it is then easy to write down the rules for the distribution functions by inspecting their boundary conditions:

1. For the distribution function in question, draw the corresponding incoming advanced and outgoing retarded line.

2. Draw all possible paths connecting these lines through elementary scattering events, particle-hole or hole-particle conversions and incoming distribution functions. Only incoming lines can scatter, only outgoing lines can undergo a particle-hole or hole-particle conversion or be connected to an incoming distribution function. A scattering event converts a path from incoming to outgoing, a coherence or distribution function from outgoing to incoming.

3. Reject all paths containing the final outgoing line or the initial incoming line at an intermediate step.

4. Also reject all paths that contain the incoming distribution function with opposite particle/hole-type and the same channel-label as the outgoing distribution function that is to be calculated.

5. Starting from the single incoming distribution function, write down the retarded branch of the path from right to left and the advanced one from left to right.

6. Take the sum over all paths.

A few comments are in order. The structure of the incoming distribution functions guarantees that every path constructed from these rules contains exactly one incoming distribution function. Thus, this must not be demanded explicitly. Another complication arises from the fact that the forward-scattering amplitude is subtracted in all coherence functions. An inspection of the first term of the boundary conditions shows that the rule "Reject all paths that contain the final outgoing line or the initial incoming line at an intermediate step" describes all contributions to this term correctly. If the forward scattering amplitude was to appear here, the final outgoing line would immediately appear after the first scattering vertex at the distribution function and the path must end, which is the case covered by the Kronecker-deltas. In the second term, however, we need an additional rule to avoid the forward scattering amplitude. In fact, the paths that we thus reject do still enter the Keldysh-Green's function, but not X^{K}.

Although the number of paths contributing to the solutions is infinite, we can obviously state closed algebraic expressions to describe them all. This implies that these paths can be represented by a finite graph, involving only elementary diagrams. This is illustrated in the appendix for the three channel case relevant to us.

The rules stated here do certainly not provide any kind of technical advantage, since the algebraic solution of the boundary conditions, being nothing but a system of linear equations, poses no problem at all. We still believe that they may facilitate the interpretation of results obtained with this formalism.

2.5. The Riccati Technique for Matsubara Green's Functions

Our study of the Josephson effect will be carried out in the Matsubara framework. The corresponding Riccati amplitudes are obtained from the retarded and advanced coherence functions in a straight-forward way. The corresponding relations are briefly reviewed here.

The quasiclassical Matsubara-Green's function $\hat{g}^{\mathrm{M}}$ depends on the Matsubara frequency $\epsilon_n = 2\pi \cdot (n + 1/2) \cdot k_{\mathrm{B}}T$ instead of the energy ε [114], the Riccati parameterisation is defined as above:

$$\hat{g}^{\mathrm{M}} = \mp 2\pi i \begin{pmatrix} \mathcal{G} & \mathcal{F} \\ -\tilde{\mathcal{F}} & -\tilde{\mathcal{G}} \end{pmatrix}^{\mathrm{M}} \pm i\pi\hat{\tau}_3, \tag{2.36}$$

where $\mp$ and $\pm$ now correspond to positive/negative Matsubara-frequencies. The Eilenberger-equation transforms to:

$$i\hbar\vec{v}_{\mathrm{F}} \cdot \nabla_{\vec{R}}\hat{g}^{\mathrm{M}} + [i\epsilon_n\hat{\tau}_3 - \hat{\Delta} - \hat{h}, \hat{g}]^{\mathrm{M}} = \hat{0}, \tag{2.37}$$

with the normalisation condition: $\hat{g}^{\mathrm{M}}\hat{g}^{\mathrm{M}} = -\hat{1}\pi^2$. Consequently, the Riccati-transport equations become:

$$(i\hbar\mathbf{v}_{\mathrm{F}} \cdot \nabla + 2i\epsilon_n)\gamma^{\mathrm{M}} = [\gamma\tilde{\Delta}\gamma + \Sigma\gamma - \gamma\tilde{\Sigma} - \Delta]^{\mathrm{M}}, \tag{2.38}$$

$$(i\hbar\mathbf{v}_{\mathrm{F}} \cdot \nabla - 2i\epsilon_n)\tilde{\gamma}^{\mathrm{M}} = [\tilde{\gamma}\Delta\tilde{\gamma} + \tilde{\Sigma}\tilde{\gamma} - \tilde{\gamma}\Sigma - \tilde{\Delta}]^{\mathrm{M}}.$$

The particle-hole symmetry relation is:

$$\tilde{Q}^{\mathrm{M}}(\vec{p}_{\mathrm{F}}, \vec{R}, \epsilon_n, t) = [Q^{\mathrm{M}}(-\vec{p}_{\mathrm{F}}, \vec{R}, \epsilon_n, t)]^*, \tag{2.39}$$

and the one between retarded and advanced amplitudes transforms to:

$$\gamma^{\mathrm{M}}(-\epsilon_n) = [\tilde{\gamma}^{\mathrm{M}}(\epsilon_n)]^{\dagger}. \tag{2.40}$$

The equilibrium current density, which is the only observable that we calculate with this technique, is [114]:

$$\mathbf{j}(\mathbf{R}, t) = eN_\mathrm{F} k_\mathrm{B} T \sum_{\epsilon_n} \frac{1}{2} \mathrm{Tr} \Big\langle \mathbf{v}_\mathrm{F}(\mathbf{p}_\mathrm{F}) \hat{\tau}_3 \hat{g}^\mathrm{M}(\mathbf{p}_\mathrm{F}, \mathbf{R}, \epsilon_n, t) \Big\rangle. \tag{2.41}$$

The symmetry between negative and positive Matsubara frequencies allows us to consider only the positive ones. For these, the boundary conditions are exactly the same as those of the retarded amplitudes.

3. Model of the SC/FM Contact within Quasiclassical Theory

In this chapter, we discuss the model that allows us to describe SC/FM heterostructures in which the ferromagnetic materials are strongly spin-polarised with quasiclassical theory. This is a new approach based on the generalisation of the quasiclassical boundary conditions to multi-channel scattering.

The fundamental problem here is the following. Recall that quasiclassical theory is based on a separation of two energy scales, which can be defined as the Fermi-energy E_{F} on the one hand, and the superconducting energy gap Δ on the other hand. The treatment of ferromagnetism within this theory so far consisted in including the ferromagnetic exchange-field as an external field in the Eilenberger-equation, thus making the implicit assumption that the exchange energy J is roughly of order Δ. This is reasonable for weakly spin-polarised alloys such as $\mathrm{Cu}_x\mathrm{Ni}_{1-x}$, in which $0 - \pi$ oscillations of the Josephson effect were first observed [104]. However, most natural ferromagnets such as Fe, Co and Ni do not comply to this requirement, as their exchange splitting is of order E_{F} rather than Δ. In a sense, this is still good news, since the separation of energy scales also holds for these materials; the difference being, however, that the exchange field must be treated on the 'high energy' scale. This is achieved by considering the majority and minority band of the ferromagnet at the Fermi-level as independent and defining two independent Green's functions [52, 53]. The technicalities of this model are introduced in the following section. In section 3.2, we then discuss quasiparticle scattering at the contact and solve the boundary conditions at the SC/FM interface in section 3.3. Finally, we analyse the result in terms of the diagrammatic technique.

3.1. Ferromagnets with Large Exchange Splitting in Quasiclassical Theory

If the exchange splitting of the ferromagnet is large, it is obvious that pairing correlations between electrons in different spin-bands – even if induced at the SC/FM interface – are rapidly suppressed on the interatomic scale, as there is a large difference in momentum between the paired particles. In principle, this is known for a long time already [30] and was explicitly shown with microscopic calculations by, e.g., Halterman and Valls [55]. It is therefore sufficient to devise a theory which only describes inter-band pairing, i.e. correlations with equal-spin triplet character. This is readily achieved within quasiclassical
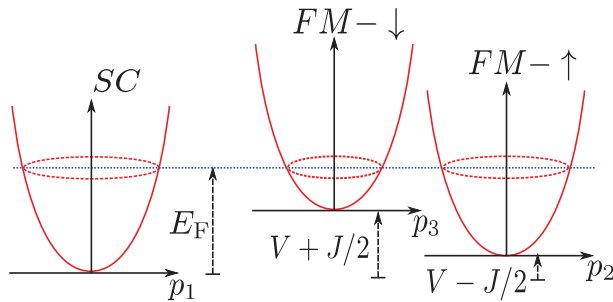
Figure 3.1. – Model band structure of the SC/FM system.

theory by defining independent quasiclassical Green's functions for different spin-bands in the ferromagnet. This approximation is well-suited if $J > 0.1E_F$ for most conventional superconductors [53], or generally, if the decay length $\xi_J = \hbar/(p_\uparrow - p_\downarrow)$ is a lot shorter than the normal metal coherence length ξ_0, which one may define as $\hbar(v_\uparrow + v_\downarrow)/4\pi k_B T_c$ inside the ferromagnet. Specifically, we assume two metallic bands at the Fermi-energy with complete and opposite spin-polarisation. In the parabolic band approximation, this consists in shifting the dispersion by $-J/2$ for the majority or spin-↑-band and by $+J/2$ for the minority or spin-↓-band. In the superconductor, we assume a single, spin-degenerate band. Thus, the normal-state dispersion relations are:

$$\xi_1(\mathbf{p}_1) = \frac{\mathbf{p}_1^2}{2m} - E_F, \tag{3.1}$$

$$\xi_2(\mathbf{p}_2^2) = \frac{\mathbf{p}_2^2}{2m} - J/2 + V - E_F, \quad \xi_3(\mathbf{p}_3^2) = \frac{\mathbf{p}_3^2}{2m} + J/2 + V - E_F,$$

where we introduce the band index η: $\eta = 1 \equiv$ SC, $\eta = 2 \equiv$ FM, ↑-band and $\eta = 3 \equiv$ FM, ↓-band. For simplicity, we use the same effective mass in all bands $m = p_{F1}^2/2E_F$, V corresponds to a global shift of the FM-bands with respect to that of the SC as shown in Fig. 3.1. The individual Green's functions are defined accordingly as:

$$\check{g}_\eta(\mathbf{p}_{F\eta}, \mathbf{R}, \varepsilon, t) = \frac{1}{a(\mathbf{p}_{F\eta})} \int \mathrm{d}\xi_{p\eta} \hat{\tau}_3 \check{G}(\mathbf{p}, \mathbf{R}, \varepsilon, t), \tag{3.2}$$

where $\check{g}_1$ is a matrix in spin-space while $\check{g}_{2,3}$ are spin-scalars. The relevant observables thus read for the respective bands:

$$\frac{N_1(\mathbf{R}, \varepsilon, t)}{N_{F1}} = -\frac{1}{2\pi}\mathrm{Im}\Big(\mathrm{Tr}\langle g^R(\mathbf{p}_{F1}, \mathbf{R}, \varepsilon, t)\rangle_{p_{F1}}\Big), \tag{3.3}$$

$$\frac{N_{2,3}(\mathbf{R}, \varepsilon, t)}{N_{F2,3}} = -\frac{1}{\pi}\mathrm{Im}\Big(\langle g^R(\mathbf{p}_{F2,3}, \mathbf{R}, \varepsilon, t)\rangle_{p_{F2,3}}\Big),$$

$$\mathbf{j}_\eta(\mathbf{R}, t) = eN_{F\eta}\int \frac{\mathrm{d}\varepsilon}{8\pi i}\mathrm{Tr}\Big\langle \mathbf{v}_{F\eta}(\mathbf{p}_{F\eta})\hat{\tau}_3 \hat{g}_\eta^K(\mathbf{p}_{F\eta}, \mathbf{R}, \varepsilon, t)\Big\rangle_{p_{F\eta}}.$$

The missing trace and factor $1/2$ in the normalised DOS for $\eta = 2, 3$ are due to the missing spin degree of freedom in the FM-bands. The Fermi-surface average and density of states are defined accordingly:

$$\langle \bullet \rangle_{p_{F\eta}} = \frac{1}{N_{F\eta}}\int_{FS\eta} \frac{\mathrm{d}^2 p_{F\eta}}{(2\pi\hbar)^3|\mathbf{v}_{F\eta}(\mathbf{p}_{F\eta})|} (\bullet), \tag{3.4}$$

$$N_{F\eta} = \int_{FS\eta} \frac{\mathrm{d}^2 p_{F\eta}}{(2\pi\hbar)^3|\mathbf{v}_{F\eta}(\mathbf{p}_{F\eta})|}. \tag{3.5}$$
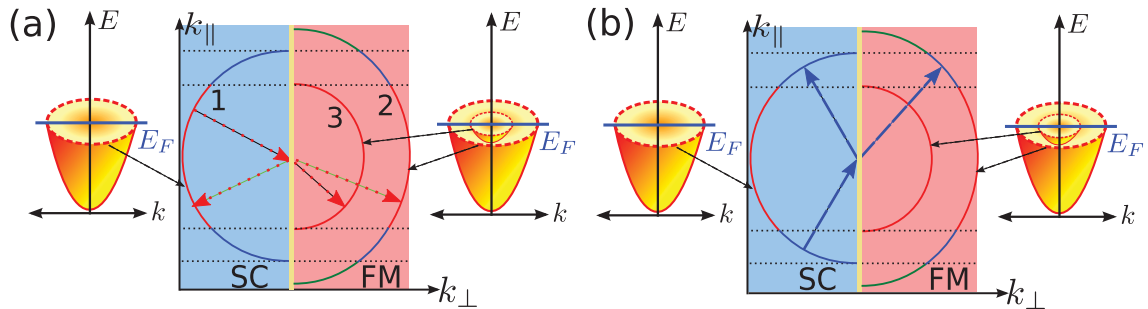
Figure 3.2. – Geometry of quasiparticle scattering at the superconductor-ferromagnet interface with the assumption of an atomically clean interface, i.e. the conservation of parallel momentum $k_{||}$. This constraint implies two types of trajectories contributing to transport across the contact, (a) trajectories connecting all three Fermi-surface sheets and (b) trajectories connecting only the SC-band and the majority band of the ferromagnet. Figure from Ref. [53]. Copyright 2010 by the American Physical Society.

3.2. Scattering Geometry

To solve the boundary conditions for this problem, we first need to specify the normal-state scattering matrix of the interface. As discussed at length in the previous chapter, this matrix cannot be obtained within quasiclassical theory, but must be provided as a set of phenomenological parameters. Here, we shall obtain this matrix from microscopic models of the interface region. The most fundamental assumption entering these models is the conservation of parallel momentum $k_{||}$ when a quasiparticle scatters at the interface. This corresponds to an interface which is translationally invariant in the plane of the interface, i.e. atomically clean.[a] Such a constraint severely reduces the number of non-zero matrix elements. In fact, for any incident quasiparticle, there will be a maximum of 3 possible outgoing states available. Depending on the Fermi-surface geometry, this number may reduce to 2 or even 1, as illustrated in Fig. 3.2. For any incoming trajectory, backscattering is always possible; if no other band can be accessed, such a trajectory cannot contribute to transport. We are hence only interested in those trajectories with 2 or 3 outgoing channels. We shall call the first 'half metallic' trajectories and the latter 'ferromagnetic' trajectories, since only the first type exists in a half metal [52, 53].

Thus, when considering solutions of the quasiclassical boundary conditions for this problem, we need to distinguish two cases. For half metallic trajectories, two transport channels must be matched and three for the ferromagnetic ones. The corresponding solutions are discussed in the next section.

The S-matrix has the following structure for these cases [53]:

$$S_{\mathrm{FM}}^{\mathrm{R}} = \left(\begin{array}{c|c|c} R_1 & T_{12} & T_{13} \\ \hline T_{21} & r_2 & r_{23} \\ \hline T_{31} & r_{32} & r_3 \end{array}\right), \quad S_{\mathrm{HM}}^{\mathrm{R}} = \left(\begin{array}{c|c} R_1 & T_{12} \\ \hline T_{21} & r_2 \end{array}\right). \tag{3.6}$$

Here, R_1 is a 2×2-matrix, T_{12} and T_{13} are 2×1 matrices, T_{21} and T_{31} are 1×2-matrices, r_2, r_3, r_{23} and r_{32} are scalars. This choice of parameters may seem awkward at first, but will turn out to be convenient for solving the boundary conditions. The matrix elements $S_{kk'}^{\mathrm{R}}$ used in the definitions of the elementary scattering amplitudes $[\gamma']^{\mathrm{R}}$ and $[x']^{\mathrm{R}}$ are exactly these components. This is because we match two spin-scalar channels ($\eta = 2, 3$) with one spin-degenerate channel ($\eta = 1$).

---

[a] Strictly speaking, our approach for calculating the S-matrix also requires that the band structure is centrosymmetric or time-reversal invariant on both sides of the interface, otherwise there may be no scattering states available if both $\mathbf{k}_{||}$ and energy are to be conserved [37].

3.3. Solution of the Boundary Conditions

We discuss the solutions of the boundary conditions for the two types of trajectories in terms of the general scattering matrices given in equation (3.6). The models from which we obtain the values of the S-matrix parameters will be discussed in the next chapter.

Coherence functions

As for the incoming coherence functions, we assume that they are given by the bulk solution (2.19) in the superconductor, i.e., $\gamma_1^R = \gamma_{\text{eq,hom}}^R$ and $\tilde{\gamma}_1^R = \tilde{\gamma}_{\text{eq,hom}}^R$, with $\Delta^R = |\Delta| i\sigma_y$, i.e. a singlet gap, and no other self-energy terms. In the ferromagnet, the incoming coherence functions are zero in the point-contact geometry but have a finite value originating from the opposite surface or interface in the Josephson junction geometry. We only discuss the point-contact case here and illustrate how the diagrammatic technique can be used to obtain a physical interpretation of the result. The more general solution for finite $\gamma_{2,3}$ is given in the appendix.

An additional comment concerning the physical assumptions that underly our point contact theory is in order. The dimensions characterising the contact area of the point contact are assumed to be small compared the superconducting coherence length but imply a macroscopic number of transport channels, i.e., there is no conductance quantisation [53]. This is usually a good assumption for point-contact Andreev spectroscopy and it is also implicit in BTK-theory [15].

Thanks to symmetry relations between advanced and retarded propagators, it will be sufficient to consider retarded quantities. Hence, the boundary conditions for ferromagnetic trajectories reduce to [53]:

$$
\begin{aligned}
\Gamma_{2\leftarrow 1}^R &= [\gamma_{21}' + \Gamma_{2\leftarrow 1}\tilde{\gamma}_1\gamma_{11}']^R, & \Gamma_2^R &= [\gamma_{22}' + \Gamma_{2\leftarrow 1}\tilde{\gamma}_1\gamma_{12}']^R, & (3.7)\\
\Gamma_{2\leftarrow 3}^R &= [\gamma_{23}' + \Gamma_{2\leftarrow 1}\tilde{\gamma}_1\gamma_{13}']^R, & \Gamma_{3\leftarrow 1}^R &= [\gamma_{31}' + \Gamma_{3\leftarrow 1}\tilde{\gamma}_1\gamma_{11}']^R,\\
\Gamma_3^R &= [\gamma_{33}' + \Gamma_{3\leftarrow 1}\tilde{\gamma}_1\gamma_{13}']^R, & \Gamma_{3\leftarrow 2}^R &= [\gamma_{32}' + \Gamma_{3\leftarrow 1}\tilde{\gamma}_1\gamma_{12}']^R,\\
\Gamma_1^R &= [\gamma_{11}']^R, & \Gamma_{1\leftarrow 2}^R &= [\gamma_{12}']^R, \quad \Gamma_{1\leftarrow 3}^R = [\gamma_{13}']^R,
\end{aligned}
$$

with $[\gamma_{ij}']^R = S_{i1}\gamma_1^R S_{1j}^*$ for $i, j = 1, 2, 3$. The boundary condition for Γ_1^R, $\Gamma_{1\leftarrow 2}^R$ and $\Gamma_{1\leftarrow 3}^R$ are trivial, the remaining explicit solutions are [53]:

$$
\begin{aligned}
\Gamma_{2\leftarrow 1}^R &= [\gamma_{21}'(1 - \tilde{\gamma}_1\gamma_{11}')^{-1}]^R, & (3.8)\\
\Gamma_2^R &= [\gamma_{22}' + \gamma_{21}'(1 - \tilde{\gamma}_1\gamma_{11}')^{-1}\tilde{\gamma}_1\gamma_{12}']^R,\\
\Gamma_{2\leftarrow 3}^R &= [\gamma_{23}' + \gamma_{21}'(1 - \tilde{\gamma}_1\gamma_{11}')^{-1}\tilde{\gamma}_1\gamma_{13}']^R,\\
\Gamma_{3\leftarrow 1}^R &= [\gamma_{31}'(1 - \tilde{\gamma}_1\gamma_{11}')^{-1}]^R,\\
\Gamma_3^R &= [\gamma_{33}' + \gamma_{31}'(1 - \tilde{\gamma}_1\gamma_{11}')^{-1}\tilde{\gamma}_1\gamma_{13}']^R,\\
\Gamma_{3\leftarrow 2}^R &= [\gamma_{32}' + \gamma_{31}'(1 - \tilde{\gamma}_1\gamma_{11}')^{-1}\tilde{\gamma}_1\gamma_{12}']^R.
\end{aligned}
$$

In Fig. 3.3, we show the diagrammatic representation of these solutions.

As an example, we consider $\Gamma_{2\leftarrow 1}^R$. The incoming line is hole-like in band 1 and the outgoing line particle-like in band 2. Taking into account that $\gamma_2^R = \gamma_3^R = 0$, the required hole-particle conversion must take place in band 1. This requires an elementary scattering event first, in order to convert the hole-like line from incoming to outgoing. Then the conversion takes place and we have an incoming particle line which can now scatter to band 2, which gives us the final outgoing line. This path can be extended by adding further pairs of particle-hole and hole-particle conversions in band 1 with the corresponding scattering events. Since the final line is in band 2, these paths are allowed and denoted by the 'bubble' in the diagram. The resulting geometric series yields $[(1 - \tilde{\gamma}_1\gamma_{11}')^{-1}]^R$ for the bubble.
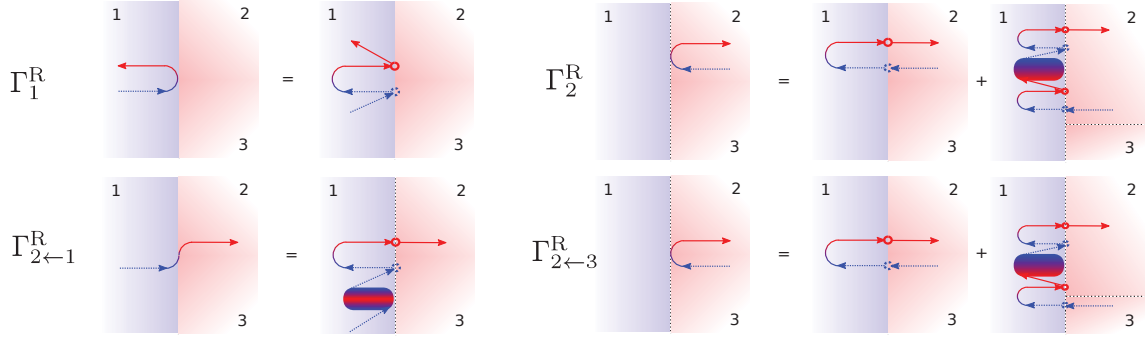
Figure 3.3. – Diagrammatic representation of the outgoing coherence functions at the SC/FM point-contact.

Distribution functions

The boundary conditions for the distribution function are already explicit in the sense that no further algebraic elimination is necessary once the outgoing coherence amplitudes $\Gamma_{k \leftrightarrows k'}$ are known. The distribution functions are not uniquely defined [37]. This allows us to choose a set of incoming distribution functions which simplifies the solution of the problem. The bias-voltage across the contact is modelled by shifting the chemical potential on the ferromagnetic side by eV. The 'gauge freedom' for the distribution functions can be used to put $x_1 = \tilde{x}_1 = 0$, which results in [53]:

$$x_{2,3} = \tanh\left(\frac{\varepsilon + \mathrm{eV}}{2k_B T}\right) - \tanh\left(\frac{\varepsilon}{2k_B T}\right), \tag{3.9}$$

$$\tilde{x}_{2,3} = -\tanh\left(\frac{\varepsilon - \mathrm{eV}}{2k_B T}\right) + \tanh\left(\frac{\varepsilon}{2k_B T}\right).$$

The solutions then read [53]:

$$X_2 = [x'_{22}] + [\Gamma_{2\leftarrow 1}\tilde{\gamma}_1]^{\mathrm{R}}[x'_{12}] + [x'_{21}][\gamma_1\tilde{\Gamma}_{1\rightarrow 2}]^{\mathrm{A}}$$
$$+ [\Gamma_{2\leftarrow 1}\tilde{\gamma}_1]^{\mathrm{R}}[x'_{11}][\gamma_1\tilde{\Gamma}_{1\rightarrow 2}]^{\mathrm{A}} - \Gamma^{\mathrm{R}}_{2\leftarrow 3}\tilde{x}_3\tilde{\Gamma}^{\mathrm{A}}_{3\rightarrow 2}, \tag{3.10}$$

$$X_3 = [x'_{33}] + [\Gamma_{3\leftarrow 1}\tilde{\gamma}_1]^{\mathrm{R}}[x'_{13}] + [x'_{31}][\gamma_1\tilde{\Gamma}_{1\rightarrow 3}]^{\mathrm{A}}$$
$$+ [\Gamma_{3\leftarrow 1}\tilde{\gamma}_1]^{\mathrm{R}}[x'_{11}]^{\mathrm{K}}[\gamma_1\tilde{\Gamma}_{1\rightarrow 3}]^{\mathrm{A}} - \Gamma^{\mathrm{R}}_{3\leftarrow 2}\tilde{x}^{\mathrm{K}}_2\tilde{\Gamma}^{\mathrm{A}}_{2\rightarrow 3}, \tag{3.11}$$

$$X_1 = [x'_{11}]^{\mathrm{K}} - \Gamma^{\mathrm{R}}_{1\leftarrow 2}\tilde{x}_2\tilde{\Gamma}^{\mathrm{A}}_{2\rightarrow 1} - \Gamma^{\mathrm{R}}_{1\leftarrow 3}\tilde{x}_3\tilde{\Gamma}^{\mathrm{A}}_{3\rightarrow 1}. \tag{3.12}$$

with $[x'_{ij}] = S_{i2}x_2 S^{\dagger}_{j2} + S_{i3}x_3 S^{\dagger}_{j3}$ for $i, j = 1, 2, 3$. In Fig. 3.4, we illustrate this for X_1. X_1 has a retarded quasi-particle leg pointing away from the interface and an advanced one pointing towards it. Taking into account that $x_1 = \tilde{x}_1 = 0$ and $\gamma^{\mathrm{R,A}}_{2,3} = \tilde{\gamma}^{\mathrm{R,A}}_{2,3} = 0$, we find four contributing paths. Two of these connect to the particle-like distribution functions in the FM-bands through elementary scattering events. These paths could be extended by adding pairs of particle-hole and hole-particle conversions with the corresponding scattering events on the SC-side. This, however, would imply that the final outgoing line appears at an intermediate step, which is excluded. For connecting to the hole-like distribution function, we need a particle-hole/hole-particle conversion on the advanced/retarded branch of the path. This yields the remaining contributing paths. The extra rule for distribution functions, which would prohibit paths involving $\tilde{x}_1$, is irrelevant thanks to $\tilde{x}_1 = 0$.

Transport processes

The Andreev spectrum is given by the differential conductance across the contact, which is related to the current and hence the diagonal part of the Keldysh-Green's function. Since
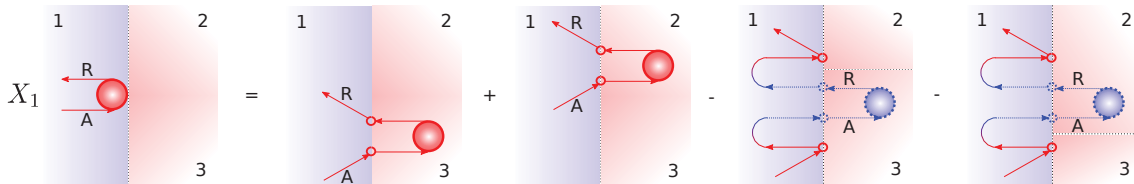
Figure 3.4. – Diagrammatic representation of X_1 at the SC/FM-interface.

current is conserved across the contact, it does in principle not matter on which side of the interface it is calculated. Andreev reflection, i.e. the process which allows for charge transfer at energies below the superconducting energy gap, is understood as a particle incident to the contact from the non-superconducting region being coherently reflected as a hole, while on the superconducting side, the corresponding current is carried by the condensate. To study this process, it is therefore advisable to calculate the current on the normal side of the contact. We have [53]:

$$\mathbf{j}_\eta = -\frac{eN_{F\eta}}{2} \int d\varepsilon \, \langle \mathbf{v}_\eta \cdot j_{\varepsilon,\eta} \rangle_{p_{F\eta+}}, \tag{3.13}$$

$$j_{\varepsilon,\eta} = X_\eta - x_\eta - \Gamma_\eta^R \tilde{x}_\eta \tilde{\Gamma}_\eta^A, \tag{3.14}$$

for the currents in bands $\eta = 2, 3$, where $\langle \bullet \rangle_{p_{F\eta+}}$ denotes a Fermi-surface average over trajectories pointing away from the interface. The trajectories pointing towards it are included through the term $-x_\eta$ in the integrant. The current is hence given by the sum of the imbalance $X_\eta - x_\eta$ of incoming and outgoing distribution functions and the term $\Gamma_\eta^R \tilde{x}_\eta \tilde{\Gamma}_\eta^A$, which is proportional to the incoming hole-like distribution function. This term, by the way, contains exactly the paths that we rejected for X_η by the additional rule for distribution functions. Note that, in principle, $j_{\varepsilon,\eta} \propto \text{Tr}(\hat{\tau}_3 \hat{g}^K)$. However, the second diagonal component of the Keldysh-Green's function must not be considered explicitly, as it is related to the first by symmetry.

We will now identify the elementary transport processes contributing to the current by studying (3.14). To identify the Andreev processes, we focus on the terms in $j_{\varepsilon,\eta}$ which are proportional to a hole-like distribution function, as this implies a conversion of incoming hole-like to reflected particle-like quasiparticles, which is precisely the property of Andreev reflection.[a] Apart from the terms $\Gamma_\eta^R \tilde{x}_\eta \tilde{\Gamma}_\eta^A$ entering (3.14), these are $\Gamma_{2\leftarrow 3}^R x_3 \tilde{\Gamma}_{2\rightarrow 3}^A$ and $\Gamma_{3\leftarrow 2}^R x_2 \tilde{\Gamma}_{2\rightarrow 3}^A$, entering X_2 and X_3, respectively. The latter two terms correspond to processes where the coherently reflected particle travels in the opposite spin-band with respect to the incoming hole; for the first terms, the band remains the same. The process where incoming and outgoing quasiparticle have opposite spin is the usual Andreev reflection process known from normal metal/singlet-superconductor contacts.[b] The other terms imply a spin-flip in the interface region, otherwise this process cannot be reconciled with the singlet-symmetry of the superconducting condensate. We will show in the next section that the amplitude of this process is indeed only non-zero if the scattering matrix contains spin-flip scattering and spin-mixing.

The remaining terms contained in $X_\eta - x_\eta$ describe quasi-particle transmissions across the

---

[a]Actually, it is usually the other way around. That these terms appear here rather than the particle-to-hole terms is due to the fact that we chose to eliminate the hole-hole entry of $\hat{g}^K$ instead of the particle-particle one.

[b]In the literature, one will usually find 'the same spin'. This is because the spin of a hole-like quasiparticle is often defined as opposite to that of the unoccupied state it is associated to. In the context of the method employed here, this would be confusing, as we would call hole-like amplitudes belonging to the spin-down band 'spin-up'.
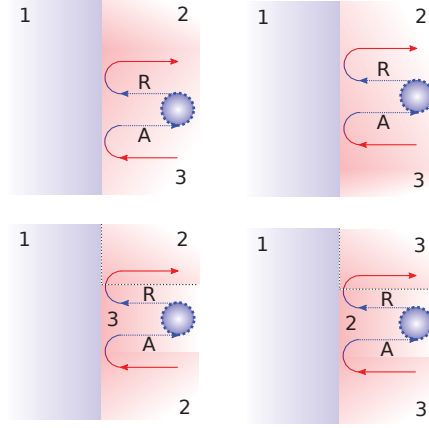
Figure 3.5. – Diagrams contributing to spin-flip Andreev reflection (upper diagrams) and normal Andreev reflection (lower diagrams).

interface. For energies below the gap ($|\varepsilon| < |\Delta|$), one can show that:

$$[X_2 - x_2 + \Gamma^{R}_{2\leftarrow 3}\tilde{x}_3\tilde{\Gamma}^{A}_{3\rightarrow 2}](\varepsilon) = [-\Gamma^{R}_{2\leftarrow 3}\tilde{x}_3\tilde{\Gamma}^{A}_{3\rightarrow 2} - \Gamma^{R}_2\tilde{x}_2\tilde{\Gamma}^{A}_2](-\varepsilon), \qquad (3.15)$$

$$[X_3 - x_3 + \Gamma^{R}_{3\leftarrow 2}\tilde{x}_2\tilde{\Gamma}^{A}_{2\rightarrow 3}](\varepsilon) = [-\Gamma^{R}_{3\leftarrow 2}\tilde{x}_2\tilde{\Gamma}^{A}_{2\rightarrow 3} - \Gamma^{R}_3\tilde{x}_3\tilde{\Gamma}^{A}_3](-\varepsilon), \qquad (3.16)$$

implying that these remaining terms contain exactly the second charge associated to each Andreev process. For energies above the gap, normal quasiparticle tunnelling will also contribute and cannot – to our present knowledge – be disentangled from the Andreev part [53]. Still, the contribution of Andreev reflection to the current is given by twice the contribution of the diagrams shown in Fig. 3.5 at energies above the gap, too.

The solutions for half metallic trajectories are obtained by putting all terms that contain the band index 3 to zero in the above relations. Obviously, this implies that there can only be spin-flip Andreev reflection for these channels.

4. Models for Quasiparticle Scattering at Superconductor-Ferromagnet Interfaces

The purpose of this chapter is to discuss microscopic models from which the normal state scattering matrix of the SC/FM contact can be inferred. The constraint of translational invariance in the contact plane implies that such a model is essentially limited to a scattering potential which varies in the z-direction. To obtain spin-active scattering from this scenario, this potential must be spin-dependent.[a] We investigate the 'classical' idealisations of such a potential, namely the box-shaped and δ-function potentials and show that these generically imply a relatively small spin-mixing effect. We then show that assuming the more realistic case of a smooth potential leads to a significant boost of the mixing angle. As a result of this analysis, we identify two basic mechanisms behind the spin-mixing effect.

The normal-state band structure of the FM and SC have been introduced in the previous chapter. We still need to specify the Hamiltonian of the interface:

$$H_{\mathrm{I}} = \frac{\mathbf{p}^2}{2m} - E_{\mathrm{F}} + V_{\mathrm{I}} + \frac{\vec{J_{\mathrm{I}}}}{2} \cdot \vec{\sigma}. \tag{4.1}$$

So in principle, we have exactly the same model for the interface as for the FM. However, we will assume that the exchange fields $\vec{J_{\mathrm{I}}}$ and $\vec{J}_{\mathrm{FM}}$ are misaligned. And we can choose V_{I} to tune the interface potential from a metallic to an insulating state. V_{I} and $|\vec{J_{\mathrm{I}}}|$ will vary as a function of z in the smooth potential model.

In the box-potential case, the scattering matrix is then obtained from matching wave functions which can be labeled by the conserved quantum numbers ε, $\mathbf{k}_{||}$. The details of this procedure are explained in the appendix. In the case of a δ-function potential, the SC and FM solutions are matched directly. The interface potential enters only through the matching conditions for derivatives [53]. We will not discuss this case explicitly here, but the qualitative result – a relatively small mixing angle – is analogous to the box-potential case [53].

The smooth potential model can be solved within the WKB-approximation if the variation is slow on the scale of the Fermi-wavelength. This, however, results in large interfaces and,

---

[a]This is, strictly speaking, only true for spin-flip scattering, the spin-mixing effect can in principle be induced by the spin-splitting of the FM band structure alone.

as a consequence, yields a weak coupling between the SC and the FM. It does also not really correspond to the experimental situation we are interested in, since the interfaces do certainly not extend over several Fermi-wavelengths. Instead, we can use the Recursive Green's Function method, which will be discussed at length in the second part of this thesis, to obtain the scattering matrix numerically.

4.1. Parameterisation of the Scattering Matrix

Using a partial singular value decomposition of general $U(4)$- and $U(3)$-matrices, we are able to show that the S-matrices discussed here can be parameterised as follows. Again, we refer to appendix A and Ref. [53] for details. For FM-trajectories, the S-matrix reads [53]:

$$S_{\text{FM}} = \left(\begin{array}{cc|c|c} r_{1\uparrow}e^{i\vartheta/2} & r_{1\uparrow\downarrow} & t_2 e^{i\vartheta_2/2} & t'_3 e^{i\vartheta_3/2} \\ r_{1\uparrow\downarrow} & r_{1\downarrow}e^{-i\vartheta/2} & t'_2 e^{-i\vartheta_2/2} & t_3 e^{-i\vartheta_3/2} \\ \hline t_2 e^{i\vartheta_2/2} & t'_2 e^{-i\vartheta_2/2} & r_2 & r_{23} \\ \hline t'_3 e^{i\vartheta_3/2} & t_3 e^{-i\vartheta_3/2} & r_{23} & r_3 \end{array} \right). \tag{4.2}$$

In the HM case, where the matrix is 3×3, we have [53]:

$$S_{\text{HM}} = \left(\begin{array}{cc|c} r_{1\uparrow}e^{i\vartheta/2} & r_{1\uparrow\downarrow} & t_2 e^{i\vartheta/4} \\ r_{1\uparrow\downarrow} & r_{1\downarrow}e^{-i\vartheta/2} & t'_2 e^{-i\vartheta/4} \\ \hline t_2 e^{i\vartheta/4} & t'_2 e^{-i\vartheta/4} & r_2 \end{array} \right). \tag{4.3}$$

This parameterisation exploits the $SU(2)$ spin-rotation invariance of the SC and neglects irrelevant scattering phases. Moreover, the second spherical angle characterising the misalignment of $\vec{J}_{\text{FM}}$ and $\vec{J}_{\text{I}}$, φ, was put to zero here (see Fig. 1.2 for its definition). If φ is finite, the scattering matrix is simply obtained from [52]:

$$S_{\text{FM}}(\varphi) = \Phi^*_{4\times4} S_{\text{FM}} \Phi_{4\times4}, \quad S_{\text{HM}}(\varphi) = \Phi^*_{3\times3} S_{\text{HM}} \Phi_{3\times3}, \tag{4.4}$$

with

$$\Phi_{4\times4} = \left(\begin{array}{cc} e^{i\sigma_z\varphi/2} & 0 \\ 0 & e^{i\sigma_z\varphi/2} \end{array} \right), \quad \Phi_{3\times3} = \left(\begin{array}{cc} e^{i\sigma_z\varphi/2} & 0 \\ 0 & e^{i\varphi/2} \end{array} \right). \tag{4.5}$$

Moreover, the parameters r_2, r_{23}, r_{32}, r_3 may contain additional complex phases which cannot be eliminated. Yet, only a relative phase between r_{32} and r_{23} is physically relevant. It plays an important role for the Josephson effect, as we shall see later on, but has no influence on the conductance of point contacts. Since $S = S^T$ if $\varphi = 0$, this relative phase is always given by 2φ. All other phases are irrelevant and hence neglected.

The phases ϑ, ϑ_2, ϑ_3 are all relevant for the creation of triplet correlations. ϑ is usually called 'spin-mixing angle'. It is responsible for the creation of triplet correlations inside the superconductor, as it enters the reflection matrix on the non-magnetic side of the interface. For ferromagnetic trajectories, the situation is somewhat more complicated – there is no simple relation between the mixing phases entering the transmission part of the S-matrix, ϑ_2 and ϑ_3, and the spin-mixing angle ϑ.

In the next section, we focus on ϑ only and try to provide some intuitive understanding as to how these scattering phases come about.

4.2. Basic Mechanisms behind the Spin-mixing Effect

It is rather obvious that if a difference of scattering phases between quasiparticles with different spin is to appear upon scattering at some potential, this potential must itself be spin-dependent. Quite generally, this simply implies that we have two different potentials for spin-up and spin-down particles. Consequently, such a potential also introduces a spin-quantisation axis, i.e., a basis in spin-space in which it is diagonal.

The appearance of scattering phases can be studied analytically in two limiting cases. These are (a) an abrupt change of the potential V, where bulk solutions can be defined and subsequently matched on both sides of the potential step, and (b) a smooth potential that varies slowly on the scale set by the typical wavelength of the eigenfunctions in question. This is the Fermi-wavelength in our case, and the method we can employ in this scenario is the WKB-approximation.

The first case was studied by Tokuyasu et al. [126] in the context of scattering at an interface between a normal metal and a ferromagnetic insulator. The matching conditions read:

$$1 + B_{\uparrow,\downarrow} = C_{\uparrow,\downarrow}, \quad ik(1 - B_{\uparrow,\downarrow}) = -\kappa_{\uparrow,\downarrow}C_{\uparrow,\downarrow}, \tag{4.6}$$

using the plane wave ansätze $e^{ik\cdot z} + B_{\uparrow,\downarrow}e^{-ik\cdot z}$ and $C_{\uparrow,\downarrow}e^{-\kappa_{\uparrow,\downarrow}\cdot z}$ for the normal and ferromagnetic side, respectively. We choose a decaying solution for the ferromagnet, as it is supposed to be an insulator. κ is spin-dependent due to the exchange field. The reflection matrix R of this interface is then easily found to be:

$$R = \begin{pmatrix} -\frac{1+ik/\kappa_\uparrow}{1-ik/\kappa_\uparrow} & 0 \\ 0 & -\frac{1+ik/\kappa_\downarrow}{1-ik/\kappa_\downarrow} \end{pmatrix} = e^{i\eta} \cdot e^{i\sigma_z \vartheta}. \tag{4.7}$$

Obviously, there is only a complex phase because we matched a propagating with an evanescent solution, otherwise there would be either no imaginary unit appearing in the matching conditions or there would be two that cancel. Secondly, the spin-mixing angle ϑ is only non-zero because $\kappa_\uparrow$ is different from $\kappa_\downarrow$. We hence conclude that spin-dependent wave vector mismatches lead to a scattering phase if one of the two wave vectors is imaginary.

We may consider another scenario where two interfaces are involved. This the relevant case for us, since we always assume an interlayer with a finite width in the following. Specifically, we consider a N/FM/N system, where the FM-layer has a width of the order of the Fermi-wavelength but is metallic.

We need to solve matching conditions at two interfaces now:

$$1 + B_{\uparrow,\downarrow} = C_{\uparrow,\downarrow} + D_{\uparrow,\downarrow}, \quad C_{\uparrow,\downarrow}e^{ik_{\uparrow,\downarrow}\cdot d} + D_{\uparrow,\downarrow}e^{-ik_{\uparrow,\downarrow}\cdot d} = E_{\uparrow,\downarrow}e^{ik\cdot d}, \tag{4.8}$$

$$k \cdot (1 - B_{\uparrow,\downarrow}) = k_{\uparrow,\downarrow} \cdot (C_{\uparrow,\downarrow} - D_{\uparrow,\downarrow}), \quad k_{\uparrow,\downarrow} \cdot (C_{\uparrow,\downarrow}e^{ik_{\uparrow,\downarrow}\cdot d} - D_{\uparrow,\downarrow}e^{-ik_{\uparrow,\downarrow}\cdot d}) = k \cdot E_{\uparrow,\downarrow}e^{ik\cdot d}.$$

Again, we obtain the reflection matrix at the first interface by solving for B:

$$R = \begin{pmatrix} r_\uparrow & 0 \\ 0 & r_\downarrow \end{pmatrix}, \quad r_{\uparrow,\downarrow} = \frac{(k^2 - k_{\uparrow,\downarrow}^2) \cdot (1 - e^{2ik_{\uparrow,\downarrow}\cdot d})}{(k + k_{\uparrow,\downarrow})^2 - (k - k_{\uparrow,\downarrow})^2 \cdot e^{2ik_{\uparrow,\downarrow}\cdot d}}. \tag{4.9}$$

In this case, the complex phase of the reflection parameter is due to $e^{2ik_{\uparrow,\downarrow}\cdot d}$. It can be understood as the contribution from waves that are transmitted at the first interface, then propagate forth and back in the interlayer an arbitrary number of times, and are eventually transmitted back into the first N-region. Yet, the leading order process contributing to
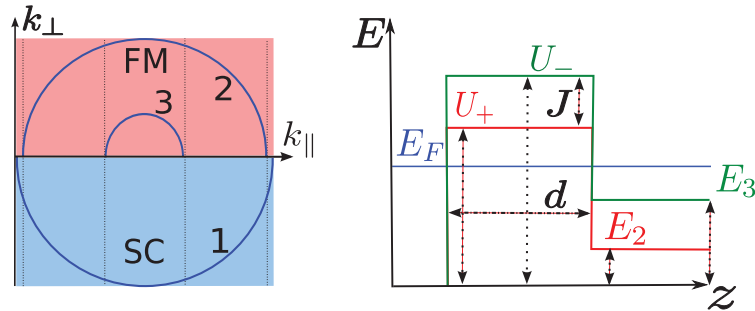
Figure 4.1. – Sketch of the interface model for the box-potential. The left sketch shows the Fermi-surface geometry at the contact, both FM-bands are assumed to be smaller than that of the SC. The right sketch shows the variation of the band bottom in the minority (green) and majority (red) band. The exchange splitting $J = J_{\mathrm{FM}} = J_{\mathrm{I}}$ is assumed to be identical in the FM and the interlayer. The quantisation axis is different in the interlayer and the FM. This is denoted by the different indices of $E_{2,3} = V_{\mathrm{FM}} \mp J/2$ and $U_{\pm} = V_{\mathrm{I}} \mp J/2$. Figure from Ref. [53]. Copyright 2010 by the American Physical Society.

the reflection is the direct reflection at the first interface, and there is no scattering phase arising from this process. This can easily be seen by assuming $k_{\uparrow,\downarrow} \approx 0$ in the expression above, which maximises the wave vector mismatch. The expression then becomes real and there is no spin-mixing phase.

Thus, there is a second mechanism contributing to the spin-mixing angle, which is simply the dephasing of two waves propagating over a certain length with different wave vectors. However, the step-potential scenario cannot make good use of this effect for the reasons explained above. It can be enhanced when the potential is smooth, which leads us to the WKB-scenario.

Effects due to wave vector mismatches are generically eliminated in WKB-approximation. This implies that there is only a finite reflection if the potential rises above the Fermi-energy over a certain length. The spin-mixing angle is then simply given by the phase-difference that quasiparticles accumulate inside the N-region until the point where $V_{\mathrm{I}} = E_{\mathrm{F}}$ [53], which we denote by $z_{\uparrow,\downarrow}$ for the respective band:

$$\vartheta = 2 \left[\int_{-\infty}^{z_{\uparrow}} \mathrm{d}z \, k_{\uparrow}(z) - \int_{-\infty}^{z_{\downarrow}} \mathrm{d}z \, k_{\downarrow}(z) \right]. \tag{4.10}$$

The very slow variation of the potential, which is mandatory for the WKB-approximation, is not realistic for the atomically thin interlayer regions that we wish to discuss here. We therefore resorted to a numerical calculation of the S-matrix for the smooth-potential model.

After this introductory discussion, we now turn to the models that we actually used for our calculations.

4.3. Box-shaped Scattering Potential and Influence of the Fermi-surface Geometry

The model we consider in this section is depicted in Fig. 4.1. We are dealing with a magnetic insulator of width d as the interlayer. The Fermi-surface geometry of the conducting bands which connect at the interface is shown on the left-hand side of the figure. The misalignment of the interface quantisation axis with respect to the bulk magnetisation of the FM is taken to be $\alpha = 0.5\pi$. Moreover, we have $V_{\mathrm{FM}} = 0.5 \, E_{\mathrm{F}}$, $V_{\mathrm{I}} = 1.5 \, E_{\mathrm{F}}$ and
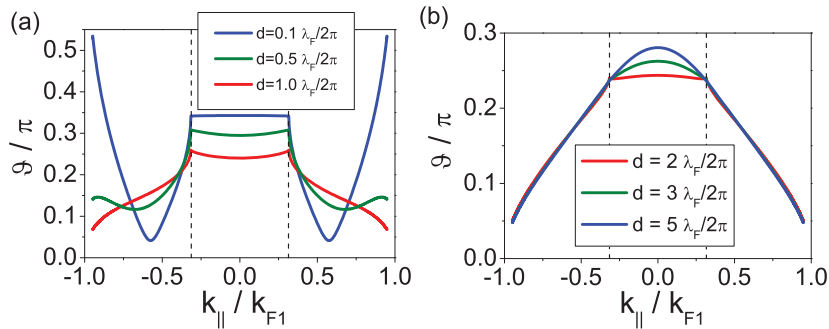
Figure 4.2. – The spin-mixing angle as a function of $k_{||}$ for different widths of the interlayer. Parameters are stated in the text. Figure from Ref. [53] with slight modifications.

$J = 0.8\, E_F$. In what follows, λ_F and k_F refer to the Fermi-wavelength and -vector in band 1.

In Fig. 4.2, we show the spin-mixing angle as a function of $k_{||}$ for different values of the interlayer width. Dashed lines indicate the separation of half metallic and ferromagnetic trajectories. We focus on the right plot first. These 'thick' interlayers correspond to the tunnelling limit situation, in which the spin-mixing angle is understood from the reflection of a magnetic insulating barrier as discussed in the previous section. The expression for ϑ that one can derive from eq. (4.7) reads [53]:

$$\vartheta = 2\left[\arctan\left(\frac{k_1}{\kappa_+}\right) - \arctan\left(\frac{k_1}{\kappa_-}\right)\right], \tag{4.11}$$

where $\kappa_\pm$ are the perpendicular components of the wave vectors in the interlayer and k_1 that of the superconductor. It fits the plot quite well, the maximum value of this expression is 0.29π at $k_{||} = 0$ for the given parameters, and it monotonically approaches 0 for grazing impact [53].

For thin interlayers, shown on the left-hand side, the behaviour is more intriguing – the reason being that the presence of the ferromagnetic bands on the other side of the interface can no longer be ignored in this case. The mixing angle remains relatively constant for ferromagnetic trajectories and shows a non-monotonical behaviour for half metallic ones if the interlayer is very thin. The increase for grazing impact can in this case be understood as resulting from the influence of the minority band in the FM, which has an evanescent mode for these trajectories. In the limit of an absent interlayer ($d = 0$), an analytical expression can be obtained [53]:

$$\vartheta = \pi - 2\arctan\left(\frac{k_1}{\kappa_3}\right), \tag{4.12}$$

where κ_3 is the evanescent wave vector of the minority band. Only the ration k_1/κ_3 enters here, as there is no complex phase from the second wave vector mismatch (k_1/k_2). Since k_1 approaches 0 for grazing impact (the majority band of the FM and the SC band have comparable Fermi wave vectors) while κ_3 increases, this expression approaches π for $k_{||} \to k_F$.[a] This explains the diverging behaviour of the mixing angle for grazing impact observed for $d = 0.1\, \lambda_F/2\pi$. Other than that, the functional dependence $\vartheta(k_{||})$ is difficult to explain from simple limiting cases, since all parts of the scattering problem play an important role.

---

[a] Unfortunately, there is a lapse in our original publication (Ref. [53]) in this respect. The second half of the statement "the wave vector k_1 drops to zero for grazing impact and so does the spin-mixing angle", is not correct.
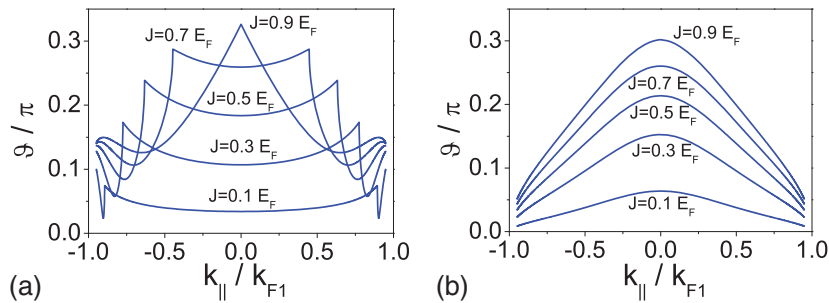
Figure 4.3. – Spin-mixing angle as a function of $k_{\parallel}$ for different values of the exchange field J (U_+ and E_2 are kept constant). (a) $d = 0.5\,\lambda_{\mathrm{F}}/2\pi$, (b) $d = 5.0\,\lambda_{\mathrm{F}}/2\pi$. Figure from Ref. [53]. Copyright 2010 by the American Physical Society.

In Fig. 4.3, we plot the mixing angle for different values of the exchange field J, k_{F2} is kept constant, so both V_{FM} and J_{FM} change. Not surprisingly, increasing the exchange field enhances the mixing angle, but not dramatically. The crossover point between half metallic and ferromagnetic trajectories now changes, which can be seen clearly in Fig. 4.3a. The mixing angle remains limited to values smaller than 0.5π.

Fig. 4.4 shows the mixing phases $\vartheta_{2,3}$ which enter the transmission blocks of the scattering matrix. In the next chapter, we will see that these phases are important for the magnitude of triplet correlations transmitted into the ferromagnet. Naturally, ϑ_3 is only defined for $k_{\parallel} < k_{\mathrm{F3}}$, while ϑ_2 is identical to $\vartheta/2$ for $k_{\parallel} > k_{\mathrm{F3}}$. For $k_{\parallel} < k_{\mathrm{F3}}$, we see that ϑ_2 is significantly enhanced compared to $\vartheta/2$ if the interlayer is thick (Fig. 4.4b). This will be important later on, as it is one reason why the triplet Josephson current that we find is enhanced for ferromagnets with intermediate polarisation compared to fully half metallic ones. Other than that, we see that ϑ_2 and ϑ_3 have a different functional dependence on $k_{\parallel}$ and that there is a crossover from a local minimum at $k_{\parallel} = 0$ to a local maximum as the width of the interlayer increases.

Transmitting pairing correlations between quasiparticles through an interface happens by transmitting the quasiparticles themselves. Accordingly, we shall see in the next chapter that the magnitude of induced triplet correlations depends on the absolute value of the transmission parameter $|t_\eta t'_\eta|$. The reason is clear. Since we transform singlet to triplet correlations, one of the quasiparticles involved must undergo a spin-flip, while the other does not. The relevant probability amplitude is hence the product of a spin-flip transmission, t'_η, and one without spin-flip, t_η. This quantity is plotted in Fig. 4.5 for both FM-bands. In Fig. 4.5b and d, the thick interlayers are shown and the transmission decreases monotonically. The latter is governed by the decay of the wave functions in the insulating interlayer in this case, and hence suppressed for grazing trajectories, since κ_+, κ_- increase with growing $k_{\parallel}$. When the interlayer is thin, the wave vector mismatches dominate the transparency of the interface and this leads – again – to a relatively complicated behaviour. Interestingly, the maxima of the transmission for half metallic trajectories, shown in Fig. 4.5a, coincide with the minima of ϑ [53]. We cannot offer a simple explanation for this, but it is important to keep in mind that all relevant scattering parameters may be non-monotonical, and the most relevant transport channels contributing to the current will hence not always be those close to perpendicular impact. Note also that the transmission first increases with growing thickness of the interlayer before showing the expected suppression for ever thicker interfaces. The reason is that the spin-flip transmission t'_η is relatively ineffective if the misaligned interlayer is to small.
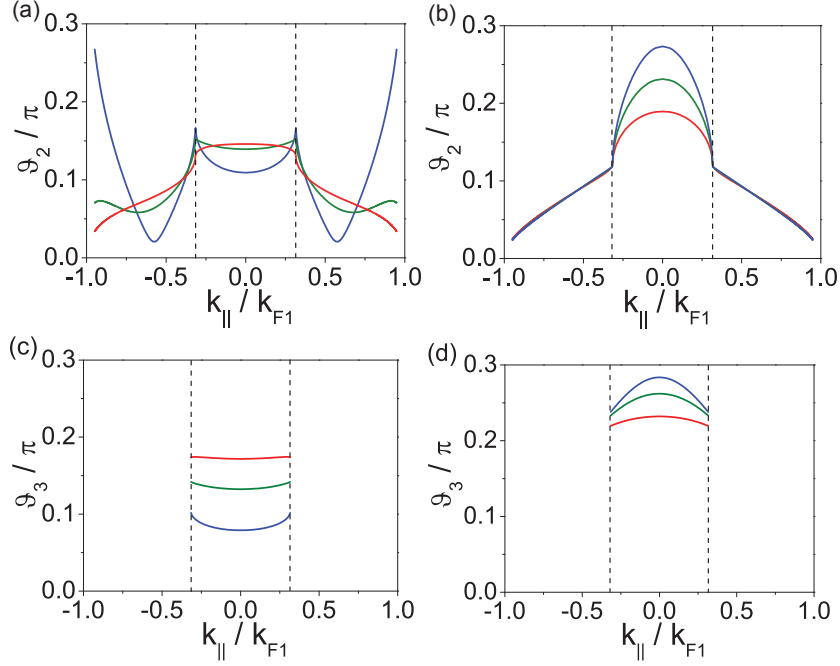
Figure 4.4. – ϑ_2 (top) and ϑ_3 (bottom) as a function of $k_{||}$ for different values of the interlayer thickness. As in Fig. 4.2, we have $d = 0.1\ \lambda_F/2\pi$ (blue), $d = 0.5\ \lambda_F/2\pi$ (green), $d = 1.0\ \lambda_F/2\pi$ (red) on the left-hand side, and $d = 2\ \lambda_F/2\pi$ (red), $d = 3\ \lambda_F/2\pi$ (green), $d = 5\ \lambda_F/2\pi$ (blue) on the right-hand side. Figure from Ref. [53] with slight modifications.

Figure 4.5. – The transmission parameters $|t_2 t_2'|$ (top) and $|t_3 t_3'|$ (bottom) as a function of $k_{||}$ for different values of the interlayer thickness. $d = 0.1\ \lambda_F/2\pi$ (blue), $d = 0.5\ \lambda_F/2\pi$ (green), $d = 1.0\ \lambda_F/2\pi$ (red) on the left-hand side, and $d = 2\ \lambda_F/2\pi$ (red), $d = 3\ \lambda_F/2\pi$ (green), $d = 5\ \lambda_F/2\pi$ (blue) on the right-hand side. Figure from Ref. [53] with slight modifications.

Figure 4.6. – Sketch of the interface model for the smooth-potential. The left sketch shows the Fermi-surface geometry at the contact, both FM-bands are assumed to be larger than that of the SC. The right sketch shows the variation of the band bottom in the minority (green) and majority (red) band. The exchange splitting $J = J_{\mathrm{FM}} = J_{\mathrm{I}}$ is kept constant once it reaches its maximum (not true for the sketch) and increases monotonically on the SC side of the interface. Figure from Ref. [53]. Copyright 2010 by the American Physical Society.

4.4. Scattering Potentials with Arbitrary Shape

We now turn to the smooth potential model and demonstrate that a spin-mixing angle well above 0.5π can be achieved in this case. The considered model is shown in Fig. 4.6. We choose a different Fermi-surface geometry here, where only ferromagnetic trajectories are relevant. This simplifies our calculations and is sufficient to prove the point we want to make. The variation of the potential is sketched on the right-hand side of that figure, while the exact functional dependence is given by [53]:[a]

$$
U_\pm = \begin{cases}
(V_{\mathrm{I}} \mp J/2) \cdot e^{-(z+d)^2/\sigma^2} & z < -d \\
V_{\mathrm{I}} \mp J/2 & -d < z < 0 \\
V_{\mathrm{FM}} \mp J/2 + (V_{\mathrm{I}} - V_{\mathrm{FM}})e^{-z^2/\sigma^2} & z > 0
\end{cases}
\tag{4.13}
$$

The potential V_{I} and exchange field J hence increase with a Gaussian slope for $z < -d$, remain constant over a width d and then decrease to $E_{2,3}$, where the slope is chosen so that the exchange splitting remains constant. σ controls the smoothness of the potential. The exact functional dependence of V_{I} is shown in Fig. 4.7a, for the choice of parameters that we consider. Since increasing σ while keeping d constant would widen the interface substantially and hence reduce the transmission, we keep $\sigma + d = 0.7\ \lambda_{\mathrm{F}}$ [53]. The quantisation axis is assumed to switch abruptly at $z = -d/2$ by an angle of $\alpha = 0.5\pi$. Taking into account a smooth variation of the magnetisation direction would pose no difficulty within this approach, but the important point is the enhanced spin-mixing effect due to the smoothened slopes of the potential.

For calculating the scattering matrix, the Schrödinger equation was discretised in the z-direction. The Green's function of the resulting tight-binding Hamiltonian was then calculated with the Recursive Green's Function technique and the scattering matrix can subsequently be obtained from the Fisher-Lee relations[b] [45, 53]. Details are provided in appendix C.

The result is shown in Fig. 4.7b, where the mixing angle increases monotonically as the 'smoothness' of the interface increases and easily reaches values well above 0.5π. ϑ also

---

[a]In our original publication (Ref.[53]), the ±-signs on the right-hand side of this equation are erroneously interchanged.

[b]This calculation was implemented by Georgo Metalidis.

Figure 4.7. – The spin-mixing angle in the smooth potential model. (a) V_I as a function of z for $\sigma = 0, ..., 0.7 \, \lambda_{F1}$, increasing in steps of $0.1 \, \lambda_{F1}$. $d + \sigma = 0.7 \, \lambda_{F1}$, $J = 0.7 \, E_F$, and $V_{FM} = -0.5 \, E_F$. (b) spin-mixing angle for the potentials shown in (a), ϑ increases monotonically with σ. Figure from Ref. [53] with slight modifications and additional data.

decreases monotonically with $k_\|$, which corresponds to the fact that the potential is in the tunnelling limit, and that there is no cross-over from ferromagnetic to half metallic trajectories due to the Fermi-surface geometry that we assume. In this scenario, there is no real separation between the two mechanisms for acquiring a spin-mixing phase discussed in the previous section, since the potential is neither in the step-function nor in the WKB-limit.

Given that the smoothening of the potential has such an important effect, the dephasing of quasiparticles on the superconducting side seems to be the dominating mechanism. We underline that this model is also more reasonable from an experimental point of view, as the variation we assume happens on the scale of a Fermi-wavelength which is more realistic than a fully abrupt change of the potential.

In the next chapter, we discuss the Andreev spectra that we obtained from the interface models presented here.

5. Conductance Spectra of Point-Contacts

In this chapter, we summarise our results on conductance spectra of superconductor-ferromagnet (SC-FM) point-contacts. In most experiments, these contacts are created by pressing a superconducting tip into a ferromagnetic sample. A more laborious technique consists in growing them in planar junctions by drilling a nanoscale hole into an insulating buffer layer [127, 97]. In both cases, contacts with a macroscopic number of transport channels are created, i.e., there is no sign of conductance quantisation. On the other hand, the contact is small compared to the coherence length of the superconductor, ξ, which implies that the inverse proximity effect can usually be neglected. As anticipated in the introduction, such contacts have been studied intensively, since they may provide information about the spin-polarisation P of charge carriers. Here, we will show that other features related to the triplet proximity effect can also show up in such spectra and that spin-active scattering may invalidate the inferred values of P.

The fundamental assumption underlying our model is that the diameter a of the contact complies to $\lambda_F < a < \xi$. If the contact was small compared to the Fermi-wavelength, the assumption of translational invariance in the contact plain would definitely be ill-founded. And since the contact is small compared to the coherence length, we can assume that the superconductor is unperturbed and can thus use the bulk-coherence functions as incoming solutions on the SC-side of the contact.

In the first section, we shortly review some analytical results and in particular discuss the creation of triplet pairing correlations and Andreev bound states at the contact. We then turn to the conductance spectra which were calculated on the basis of the interface models introduced in the previous chapter. After that, we show that earlier theoretical
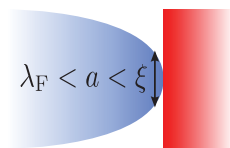
Figure 5.1. – A superconducting tip (blue) is pressed into a ferromagnetic sample (red). The size of the contact is small compared to the superconducting coherence length ξ, but large compared to the Fermi-wavelength.

models obtained from Bogoliubov-de-Gennes (BdG) wave function matching are contained in our theory and eventually turn to the comparison with experiment. In the last section, we briefly compare our approach to other theoretical models used in the study of this problem.

5.1. Analytical Analysis

The general solutions of the boundary conditions at the SC/FM contact were introduced in chapter 3. We now discuss analytical expressions for the relevant coherence functions Γ_1^R, Γ_2^R, Γ_3^R, and $\Gamma_{2 \leftrightarrows 3}^R$.[a]

We start with the solutions on the SC side and discuss the symmetry classification of pairing correlations and the emergence of Andreev bound states in the local density of states (DOS) in this context. We then turn to the solutions on the FM side to analyse the pairing correlations induced there and discuss their significance for Andreev reflection.

Symmetry classification of induced pairing correlations

Since the incoming coherence functions from the FM-side are zero, only the reflection matrix on the superconducting side enters. As shown in the appendix, the reflection parameters can be written as [53]:[b]

$$
\begin{aligned}
r_{1\uparrow} &= r_\uparrow \cos(\alpha_Y/2)^2 + r_\downarrow \sin(\alpha_Y/2)^2 \\
r_{1\downarrow} &= r_\uparrow \sin(\alpha_Y/2)^2 + r_\downarrow \cos(\alpha_Y/2)^2 \\
r_{1\uparrow\downarrow} &= (r_\uparrow - r_\downarrow)\frac{\sin(\alpha_Y)}{2}.
\end{aligned}
\tag{5.1}
$$

Here, α_Y is related to a spin-rotation defined in the context of the partial singular value decomposition discussed in appendix A. It has no simple connection to the physical misalignment angle α between the interlayer magnetisation and that of the FM bulk. Yet, $\alpha_Y = 0$ if $\alpha = 0$ holds, since spin-rotation symmetry is restored in that case. $r_{\uparrow,\downarrow}$ are the eigenvalues of the reflection matrix. In terms of these parameters, we have:

$$
\begin{aligned}
\hat{\Gamma}_1^R &= [\hat{S}_{11}\hat{\gamma}_1\hat{\tilde{S}}_{11}]^R \\
&= \Big[2i\sin(\vartheta/2)\hat{\rho} + [(\rho + \rho_s)\cos(\vartheta) - \rho_s]\,i\hat{\sigma}_y + (\rho + \rho_s)\,i\sin(\vartheta)\hat{\sigma}_x\Big]\gamma,
\end{aligned}
\tag{5.2}
$$

with

$$
\begin{aligned}
\rho &= r_\uparrow r_\downarrow, \qquad \rho_s = (r_\uparrow - r_\downarrow)^2 \frac{\sin^2(\alpha_Y)}{4}, \\
\hat{\rho} &= \sqrt{\rho_s} \cdot \mathrm{diag}[r_\uparrow \cos^2(\alpha_Y/2) + r_\downarrow \sin^2(\alpha_Y/2), \qquad r_\downarrow \cos^2(\alpha_Y/2) + r_\uparrow \sin^2(\alpha_Y/2)].
\end{aligned}
\tag{5.3}
$$

This simple formula teaches us a lot already. The outgoing coherence function on the SC side has three contributions which correspond to the different spin-symmetries of the associated anomalous Green's function:

$$
\hat{f}_1^R(p_{F,z} < 0) = -i2\pi\left[(1 - \hat{\Gamma}_1\hat{\tilde{\gamma}}_1)^{-1}\hat{\Gamma}_1\right]^R, \quad \hat{f}_1^A(p_{F,z} > 0) = i2\pi\left[(1 - \hat{\Gamma}_1\hat{\tilde{\gamma}}_1)^{-1}\hat{\Gamma}_1\right]^A. \tag{5.4}
$$

---

[a]In this section only, we use $\hat{\bullet}$ to indicate a matrix in spin-space.

[b]Note the sign change in the last equation compared to Ref. [53]. This is due to the parameterisation of $SU(2)$, which we choose consistently here, but which is unfortunately not consistent across all of our publications. Specifically, the definition of the original article is recovered by $\alpha_Y \mapsto -\alpha_Y$.
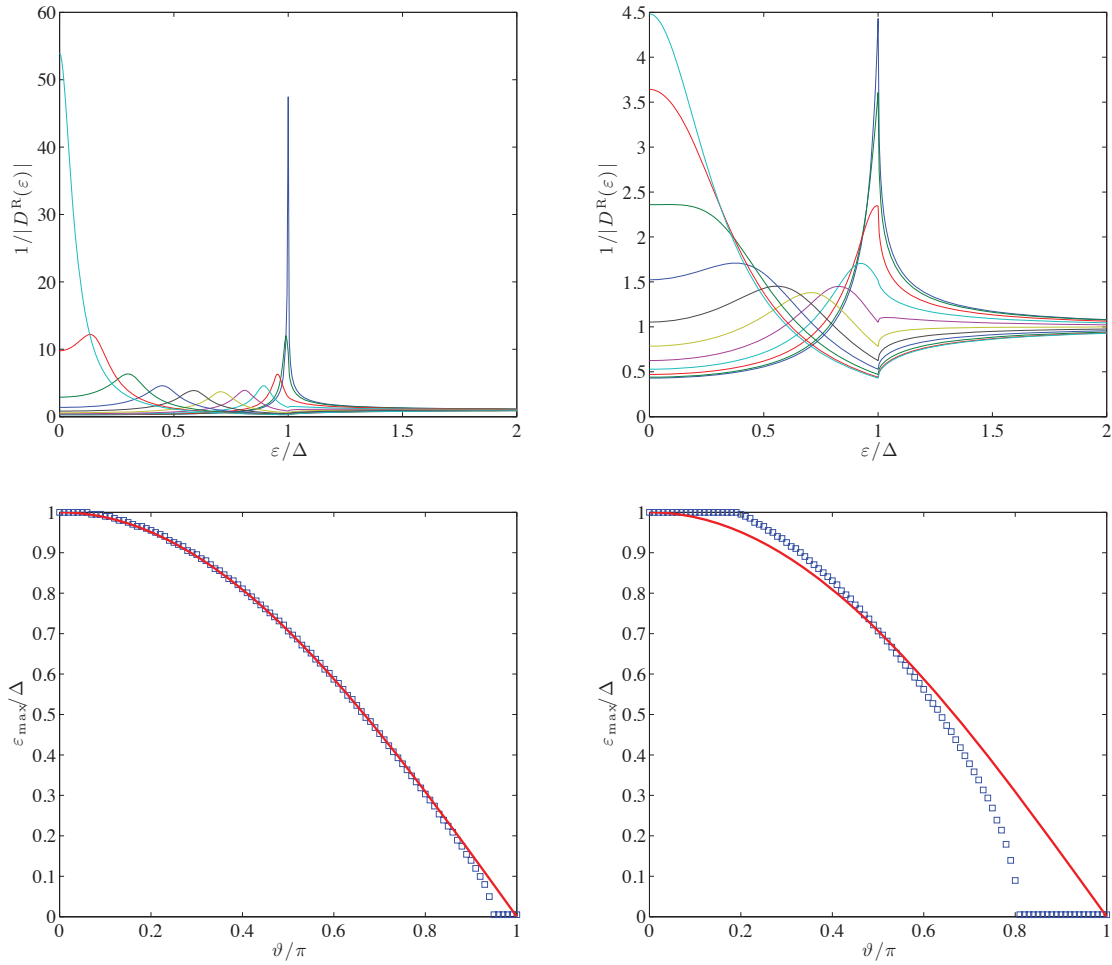
Figure 5.2. – Top row: $1/|D^{\mathrm{R}}|$ (see text for the definition) as a function of energy, for $\vartheta = 0.0\pi, ..., 1.0\pi$ in steps of 0.1π and $r_\uparrow = 0.9$, $r_\downarrow = 0.95$ (left column), $r_\uparrow = 0.7$, $r_\downarrow = 0.75$ (right column). $\alpha_Y = 0.5\pi$. With increasing mixing angle, the maxima move to smaller energies. The function is symmetric in energy. Bottom row: position of the maximum as a function of the mixing angle (blue) compared to the tunnelling limit formula $\cos(\vartheta/2)$ (red).

Here, $\hat{\tilde{\gamma}}$ is an incoming and $\hat{\Gamma}$ an outgoing amplitude with respect to the interface. In terms of the above parameters, we have:

$$f_1^{\mathrm{R}}(p_{\mathrm{F,z}} < 0) = -i2\pi \left[\frac{\hat{\Gamma}_1 + \tilde{\gamma}\gamma^2\rho^2 i\hat{\sigma}_y}{D} \right]^{\mathrm{R}} \tag{5.5}$$

$$D^{\mathrm{R}} = \left[1 + 2\gamma\tilde{\gamma}[\rho\cos\vartheta - \rho_s(1 - \cos\vartheta)] + (\gamma\tilde{\gamma})^2\rho^2 \right]^{\mathrm{R}}.$$

Here, γ and $\tilde{\gamma}$ are defined by $\hat{\gamma}_1 = \gamma i\hat{\sigma}_y$ and $\hat{\tilde{\gamma}}_1 = \tilde{\gamma} i\hat{\sigma}_y$, respectively. It is easy to see that if only the 'green' term is present in equation (5.2), f_1^{R} is proportional to $i\hat{\sigma}_y$ and therefore a pure singlet. If the 'red' term is present, there is an additional component proportional to $\hat{\sigma}_x$, which is the $S_z = 0$ triplet. And finally, in case that the diagonal 'blue' term appears, f_1^{R} will have an equal-spin triplet component. Inspecting these terms more closely shows that the red term is present if there is a spin-mixing phase ($\vartheta \neq 0$), and the blue term only if there is also a finite misalignment $\alpha_Y \neq 0$ in addition to that. This finding is in line with our introductory discussion regarding the creation of triplet correlations at such interfaces.

The denominator D^{R} enters all outgoing-coherence functions and plays an important role in the following. We plot $1/|D^{\mathrm{R}}|$ for two parameter sets in Fig. 5.2. The maximum of this function imprints itself both in the density of states and in the Andreev reflection amplitude. For perfect reflection, i.e. $r_\uparrow = r_\downarrow = 1$, the maximum becomes a pole whose position is given by [46, 53]:

$$\varepsilon_{\mathrm{pole}} = \pm\Delta\cos(\vartheta/2), \tag{5.6}$$

but as the transmission increases the maximum remains at $\varepsilon_{\mathrm{max}} = \Delta$ and just decreases in magnitude before it starts to move to smaller energies. The same happens at the final position $\varepsilon_{\mathrm{max}} = 0$, where the maximum then increases in magnitude with growing ϑ.

Now, how do we see that the validity of the Pauli principle is maintained, i.e., that the triplet contributions are indeed odd in frequency? For real frequencies, the symmetry implied by the Pauli principle connects advanced and retarded amplitudes:

$$\hat{f}^{\mathrm{A}}(\varepsilon, \mathbf{p}_{\mathrm{F}}) = -\left[\hat{f}^{\mathrm{R}}(-\varepsilon, -\mathbf{p}_{\mathrm{F}}) \right]^T. \tag{5.7}$$

This can easily be inferred from the definition of these amplitudes in terms of field-operators [102], or, alternatively, from the basic symmetry relations that hold for the coherence functions:

$$\hat{\gamma}^{\mathrm{A}}(\varepsilon, \mathbf{p}_{\mathrm{F}}) = \left[\hat{\tilde{\gamma}}^{\mathrm{R}}(\varepsilon, \mathbf{p}_{\mathrm{F}}) \right]^\dagger = \left[\hat{\gamma}^{\mathrm{R}}(-\varepsilon, -\mathbf{p}_{\mathrm{F}}) \right]^T. \tag{5.8}$$

From the last equation, we directly infer $\gamma^{\mathrm{A}}(\epsilon) = -\gamma^{\mathrm{R}}(-\epsilon)$, since $i\hat{\sigma}_y^T = -i\sigma_y$ and the bulk-coherence function is independent of momentum. Moreover, $S_{11}^{\mathrm{A}} = [S_{11}^{\mathrm{R}}]^\dagger$. Thus, $f_1^{\mathrm{A}}(p_{\mathrm{F,z}} > 0, \epsilon > 0)$ is obtained from the expression for $f_1^{\mathrm{R}}(p_{\mathrm{F,z}} < 0, \epsilon < 0)$ by replacing $\vartheta \mapsto -\vartheta$ and $(\gamma, \tilde{\gamma}) \mapsto (-\gamma, -\tilde{\gamma})$ and multiplying the resulting expression with -1. This implies $(-1)^3 = -1$ for the triplet terms, since these are odd functions of ϑ and $(-1)^2 = 1$ for the singlet-terms. The third minus-sign for the singlet term is generated by the transposition in equation (5.7) and together with the minus-sign in that relation we find the symmetry to be fulfilled. In other words, the sign change for the triplet component was provided by $\vartheta \mapsto -\vartheta$; so, as momentum is irrelevant in all of the above expressions, *being an odd-function of ϑ can be identified with being odd in frequency in this context.* ϑ is a scattering phase originating from the presence of an exchange field. It is hence
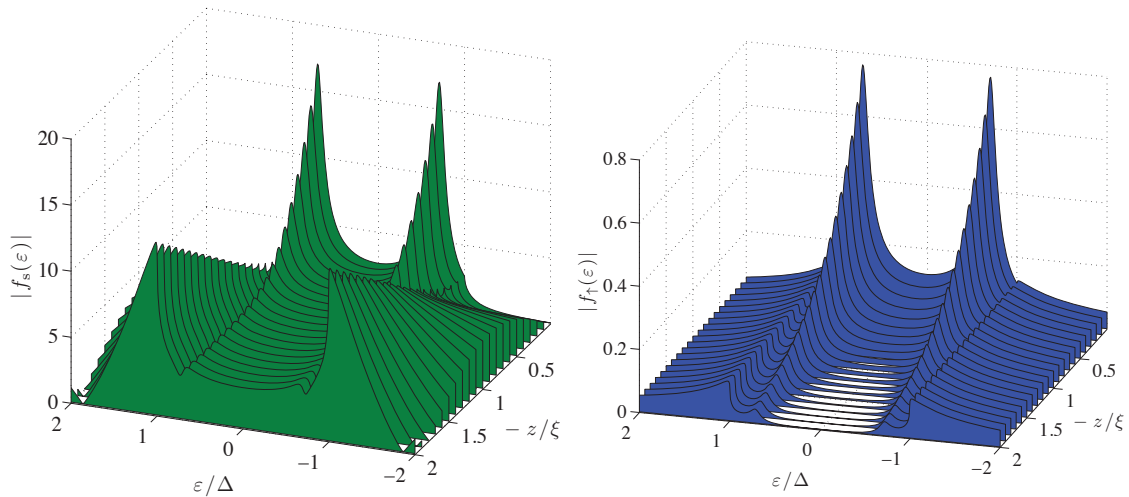
Figure 5.3. – The singlet (green) and ↑↑-triplet (blue) component of $f_1^R(p_{F,z} < 0)$ for a single trajectory with $r_\uparrow = 0.9$, $r_\downarrow = 0.95$, $\alpha_Y = 0.5\pi$ and $\vartheta = 0.5\pi$. $\xi = \hbar v_{F1}/\Delta$. $-z$ is the distance to the interface.

not surprising that it breaks time-reversal symmetry, i.e., changes sign for the advanced scattering matrix.

To see how these components decay into the superconductor, we need to consider the solution of the Riccati-equation for $\hat{\Gamma}_1^R$. Neglecting the self-consistency of the order parameter, we assume $\hat{\Delta} = const$ and may use the analytic solution for homogenous self-energies [37]:

$$\hat{\gamma}^R(s) = \left[\hat{\gamma}_h + e^{is\hat{\Omega}} \cdot [\hat{\gamma}_0 - \hat{\gamma}_h] \cdot \left(e^{-is\hat{\Omega}} + \frac{\hat{\tilde{\Delta}}}{\hat{\Omega}} \cdot i\sin(s\hat{\Omega}) \cdot [\hat{\gamma}_0 - \hat{\gamma}_h]\right)^{-1}\right]^R. \qquad (5.9)$$

Here $\hat{\Omega} = \varepsilon\hat{1} - \hat{\gamma}_h\hat{\tilde{\Delta}}^a$, $\hat{\gamma}_h$ is the homogeneous bulk solution inside the SC and $\hat{\gamma}_0 = \hat{\Gamma}_1$. ρ parameterises the trajectory ($\mathbf{R} = s\mathbf{v}_{F,1} + \mathbf{R}_0$) [37]. As can be seen from the plots in Fig. 5.3, the triplet components of $\hat{\Gamma}_1$ decay only for energies smaller than the gap if real frequencies are considered. This is a consequence of the fact that we do zero-temperature calculations in the clean limit, which implies that there is basically no source of decoherence in our calculation. Note also that the singlet component shows an oscillating behaviour above the gap-energy. The simplest way to convince oneself that the triplet correlations decay globally is to consider Matsubara-Green's functions instead, i.e. finite temperatures. For our purpose, it is sufficient to replace $\varepsilon \mapsto i\epsilon_n$, with $\epsilon_n > 0$, to achieve this. It is then immediately obvious that the $e^{i\rho\hat{\Omega}}$-term becomes a decaying exponential. Thus, the second term on the right-hand side of equation (5.9) is suppressed and only the bulk solution, which is a singlet, remains.

Finally, we plot the spin-resolved density of states on the superconducting side of the contact in Fig. 5.4. In this case, the Fermi-surface average reduces to:

$$\langle g^R(\varepsilon, \mathbf{p}_F)\rangle = \frac{1}{2}\left[g^R(\varepsilon, p_{F,z} > 0) + g^R(\varepsilon, p_{F,z} < 0)\right]. \qquad (5.10)$$

We see that the bound states are fully polarised, i.e. the bound state at positive energy appears only in the spin-up DOS and the bound state at negative energy only in the spin-down DOS. The bound states decay on the scale of the superconducting coherence length $\xi = \hbar v_{F1}/\Delta$ and are thus localised at the interface.

---

[a]Note that this is proportional to the unit matrix.
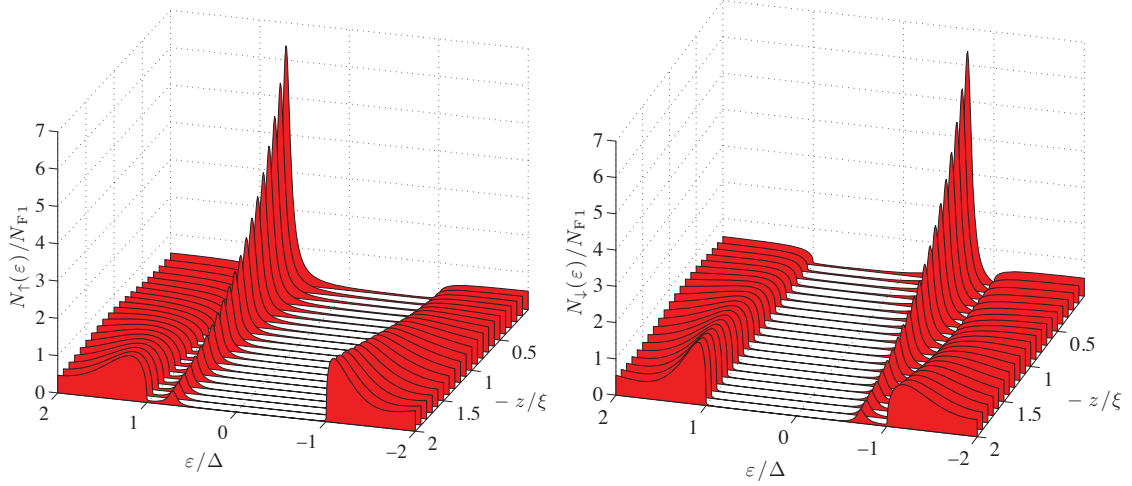
Figure 5.4. – Spin-resolved density of states on the superconducting side of the interface for a single trajectory with $r_\uparrow = 0.9$, $r_\downarrow = 0.95$, $\alpha_Y = 0.5\pi$ and $\vartheta = 0.5\pi$. $\xi = \hbar v_{F1}/\Delta$. $-z$ is the distance from the interface.

Andreev amplitudes

In chapter 3, we argued that the current contributions of Andreev reflection are given by $\Gamma_2^R x_2 \tilde{\Gamma}_2^A$ and $\Gamma_{2\leftarrow 3}^R x_3 \tilde{\Gamma}_{3\rightarrow 2}^A$ for band 2, and $\Gamma_3^R x_3 \tilde{\Gamma}_3^A$ and $\Gamma_{3\leftarrow 2}^R x_2 \tilde{\Gamma}_{2\rightarrow 3}^A$ for band 3. Since $\tilde{\Gamma}_\eta^A = [\Gamma_\eta^R]^\dagger$ and $\tilde{\Gamma}_{2,3\rightarrow 3,2}^A = [\Gamma_{3,2\leftarrow 2,3}^R]^\dagger$, $|\Gamma_\eta^R|^2$ can be interpreted as the amplitude of spin-flip Andreev reflection in the respective band, and $|\Gamma_{2\rightarrow 3}^R|^2$ and $|\Gamma_{3\rightarrow 2}^R|^2$ as the amplitude of normal Andreev reflection in band 2 or 3, respectively. The analytical expressions for these amplitudes in terms of the parameters defined above are [53]:[a]

$$\Gamma_\eta^R = \left[\frac{T_{\eta 1}\hat{N}i\hat{\sigma}_y T_{1\eta}^*}{D}\right]^R \quad \Gamma_{2\leftarrow 3}^R = \left[\frac{T_{21}\hat{N}i\hat{\sigma}_y T_{13}^*}{D}\right]^R, \quad \Gamma_{3\leftarrow 2}^R = \left[\frac{T_{31}\hat{N}i\hat{\sigma}_y T_{12}^*}{D}\right]^R \quad (5.11)$$

$$\hat{N} = \gamma(1 + \gamma\tilde{\gamma}\left[e^{-i\vartheta\hat{\sigma}_z}(\rho + \rho_s) - \rho_s + 2\hat{\sigma}_y\hat{\rho}\sin(\vartheta/2)\right]). \quad (5.12)$$

These expressions are quite cumbersome, we limit the discussion to the tunnelling limit, where $r_\uparrow \approx r_\downarrow \approx 1$ and hence the off-diagonal elements of S_{11} vanish. In that case, we have [53]:

$$\Gamma_\eta^R = \left[2i\ t_\eta t'_\eta \gamma \frac{\sin\vartheta_\eta - \sin(\vartheta - \vartheta_\eta)\gamma\tilde{\gamma}}{1 + (\gamma\tilde{\gamma})^2 + 2\cos(\vartheta)\gamma\tilde{\gamma}}\right]^R \quad (5.13)$$

$$\Gamma_{2\leftarrow 3}^R = \left[\gamma \frac{\tau + \tau_\vartheta\gamma\tilde{\gamma}}{1 + (\gamma\tilde{\gamma})^2 + 2\cos(\vartheta)\gamma\tilde{\gamma}}\right]^R = \Gamma_{3\leftarrow 2}^R, \quad (5.14)$$

with

$$\tau^R = t_2 t_3 e^{i\vartheta_{23}} - t'_2 t'_3 e^{-i\vartheta_{23}}, \quad \tau_\vartheta^R = t_2 t_3 e^{i(\vartheta_{23}-\vartheta)} - t'_2 t'_3 e^{-i(\vartheta_{23}-\vartheta)}, \quad \vartheta_{23} = (\vartheta_2 + \vartheta_3)/2.$$

We observe that both $\alpha \neq 0$ and either $\vartheta_\eta \neq 0$ or $\vartheta \neq 0$ are required for Γ_η^R to be finite, which again confirms our arguments in regard to the triplet proximity effect. No such requirements apply to $\Gamma_{2\leftarrow 3}^R$.

Note that the expressions shown here have the same denominator, D^R, as those of the previous section. The Andreev amplitudes will hence be enhanced at energies where $1/|D^R|$

---

[a]Note that there is a typo in the equation for $\hat{N}$ in Ref. [53].

has a maximum. This maximum thus imprints itself both in the density of states at the interface, where it gives rise to an interface bound state inside the energy gap, and in the Andreev-amplitudes, which implies an enhanced current contribution from Andreev reflection [46, 142]. Since the interface bound states are localised, they do not facilitate quasiparticle tunnelling in this single-contact geometry. However, quasiparticle tunnelling through these states turned out be crucial for understanding the non-local conductance signal in FM/SC/FM-heterostructures, where the FM-contacts are separated by a distance comparable to or smaller than the coherence length [88].

For half metallic trajectories, there is only Γ_2^R and the corresponding expression can be inferred from the one given above, but the S-matrix becomes a bit simpler in this case [37, 53]:

$$\Gamma_2^R = \frac{-i\mathcal{T}_\alpha t^2(1+r)\gamma^R(1-\gamma^R\tilde{\gamma}^R)}{1+\gamma^R\tilde{\gamma}^R[2r\cos\vartheta - \mathcal{T}_\alpha^2 t^4] + (\gamma^R\tilde{\gamma}^R)^2 r^2} \tag{5.15}$$

with $\mathcal{T}_\alpha = \sin(\vartheta/2)\sin(\alpha_Y)/(1+r)$. $r = r_\uparrow$, $t = \sqrt{1-r^2}$ $(r_\downarrow = 1)$, and $\vartheta_2 = \vartheta/2$ hold in comparison to the formula for the FM-trajectories. Quite importantly, $(1-\gamma^R\tilde{\gamma}^R)$ enters the nominator here. At $\varepsilon = 0$, we have $\gamma^R(\varepsilon = 0) = i$ and $\tilde{\gamma}^R(\varepsilon = 0) = -i$ and hence $(1-\gamma^R\tilde{\gamma}^R) = 0$. Thus, the Andreev amplitude for spin-flip AR vanishes at zero energy and so does the conductance if the material is a half metal [53, 81].[a] This is an important difference compared to the normal Andreev reflection contribution and may allow experimentalists to pin down whether spin-flip Andreev reflection is responsible for the conductance signal at sub-gap energies. We shall discuss this idea in more detail later on, when we turn to the analysis of CrO$_2$ conductance spectra. Note also that the spin-flip AR amplitude for FM-trajectories does not necessarily have this property, the crucial point being the relation $\vartheta_2 = \vartheta/2$. This equation is directly imposed by the unitarity of the 3×3 S-matrix and thus an ubiquitous property of half metallic trajectories. This was also noted before by Béri et al. [12], who carried out a BdG-calculation of a superconductor-half metal contact.

We will not state analytical expressions for the current here, as they would be quite cumbersome for the FM trajectories and, as a consequence of that, not very instructive. An analytical formula for the HM contribution is provided in Refs. [81, 37].

5.2. Conductance Spectra

In the following, we discuss results for the conductance spectra of SC/FM point-contacts based on the models introduced in chapters 3 and 4. We start with the box-potential model and compare the current contributions of quasiparticle tunnelling, normal Andreev reflection and spin-flip Andreev reflection. We address the implications of spin-flip scattering at the contact and the influence of the spin-mixing effect. The latter gives rise to anomalies in the Andreev spectrum that can be interpreted as imprints of the bound states induced at the interface [142, 53]. As anticipated earlier, we show that they can generically not be observed at finite temperatures if a box-potential is assumed, but may move to low enough energies if the potential is smooth.

The general expressions for the current were stated in chapter 3 (equation (3.13)). The conductance is obtained by taking the derivative with respect to the bias voltage V. The voltage enters only in the incoming distribution functions and the derivative can be taken explicitly:

$$\partial_V x_\eta = \frac{e}{2k_BT} \cdot \frac{1}{\cosh^2((\varepsilon + eV)/2k_BT)}, \quad \partial_V \tilde{x}_\eta = \frac{e}{2k_BT} \cdot \frac{1}{\cosh^2((\varepsilon - eV)/2k_BT)}. \tag{5.16}$$

---

[a]Technically, this is true in all but the special case where $\vartheta = \pi$ and $\alpha_Y = 0.5\pi$ [53].
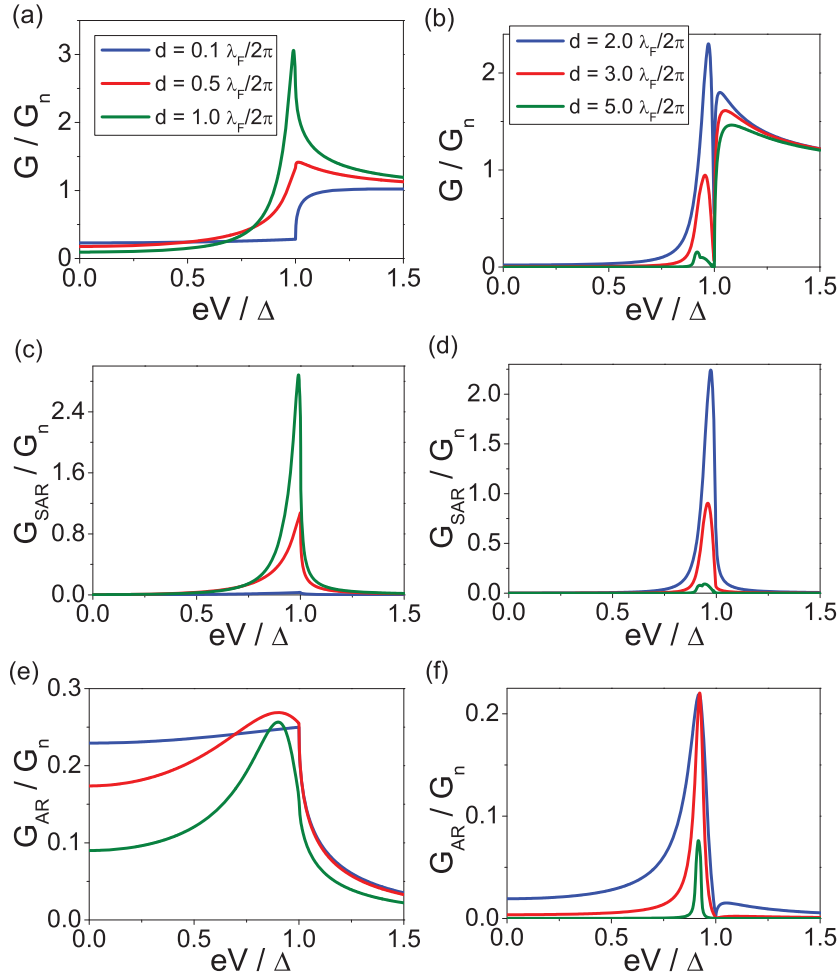
Figure 5.5. – Total conductance (top row), conductance due to spin-flip AR (second row) and conductance due to normal AR (bottom row) as a function of voltage and for six different inter-layer thicknesses (left column: $d = 0.1, 0.5, 1.0\ \lambda_{\rm F}/2\pi$, right column: $d = 2.0, 3.0, 5.0\ \lambda_{\rm F}/2\pi$). G_n is the normal state conductance of the contact. The other parameters are $V_{\rm I} = 1.5\ E_{\rm F}$, $V_{\rm FM} = 0.5\ E_{\rm F}$, $J = 0.8\ E_{\rm F}$ and $\alpha = 0.5\pi$. $T = 0$. Figure from Ref. [53] with slight modifications.

In the $T \to 0$ limit, these expressions reduce to $2e\delta(\varepsilon \pm eV)$, and broaden for higher temperatures. We thus obtain the conductance spectra at finite temperatures by simply convoluting the zero-temperature spectra with the respective derivative stated above. The conductance contributions of normal Andreev reflection and spin-flip Andreev reflection can be defined as [53]:

$$\frac{G_{\rm AR,2}}{2} = \partial_V \frac{e N_{\rm F2}}{2} \int_\varepsilon {\rm d}\varepsilon\ \langle \Gamma^R_{2\leftarrow 3} \tilde{x}_3 \tilde{\Gamma}^A_{3\to 2} \rangle_{2+}, \tag{5.17}$$

$$\frac{G_{\rm SAR,2}}{2} = \partial_V \frac{e N_{\rm F2}}{2} \int_\varepsilon {\rm d}\varepsilon\ \langle \Gamma^R_2 \tilde{x}_2 \tilde{\Gamma}^A_2 \rangle_{2+},$$

for band 2. The expressions for band 3 are simply obtained by replacing $2 \leftrightarrow 3$. The factor $1/2$ on the left-hand side of these equations is included because the terms on the right-hand side account for only half of the current due to the respective Andreev reflection process, as discussed in chapter 3.

In Fig. 5.5, we plot the conductance for exactly the same parameter set that we used in the discussion of the box-potential in the previous chapter. The spin-polarisation of the
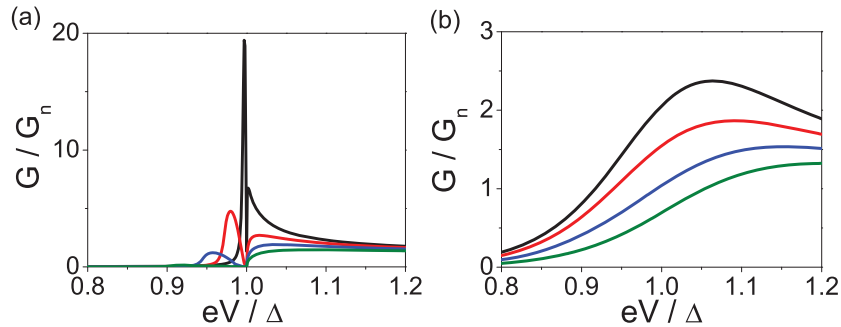
Figure 5.6. – The total conductance for different values of the exchange field $J = 0.1$(black), 0.3(red), 0.5(blue), and 0.8(green) E_F, and for (a) $T = 0$ and (b) $T = 0.1\ T_c$. V_I and V_{FM} increase also, so that $E_2 = V_{FM} - J/2 = 0.1\ E_F$ and $U_+ = V_I - J/2 = 1.1\ E_F$ stay constant. $\alpha = 0.5\pi$ and $d = 5.0\ \lambda_F/2\pi$. Figure from Ref. [53] with slight modifications.

FM, which we define as [53]:

$$P = \frac{N_{F2} - N_{F3}}{N_{F2} + N_{F3}}, \tag{5.18}$$

is $P = 0.5$ in this case. For $d = 0.1\ \lambda_F$, the conductance drops from its normal state value to about $0.24\ G_n$ below the gap and remains relatively constant. We also see that the conductance below the gap-energy is entirely due to normal Andreev reflection. This curve can be well understood from the usual BTK picture. The transmission of this contact is relatively high, which is why the Andreev conductance hardly varies as a function of energy. Still, due to scattering caused by wave vector mismatches and in particular the finite spin-polarisation, the AR conductance is reduced from its perfect transmission value of $2\ G_n$. Spin-flip Andreev reflection gives hardly any contribution in this case, since spin-flip scattering is largely ineffective for such a thin interlayer. As the thickness of the interlayer increases to $d = 0.5, 1.0\ \lambda_F$, the conductance becomes enhanced close to the gap-energy and is mostly carried by spin-flip Andreev reflection. The reason is that this process is insensitive to the spin-polarisation of the FM, as opposed to the normal Andreev process. In terms of energy dependence, spin-flip AR decays rapidly to zero for energies smaller than the gap-energy. The AR contribution also shows a stronger variation but still reaches a finite value at $\varepsilon = 0$.

As the interface thickness increases further, we see that signatures of Andreev bound states emerge in the spectrum. Since the mixing angle is relatively small, these states are located very close to the gap edge. The magnitude of the bound state signature decreases for even thicker interlayers, as the probability for Andreev reflection is proportional to t^4, while quasiparticle tunnelling scales with t^2. As expected from the analytical discussion, this signature – which is due to the denominator D – appears in both spin-flip and normal AR. The reason why it only appears for relative thick interfaces is that the spectral weight of normal AR fills the tiny gap between the bound state signature and the SC gap edge for thin interfaces. However, one also sees that both the contributions of spin-flip and normal AR are peaked at the bound state energy rather than the gap energy for interfaces with $d \geq 1.0\ \lambda_F/2\pi$.

We investigate the appearance of the bound state signature more closely in Fig. 5.6, where we plot the conductance spectrum for a thick interface and different values of the exchange field. The zero-temperature spectrum shows signs of the bound state close to the gap edge. As the exchange field increases, the maximum of the state does indeed move to lower energies, but is also rapidly suppressed. Consequently, the signature of this state is completely washed out at $T = 0.1\ T_c$ already, as shown in the second plot. While ramping
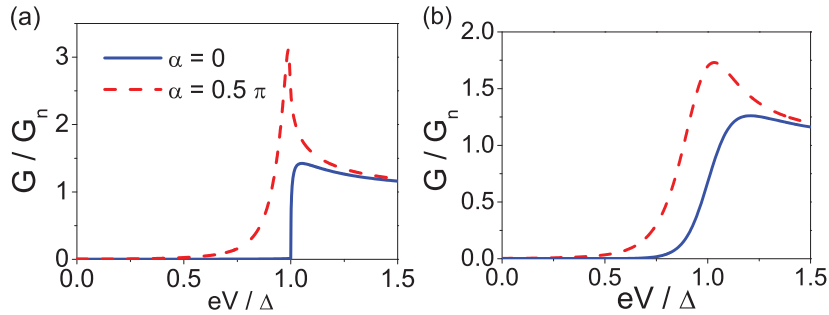
Figure 5.7. – Total conductance at (a) $T = 0$ and (b) $T = 0.1\,T_c$ for a collinear (blue) and misaligned (red) interface magnetisation. $J = 0.89\,E_F$, $V_F = 0.545\,E_F$, $V_I = 1.545\,E_F$, $d = 1.0\,\lambda_F/2\pi$. Figure from Ref. [53]. Copyright 2010 by the American Physical Society.

up the exchange field does increase the mixing angle and hence pushes the bound state to lower energies, it also reduces the transmission, since the scattering potential of the minority band increases in energy. It is exactly this dilemma that can be circumvented by dropping the box-potential idealisation and considering a smoother scattering potential.

Lastly, we consider the case of a highly spin-polarised contact ($P = 0.8$) in Fig. 5.7, to show that spin-flip scattering at the contact can have an important effect on the conductance spectrum in such a case. Due to the high polarisation, the Andreev conductance is almost completely suppressed if the interface magnetisation is collinear with that of the FM bulk. This is in agreement with standard BTK-theory, the minority band is almost depleted and normal Andreev reflection cannot occur. However, if the interface is misaligned, which implies the presence of spin-flip scattering, we find a finite conductance below the gap-energy which shows the typical energy dependence of spin-flip AR. The latter is not affected by the high polarisation and thus, its presence or absence can make a big difference in this scenario. As shown in Fig. 5.7b, this is also true for finite temperatures. The conclusion one may draw from this is that spin-active scattering can modify the spectra a lot and may therefore obscure polarisation values obtained by fitting them to the extended BTK-model.

We now turn to the smooth potential model. The scattering potentials we consider are exactly the same as those shown in Fig. 4.7 and we present the resulting conductance spectra in Fig. 5.8. The last curve shows the box-potential case, we clearly see that the junction is in the tunnelling limit ($t^2 < 0.01$ in all cases). We see the same relatively small bound state signature close to the gap edge that we observed in the box-potential analysis. As the smoothness of the interface increases, the states move to lower energies and are enhanced. For even broader interlayers, the bound states broaden in energy and decrease in height. The dispersion of the bound states is related to the Fermi-surface geometry and the $k_{||}$-dependence of the mixing-angle ϑ. For a given trajectory, the formula $\varepsilon_{pole} = \Delta \cos(\vartheta/2)$ is a good approximation for the bound state position, but ϑ sweeps over the whole range between its maximum value and zero as a function of $k_{||}$. This implies a broadening of the state caused by the Fermi-surface average. The energy-profile of these states also depends on the respective transmission values. Since the transmission is maximal for perpendicular impact, and so is the mixing angle, the maximum of the bound state should give a good estimate of the maximal mixing angle.

We also see that the bound state signatures may now survive at finite temperatures and should hence be observable in experiments, provided that interlayers with such properties can be engineered. While we are well aware that experimental techniques are far from providing perfect control over interface properties, we still believe that the model we considered here is not artificial and that insulating contact barriers that boost the spin-
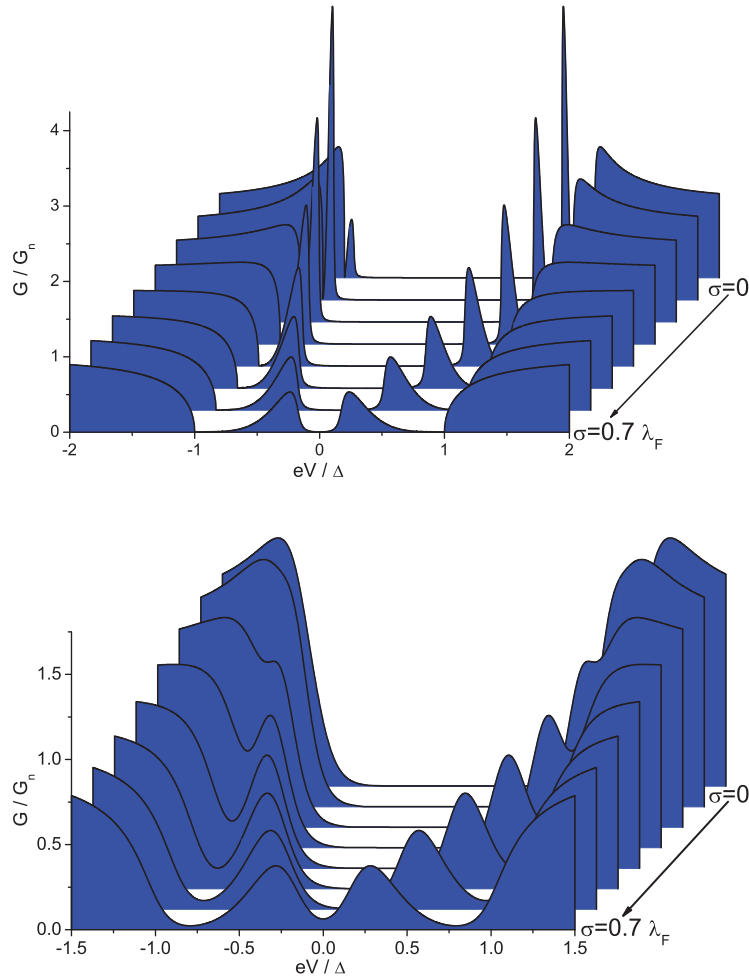
Figure 5.8. – Total conductance for the smooth potential model, $T = 0$ (top) and $T = 0.1\,T_c$ (bottom). Figure from Ref. [53]. Copyright 2010 by the American Physical Society.

mixing effect sufficiently may even form spontaneously. This view is also supported by recent findings of Hübler et al. [61]. They estimate a mixing angle close to π from the bound state positions in their Al/Fe spectra, but it should be noted that the signature of these states in the AR spectrum is very weak.

When comparing our theoretical results to experimental data in the final section of this chapter, we shall also see that the mixing effect – even if it does not lead to the emergence of bound state signatures – may still be of importance for the understanding of currently available data.

5.3. Relation to the Extended BTK-Model

The extended BTK-model was shortly introduced in chapter 1. In this section, we will demonstrate that this model is contained as a limiting case in our formalism and that we obtain exactly the same expressions for the conductance if an appropriate choice is made for the scattering matrix. The reason for this is probably that approximations are made in the derivation of the BTK-formulas from BdG wave function matching [15] which are in a sense equivalent to the quasiclassical approximation.[a]

---

[a]Specifically, the wave vector solutions $k^{\pm}$ and $q^{\pm}$ are replaced by k_{F} in some places, which is justified if $E_{\mathrm{F}} \gg \Delta$. See Ref. [15], p. *4531*.

Recall that in the extended BTK-model the conductance of the point contact is given by [119]:

$$G(V) = (1 - P_C)G_{\mathrm{BTK}}(V) + P_C G_H(V), \tag{5.19}$$

with

$$P_C = \frac{N_{\mathrm{F}\uparrow}v_{\mathrm{F}\uparrow} - N_{\mathrm{F}\downarrow}v_{\mathrm{F}\downarrow}}{N_{\mathrm{F}\uparrow}v_{\mathrm{F}\uparrow} + N_{\mathrm{F}\downarrow}v_{\mathrm{F}\downarrow}}. \tag{5.20}$$

Note the difference between P_C, called the transport spin-polarisation, and the bulk-polarisation P introduced in the previous chapter. Thus, the conductance is a weighted average of two contributions, G_{BTK} and G_H, and the weight factor is P_C. G_{BTK} is the standard conductance formula of BTK-theory, while G_H is due to the contribution of half-metallic trajectories. The first formula used for this contribution, proposed by Soulen et al. [119], was simply obtained from the BTK formula by putting the Andreev reflection amplitude to zero and renormalising all other transport amplitudes so that current conservation is maintained. Obviously, this was not a rigorous calculation, and we shall hence compare your theory to later work of Mazin et al. [83], who obtained an expression for G_H on the basis of wave function matching in the BdG framework.

Apart from P_C, the usual barrier parameter Z enters as a second free parameter in G_{BTK} and G_H. Moreover, the mismatch parameter $K = \kappa/k$ between the wave vector k of the superconductor and the imaginary wave vector $i\kappa$ of the evanescent mode in the FM enters G_H [83]. To make this very clear, we are dealing with a model based on the following assumptions [53]:

1. We consider only three types of transport channels. The channels in the SC have wave vector k, while in the FM we consider spin-degenerate channels (called 'non-magnetic' contribution [83]) with $k_2 = k_3 = k$ and half-metallic channels with $k_2 = k$ and $k_3 = i\kappa$. Matching a SC channel with either a non-magnetic or a half metallic channel gives the two conductance contributions introduced above.

2. The interface barrier is modelled by the same spin-degenerate δ-function for both the non-magnetic and the half metallic matching problem.

3. The FS-average is taken by simply multiplying the individual contributions with their respective total number of transport channels, which results in the weighting formula for the total conductance. The number of transport channels for the 'non-magnetic' trajectories is set by the minority band and is proportional to $2v_{\mathrm{F}3}N_{\mathrm{F}3}$. The 'excess' channels of the majority band, whose number is proportional to $N_{\mathrm{F}2}v_{\mathrm{F}2} - N_{\mathrm{F}3}v_{\mathrm{F}3}$, give the 'half metallic' contribution.

These assumptions imply that the scattering matrix for the G_{BTK} contribution is spin-degenerate and does not contain any scattering phases or spin-flip elements. It is thus described by a single parameter:

$$T_N = t_2^2 = t_3^2 = 1/[1 + Z^2] = 1 - R_N = 1 - r_{1\uparrow}^2 = 1 - r_{1\downarrow}^2. \tag{5.21}$$

We hence established the scattering matrix, which is all we need to calculate the conductance. We obtain the following expression for the spectral current for the two FM bands ($\eta = 2, 3$):

$$j_\varepsilon(\varepsilon,\ \mathrm{V}, \mathbf{p}_\eta) = X_\eta - x_\eta - \Gamma_\eta^R \tilde{x}_\eta \tilde{\Gamma}_\eta^A \tag{5.22}$$

$$= \left[\frac{-T_N \cdot |\mathcal{N}|^2 - 2T_N R_N \cdot \mathrm{Re}[\gamma^2 \mathcal{N}^*] + T_N^2 R_N |\gamma|^4}{|\mathcal{N}|^2} x - \frac{T_N^2 |\gamma|^2}{|\mathcal{N}|^2} \tilde{x} \right] \Theta(p_{\mathrm{F}3} - |p_\parallel|).$$

where the Θ-function makes sure that this expression is used for the FM trajectories in the FS-average. Furthermore, we have:

$$\gamma = -\frac{\Delta}{\varepsilon - i\sqrt{\Delta^2 - \epsilon^2}}, \quad \mathcal{N} = 1 - \gamma^2 R_N. \tag{5.23}$$

The expressions for x and $\tilde{x}$ are stated in equation (3.9). Note that $\tilde{\gamma} = -\gamma$ if the order parameter is real. If $\varepsilon < \Delta$, we have $|\gamma| = 1$ and (5.22) reduces to [53]:

$$j_\varepsilon(\varepsilon, \text{ V}, \mathbf{p}_\eta) = -\frac{T_N}{|\mathcal{N}|^2} [x + \tilde{x}] \Theta(p_{F3} - |p_\parallel|), \quad \epsilon < \Delta. \tag{5.24}$$

For $\epsilon > \Delta$, γ and $\mathcal{N}$ are real, so we have:

$$j_\varepsilon(\varepsilon, \text{ V}, \mathbf{p}_\eta) = \left[\frac{-T_N + T_N R_N \gamma^4}{\mathcal{N}^2} x - \frac{T_N \gamma^2}{\mathcal{N}^2} \tilde{x}\right] \Theta(p_{F3} - |p_\parallel|), \quad \epsilon > \Delta. \tag{5.25}$$

The current density is given by [53]:

$$\vec{j}(\text{V}) = -\sum_\eta \frac{eN_{F\eta}}{2} \int_\varepsilon d\varepsilon \langle \mathbf{v}_\eta j_\varepsilon \rangle_{\eta+}. \tag{5.26}$$

In the next step, we carry out the FS-average explicitly [53]:

$$\vec{j} = -\frac{e}{2} \int_\varepsilon d\varepsilon \left[\int_{v_{F2,z}>0} \frac{d^2 p'_{F2}}{(2\pi\hbar)^3} \frac{\mathbf{v}_{F2} j_\varepsilon(\mathbf{p}_{F2})}{|\mathbf{v}_{F2}(p'_{F2})|} + \int_{v_{F3,z}>0} \frac{d^2 p'_{F3}}{(2\pi\hbar)^3} \frac{\mathbf{v}_{F3} j_\varepsilon(\mathbf{p}_{F3})}{|\mathbf{v}_{F3}(p'_{F3})|}\right]. \tag{5.27}$$

Note that the functional dependence of j_ε on $\mathbf{p}_{F\eta}$ is given by $\Theta(p_{F3} - |p_\parallel|)$, i.e. a constant for $p_\parallel < p_{F3}$ and zero for $p_\parallel > p_{F3}$. Due to the rotational invariance in the x-y-plane, the integrals hence reduce to calculating [53]:

$$S_\eta = \int_{v_{F\eta,z}>0} d^2 p'_{F\eta} \frac{\mathbf{v}_{F\eta}}{|\mathbf{v}_{F\eta}(p'_{F\eta})|} \cdot \mathbf{e}_z \cdot \Theta(p_{F3} - |p_\parallel|), \tag{5.28}$$

and it is easy to convince oneself that S_3 is exactly the projection of the minority band Fermi-surface onto the contact plane, while S_2 is the projection of that part of the majority band Fermi-surface which covers the minority FS. In other words $S_2 = S_3$, and this would even hold if we dropped the spherical band approximation. We hence obtain for the total current:

$$\vec{j} = j\mathbf{e}_z = -\frac{ev_{F3}N_{F3}}{4} \int_\varepsilon d\varepsilon \ j_\varepsilon(\varepsilon, \text{ V})\mathbf{e}_z. \tag{5.29}$$

The conductance is then given by:

$$G_N^{\text{quasi}}/G_{N,0} = A\partial_V j/G_{N,0} = \mathcal{T}_N, \tag{5.30}$$

where A is the contact area. $G_{N,0} \cdot T_N$ is the normal state conductance of the non-magnetic trajectories. Specifically, we have $G_{N,0} = (2e^2 A v_{F3} N_{F3})/4$.[a] This yields exactly the BTK-formula [15], if $\partial_V x = 2e\delta(\varepsilon + eV)$ and $\partial_V \tilde{x} = 2e\delta(\varepsilon - eV)$ is used, which corresponds to $T = 0$. More precisely [53]:

$$G_{\text{BTK}} = [e^2 A(v_{F2} N_{F2} + v_{F3} N_{F3})/4] \mathcal{T}_N, \tag{5.31}$$

---

[a] Compared to the article of BTK, a factor $1/4$ appears here. This is because BTK assumed that all transport channels contribute with the same velocity to the current. Here, it is the projection of the velocity onto the axis perpendicular to the contact plane.

since the BTK-formula ignores that the transport channels are in fact *not* spin-degenerate.

With

$$(1 - P_C)G_{\mathrm{BTK}} = \frac{2v_{\mathrm{F3}}N_{\mathrm{F3}}}{N_{\mathrm{F2}}v_{\mathrm{F2}} + N_{\mathrm{F3}}v_{\mathrm{F3}}}G_{\mathrm{BTK}}, \qquad (5.32)$$

it is then easy to see that [53]:

$$G_N^{\mathrm{quasi}} = (1 - P_C)G_{\mathrm{BTK}}, \qquad (5.33)$$

which completes the prove.

We now turn to the half metallic or 'magnetic' trajectories. Now, the situation is complicated by the fact that we have a non-trivial wave vector mismatch $k/i\kappa$ entering the game. In accordance with the discussion presented in chapter 3, this implies the presence of a spin-mixing angle from our perspective and perfect reflection in the minority band. We hence have a scattering matrix which is characterised by $r_{1\uparrow} = re^{i\vartheta/2}$ and $r_{1\downarrow} = e^{-i\vartheta/2}$. We simply state the result without repeating the above calculation [53]:

$$G_H/G_{H,0} = \mathcal{T}_H = \frac{4T_H\beta}{2(\beta^2 + 1) - (\beta - 1)^2 T_H - 2\cos\vartheta\sqrt{1 - T_H}(\beta^2 - 1)}, \quad \mathrm{eV} > \Delta, \quad (5.34)$$

where $\beta = \mathrm{eV}/\sqrt{\mathrm{eV}^2 - \Delta^2}$, $T_H = 1 - r^2$ and $G_{H,0} = \mathrm{e}^2 A(N_{\mathrm{F2}}v_{\mathrm{F2}} - N_{\mathrm{F3}}v_{\mathrm{F3}})/4$. Since there cannot be any Andreev reflection in this case, we have $G_H = 0$ for $\mathrm{eV} < \Delta$. The above equation is in agreement with the formula stated in Ref. [83] if

$$\cos\vartheta = Z\sqrt{\frac{1}{1 + Z^2}}\left(1 - \frac{2(K/Z - 1)}{(K - 2Z)^2 + 1}\right), \qquad (5.35)$$

with $T_H = 1/[1 + Z^2]$, holds [53], where K is the defined as the ratio κ/k [83].[a] We find exactly the same formula when we calculate the mixing angle from wave function matching in the normal state, assuming a spin-degenerate δ-function potential [53]. With:

$$\Psi_{\uparrow,\downarrow}^{\mathrm{SC}} = 1e^{ikz} + B_{\uparrow,\downarrow}e^{-ikz}, \quad \Psi_{\uparrow}^{\mathrm{HM}} = C_{\uparrow}e^{ikz}, \quad \Psi_{\downarrow}^{\mathrm{HM}} = C_{\downarrow}e^{-\kappa z}, \qquad (5.36)$$

the matching conditions read:

$$\Psi_{\uparrow,\downarrow}^{\mathrm{SC}}(z = 0) = \Psi_{\uparrow,\downarrow}^{\mathrm{HM}}(z = 0), \quad \left[\partial_z\Psi_{\uparrow,\downarrow}^{\mathrm{SC}} - \partial_z\Psi_{\uparrow,\downarrow}^{\mathrm{HM}}\right](z = 0) - V\Psi_{\uparrow,\downarrow}^{\mathrm{HM}}(z = 0) = 0, \qquad (5.37)$$

from which one calculates $r_{\uparrow,\downarrow}$. $\cos\vartheta$ is then obtained from:

$$\cos\vartheta = \mathrm{Re}\left[\frac{r_{\uparrow}r_{\downarrow}^*}{|r_{\uparrow}r_{\downarrow}|}\right]. \qquad (5.38)$$

Thus, the parameter $K = \kappa/k$ appearing in the work of Mazin is related to our spin-mixing angle by equation (5.35). Such an angle does generically not appear in BTK-theory, since any kind of wave vector mismatch is absent in this model. For the half metallic trajectories, however, such a mismatch is inevitable, even in the most simplified model.

This completes our prove. The Mazin formulas, widely used by experimentalists to fit their data (see [135, 138, 95], for instance), are contained as a simple limiting case in our formalism.

---

[a]Unfortunately, the general formula for G_H printed in that paper is incorrect, as we know from personal correspondence with I.I. Mazin [53].

5.4. Experimental Results and Comparison

As pointed out in the introductory chapter, conductance spectra of point contacts have become a popular experimental tool to determine the spin-polarisation of charge carriers in ferromagnetic conductors. Since the spin – as opposed to the charge – of a carrier is usually not conserved, this is a notoriously hard to measure quantity. Thus, the idea put forward by de Jong and Beenakker [28], that the suppression of Andreev reflection induced by the spin-polarisation of charge carriers may allow for inferring the spin-polarisation from conductance spectra, was readily taken up [127, 119]. Creating a point contact by simply pressing a superconducting STM tip into the sample is a rather straightforward technique, and thus, a lot of these experiments were carried out – both on classical ferromagnets like Ni, Co, Fe [119, 62], but also more exotic materials like CrO_2 [138, 119, 135] and ferromagnetic semiconductors [95, 50]. Complementary to that, point contacts were created and investigated using more laborious techniques, i.e., growing contacts in layered structures [97, 127].

The particular problem here is, however, that the spin-polarisation is not a directly measured quantity. What is measured is the Andreev spectrum, and the only way to obtain an estimate for the polarisation from it is to fit it to some theoretical model. Even though that is a nice idea, these spectra are highly sensitive to almost anything that may possibly go on in the contact. It is therefore not surprising that theoretical studies questioning the validity of the extended BTK-model appeared soon after the first experimental works using this approach were published [136, 123]. These studies are based on ab initio calculations and show that the polarisation inferred from the BTK-model may differ largely from the true bulk polarisation of the respective material. On the other hand, these 'ab initio' calculations can also not reproduce the spectra without a number of ad-hoc assumptions and are thus, in our opinion, not necessarily more conclusive than our scattering approach. We shall discuss this in more detail at the end of this section.

As a final introductory comment, it should be noted that in comparing all these theoretical and experimental investigations, one must pay attention to the particular definition of 'spin-polarisation' used in the respective works. We introduced the bulk-polarisation P and the transport polarisation P_C already. The latter would be further modified in a diffusive picture.[a] This is no fundamental problem, since, in any case, the polarisation is obtained from a model and not directly measured – one may hence infer a value for any of the above definitions from an appropriate model.

Spin-Polarisation of (Ga,Mn)As

Ferromagnetic semiconductors are considered an ideal source of spin-polarised charge carriers in electronic devices designed to exploit the spin rather than the charge of electrons for information processing – an idea which was popularised under the name 'spintronics' [134, 7]. Since our present electronic devices are based on semiconductor technology, ferromagnetic semiconductors, usually obtained by magnetic doping of known semiconducting compounds, would be easy to integrate in these circuits [134]. (Ga,Mn)As is probably the most prominent representative of the (III, Mn)V family of ferromagnetic semiconductors, with a Curie-temperature of up to $T_C = 185$ K [94]. A lot of theoretical effort was invested in understanding the origin of ferromagnetism and magnetotransport properties of these materials, the general purpose being to push the Curie-temperature above the room-temperature limit [63]. Increasing this temperature to ever higher values was mainly due to improvements of non-equilibrium growth techniques [63](molecular beam epitaxy), but whether the ultimate goal can be reached is unclear as of now.

---

[a]Provided the contact is sufficiently small, it should be in the ballistic limit.

Apart from the ferromagnetic transition temperature, the degree of spin-polarisation which can be attained is naturally also an important question to address. Mn does not only provide magnetic moments, but also acts as an acceptor, i.e. (Ga,Mn)As is a hole-doped semiconductor. Samples reaching a very high T_C are strongly doped and therefore heavily disordered. Moreover, doping defects like interstitial and anti-site doping partly compensate the hole-doping and it is therefore not clear a priori, how many charge carriers are really provided at a given level of Mn doping. Further complications arise due to the warping of the Fermi-surface and spin-orbit coupling. We are hence dealing with a very complicated material.

A peculiar problem that arose in the context of point contact Andreev reflection (PCAR) spectroscopy on these materials was that fits with the extended BTK-model required the introduction of a 'effective temperature' T^* in the contact, which is a lot higher than the actual temperature in the sample and even higher than the superconducting transition temperature in the tip [95, 98]. The reason is that the typical 'shoulder peaks' at the gap energy, that are present in any spectrum of a non-ideal contact, were completely absent in this case. This can only be reconciled with BTK-theory if an additional (and very strong) smearing of the spectrum is included. The simplest way to do this is to attribute it to temperature smearing.[a] In fact, it was argued before that this procedure could be justified as a heuristic model for inelastic scattering [95].[b] Yet, assuming a T^* which is more than five times as high as the measured temperature in the sample [98], which was indeed necessary, is highly unsatisfactory. At this point, it occurred to us that the spin-mixing effect provides a shift of spectral weight from the gap edge to energies inside the gap and that although it may not be possible to observe the bound states at finite temperatures, this may provide an explanation for the absence of peaks at the gap edge and allow for fitting the spectra with the real temperature. This turned out to work if, in addition to the spin-mixing effect, an average over different transport channels and the presence of a series resistance in the setup were taken into account.

We shall discuss these results in the following.[c] We model three data sets obtained from pressing a superconducting Nb-tip into the same (Ga,Mn)As sample at different points. Since we were not directly involved in the experiment, we quote the original article for its description: *"We have investigated 7% Mn-doped, 25-nm-thick (Ga,Mn)As samples. They are grown on a 400-nm-thick, highly carbon-doped ($\approx 10^{19}$cm^{-3}) buffer layer to minimize series resistance. The Curie temperature T_C is $\approx$ 70 K for the as-grown sample and $\approx$ 140 K after 24 hours of annealing at 190 °C. The details of the sample growth and preparation are described elsewhere [19]. The experiments were carried out by means of a variable temperature (1.5 – 300 K) cryostat. Sample and Nb tip (chemically etched) were introduced into the PCAR probe, in which a piezo motor and scan tube can vary the distance between tip and sample. The PCAR junctions were formed by pushing the Nb tip on the (Ga,Mn)As surface with the probe thermalized in ^{4}He gas. The current-voltage I versus V characteristics were measured by using a conventional four-probe method, and by using a small ac modulation of the current, a lock-in technique was used to measure the differential conductance dI/dV versus V."*, S. Piano et al., PRB 83, 081305(R)-2 (2011).

Specifically, we made the following model assumption to fit this data with our theory, that we shall call the 'spin-active' model here [98]:

---

[a] Which enters through the convolution of the $T = 0$-spectrum with the $1/\cosh^2[(\varepsilon - eV)/2\mathrm{k_B}T]$ factor.

[b] This article of Panguluri et al. cites the classical paper of Dynes [32] as a justification for this effective temperature. However, the renowned Γ_{Dynes} parameter added as an imaginary part to the energy is not equivalent to assuming $T^* \neq T$.

[c] Concerning the author's contribution to the work discussed in this section: The data was taken by S. Piano, fits with the BTK-model were done by S. Piano, modelling and fitting with the spin-active model was done by the author. Kane-model calculations were done by K. Výborný. The figures shown were prepared by S. Piano.

- We assume three isotropic bands, one in the superconductor, characterised by its Fermi wave vector k_{SC}, and a single pair of majority/minority-bands in the ferromagnet, characterised by the Fermi wave vectors $k_{\uparrow,\downarrow}$. Since the FM is a semiconductor, the FM-bands are assumed to be smaller than that of the SC. The transmission and reflection parameters for a given $k_{\parallel}$ are then calculated from wave function matching on this basis, i.e., we average over an ensemble of transmission values and naturally we have $t_{\uparrow} \neq t_{\downarrow}$. The bulk-DOS of the respective bands is assumed to be proportional to the Fermi wave vector, which is in line with the spherical band approximation.

- The spin-mixing effect is introduced ad-hoc, i.e., we assume a mixing angle ϑ to be present, although it is not automatically implied by the above matching problem. It can be assumed to arise from the presence of magnetic moments in the contact. The trajectory dependence of the mixing-angle is $\vartheta(k_{\parallel}) = \vartheta \cdot \sqrt{(1 - k_{\parallel}^2/k_{SC}^2)}$, which models the decay of the mixing angle with increasing impact angle. Yet, this dependence turned out to have little influence on the result, since trajectories with perpendicular impact are most relevant, i.e., assuming $\vartheta(k_{\parallel}) = const.$ instead did not make a big difference.

- Finally, a series resistance R_s was assumed, which renormalised both the normalised conductance and the voltage scale. This renormalisation was taken into account with a simple Kirchhoff's rule calculation:

$$V = (1 + \alpha \frac{G_c}{G_{cn}}) \cdot V_c, \quad \frac{G}{G_n}(V) = \left[\frac{(1 + \alpha) \cdot (G_c/G_{cn})}{1 + \alpha(G_c/G_{cn})}\right](V_c). \quad (5.39)$$

  Here, G_c/G_{cn} is the normalised conductance of the contact and V_c the voltage that drops across the contact. The normalised conductance G/G_n and voltage V measured in the experiment are renormalised by the series resistance, which enters through the parameter $\alpha = R_s/R_c$, where R_c is the contact resistance in the normal state.

Moreover, the value of the superconducting gap was fitted to the spectrum while the temperature was taken from experiment. This is reasonable, since a suppression of the bulk gap can be assumed to occur in a magnetic point contact due to the inverse proximity effect and the small size of the tip. This brings us to a total of 5 fit parameters, $k_{\uparrow}, k_{\downarrow}, \vartheta, R_s, \Delta$, while the BTK-model uses 4: T^*, Δ, Z, P_C.

The results for the lowest temperatures reached in the respective experiment are shown in Fig. 5.9. Fig. 5.9a shows the BTK-fit to the first data set, the corresponding spin-active fit is shown in Fig. 5.9b. T^* equals 10.95 K and is hence almost six times larger than the actual temperature in the sample and even higher than the bulk transition temperature of Nb (about 9.2 K). The P_C value inferred from the BTK fit is 0.9, pointing to a very high degree of spin-polarisation. This is not surprising, since the extreme smearing implied by this value of T^* requires a high P_C in order to obtain a sizeable dip of the conductance at energies below the gap. Increasing Z, on the other hand, would not only enhance the dip but also the peaks at the gap edge, which are completely absent.

Another reason why assuming an effective temperature works so well is the blown up voltage scale. From the data, one would assume that the superconducting gap was about 4 meV, but the bulk gap of Nb is only 1.5 meV, approximately. If one wishes to fit this data with the real temperature, there are basically two ways of addressing this voltage-scale problem. (a), one sticks with the non-thermal smearing of the DOS, but models it with a non-thermal broadening parameter in the standard way $\varepsilon \mapsto \varepsilon + i\Gamma$ [32] instead of an effective temperature, or (b), one takes into account a series resistance, which leads to a modification of the voltage scale. We settle for option (b) in our model, but the truth

is probably a compromise between the two. An issue here is that the spectral properties which matter are those of the superconductor and the broadening would hence have to happen in the Nb tip.[a] Yet, this problem is absent or at least a lot less pronounced in other PCAR studies of ferromagnetic point contacts and thus more likely to be a feature related to (Ga,Mn)As. One may assume that the conductivity of this semiconductor sample is poor compared to a ferromagnetic metal, and consequently, a significant series resistance may indeed be present. However, there is apparently no experimental way of estimating it independently.
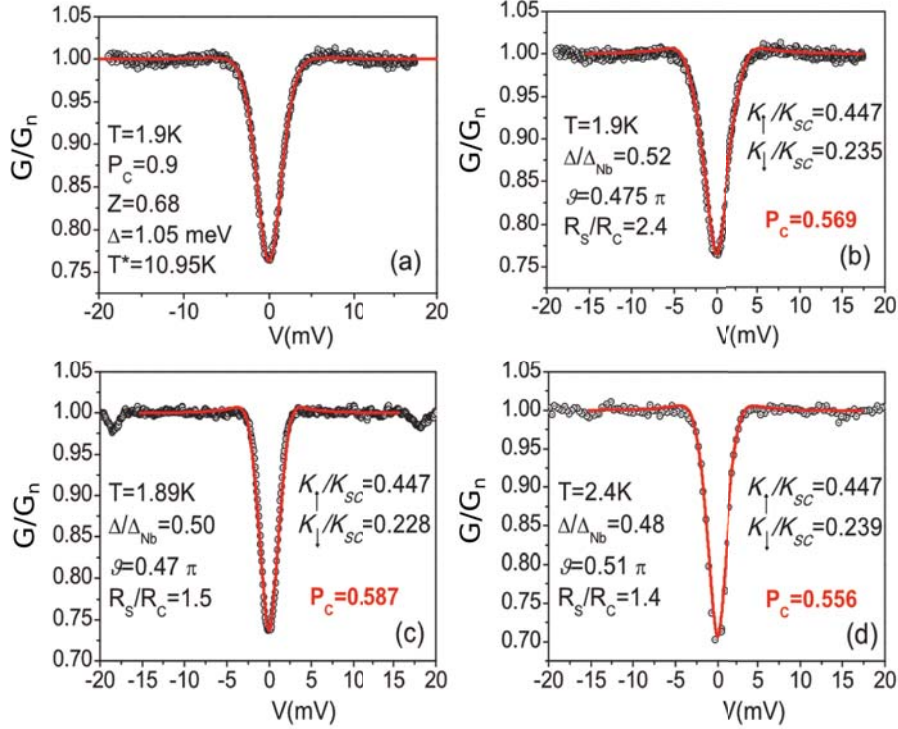
Figure 5.9. – Data sets of three Nb-contacts on the same (Ga,Mn)As sample. (a) and (b) show the same data set and fits with the BTK (a) and the spin-active model (b), respectively. (c) and (d) show two further data sets fitted with the spin-active model. Fit-parameters are stated in the respective figure. Figure from Ref. [98] with slight modifications. Copyright 2011 by the American Physical Society.

Not surprisingly, we find an elevated ratio $R_s/R_c \geq 1.4$ for all three data sets. In the CrO_2 fits that we discuss in the next section, this value is significantly smaller. The fitted values for $k_{\uparrow,\downarrow}$ vary little for the three data sets. In fact, we keep $k_\uparrow$ constant for all three fits. Since these are parameters supposed to characterise bulk-properties of the sample, this seems to be a very reasonable result. Accordingly, the value we infer for the spin-polarisation P_C, which we calculate from:

$$P_C = \frac{k_\uparrow^2 - k_\downarrow^2}{k_\uparrow^2 + k_\downarrow^2}, \tag{5.40}$$

in agreement with the spherical band approximation,[b] also remains relatively constant at about $P_C \approx 0.57$, and is hence a lot smaller than the value inferred from BTK-fitting. The spin-mixing angle and the SC gap also vary little, but the suppression of the latter is significant. In any case, the quality of the fits is as good as that of the BTK-fit.

---

[a]Recall that the dependence on energy is entirely due to the coherence functions in the SC.
[b]This also requires the effective mass to be the same in both bands.
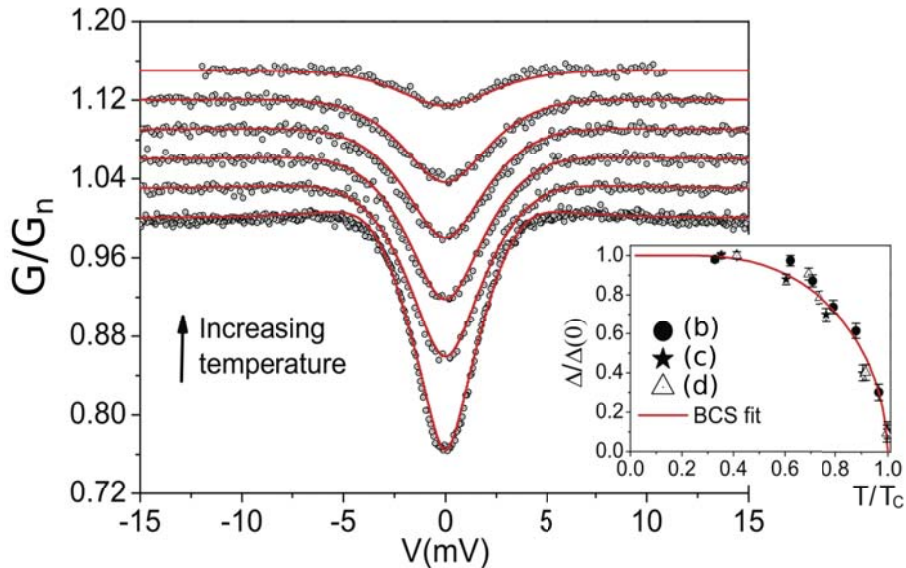
Figure 5.10. – Temperature dependence of the conductance spectrum for the sample shown in Fig. 5.9a,b. The inset shows the fitted gap values for all three samples. Figure from Ref. [98] with slight modifications. Copyright 2011 by the American Physical Society.

We are also able model the temperature dependence of the spectra by changing the value of Δ only, which is also the only parameter that should vary with temperature. This is illustrated in Fig. 5.10 for the contact of Fig. 5.9a,b. The inset shows how our fitted gap values for all three contacts compare to the BCS-relation. Note, however, that both Δ and T are normalised independently in this figure and thus, there is an additional fudge parameter which fixes the ratio between $\Delta(0)$ and T_c. This parameter is significantly smaller than the theoretical strong-coupling BCS-ratio for Nb ($2\Delta/k_B T_c \approx 3.95$), we find $2\Delta/k_B T_c \approx 3.3 \pm 0.3$ [98]. This is an expression of the gap suppression in the contact.

Complementary to our efforts of modelling this data, theorists from Prague carried out calculations of the bulk-electronic structure with a six-band Kane-model, treating magnetism in a mean-field approach with an exchange coupling between localised Mn-moments and the itinerant charge carriers [1]. The strong warping and spin-orbit coupling require a different definition of the transport spin-polarisation [98]:

$$P_C = \sum_i \frac{\langle s_z v \rangle_i + \langle s_z v \rangle_i}{\langle v \rangle_i + \langle v \rangle_i}. \tag{5.41}$$

Here, $v_i(\mathbf{k})$ is the Fermi-velocity $(1/\hbar)|\nabla_k \epsilon_{\mathbf{k},i}|$ of band i, and $\langle f \rangle_i = \int d^3 k f(\mathbf{k}) \delta(E_F - \varepsilon_{\mathbf{k},i})$ the respective FS-average. The operator s_z projects the spin-quantisation axis $\vec{s}(\mathbf{k})$ at a given $\mathbf{k}$-point on its z-component. P_C was calculated by averaging over all six-bands appearing in the Kane-model, although the pair of heavy-hole bands should predominantly contribute to transport. For further details on this model, we refer to [1, 98]. P_C is found to be of the order $P_C \approx 0.35$ from this calculation, which is considerably lower than the estimate we inferred from the spin-active model, but even further away from the BTK-result ($P_C = 0.9$). An important deficiency of this model is that it completely neglects the effects of strong disorder in highly doped (Ga,Mn)As. The discrepancy with our model is not really surprising, since we did not take into account the anisotropy of the Fermi-surface. On the other hand, it also not clear how much that really matters as long as the influence of disorder has not been elucidated.

In this sense, our results have to be taken with a grain of salt, but we were still able to show that there are likely more reasonable explanations for the particular shape of PCAR spectra in (Ga,Mn)As – which was not only observed in this experiment, but also by Panguluri et al. [95] – than an effective temperature, and that this may be related to the spin-mixing effect.

Half metallicity of CrO$_2$

A second comparison to experimental results that we wish to discuss here is related to CrO$_2$, being one of the few half metallic materials around [23, 66] and the first material through which a triplet supercurrent was observed [67]. There is also a vast literature on PCAR spectra probing this material (see Ref. [81] and references therein). The data published in these articles was fitted with some version of the extended BTK-model, which turned out to give a large spread of the estimated P_C values. To make these value comparable, T. Löfwander carried out a reanalysis of all this data, using the formulas of Mazin et al., that we discussed in the previous section [81].[a] He used four fit parameters (P_C, Z, R_s, Δ) and obtained a spread of P_C ranging from 0.54 to 1.0. This is highly unsatisfactory, since both theoretical [66] and experimental work using the Meservey-Tedrow technique point to the half-metallicity of CrO$_2$ [96].

As shown in Ref. [81], this contradiction can be overcome if spin-active scattering at the interface is taken into account. Specifically, the full polarisation ($P = 1.0$) was assumed from the outset, which implies that only the half metallic contribution to the current exists. The fitting formula was obtained from the theory described in chapter 3 and 4, an analytical expression is stated in Ref. [37]. Here, we simply formulate the model assumptions in terms of the relevant scattering matrix, which we presented in equation (4.3):

- There is a single transmission parameter t, which can be expressed in terms of the usual BTK barrier parameter Z as $t^2 = 1/[1 + Z^2] = 1 - r^2$. The functional dependence $t(k_{||})$ is consistent with the one inferred from wave function matching in the presence of a δ-function potential, i.e., the Z parameter stated in Ref. [81] is $Z(k_{||} = 0)$.

- The misalignment angle α_Y[b] is kept constant at $\pi/2$, but the conclusions drawn from this model do not change for $\alpha_Y > 0.3\pi$ [81].

- The spin-mixing angle ϑ is assumed to vary with $k_{||}$ as $\vartheta(0) \cdot (1 - k_{||}^2/k_{\mathrm{F}}^2)$, in agreement with the functional dependence inferred from a δ-function potential.

- A spread-resistance R_s is taken into account in exactly the same way as in our (Ga,Mn)As model.

Most importantly, the gap was not fitted in this case, which implies that only three parameters $(Z, \vartheta(0), R_s)$ were used for the spin-active fits here. In general, the spin-active fits are fully competitive in quality with the BTK fits, notwithstanding the full spin-polarisation which is assumed [81]. This can be considered the most important result of this work. If the gap is kept fixed at its bulk value, the BTK fits become considerably worse for the majority of the data sets.

To get to the bottom of this, we proposed that investigating the zero-bias conductance of these contacts at even lower temperatures may provide a univocal indication as to which of these two pictures is correct [53, 81]. The reason being that if the polarisation is finite,

---

[a]The calculations done in this work are entirely due to T. Löfwander.

[b]Called α in the original article. But in the context of this thesis it corresponds to the angle α_Y introduced in chapter 4.

the zero-bias conductance due to normal Andreev reflection will level out at some constant value, which is basically determined by the transparency of the interface and the degree of spin-polarisation. On the other hand, spin-flip Andreev reflection has *always* zero spectral weight at zero energy, and does therefore not contribute to the zero-bias conductance if temperature smearing is absent. Recent results obtained by a group at Imperial College,[a] measuring the zero-bias conductance as a function of temperature, seem to further support the spin-active model in this respect.

Comparing this work to our (Ga,Mn)As results, we have to admit that the story is more sound in the CrO_2 case – there are less fit parameters, and in particular, there is no need to fit the gap. The spread-resistance is also substantially smaller ($R_s/R_n < 0.2$ in all cases). On the other hand, the CrO_2 spectra are also more 'regular', in the sense that the gap edge is well defined, which is absolutely not the case for the (Ga,Mn)As data.

5.5. Other Theoretical Approaches

As already noted in the previous section, there is a second 'branch' of theoretical effort to do better than BTK-theory, based on ab initio calculations. For definiteness, we refer to the work of F. Taddei et al. [123] in the following, in which the differential conductance of a Co/Pb-contact is calculated from a tight-binding model whose material specific parameters were fitted to the DFT band structure of the respective materials. The authors claim on these grounds that polarisation values inferred from the BTK-model are highly questionable. The interface is modelled by a transfer-Hamiltonian whose hopping-elements are chosen to be the mean square of the bulk-elements.[b] This is an ad-hoc choice, ultimately justified by the agreement with experimental data. The latter also requires the assumption of *"enhanced magnetic moment"* at the interface.

Using a realistic band structure is incontrovertibly an important improvement compared to our model assumptions. However, the spherical band-approximation which we used is not a result of fundamental limitations of quasiclassical theory in this respect, but only a matter of convenience. Other than that, the calculation is as much in the clean limit as the one presented here and maintains translational invariance in the x-y-plane, although it is not clear from the article whether the conservation of parallel momentum was exploited explicitly. The transfer-Hamiltonian required in this approach is replaced by a scattering matrix in ours, and although the results were interpreted to provide an indication for enhanced surface magnetisation, this is foremost another ad-hoc assumption required for the agreement with experimental data.

To conclude, although using a material specific band structure is certainly important for realistic modelling, the ab initio+tight-binding approach is not per se more general than the quasiclassical scattering approach or wave function matching in BdG theory [78]. Addressing the issue of impurity scattering in these systems is likely more efficient within quasiclassical theory, but performing tight-binding calculations with a huge computational effort could shed light on the influence of interface disorder more easily. The problem here is the breaking of translational invariance, which requires a three-dimensional discretisation in real space.

---

[a]Private communication from K. A. Yates and L. F. Cohen.
[b]In fact, the calculation done here uses exactly the same method that we shall describe and apply to topological insulators in the second part of this thesis.

6. Long Range Triplet Supercurrents

In this chapter, we study the long range Josephson effect in ferromagnetic junctions carried by $S_z = \pm 1$ triplet correlations. The experimental state of affairs has been reviewed in the introduction and all modelling assumptions we make were introduced in the chapters on point-contact spectra already. On the technical level, complications arise due to the fact that we need to consider at least two interfaces now, as the ferromagnet is sandwiched between superconducting electrodes. The problem is then no longer amenable to an analytical solution in the general case – boundary conditions and propagations through the FM interlayer have to be iterated self-consistently.

Previous work on the Josephson effect through half-metallic junctions with the same approach [40] were carried out in a so-called 'linearised' approximation. This implies that the proximity effect in the FM layer is weak – due to poor transparency of the interfaces, small spin-mixing effect or both. In that case, an analytical solution of the Josephson problem can be obtained, also in the more general ferromagnetic case [51, 52]. The hallmark of a junction conforming to this limit is a current-phase relation (CPR) which only depends on the first order Fourier-components in the order parameter phase difference $\Delta\chi$:

$$J = J_c \cdot \sin(\Delta\chi + \varphi). \tag{6.1}$$

In the standard case of a non-magnetic tunnelling barrier sandwiched between two superconductors $\varphi = 0$ holds, but this is not true here. This additional phase factor describes the CPR of a half metallic junction in the linearised, or tunnelling, limit [40]. It is related to the relative misalignment between the quantisation axes of the two spin-active interfaces.

We show here that such phases play a role that is comparable but not identical to that of the order parameter phase difference $\Delta\chi$. They lead to highly irregular current-phase relations if the proximity effect is not weak and may even imply the presence of spin-supercurrents in ferromagnetic layers that are coupled to a single superconductor. We perform a systematic analysis of the CPR by means of a Fourier-analysis and identify two principal contributions to the Josephson current. In terms of novel physics, this is certainly the main result of this chapter.

We also investigate the critical current and the temperature anomaly predicted for half metallic junctions [40] in the ferromagnetic case. Due to the competition between the enhancement of singlet-triplet conversions by larger exchange fields on the one hand, and the elimination of the minority band for high spin-polarisations on the other hand, we
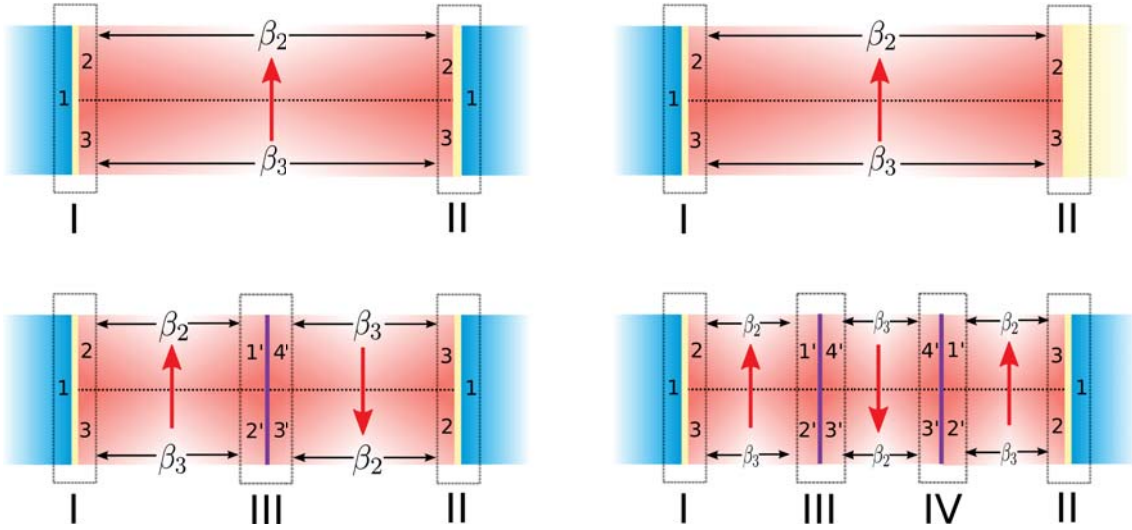
Figure 6.1. – Multilayer structures considered here and notation. Superconducting parts are blue, ferromagnetic parts red. Yellow regions indicate interfaces or surfaces. Purple regions indicate domain boundaries. The single domain Josephson junction is shown in the upper-left figure. The upper-right figure shows a bilayer terminated by a spin-active surface. The bottom figures show junctions with two or three domains, respectively. Channel labels are indicated.

find the critical current to be maximal when the polarisation takes intermediate values. We show that the temperature anomaly is predominantly caused by half metallic trajectories and thus suppressed if the spin-polarisation is weak or if the junction contains anti-ferromagnetic domains. We also study the critical current as a function of junction length and in the presence of domain structure.

Finally, we shortly comment on the proposal of inducing $p_x \pm ip_y$ superconductivity by means of an interface with Rashba spin-orbit coupling [22] and show that such states are induced in both spin-bands with opposite chirality.

Before we discuss these results, the general numerical scheme that we employ is shortly sketched in section 6.1 and the linearised equations, which are helpful for the interpretation of results, are introduced in section 6.2.

6.1. Full Solutions

The multilayer structures we consider are shown in Fig. 6.1, we assume that the junctions are grown in the z-direction and that they are translationally invariant in the x-y-plane. In all cases, $z = 0$ is the position of the first interface. To determine the Riccati-amplitudes inside these structures, we must solve the boundary conditions at interfaces and domain boundaries and the transport equations in the ferromagnetic layers. A fully self-consistent calculation also requires to calculate the coherence functions inside the SC-electrodes and to determine the spatial profile of the SC-gap. We neglect the latter and assume that the incoming coherence functions of the SCs are given by the homogenous bulk solutions. Obviously, this is a rather complicated inhomogeneous problem, but at finite temperatures, or in the presence of inelastic scattering, there is a well-controlled numerical scheme for solving it, as we will show in the following.

We will only study equilibrium problems here and are exclusively interested in thermodynamic quantities. Thus, we can employ the Matsubara technique. This implies that the distribution functions are irrelevant and we only need to find the coherence functions.

The relevant solutions of the boundary conditions are discussed in the appendix, we already discussed them in detail in chapter 3 for the point-contact geometry. This leaves us with the solution of the transport equation.

We only consider the clean limit, where the Riccati equation inside the FM takes the simple form:

$$2i\epsilon_n \gamma_\eta + i\hbar v_{F\eta}\mu\partial_z\gamma_\eta = 0. \tag{6.2}$$

Here, $\eta \in 2, 3$ is again the band index and $\mu = \cos\theta$ refers to the impact angle θ of the quasiparticle trajectory with respect to the z-axis. The equation has a simple analytical solution:

$$\gamma_\eta(z') = \beta_\eta(z'-z) \cdot \gamma_\eta(z), \quad \beta_\eta(z) = \exp\left(-\frac{2\epsilon_n}{\hbar v_{F\eta}\mu} \cdot z\right). \tag{6.3}$$

Obviously, β_η can be understood as a propagation-factor that is simply multiplied with the initial value of γ at an interface or surface to obtain the incoming value at the next interface or surface. There, the boundary conditions have to be solved and the next propagation takes place. It is therefore obvious that the solutions can be assembled by summing over all possible paths through the structure that contribute to the amplitude of γ at a given point.[a] We also observe that β_η is real and smaller than 1, i.e. the more propagations a path contains, the stronger its contribution will be suppressed. One may hence also adopt the standpoint that this sum over paths is an expansion of the solution in powers of β_η, in which higher order terms are exponentially suppressed. We hence adopt an iterative scheme for calculating the coherence functions which is designed so that after a given number n of iterations, all paths up to order n in β_η are taken into account. This is achieved by iterating the solutions of the boundary conditions and of the transport equations along certain loops through the structure, details are provided in the appendix. At $T \to 0$ the modulus of the propagation factors approaches 1 for the lowest Matsubara-frequency. I.e., the coherence functions do not decay inside the FM. In this case, inelastic scattering must be taken into account to ensure convergence.[b]

In the presence of impurities, the Riccati-equation must be solved numerically and the impurity self-energy has to be determined self-consistently. Other than that, the basic scheme remains the same.

The equation from which we calculate the current inside the FM-layer can be simplified to:

$$\vec{j}_\eta(\vec{R},t) = 4eN_{F\eta}k_BT \sum_{\epsilon_n>0} \left\langle \vec{v}_{F\eta}(\vec{p}_{F\eta})\text{Re}\left[g_\eta^M\right] \right\rangle_{\eta+}, \tag{6.4}$$

by exploiting the symmetry relations and the fact that the Green's functions inside the FM are spin-scalar. Again, $\langle\bullet\rangle_{\eta+}$ denotes an FS-average over trajectories whose momentum projection on the z-axis is positive.

6.2. Linearised Solutions

If the proximity effect inside the FM-layer is weak, we can obtain analytical solutions for the coherence functions in the clean limit. This situation is typically realised when the transparency of the interfaces is small. The approximation consists in retaining only those

---

[a] This is not to be confused with the summation-over-paths reasoning that applies to the diagrammatic technique and the boundary conditions.

[b] The same is true if real frequencies are considered.
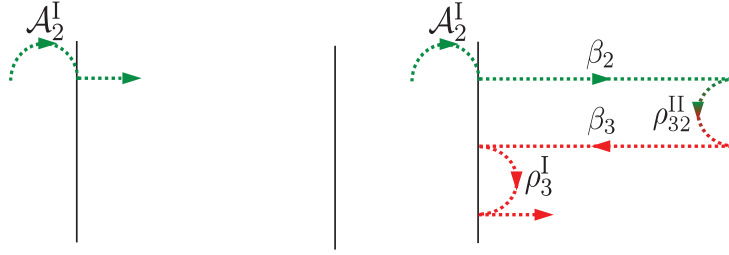
Figure 6.2. – Paths contributing to the solutions of equation 6.6. The terms corresponding to these paths are $\mathcal{A}_2^\mathrm{I}$ (left) and $\rho_3^\mathrm{I}\beta_3\rho_{32}^\mathrm{II}\beta_2\mathcal{A}_2^\mathrm{I}$ (right).

terms which are maximally second order in t, where t is any of the transmission elements of the S-matrix. This allows us to separate the solutions of the boundary conditions at an SC-FM interface into a 'source-term' part, which depends on the incoming coherence function from the SC-side only, and a reflection part, which arises from reflections of quasiparticles on the FM-side of the interface. The source-terms can easily be assembled with the diagrammatic technique, by neglecting all paths which contain incoming coherence functions from the FM-side:

$$\mathcal{A}_\eta = T_{\eta 1}\gamma_1\tilde{T}_{1\eta} + \sum_n T_{\eta 1}\gamma_1\tilde{R}_1(\tilde{\gamma}_1 R_1\gamma_1\tilde{R}_1)^n\tilde{\gamma}_1 R_1\gamma_1\tilde{T}_{1\eta}$$

$$= T_{\eta 1}\gamma_1\tilde{T}_{1\eta} + T_{\eta 1}\gamma_1\tilde{R}_1(1 - \tilde{\gamma}_1 R_1\gamma_1\tilde{R}_1)^{-1}\tilde{\gamma}_1 R_1\gamma_1\tilde{T}_{1\eta}. \tag{6.5}$$

These source-terms are identical to the solutions of the outgoing coherence functions for the point-contact geometry that were discussed in chapter 5. Moreover, the reflection amplitudes are given by the trivial paths $r_{\eta 2}\gamma_2\tilde{r}_{2\eta}$, and $r_{\eta 3}\gamma_3\tilde{r}_{3\eta}$. All other paths are neglected in this approximation.

In combination with the propagation through the FM-layer, this yields the following set of linear equations [51, 52]:

$$\Gamma_2^\mathrm{I} = \mathcal{A}_2^\mathrm{I} + [|r_2|^2]^\mathrm{I}\beta_2\Gamma_2^\mathrm{II} + [r_{23}r_{32}^*]^\mathrm{I}\beta_3\Gamma_3^\mathrm{II}, \quad \Gamma_3^\mathrm{I} = \mathcal{A}_3^\mathrm{I} + [r_{32}r_{23}^*]^\mathrm{I}\beta_2\Gamma_2^\mathrm{II} + [|r_3|^2]^\mathrm{I}\beta_3\Gamma_3^\mathrm{II}, \quad (6.6)$$

$$\Gamma_2^\mathrm{II} = \mathcal{A}_2^\mathrm{II} + [|r_2|^2]^\mathrm{II}\beta_2\Gamma_2^\mathrm{I} + [r_{23}r_{32}^*]^\mathrm{II}\beta_3\Gamma_3^\mathrm{I}, \quad \Gamma_3^\mathrm{II} = \mathcal{A}_3^\mathrm{II} + [r_{32}r_{23}^*]^\mathrm{II}\beta_2\Gamma_2^\mathrm{I} + [|r_3|^2]^\mathrm{II}\beta_3\Gamma_3^\mathrm{I},$$

for the outgoing amplitudes at interfaces I and II. These equations can be solved explicitly, the solutions are stated in the appendix. However, these explicit solutions are not very instructive. Again, more insight can be gained by understanding them as a sum over paths through the structure. Such an interpretation is obvious. Each of the above equations states that the outgoing coherence functions at a given interface are the sum of a source term and contributions arising from outgoing coherence functions at the opposite interface which propagate through the structure and undergo reflection. Thus, every such path starts with a source-amplitude that propagates and reflects an arbitrary number of times. Two such paths are illustrated in Fig. 6.2, the left path is the elementary contribution to Γ_2^I, i.e. simply the source term. The right path is a contribution to Γ_3^I, arising from the same source term. This reasoning will prove to be useful for understanding the exotic current-phase relation that we discuss in the next section and the Josephson effect in multi-domain junctions.

6.3. Current-Phase Relation

We first investigate the exotic current-phase relation of a SC/FM/SC Josephson junction with a single ferromagnetic domain, depicted in Fig. 6.3. We shall see that a very important
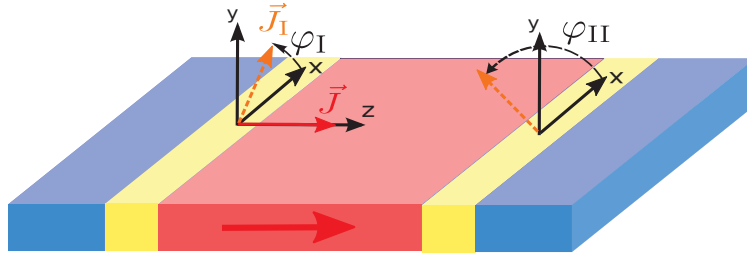
Figure 6.3. – Sketch of the single domain junction illustrating the orientation of quantisation axes in the system. The relative misalignment between interface quantisation axes, $\Delta\varphi = \varphi_{\mathrm{II}} - \varphi_{\mathrm{I}}$, implies important modifications of the current-phase relation.
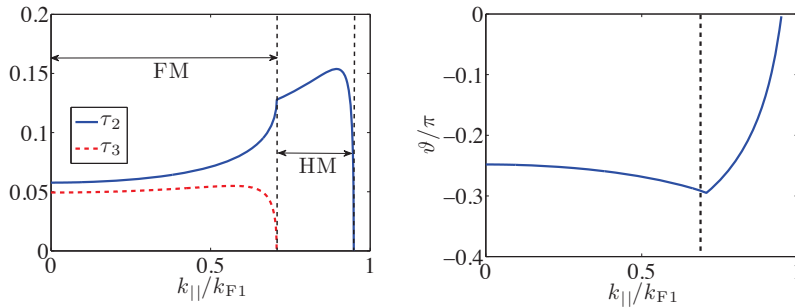
Figure 6.4. – τ-parameters as defined in the text and spin-mixing angle ϑ as a function of parallel momentum for the interface parameters stated in Fig. 6.5.

quantity in this regard is the relative misalignment of the interface quantisation axes, given by $\Delta\varphi = \varphi_{\mathrm{II}} - \varphi_{\mathrm{I}}$ here. To avoid a large 'zoo of angles', we assume that both interface quantisation axes rotate in the x-y-plane, while that of the FM is aligned with the z-axis. This implies that the second spherical angle characterising the misalignment is $\alpha = 0.5\pi$ for both interfaces. In the tunnelling limit, the functional dependence of the critical current on α is $\propto \sin(\alpha_{\mathrm{I}})\sin(\alpha_{\mathrm{II}})$, i.e., the critical current is maximal if the interface quantisation axes are perpendicular to that of the bulk – which is what we assume. The calculations done here are in the clean limit and for high-transparency junctions, since we are mainly interested in higher harmonics contributions to the current-phase relation (CPR). In Fig. 6.5, we consider a junction with a thin interface layer, $a = 0.25 \ \lambda_{\mathrm{F}}/2\pi$. We assume that the interfaces are exactly mirror symmetric, which implies that the φ-angles are identical, i.e. $\Delta\varphi = \varphi_{\mathrm{II}} - \varphi_{\mathrm{I}} = 0$. Moreover, we have chosen $V_{\mathrm{I}} = 1.05 \ E_{\mathrm{F}}$, $V_{\mathrm{FM}} = 0.3 \ E_{\mathrm{F}}$ and $h = J = 0.2 \ E_{\mathrm{F}}$. This implies that the interface layer is not fully insulating but half metallic. This has some influence on the spin-mixing angle ϑ, which we define here as $\vartheta = \arg[(R_1)_{11} \cdot (R_1)_{22}^*]$ here. ϑ is plotted on the right-hand side of Fig. 6.4, and is found to be negative for this choice of parameters. The sign of the angle has no relevance for the Josephson effect, what is important, however, is that is enhanced for larger values of $k_{||}$. As can be seen from inspecting the solutions of the boundary conditions for Γ_2^{R} and Γ_3^{R}, the 'injection' of superconducting correlations from the SC to the FM is proportional to $\tau_2 = T_{21}i\sigma_y T_{12}^*$ and $\tau_3 = T_{31}i\sigma_y T_{13}^*$, respectively. We plot these quantities on the left-hand side of Fig. 6.4 as a function of parallel momentum and observe that τ_2 is enhanced for half metallic trajectories. The reason for this counterintuitive enhancement at high-impact angles was discussed in chapter 4. It is important here, as it helps to understand the different contributions to the supercurrent in the following. While the absolute values of $\tau_{2,3}$ suggest that the junction is in the low transparency limit, we still find a current-phase relation with substantial contributions from higher harmonics at
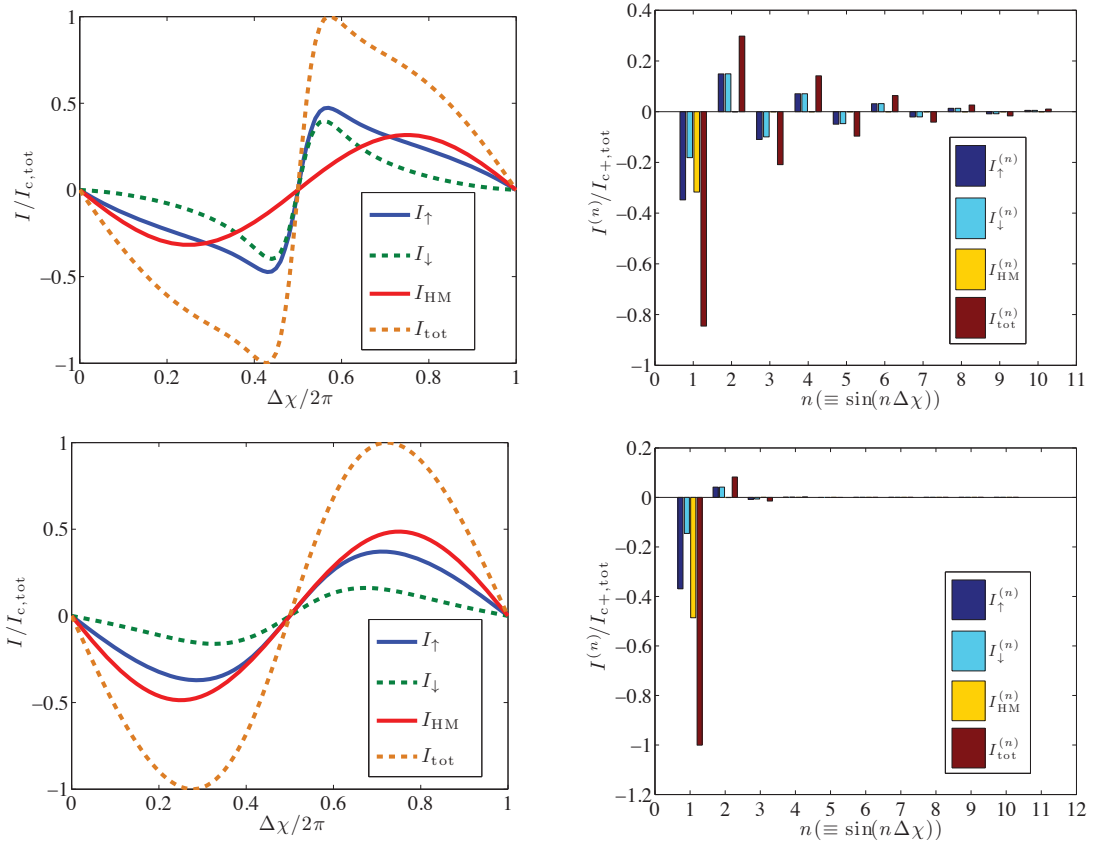
Figure 6.5. – Current phase relation of a high transmission junction ($a = 0.25\ \lambda_{\mathrm{F}}/2\pi$) for $T = 0.1\ T_{\mathrm{c}}$ (top panel) and $T = 0.5\ T_{\mathrm{c}}$ (lower panel) and $\Delta\varphi = 0$. The parameters defining the normal state dispersion are $V_{\mathrm{I}} = 1.05\ E_{\mathrm{F}}$, $V_{\mathrm{FM}} = 0.3\ E_{\mathrm{F}}$ and the exchange fields $J = h = 0.4\ E_{\mathrm{F}}$. The junction length is $L = 0.5\ \xi_0$ ($\xi_0 = \hbar v_{\mathrm{F1}}/2\pi k_{\mathrm{B}}T_c$). The right plots show the odd Fourier-components, the even ones are 0 for $\Delta\varphi = 0$.
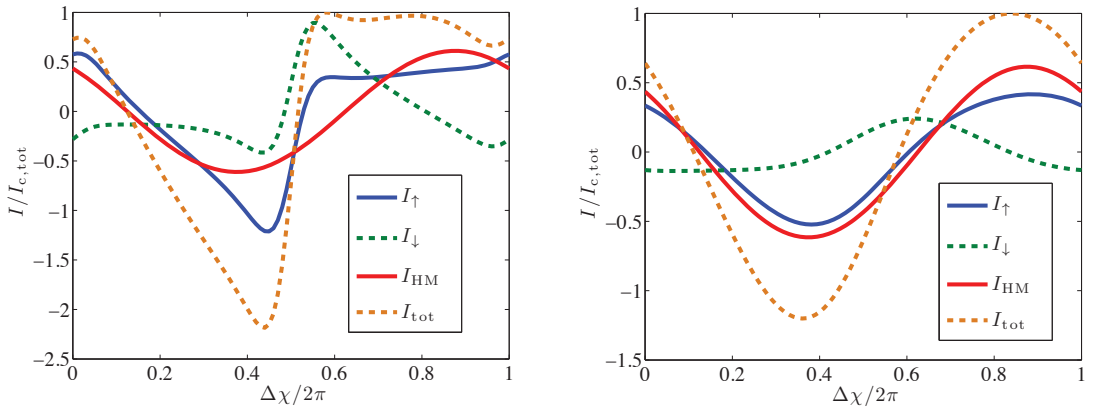
Figure 6.6. – Current phase relation with the same parameters as in Fig.6.5, but with $\Delta\varphi = 0.25\pi$, $T = 0.1\ T_{\mathrm{c}}$ (left) and $T = 0.5\ T_{\mathrm{c}}$ (right).

$T = 0.1\,T_{\rm c}$, as shown in Fig. 6.5. The junction is in a π-state, which is a ubiquitous feature of the long range triplet Josephson effect. We plot the total current and the individual contributions from the HM-trajectories ($I_{\rm HM}$) and the majority ($I_{\uparrow}$) and minority ($I_{\downarrow}$) band part of the FM-trajectories. The current-phase relation (CPR), being a 2π-periodic function, can be expanded in the complete basis set $\{\sin(n\Delta\chi), \cos(n\Delta\chi)|n \in \mathbb{N}\}$. The even Fourier-components are strictly zero for the $\Delta\varphi = 0$ junction. The first 10 odd-components are shown for $T = 0.1\,T_{\rm c}$ and $T = 0.5\,T_{\rm c}$. At $T = 0.5\,T_{\rm c}$, higher harmonics are almost completely suppressed. A first observation that we make is that the odd-components alternate in sign, which can likely be attributed to the π-state behaviour, i.e., when n Cooper-pairs travel coherently across the junction, the additional phase is $n \cdot \pi$. As far as the individual contributions are concerned, we see that their CPRs are very different at $T = 0.1\,T_{\rm c}$. The HM-contribution has no higher moments, the reason for this is that trajectories with high impact angles contribute to this part of the current. Their effective path-length through the junction is a lot longer than that of trajectories with almost perpendicular impact angle and consequently, the decay of the coherence functions after one passage through the junction is stronger. Higher harmonics of the current-phase relation arise from trajectories traversing the junction at least two times. The long path-length suppresses these contributions. The contributions from the FM-trajectories, $I_{\uparrow}$ and $I_{\downarrow}$, both show higher harmonics, but are still different from one another. Surprisingly, higher harmonics are more important for the minority band than for the majority band. This could be related to the fact that τ_2 is strongly enhanced for trajectories with high impact angle, leading to an enhanced injection of correlations from the SC, which then decay faster due to the longer path-length and hence contribute little to higher harmonics. τ_3, on the other hand, stays almost constant, implying that trajectories with perpendicular impact, being the most relevant for higher harmonics, have a higher relative weight in $I_{\downarrow}$ compared to $I_{\uparrow}$. Generally, one can conclude from this that the Fermi-surface geometry and scattering properties at the interfaces are of utmost importance for understanding the Josephson effect of such junctions in the clean limit.

We now turn to the more interesting case of a junction where the magnetisation directions of the two interfaces are rotated against each other in the x-y-plane, i.e. $\Delta\varphi \neq 0$. In the simplest case, this angle results in a phase-shift of the CPR [40], a situation which has also been referred to as φ-junction [17]. There are different proposals for realising such a phase-shift of the CPR,[a] we shortly comment on the case of triplet superconductors at the end of this section.

If, however, higher harmonics are present, the situation is more complicated, as can clearly be seen in Fig. 6.6, where we plot the CPR for $\Delta\varphi = 0.25\pi$. While still being 2π-periodic, the CPR acquires a highly irregular form. In Ref. [52], we showed that this CPR can be well approximated by:[b]

$$I_{\sigma}(\Delta\chi) \approx I_{\rm cp}(2\Delta\chi) - I_{\sigma}(2\Delta\chi) \cdot \sin(\Delta\chi - \sigma\Delta\varphi), \tag{6.7}$$

where $\sigma = \pm$ for the majority/minority band and $I_{\rm cp}$ was called crossed-pair-transmission contribution. The intuitive picture is the following. The higher harmonic contributions to the CPR in $n\Delta\chi$ are usually interpreted as the coherent transfer of n Cooper-pairs across the junction, i.e., $\Delta\chi$ acts as a counting field for the number of pairs. Obviously, the first contribution to the approximative relation (6.7) is an even function of $\Delta\chi$ and therefore all processes contributing to this term involve an even number of pairs. Secondly, this contribution is the same in both spin-bands and independent of the phase difference $\Delta\varphi$. These facts led us to the conclusion that this term must be interpreted in terms of

---

[a]See, for instance, Ref. [17] and references therein.
[b]Note that there is a sign change again, since the definition of $\Delta\varphi$ is different in the original article.
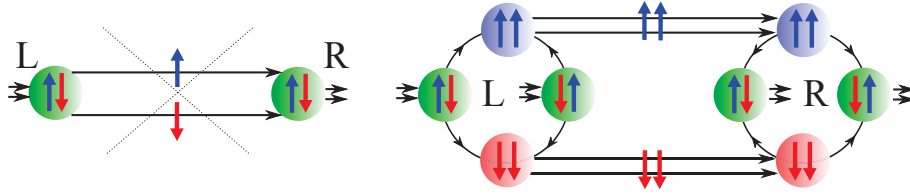
Figure 6.7. – Sketch of the crossed-pair transmission process (right), where two triplet pairs with opposite spin-orientation are transmitted coherently across the junction. This process can be understood as the analogue of the singlet Cooper-pair transmission in a normal-metal junction (left), which is suppressed here due to the exchange field. Figure from Ref. [52]. Copyright 2009 by the American Physical Society.

processes where the same number of Cooper-pairs is transferred in both spin-bands, as illustrated in Fig. 6.7 – we thus called it crossed-pair transmission contribution. The second contribution to eq. (6.7) is an odd-function of $\Delta\chi$ and only contains first order harmonics in $\Delta\varphi$. In line with the above discussion, we interpret this as a contribution of processes that involve an odd number of pairs which depends on $\Delta\varphi$, since these processes are not spin-neutral. $\Delta\varphi$ enters with opposite sign for opposite spin, which is immediately clear from the structure of the scattering matrix.

To get to the bottom of this, we analyse the CPR for a single trajectory as a function of $\Delta\chi$ and $\Delta\varphi$. It is convenient to rewrite the current density in terms of the dimensionless quantity

$$j_\eta(\varepsilon_n, p_{||}) = \text{Re}[g_\eta^M(\varepsilon_n, p_{||}, p_z > 0)]. \tag{6.8}$$

We then consider:

$$\mathcal{J}_\eta = 4k_B T \sum_{\varepsilon_n} j_\eta(\varepsilon_n, p_{||} = 0) \tag{6.9}$$

to analyse the CPR of the perpendicular trajectory, for which the contribution of higher harmonics is maximal. Note that the respective Fermi-velocity does not enter this expression. The reason for this is:

$$j_2(\varepsilon_n, p_{||}) = j_3(\varepsilon_n, p_{||}), \ \forall p_{||} \ \Rightarrow \ \langle \vec{v}_{F2}(\vec{p}_{F2}) j_2(\varepsilon_n, p_{||}) \rangle_{2+} = \langle \vec{v}_{F3}(\{\vec{p}_{F3}\}) j_3(\varepsilon_n, p_{||}) \rangle_{3+}, \tag{6.10}$$

i.e., $j_{2,3}$ being identical for all $p_{||}$ is equivalent to total currents being identical.

In Fig. 6.8, we present the Fourier-analysis of $\mathcal{J}(\Delta\chi, \Delta\varphi)$. It indeed turns out that the CPR can be written as:

$$\mathcal{J}_\eta = \sum_{n \geq 1} \mathcal{J}_{\text{cp},\eta}^{(2n)} \sin(2n\Delta\chi) + \tag{6.11}$$

$$+ \sum_{n \geq 1} \mathcal{J}_{\text{even},\eta}^{(2n-1)} \sin((2n-1)\Delta\chi)\cos(\Delta\varphi) +$$

$$+ \sum_{n \geq 1} \mathcal{J}_{\text{odd},\eta}^{(2n-1)} \cos((2n-1)\Delta\chi)\sin(\Delta\varphi).$$

Where $\mathcal{J}_{\text{cp},2}^{(n)} = \mathcal{J}_{\text{cp},3}^{(n)}$ within our numerical accuracy. Moreover, $\mathcal{J}_{\text{even},2}^{(1)} = -\mathcal{J}_{\text{odd},2}^{(1)}$ and $\mathcal{J}_{\text{even},3}^{(1)} = \mathcal{J}_{\text{odd},3}^{(1)}$, but the odd moments in $\Delta\varphi$ are suppressed a lot faster than the even ones. Higher order harmonics in $\Delta\varphi$ are completely suppressed.

To fully understand this behaviour, we analyse the solutions of the linearised equations, eq. (6.6), discussed in the previous section. For simplification, we choose $\chi_I = \varphi_I =$
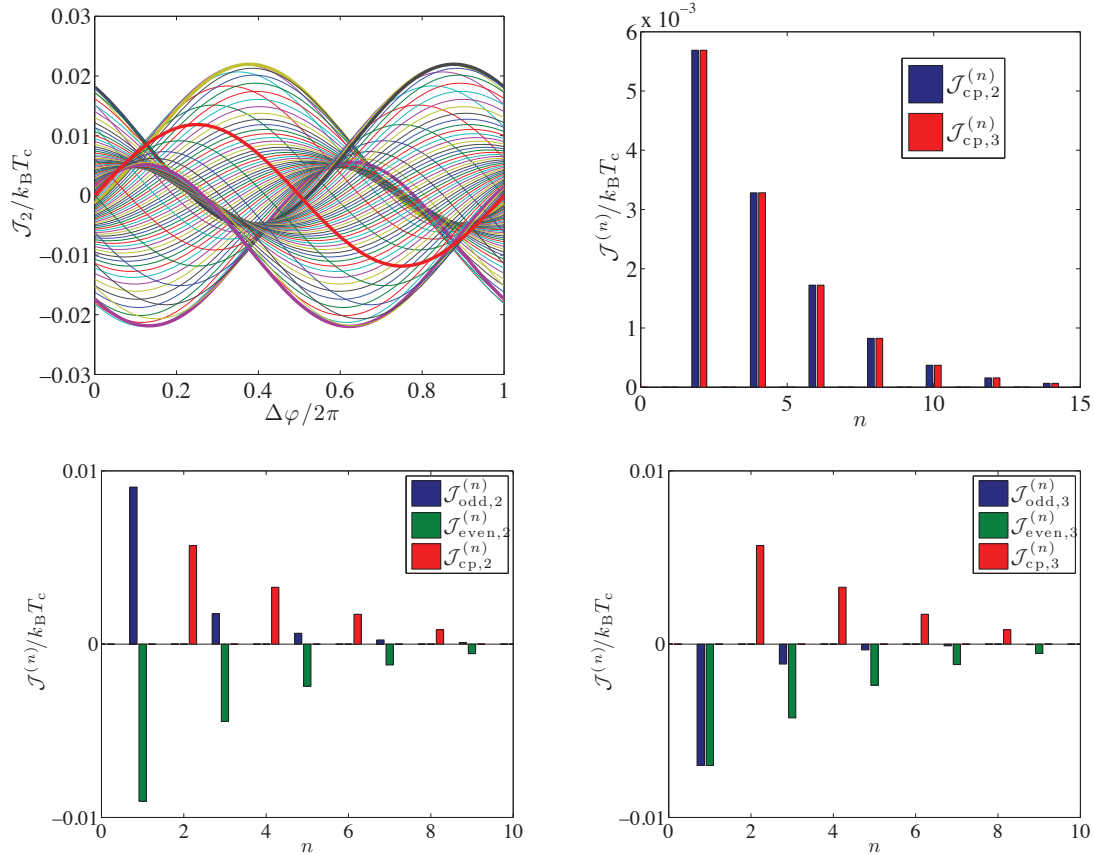
Figure 6.8. – The upper left plot shows $\mathcal{J}_2$ as a function of $\Delta\varphi$ for various values of $\Delta\chi$. The lower plots show the non-vanishing Fourier-components of $\mathcal{J}_2$ (left) and $\mathcal{J}_3$ (right). The upper right plot shows the $\mathcal{J}_{\mathrm{cp}}^{(n)}$ components of the majority and minority band. $T = 0.1\, T_{\mathrm{c}}$, other parameters are the same as in Fig. 6.5.

0 and $\chi_{\mathrm{II}} = \Delta\chi$, $\varphi_{\mathrm{II}} = \Delta\varphi$. Regarding the dependence on $\Delta\chi$ and $\Delta\varphi$, this implies $\mathcal{A}_2^{\mathrm{II}} \propto e^{i(\Delta\chi - \Delta\varphi)}$, $\mathcal{A}_3^{\mathrm{II}} \propto e^{i(\Delta\chi + \Delta\varphi)}$ and $\rho_{23}^{\mathrm{II}} \propto e^{-i2\Delta\varphi}$, $\rho_{32}^{\mathrm{II}} \propto e^{i2\Delta\varphi}$. Thus, although it is immediately clear from these equations that higher harmonics in $\Delta\chi$ are not possible in this weak proximity effect limit, the same is not true for the $\Delta\varphi$ phase. Still, we did not find higher harmonics in $\Delta\varphi$ even for a junction which is not in the tunnelling limit.

We are interested in the current, whose dependence on the coherence functions can be approximated at $z = 0$ by:

$$j_\eta(\varepsilon_n, p_{||}, p_z > 0, z = 0) \propto \mathrm{Im}\; \left[\frac{1 + \gamma\tilde{\gamma}}{1 - \gamma\tilde{\gamma}}\right]_\eta^{\mathrm{I}} = \mathrm{Im}\; 2\sum_{n=1}^{\infty}[(\gamma\tilde{\gamma})^n]_\eta^{\mathrm{I}} \approx [\mathrm{Im}\; 2\gamma_\eta^{\mathrm{I}}\tilde{\gamma}_\eta^{\mathrm{I}}](p_z > 0)$$

$$= 2 \cdot \mathrm{Im}\; \Gamma_\eta^{\mathrm{I}}\beta_\eta[\Gamma_\eta^{\mathrm{II}}]^*, \tag{6.12}$$

if the proximity effect is weak. Insight can now be gained by invoking the sum-over-paths perspective for the solution of the linearised equations (6.6). The terms contributing to the solutions of the linearised equations up to second order in path length are listed in table 6.1. One thus finds the leading order term contributing to the current at interface I ($z = 0$) with a higher order harmonic dependence on $\Delta\varphi$ to be:

$$\mathrm{Im}\; \beta_2\beta_3\Big([\hat{\mathcal{A}}_2\hat{\mathcal{A}}_3^*]^{\mathrm{I}} \cdot [\hat{\rho}_{23}^{\mathrm{II}}]^* \cdot e^{i2\Delta\varphi} + [\hat{\mathcal{A}}_3\hat{\mathcal{A}}_2^*]^{\mathrm{II}} \cdot \hat{\rho}_{23}^{\mathrm{I}} \cdot e^{i2\Delta\varphi}\Big) \propto \sin(2\Delta\varphi), \tag{6.13}$$

where a hat implies that the dependence of the given quantity on $\Delta\chi$ and $\Delta\varphi$ was factored out.

$\#\{\beta_2,\beta_3\}$	Γ_2^{I}	Γ_3^{I}	Γ_2^{II}	Γ_3^{II}
0	$\mathcal{A}_2^{\mathrm{I}}$	$\mathcal{A}_3^{\mathrm{I}}$	$\mathcal{A}_2^{\mathrm{II}}$	$\mathcal{A}_3^{\mathrm{II}}$
1	$\rho_2^{\mathrm{I}}\beta_2\mathcal{A}_2^{\mathrm{II}},$ $\rho_{23}^{\mathrm{I}}\beta_3\mathcal{A}_3^{\mathrm{II}}$	$\rho_3^{\mathrm{I}}\beta_3\mathcal{A}_3^{\mathrm{II}},$ $\rho_{32}^{\mathrm{I}}\beta_2\mathcal{A}_2^{\mathrm{II}}$	$\rho_2^{\mathrm{II}}\beta_2\mathcal{A}_2^{\mathrm{I}},$ $\rho_{23}^{\mathrm{II}}\beta_3\mathcal{A}_3^{\mathrm{I}}$	$\rho_3^{\mathrm{II}}\beta_3\mathcal{A}_3^{\mathrm{I}},$ $\rho_{32}^{\mathrm{II}}\beta_2\mathcal{A}_2^{\mathrm{I}}$
2	$\rho_2^{\mathrm{I}}\beta_2\rho_2^{\mathrm{II}}\beta_2\mathcal{A}_2^{\mathrm{I}},$ $\rho_2^{\mathrm{I}}\beta_2\rho_{23}^{\mathrm{II}}\beta_3\mathcal{A}_3^{\mathrm{I}},$ $\rho_{23}^{\mathrm{I}}\beta_3\rho_3^{\mathrm{II}}\beta_3\mathcal{A}_3^{\mathrm{I}},$ $\rho_{23}^{\mathrm{I}}\beta_3\rho_{32}^{\mathrm{II}}\beta_2\mathcal{A}_2^{\mathrm{I}}$	$\rho_{32}^{\mathrm{I}}\beta_2\rho_2^{\mathrm{II}}\beta_2\mathcal{A}_2^{\mathrm{I}},$ $\rho_{32}^{\mathrm{I}}\beta_2\rho_{23}^{\mathrm{II}}\beta_3\mathcal{A}_3^{\mathrm{I}},$ $\rho_3^{\mathrm{I}}\beta_3\rho_3^{\mathrm{II}}\beta_3\mathcal{A}_3^{\mathrm{I}},$ $\rho_3^{\mathrm{I}}\beta_3\rho_{32}^{\mathrm{II}}\beta_2\mathcal{A}_2^{\mathrm{I}}$	$\rho_2^{\mathrm{II}}\beta_2\rho_2^{\mathrm{I}}\beta_2\mathcal{A}_2^{\mathrm{II}},$ $\rho_2^{\mathrm{II}}\beta_2\rho_{23}^{\mathrm{I}}\beta_3\mathcal{A}_3^{\mathrm{II}},$ $\rho_{23}^{\mathrm{II}}\beta_3\rho_3^{\mathrm{I}}\beta_3\mathcal{A}_3^{\mathrm{II}},$ $\rho_{23}^{\mathrm{II}}\beta_3\rho_{32}^{\mathrm{I}}\beta_2\mathcal{A}_2^{\mathrm{II}}$	$\rho_{32}^{\mathrm{II}}\beta_2\rho_2^{\mathrm{I}}\beta_2\mathcal{A}_2^{\mathrm{II}},$ $\rho_{32}^{\mathrm{II}}\beta_2\rho_{23}^{\mathrm{I}}\beta_3\mathcal{A}_3^{\mathrm{II}},$ $\rho_3^{\mathrm{II}}\beta_3\rho_3^{\mathrm{I}}\beta_3\mathcal{A}_3^{\mathrm{II}},$ $\rho_3^{\mathrm{II}}\beta_3\rho_{32}^{\mathrm{I}}\beta_2\mathcal{A}_2^{\mathrm{II}}$

Table 6.1. – All contributions to the solutions of equation (6.6) up to second order in path length.
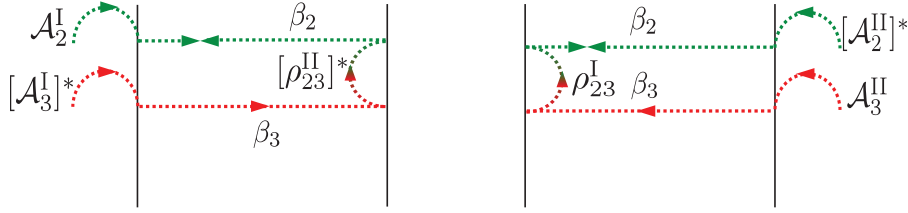
Figure 6.9. – Leading order terms contributing to $\Gamma_2^{\mathrm{I}}\beta_2[\Gamma_2^{\mathrm{II}}]^*$ with a higher harmonic dependence on $\Delta\varphi$.

The leading order contribution to the current reads, on the other hand:

$$\mathrm{Im}\,\beta_2\mathcal{A}_2^{\mathrm{I}}\big[\mathcal{A}_2^{\mathrm{II}}\big]^* \propto \sin(\Delta\chi - \Delta\varphi), \tag{6.14}$$

which contains one less propagation factor and also no additional suppression from reflection. This leading order term is contained in the $\mathcal{J}_{\mathrm{even,odd},\eta}^{(1)}$-terms of equation (6.11), and since the corresponding contribution in band 3 is proportional to $\sin(\Delta\chi + \Delta\varphi)$, the relations $\mathcal{J}_{\mathrm{even},2}^{(1)} = -\mathcal{J}_{\mathrm{odd},2}^{(1)}$ and $\mathcal{J}_{\mathrm{even},3}^{(1)} = \mathcal{J}_{\mathrm{odd},3}^{(1)}$ are now obvious. Moreover, the fact that $\mathcal{J}_{\mathrm{even},2}^{(1)} < 0$ and $\mathcal{J}_{\mathrm{even},3}^{(1)} < 0$ is consistent with the observation that the junction is in a π-state for $\Delta\varphi = 0$.

Higher moments in $\Delta\chi$ can obviously not be explained in terms of the linearised equations. By combining the sum-over-paths reasoning for the boundary conditions with that for propagations through the structure, we can identify the leading terms that generate a higher order dependence on $\Delta\chi$. To this effect, we consider the graphical solution of the boundary conditions presented in appendix D. From the structure of the graph, we infer that any path contributing to the solutions is either proportional to γ_η, where $\eta = 1, 2, 3$, or to $(\gamma_{\delta_1}\tilde{\gamma}_{\nu_1}...\gamma_{\delta_n}\tilde{\gamma}_{\nu_n})\gamma_\eta$, if the path passes n-times through a sub-loop of the graph.[a] On that basis, it is now easy to identify the higher order terms in $\Delta\chi$. We consider the solution at the second interface, where the phase is picked up, i.e., we have $\gamma_1 \propto e^{i\Delta\chi}$. The leading order contributions to $\gamma_{2,3}$ propagated only once through the interlayer, which implies that they originate from the SC-electrode at the first interface and are thus independent of $\Delta\chi$. To find the path that gives us a second order moment in $\Delta\chi$, we now look for the contribution that depends on γ_1^2, which we find in the first branch of the graph. Its contribution to Γ_2^{II} reads:

$$[T_{21}\gamma_1\tilde{T}_{13}]^{\mathrm{II}}\beta_3\tilde{\mathcal{A}}_3^{\mathrm{I}}[T_{31}\gamma_1\tilde{T}_{12}]^{\mathrm{II}}, \tag{6.15}$$

---

[a]We assume $\hat{\gamma}_1 = \gamma_1 i\sigma_y$ here, i.e., γ_1 is scalar.

where $\beta_3 \tilde{\mathcal{A}}_3^{\mathrm{I}}$ is the leading order in β contribution to $\tilde{\gamma}_3^{\mathrm{II}}$. The leading order contribution to the current is thus proportional to:

$$\mathrm{Im}\, \beta_2 \mathcal{A}_2^{\mathrm{I}} \Big\{ [T_{21}\gamma_1 \tilde{T}_{13}]^{\mathrm{II}} \beta_3 \tilde{\mathcal{A}}_3^{\mathrm{I}} [T_{31}\gamma_1 \tilde{T}_{12}]^{\mathrm{II}} \Big\}^* \propto \sin(2\Delta\chi). \tag{6.16}$$

We hence identified the first contribution to the crossed-pair transmission. Obviously, it is identical to the corresponding contribution in band 3, which is obtained by replacing $2 \leftrightarrow 3$, in agreement with our numerical findings.

In regard to the current contribution of the process described by equation (6.15), it will be second order in β-factors, since an additional propagation enters in the current expression. Thus, it is of the same order in β as the $\sin(2\Delta\varphi)$ contribution described above. Still, the latter seems to be suppressed here. This is because it is proportional to ρ_{23}, which is necessarily small if the transmission of the junction is high.

To make the $\sin(2\Delta\varphi)$ term appear, we may introduce an asymmetry in the junction by increasing the thickness of the second interface. That this works can easily be understood from eq. (6.13) and Fig. 6.9. Apparently, the processes contributing to this term couple to one of the SC-electrodes only, which is also why they are independent of $\Delta\chi$. So if one of the two electrodes is decoupled from the interlayer by making the interface a perfectly reflecting barrier, all terms that contain contributions from this second electrode are suppressed, while one of the two terms contributing to (6.13) remains. Obviously, there must be an identical contribution with opposite sign in the other spin-band to maintain charge conservation – a net charge current cannot flow through the junction if one interface is perfectly reflecting. This situation is illustrated in Fig. 6.10, where we plot $\mathcal{J}_\eta$ for different widths of the second interface, starting from a symmetric junction and arriving eventually at a junction where the second superconductor is fully decoupled from the FM-layer ($a = 20\ \lambda_\mathrm{F}/2\pi$). While the symmetric junction has only a first harmonic contribution, the second harmonic increases as the second interface becomes thicker and the first harmonic decreases. When the second superconductor is fully decoupled, the dependence on $\Delta\varphi$ is governed by the second harmonic and the total current vanishes ($\mathcal{J}_2 + \mathcal{J}_3 = 0$), which is in agreement with current conservation. This corresponds to the pure spin-supercurrent in a SC/FM-bilayer that we discussed in Ref. [52]. While we focused on the $\Delta\varphi$ dependence here, it is also clear that the current is strongly suppressed as the thickness of the second interface increases. This cannot be seen in Fig. 6.10, since the currents were normalised to their maximum value there. We discuss the critical current in these junctions in the following section.

Fig. 6.11 shows how this spin-supercurrent can be understood in terms of Cooper-pair transport. A singlet pair entering from the superconductor is converted to a triplet pair in the FM and travels through the junction to the opposite surface, which is now perfectly reflecting. Since this surface still allows for spin-flip scattering, some of the triplet pairs undergo spin-flip and travel back in the opposite band. The phase difference $\Delta\varphi$ which corresponds to the total scattering phase difference picked up by the Cooper-pairs at the interface to the superconductor and the surface plays the role of the order parameter phase difference.

An analogous effect in triplet superconductors was predicted by Brydon et al. (see Ref. [16], for instance). In this case, the spin-quantisation axis of the triplet order parameter plays a similar role as the interface magnetisation does here.

The fact that the CPR of a single-domain junction depends on φ_{II} and φ_{I} only through $\Delta\varphi$ is a fundamental requirement of the junction symmetry and can be proven rigorously in a fashion similar to what we discuss in the last section of this chapter (see appendix G).
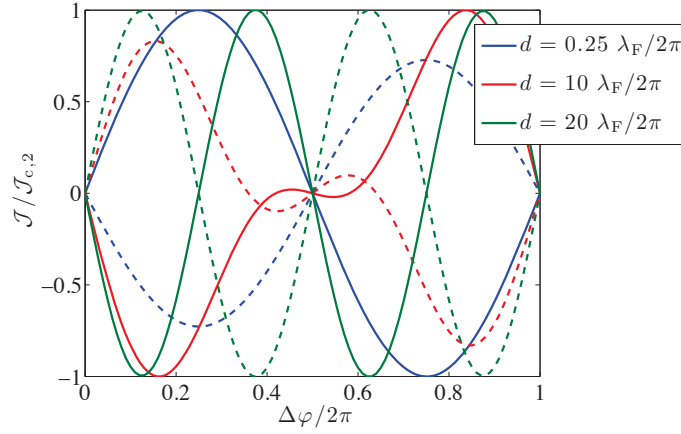
Figure 6.10. – Supercurrent for the perpendicular trajectory ($p_{||} = 0$) for the majority (solid lines) and minority (dashed lines) band as a function of $\Delta\varphi$ and for $\Delta\chi = 0$. The thickness of the first interface is kept constant at $a = 0.25\,\lambda_F/2\pi$, while that of the second interface is varied and shown for $a = 0.25,\ 5,\ 10,\ 20\,\lambda_F/2\pi$. $T = 0.1\,T_c$, other parameters are the same as in Fig. 6.5.
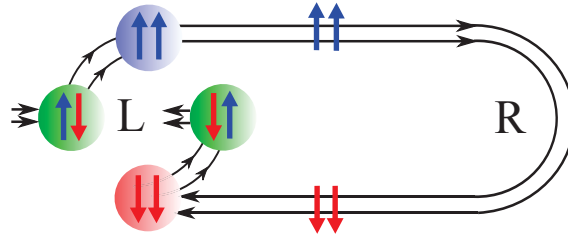
Figure 6.11. – The spin-Josephson effect in a SC/FM bilayer – Triplet Cooper-pairs propagate in opposite direction through the FM-layer and flip their spin at the opposite interface. Thus, there is no charge-current due to this process.
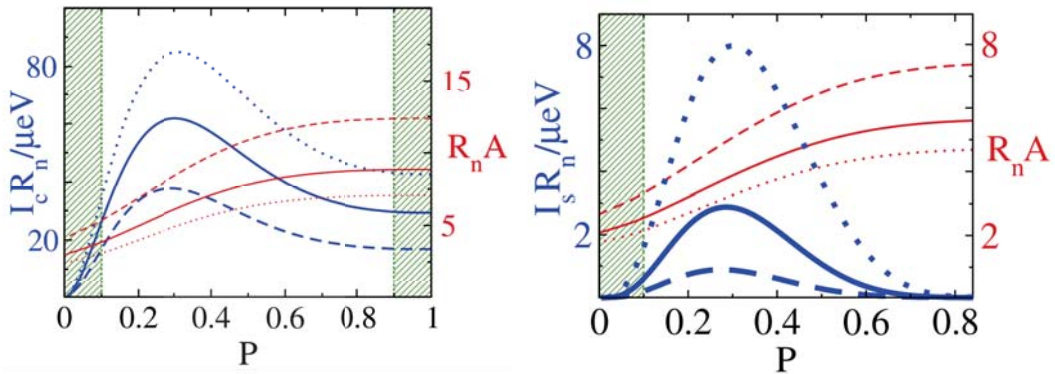
Figure 6.12. – Left: Critical current of a SC/FM/SC Josephson junction as a function of the spin-polarisation P of the FM layer (blue) and the corresponding normal state resistance of the contact (red). Right: Maximal spin-supercurrent in a SC/FM-bilayer (blue) and the corresponding normal state conductance of the SC/FM-interface (red) as function of P. Parameters (left): $a = 1\,\lambda_F/2\pi$, $\alpha = \pi/2$, $\Delta\varphi = 0$, $L = 0.5\,\xi_0$ (mistakenly 1 ξ_0 in the original article), $p_{F2} = 1.18p_{F1}$, p_{F3} is varied, $P = P(p_{F3})$. $J_I = J_{FM}$ (is also a function of p_{F3}) and $V_I - J_I/E_F = 10e^{-4}$ (dotted line), 0.2 (solid line), 0.5 (dashed line). R_nA is plotted in units of $(e^2 N_{F1} v_{F1})^{-1}$. $\Delta = 1.76$ meV, $T = 0.5\,T_c$. Parameters (right): the same as in the left figure, but the thickness of the second interface is set to infinity (perfectly reflecting barrier). Figure from Ref. [52]. Copyright 2009 by the American Physical Society.

6.4. Critical Currents as a Function of Spin-Polarisation

Now that we have a theory of the triplet Josephson effect that is valid for a wide range of spin-polarisations, an interesting question to address is the dependence of the critical current on the spin-polarisation P [52]. Recall that P was defined as $P = (p_{F2}-p_{F3})/(p_{F2}+p_{F3})$, where $p_{F2,3}$ are the Fermi-momenta of the two spin-bands. We plot the $I_c R_n$ product of a SC/FM/SC junction as a function of P on the left side of Fig. 6.12. To vary P, we varied the Fermi-momentum in the spin-down band. This implies that the normal state properties of the junction change as well, which is why we also plot the normal state resistance of the junction.[a] It is obvious from the plot that the behaviour of I_c cannot be attributed to the variation of R_n. The shaded regions indicate values of P for which the assumptions underlying the quasiclassical approximation are in principle ill-founded. For very small P, the exchange energy cannot be considered to be large compared to the SC gap. This implies that singlet-correlations will not be fully suppressed in that case, but they are generically eliminated in our quasiclassical model. For large P, the Fermi-momentum in the minority band approaches zero, and the oscillations on the k_F-scale, which are integrated out, are thus not 'fast' anymore. Not surprisingly, the current is suppressed for small P. This is because the spin-mixing angle is suppressed for small exchange fields and the singlet-triplet conversion thus becomes ineffective. That the current is maximal for about $P \approx 0.3$ and approaches a constant, smaller value for $P \to 1$, is a bit harder to understand. The reason is that the triplet-current carried by the ferromagnetic trajectories is larger than that carried by the half metallic ones. This is because the spin-mixing phases $\vartheta_{2,3}$, that control the magnitude of the spin-mixing effect for these trajectories, are enhanced compared to the mixing angle $\vartheta/2$, which is relevant for the half metallic ones.

On the right side of Fig. 6.12, we plot the maximal spin-supercurrent for the bilayer geometry discussed before. In this case, R_n refers to the resistance of the single SC/FM interface. The spin-supercurrent is suppressed for both small and large P. The explanation is obvious, the singlet-triplet conversion is suppressed for small P, while for large P, the minority band is eliminated and a half metallic ferromagnet can obviously not support the transport process shown in Fig. 6.11.

6.5. Multi-domain Junctions

We now turn to multi-domain junctions and study critical Josephson currents in these systems. As explained in the introduction, investigating this problem is very relevant for recent experiments where triplet Josephson currents were measured in Co-junctions with an anti-ferromagnetic domain structure enforced by Ru interlayers [68, 71, 70, 69]. The Ru-layer will be ignored here, we simply assume that anti-ferromagnetic domains exist, which implies backscattering due to wave vector mismatches all by itself. The transparency of the domain boundary thus depends on the wave vector mismatch between the majority and minority band in our model and consequently, the effect of backscattering at the domain boundaries will be most important for strongly spin-polarised materials. The solutions of the boundary conditions and the numerical implementation of this calculation are discussed in the appendix. What is important here, is the general structure of the S-matrix at the domain boundary:

$$S = \begin{pmatrix} R & T \\ T^\top & R \end{pmatrix}, \quad R = \begin{pmatrix} r & 0 \\ 0 & -r \end{pmatrix}, \ T = \begin{pmatrix} 0 & t \\ -t & 0 \end{pmatrix}. \tag{6.17}$$

---

[a]The normal state resistance was calculated by solving the transport equations for the distribution functions in the normal state. In the clean limit we consider here, it is exclusively determined by the interfaces. Technically, we thus calculated $G_n/A = 1/(R_n A)$. For the spin-supercurrent setup, R_n refers to the resistance of the transparent interface.
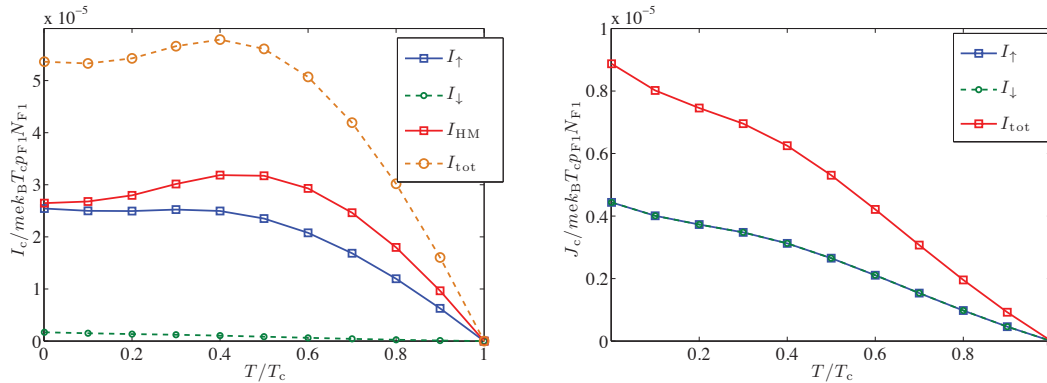
Figure 6.13. – Critical current vs. temperature for a single domain junction (left) and a two domain junction (right). The junction parameters are: $a = 2\,\lambda_{\mathrm{F}}/2\pi$, $V_{\mathrm{I}} = 2\,E_{\mathrm{F}}$, $V_{\mathrm{FM}} = 0.5\,E_{\mathrm{F}}$, $J = h = 0.9\,E_{\mathrm{F}}$, $L = 0.5\,\xi_0$, $\Delta\varphi = 0$.
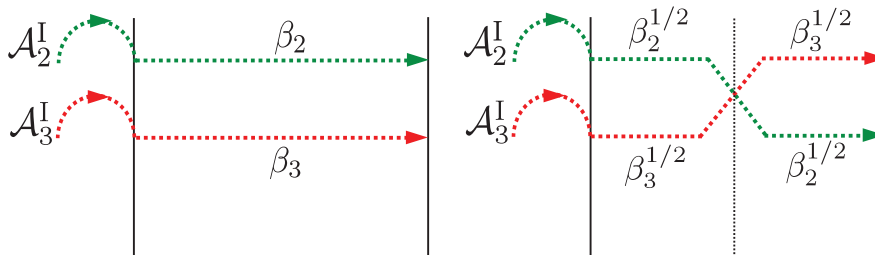
Figure 6.14. – Correlations switch channels at an anti-ferromagnetic domain boundary (right).

The anti-parallel magnetisation and the neglect of other scattering effects implies that there is no spin-flip scattering and that the domain boundary does not break pairs, but the minority and majority band are interchanged. In regard to the coherence functions, this means that they have a chance of being reflected at the domain boundary into the band they originated from, or be transmitted across the boundary into the other band (see Fig. 6.14).

In regard to the dependence of the critical current on temperature, an anomaly, i.e., a non-monotonical functional dependence on T, was predicted for half-metallic junctions [40], and later also for ferromagnetic junctions with high P [52]. From our analysis, we concluded that this anomaly is due to the half-metallic trajectories, and therefore appears in the total critical current if these dominate transport. If the FM-interlayer has at least two domains with opposite magnetisation, these trajectories cannot contribute to transport, as quasiparticles travelling in these channels will be perfectly reflected at the domain boundaries. One would hence expect a suppression of the anomaly in such junctions even if P is high.

Thus, the presence of domain boundaries implies a suppression of the critical current for two reasons. On one hand, the contribution of half-metallic trajectories is fully absent – a substantial part of the states on the Fermi-sphere does not contribute to transport. Secondly, the domain boundaries cause backscattering even for those trajectories that can pass through. This increases the effective junction length and thereby further suppresses the current. Furthermore, the fact that any quasiparticle travelling through the junction must spend some time in the minority band is important for understanding the suppression of the critical current in long junctions, $L \gg \xi_0$.
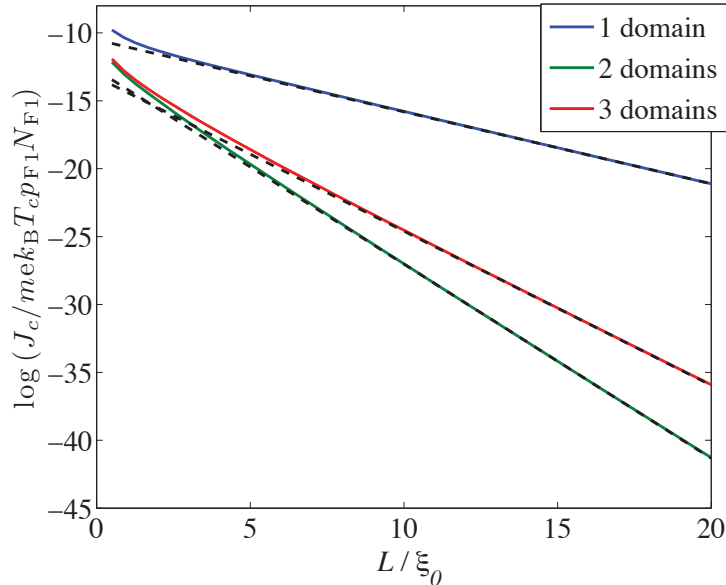
Figure 6.15. – Critical current vs. junction length on a logarithmic scale at $T = 0.5\ T_c$. All other parameters are the same as in Fig. 6.13. The dashed lines indicate exponential fits to the data. The inverse decay length κ is $\kappa = 0.52/\xi_0$ for the single domain, $\kappa = 1.43/\xi_0$ for two domains, and $\kappa = 1.135/\xi_0$ for three domains.

In Fig. 6.13, we plot the temperature dependence of the critical current for a single-domain and a two-domain junction. The junction parameters are chosen so that we are in the tunnelling limit, meaning that the CPR of these junctions contains no higher Fourier-components in $\Delta\chi$. The critical current is thus obtained for $\Delta\chi = 3/2\pi$ in the single domain junction, since the junction is in a π-state. An important finding is that this is not true for the two-domain junction, which we find to be in a 0-state, i.e., the critical current is found at $\Delta\chi = 1/2\pi$, while the three domain junction is in a π-state again. I.e., if the number of domains is even and there is an odd number of band switchings, the junction is not in a π-state. Note that one must be cautious in regard to the definition of the φ-phases when the number of domains is even. In that case, the orientation of the bulk-magnetisation will be along $-\hat{z}$ rather than $\hat{z}$ at the second interface. By mapping $-\hat{z} \mapsto \hat{z}$ with a rotation of the coordinate system around the x-axis, we see that φ_{II} must be replaced with $-\varphi_{\mathrm{II}}$. We show in the appendix that the CPR still depends on $\Delta\varphi$ only, since an even number of domains implies an odd number of band-switchings, which effectively undoes the sign change of φ_{II}.

The temperature anomaly predominantly arises from the half metallic contribution in the single domain junction and is strongly suppressed in the two domain case. Moreover, we see that the critical current is reduced in the latter scenario compared to the first. The junction is in a strongly polarised limit (P=0.63), which is why $I_\downarrow$ is very small in the single-domain case. Note also that the current contributions of $I_\uparrow$ and $I_\downarrow$ are identical in the two domain junction. This is because the junction is now symmetric with respect to an exchange of the bands. The current due to the ferromagnetic trajectories only is, as expected, smaller in the two domain case. This is understood from the fact that, due to the band switching, all coherence functions are suppressed by $\sqrt{\beta_2\beta_3}$ after one propagation through the interlayer in the two domain case. Since $\beta_3 < \beta_2$, as a result of the different Fermi-velocities, this implies a reduction of the current in band 2 and an enhancement in band 3.

In Fig. 6.15, we plot the total critical current as function of junction length. If we appeal again to the path-expansion of the current expression, we can arrange terms in orders of (β_2, β_3), that is, the total length of the paths associated to the two coherence functions which enter the current expression. The leading order contribution to the current is given by the shortest path through the junction at the lowest Matsubara frequency. If the junction is very long, this will be the only surviving contribution, since the exponential suppression of all other terms is faster. Thus, if $b_2 = \beta_2(\epsilon_0, k_{||} = 0)$ and $b_3 = \beta_3(\epsilon_0, k_{||} = 0)$, we expect that the critical current depends on the junction length as b_2 in the 1 domain case, as $\sqrt{b_2 b_3}$ in the two domain case and as $(b_2^2 b_3)^{1/3}$ in the three domain case if $L \gg \xi_0$. These are the fastest paths in the majority band, the fasted minority band path will be slower in all but the 2 domain case, since the Fermi-velocity is smaller in this band. For the parameters used in Fig. 6.15, we obtain 0.513, 1.375 and 1.087 as the respective inverse decay lengths from this reasoning. The values that we fitted to our data agree quite well with that, but are all a bit higher. This is likely due to the Fermi-surface average, i.e., transport channels with small but finite $k_{||}$ still give a non-negligible contribution at the lengths that we calculated.

That the decay seems to be super-exponential for short junctions is easily understood from the fact that longer paths with different decay lengths also contribute in that case. For short junctions, we also observe that the single domain current is substantially larger than the multi-domain one, while the latter differ little. This can be attributed to the elimination of the half-metallic contribution as explained above.

The somewhat counterintuitive result that the fastest decay of the current occurs in the 2 domain junction is hence understood as an effect of the different Fermi-velocities in the two spin bands. In the two domain junction, the shortest path must travel through half of the junction in the minority band, while in the 3 domain case, it is only one third. While backscattering at the domain boundaries does imply an additional suppression of the current, the scaling law in the long junction limit is insensitive to it, as the current is carried by the shortest path anyway, which does not undergo backscattering.

In regard to the experimental observations of Khasawneh et al. [70], it is clear that the model we investigated here cannot explain their results. They find an exponential suppression of the critical current as the number of Ru-interlayers is increased, while the total length of the junction is kept constant. We conclude that this behaviour cannot be accounted for by spin-conserving backscattering at the domain boundaries and different Fermi-velocities in the spin-bands of the FM. Including spin-flip scattering at the domain boundaries would likely allow us to model this data, since such scattering effects would break triplet pairs rather than just reflecting them. In terms of our formalism, this can straight-forwardly be included in the scattering matrix of the domain boundary.

6.6. $p_x \pm i p_y$ State induced by a Rashba-Interface

In this final section of the chapter on the triplet proximity effect, we shortly comment on a proposal that is related to what we discussed so far, but has quite different implications. More precisely, we discuss the triplet proximity effect induced by an interface whose spin-activity arises from spin-orbit coupling rather than a ferromagnetic exchange field. That this works is easily understood. The Rashba-term can be considered as an exchange field whose orientation depends on $\mathbf{k}_{||}$. Thus, the only formal difference with respect to a ferromagnetic exchange field is that the misalignment of the quantisation axes is $\mathbf{k}$-dependent. Specifically, the Rashba term has the structure:

$$H^{\mathrm{SO}} = \alpha \vec{g}_{\mathbf{k}} \cdot \vec{\sigma}, \tag{6.18}$$
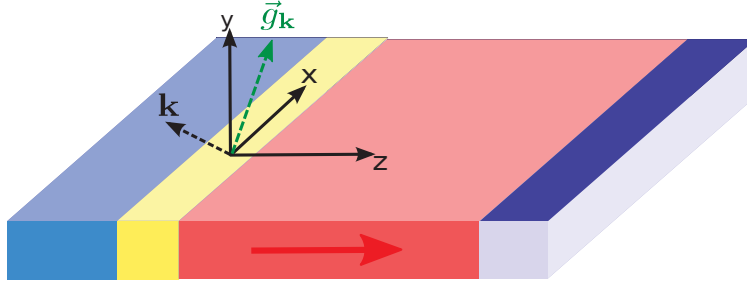
Figure 6.16. – Bilayer structure with a Rashba-interface.

with

$$\vec{g}_{\mathbf{k}} = \frac{\mathbf{k} \times \hat{z}}{|\mathbf{k} \times \hat{z}|} = \frac{1}{k_x^2 + k_y^2}(k_y, -k_x, 0) = (\sin \varphi_{\mathbf{k}}, -\cos \varphi_{\mathbf{k}}, 0), \qquad (6.19)$$

since the structure in grown in the z-direction. Thus, the quantisation axis of the spin-orbit term rotates in the x-y-plane. This implies that only the φ-angle acquires a $\mathbf{k}$-dependence. In fact, we can simply replace $\varphi \to \varphi_{\mathbf{k}}$, as shown in appendix B. This problem was first considered by Löfwander and Eschrig for half metallic junctions, but they did not publish their results so far [41]. Recently, the idea was investigated by Chung et al. [22], using a different method. They argue that this scenario may allow to engineer an instance of the spin-less $p_x + ip_y$ state in the half metal. We will see in a second that this is in fact a very obvious result. As we pointed out in the introduction, $p_x + ip_y$ superconducting states attracted a lot of attention recently in the context of topological quantum computation [93], and we will be concerned with another proposal of this type in the second part of this thesis.

As discussed at length in chapter 5, the symmetry classification of pairing correlations is based on analysing the symmetry of the anomalous Green's function $f_\eta(\mathbf{R}, \mathbf{p}_F, \epsilon_n, t)$, which, in the context of our formalism, is given by:

$$f_\eta = -\mathrm{sgn}(\epsilon_n) i\pi \frac{2\gamma_\eta}{1 - \gamma_\eta \tilde{\gamma}_\eta}. \qquad (6.20)$$

If the dependence of f_η on $\varphi_{\mathbf{k}}$ is given by $e^{i\varphi_{\mathbf{k}}}$, then it has a $p_x + ip_y$-symmetry. Recall that $\tilde{\gamma}_\eta(\epsilon_n, \mathbf{k}) = \gamma_\eta^*(-\epsilon_n, -\mathbf{k})$. Hence, if $\gamma_\eta(\epsilon_n, \mathbf{k})$ depends on $\varphi_{\mathbf{k}}$ as $e^{i\varphi_{\mathbf{k}}}$, then $\gamma_\eta(\epsilon_n, -\mathbf{k})$ depends on it as $e^{i(\varphi_{\mathbf{k}}+\pi)}$ and $\tilde{\gamma}_\eta(\epsilon_n, \mathbf{k})$ as $e^{-i(\varphi_{\mathbf{k}}+\pi)}$. Thus, f_η has a $p_x + ip_y$ symmetry if γ_η has this $\varphi_{\mathbf{k}}$ dependence. What we will prove in the following is that f_2 has a $p_x - ip_y$ symmetry and f_3 a $p_x + ip_y$ symmetry.

To this end, we consider a SC/FM bilayer structure terminated by a spin-inactive surface, as shown in Fig. 6.16. This implies that the boundary conditions at the surface are trivial, we have

$$\Gamma_\eta^{\mathrm{II}} = \gamma_\eta^{\mathrm{II}}. \qquad (6.21)$$

The reasons for considering a finite FM layer are the following. First, it is easy to see from the definition of the DOS, $N \propto \mathrm{Tr}(g)$, that there will not be a an energy gap in the single particle DOS if the FM layer is infinite. In that case, the coherence amplitudes propagating towards the SC/FM interface would be zero, as they originate from the FM bulk. In the diagonal entries of g, the coherence functions enter in $\gamma\tilde{\gamma}$ pairs, which, for a given momentum, have opposite group velocities. Hence, for any momentum, one of the

two would be zero and thus $N(\epsilon) = N_\mathrm{F} = const$. Secondly, we would like the engineered $p_x + ip_y$ state to be effectively two-dimensional, i.e., as homogenous as possible in the z-direction and confined to a thin layer. From our previous discussion of the current-phase relation, it is not obvious that $\gamma_\eta(\mathbf{k}) \propto e^{\pm i\varphi_\mathbf{k}}$ and that there are no higher moments in $\varphi_\mathbf{k}$ appearing.

The prove of this assertion is fully analogous to the one we discuss in appendix G in regard to the Josephson current. We start by writing the boundary conditions in a matrix notation [37]:

$$\mathbf{\Gamma} = \Gamma_{k \to k'}, \quad \overline{\mathbf{\Gamma}} = \mathbf{\Gamma} - \Gamma_k \delta_{kk'}, \tag{6.22}$$

$$\boldsymbol{\gamma} = \gamma_k \delta_{kk'}, \boldsymbol{\gamma}' = S \circ \boldsymbol{\gamma} \circ \tilde{S}, \tag{6.23}$$

where $\circ$ denotes a matrix product including 'channel'-space. The boundary conditions read [37]:

$$\mathbf{\Gamma} = \boldsymbol{\gamma}' + \overline{\mathbf{\Gamma}} \circ \tilde{\boldsymbol{\gamma}} \circ \boldsymbol{\gamma}'. \tag{6.24}$$

As discussed in chapter 4, the scattering matrix $S(k_{||}, \varphi_\mathbf{k})$ is related to $S(k_{||}, 0)$ by:

$$S(k_{||}, \varphi_\mathbf{k}) = \Phi S(k_{||}, 0)\Phi^*, \quad \Phi = \begin{pmatrix} e^{-i\sigma_z \varphi_\mathbf{k}/2} & 0_{2\times2} \\ 0_{2\times2} & e^{-i\sigma_z \varphi_\mathbf{k}/2} \end{pmatrix}. \tag{6.25}$$

To achieve consistency with the boundary conditions at the opposite surface (6.21), we assume $\gamma_{2,\varphi} = e^{-i\varphi_\mathbf{k}}\gamma_2$ and $\gamma_{3,\varphi} = e^{i\varphi_\mathbf{k}}\gamma_3$. Moreover, $\gamma_{1,\varphi} = \gamma_1$ and it is easy to see that:

$$\boldsymbol{\gamma} = \Phi^* \circ \boldsymbol{\gamma}_\varphi \circ \Phi^*, \quad \tilde{\boldsymbol{\gamma}} = \Phi \circ \tilde{\boldsymbol{\gamma}}_\varphi \circ \Phi. \tag{6.26}$$

Some simple algebra then shows:

$$\mathbf{\Gamma}_\varphi = \left[\boldsymbol{\gamma}' + \overline{\mathbf{\Gamma}} \circ \tilde{\boldsymbol{\gamma}} \circ \boldsymbol{\gamma}' \right]_\varphi = \Phi \circ \left[\boldsymbol{\gamma}' + \Phi^* \circ \overline{\mathbf{\Gamma}}_\varphi \circ \Phi^* \circ \tilde{\boldsymbol{\gamma}} \circ \boldsymbol{\gamma}' \right] \circ \Phi, \tag{6.27}$$

which implies

$$\mathbf{\Gamma}_\varphi = \Phi^* \circ \mathbf{\Gamma} \circ \Phi^*. \tag{6.28}$$

This result is consistent with the initial assumption and therefore proves that it is indeed a valid solution. The proof is completed by the fact that eq. (6.28) stays the same when $\gamma_{2,3} = 0$ and the observation that the coherence functions inside the FM must have originated from the SC at some point.

We hence showed that a pure $p_x \pm ip_y$ state is induced in a clean FM-layer by the triplet proximity effect, where the different spin-bands have opposite chirality. Whether the +/- state is induced in the majority/minority band or the other way around depends on whether the orientation of the magnetisation in the FM is in the z or $-z$ direction [22]. However, the assumption that the device is in the clean limit is crucial here, as disorder would destroy the bijective correspondence between φ and $\mathbf{k}$ when quasiparticles scatter between different momentum states inside the FM.

Part II.

On the Superconducting Proximity Effect in Surface States of Topological Insulators

7. The Discovery of Topological Insulators

Topological insulators represent a new phase of matter which was first proposed on theoretical grounds by Kane and Mele in 2005 [64, 65]. While the concept of the 'topological insulator' state is very general, their specific proposal was that it may be realised in graphene. However, the spin-orbit interaction which usually drives the transition from the 'trivial' band insulator to the 'topological' one, turned out to be to weak in this material [13]. In 2006, Bernevig et al. [13] predicted that this state may be realised in HgTe/CdTe quantum wells and this finding was experimentally confirmed by König et al. [72], who fabricated (Hg,Cd)Te/HgTe/(Hg,Cd)Te wells and tuned the chemical potential to lie inside the band gap. As predicted by Bernevig and coworkers, they found the longitudinal conductance to be suppressed when the thickness of the HgTe layer was smaller than approximately 6.3 nm, but a conductance of about one conductance quantum was observed when the width exceeded that threshold. It was demonstrated that this value hardly changed for different widths of the well, from which the group concluded that the current must indeed be carried by edge states. The emergence of these edge states at a certain HgTe layer thickness can be understood from the fact that the valence and conduction band of HgTe are inverted with respect to CdTe and that this inversion also happens in the quantum well if the HgTe layer is thick enough. This band inversion, which is driven by spin-orbit coupling, signals the transition from the trivial to the topological insulator [13, 56] and comes along with the edge states that were observed in the experiment.

The fundamental symmetry of the topological insulator is time-reversal invariance. In this regard, another important observation made in the experiment of König et al. was that the residual current could be destroyed by a small magnetic field, confirming the theoretical understanding that the edge states of a topological insulator are protected from elastic backscattering by time-reversal symmetry only [72].

It is instructive to compare this state to the Quantum Hall state [131], as shown in Fig. 7.1. In the Quantum Hall state, edge states counterpropagate on different sides of the sample. The longitudinal current through these states is dissipationless, since backscattering would imply that a quasiparticle must tunnel to the other side of the sample to reach the counterpropagating state. The topological insulator, on the other hand, is time-reversal invariant and this symmetry must hence also apply to its edge states. Consequently, the edge states come in Kramer's pairs of counterpropagating states with opposite spin on both sides of the sample and the robust protection from backscattering does not exist in
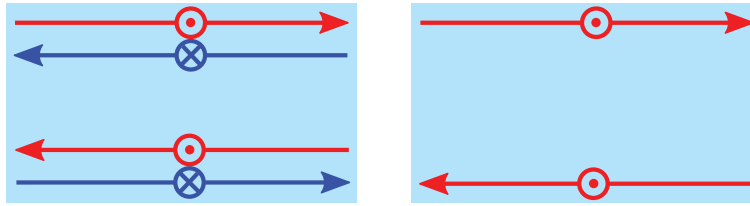
Figure 7.1. – Edge states of a two dimensional topological insulator (Quantum Spin Hall state (QSH)) on the left and of the usual Quantum Hall state on the right. The edge states of the QSH insulator come in pairs on either side of the sample, where states with opposite spin-orientation counterpropagate. In the QH state, the states are spin-polarised due to the magnetic field and counterpropagate on opposite sides of the sample. Figure adapted from Ref. [99].

this case. However, one can show that as long as time-reversal symmetry is maintained, at least elastic backscattering is prohibited [13]. If this symmetry is broken by, for instance, magnetic impurities or a magnetic field, the protection is lost, as demonstrated in the experiment.

Bernevig et al. argued that this state can essentially be understood as two copies of the Quantum Hall state with opposite magnetic field direction [14]. This restores time-reversal symmetry and implies that for any state contributing to the Hall conductance, there is a partner with the opposite contribution, and consequently, the Hall conductance vanishes. Yet, these partners also have opposite spin, which means that the spin-conductance is finite and this state was therefore dubbed Spin Quantum Hall (SQH) state [64, 65, 14]. Naturally, a spin-effect is harder to measure than a charge-effect, but this reasoning does fortunately not apply to the longitudinal current through the edge states which was measured in the experiment.

This initial discovery triggered a massive research activity over the past four years which we are utterly unable to review here. Instead, we refer the reader to two extensive review articles on the subject, authored by Kane and Hasan [56] and Qi and Zhang [101] respectively.

In the following, we will strictly focus on those parts of the story which are relevant to the problem we wish to discuss. Specifically, that is the proximity effect in the surface states of three-dimensional topological insulators. Naturally, these surface states are now two-dimensional and can be characterised as a 'helical metal' with a Dirac cone dispersion at small energies [56]. As stated in the introduction, the interest in this problem is based on the conjecture that proximity induced superconductivity in these states may create an instance of the much sought after $(p_x + ip_y)$-superconductor, which hosts Majorana excitations at vortex cores [47].

To this end, we shortly discuss what the topological order of the topological insulator actually is. We choose the band theoretical approach to this problem [64, 48, 90], which we deem to be the most transparent and – from a practical point of view – most relevant, but also the least general perspective on the matter. Band theory is naturally restraint to the single-particle picture. The interacting case can be covered by the more abstract topological field theory approach [14, 100]. Subsequently, we discuss the nature of the surface states and eventually review existing work on the proximity effect.

7.1. Topological Order in Bloch Theory

Understanding in what sense topological insulators are 'topological' is a rather subtle issue but again quite analogous to the Quantum Hall state, where the connection to topology

was first established by Thouless et al. [125].

In both cases, the physical problem at hand is mapped onto a differentiable manifold which belongs to the special class of fibre bundles. They can be understood as a 'product' of two sub-manifolds, called the base and the fibre. The bundle is then constructed by gluing one copy of the fibre to each point of the base [92]. In the context of our problem, the base is the Brillouin zone (the magnetic Brillouin zone in the case of the Quantum Hall Effect) and the fibre a Hermitian matrix whose dimensionality is given by the number of bands that are considered. For each point $\mathbf{k}$ of the base, the copy of the fibre glued to it is the Bloch-Hamiltonian $H(\mathbf{k})$ [90].[a] The topological order of the physical state can then be understood by analysing the topology of this manifold. Any property of the system which depends only on this topology is robust in the sense that it is invariant under changes of the system's Hamiltonian which result in a smooth deformation of the associated manifold.

Therefore, finding such robust quantities is identical to the mathematician's quest of identifying topological invariants. These have been studied intensively, as they can (not always) provide an answer to the prominent question whether two given topological spaces are equivalent, i.e., can be continuously deformed into each other. To this effect, one tries to find a prescription that associates certain mathematical objects, which do not change under such continuous deformations,[b] to a given topological space. In regard to fibre bundles, an important class of topological invariants are so-called Chern-numbers. In analogy to the Gauss-Bonnet theorem, they are obtained by integrating a certain relation, the Chern-form, over the base of the manifold [92]. In the case of the Quantum Hall effect, the first Chern-number characterises the topological order and has a very immediate connection to the physical problem – it is the quantised Hall conductance [6].[c]

In the case of topological insulators, the relevant manifolds – given by the Bloch-Hamiltonian over the Brillouin zone – are characterised by time-reversal symmetry. For fermionic particles, the time-reversal operator is an anti-unitary operator, and if applied to a time-reversal invariant Bloch-Hamiltonian implies the symmetry [90]:

$$H(-\mathbf{k}) = \Theta H(\mathbf{k})\Theta^{-1}, \tag{7.1}$$

where Θ is the time-reversal operator. Using nothing but this constraint, a topological classification of time-reversal invariant Bloch-Hamiltonian has been provided in arbitrary dimensions, and can also be extended to disordered systems through the classification of replica sigma-models [105]. The topological classes are characterised by $\mathbb{Z}_2$-invariants, i.e., the cyclic group with two elements. In 2 dimensions, a single invariant of this type provides the classification scheme [64, 65], while 4 are required in the 3-dimensional case [90]. This implies that there are 2 topologically distinct classes in 2 dimension and 16 in 3. However, only half of the classes in the 3D case are stable against disorder and therefore called strong topological insulators, while the other half can be deformed to a trivial band-insulator if translational invariance is broken [48].

7.2. Bulk-Boundary Correspondence - Topological Surface States

That time-reversal invariant band insulators fall into different classes whose band structures cannot be deformed continuously into each other would be a highly academic question

---

[a]The fibre at $\mathbf{k}$ can also be considered to be the Hilbert-space spanned by the Bloch-states at $\mathbf{k}$ [56].

[b]This formulation is a bit vague, but in fact, these 'objects' are not always numbers, they may be more complicated algebraic entities. The most prominent example is the homotopy group.

[c]From a pedagogical point of view, this reference is an excellent introduction to the topological perspective on the Quantum Hall effect.

to pursue, if there were no physical phenomena associated to it. As discussed in the beginning of this chapter, the principal feature setting aside the non-trivial from the trivial insulator is the existence of edge or surface states. This can be understood in an intuitive way from the fact that spin-orbit interaction leads to a band inversion of valence and conduction bands in topological insulators, if the band structure without spin-orbit interaction is taken as a reference [13, 141].[a] If an insulator with such an inverted band structure is brought into contact with a non-inverted one – as the vacuum, for instance – the inversion must be undone at the interface, i.e., the bands cross and create states inside the bulk gap that are localised at the surface [56]. Due to time-reversal symmetry, these states always come in pairs of time-reversed partners. The surface states of a three-dimensional topological insulator thus form a two-dimensional metal and were first observed in $Bi_{1-x}Sb_x$ by means of ARPES measurements [58]. The strong topological insulator in three dimensions is characterised by an odd number of surface state dispersions, 5 were observed in the case of $Bi_{1-x}Sb_x$ [58], while Bi_2Se_3 features only one [137]. Generally, one can show that an even number of surface states can always be lifted, i.e., merged and deformed so that the spectrum is fully gapped again, without destroying time-reversal symmetry or closing the bulk-gap. This provides an intuitive understanding of the even/odd-classification, formally encoded in the $\mathbb{Z}_2$-invariant [56].

The low-energy dispersion of these states can be approximated by a Dirac-cone for small energies, whose Dirac-point is pinned to one of the time-reversal invariant points in the Brillouin-zone (the Γ-point, for instance) [56]. An effective surface state Hamiltonian can be derived which has the same structure as that of graphene and describes the surface states close to the Dirac-point. The difference is, however, that the Pauli-matrices appearing in this Hamiltonian now refer to real spin instead of pseudo-spin [56]. This implies that the dispersion of a single-pair of surface states features spin-momentum locking, i.e., for every momentum $\mathbf{k} = (k_x, k_y)$, there is only one state with a definite spin-orientation and the state at $-\mathbf{k}$ has opposite spin-orientation. This was demonstrated experimentally by measuring a suppression of backscattering in the surface states [60]. We will demonstrate the derivation of this surface state Hamiltonian in chapter 10 in terms of the $\mathbf{k} \cdot \mathbf{p}$-Hamiltonian that we introduce in chapter 8.

To conclude, the bulk topological order of topological insulators gives rise to conducting states at their boundary. An odd number of surface state pairs indicates a robust topological phase. The surface states of three-dimensional topological insulators realise a new type of low dimensional conductor, dubbed 'helical metal'.

7.3. The Proximity Effect at the Surface of 3D Topological Insulators

The proximity effect in the helical metal realised at the surface of 3D topological insulators was first investigated by Fu and Kane on the basis of the following model-Hamiltonian [47]:[b]

$$\mathcal{H}_{\text{surface}} = \begin{pmatrix} H_0(\mathbf{k}) & \Delta i\sigma_2 \\ -\Delta^* i\sigma_2 & -H_0^*(-\mathbf{k}) \end{pmatrix}, \quad H_0(\mathbf{k}) = \hbar v_{\text{F}}(k_x\sigma_1 + k_y\sigma_2) - \mu. \quad (7.2)$$

Here, H_0 is the normal state effective Hamiltonian of the surface states, $\Delta i\sigma_y$ is a singlet, s-wave gap and $\mathbf{k} = (k_x, k_y)$. This phenomenological model of the proximity effect is essentially inspired by the theory of McMillan [85], who proposed that the superconducting proximity effect in a thin normal layer can be described by a self-energy. The crucial

---

[a]Switching spin-orbit interaction 'on' or 'off' in a given material is of course only possible in theory.
[b]Note that the Hamiltonian is adapted to our definition of the Nambu-spinor.
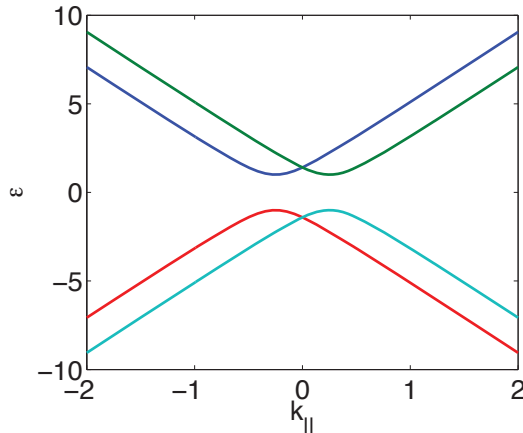
Figure 7.2. – Spectrum of the Fu-Kane Hamiltonian stated in eq. (7.3) for $\hbar v_{\mathrm{F}} = 4$, $\mu = 1.0$, $\Delta = 1.0$.

point for this model to work is that the itinerant states are localised at the interface to the superconductor, only then an effective, homogeneous pair-potential arises due to permanent interactions with the SC.[a] This condition is realised in the original McMillan theory by the assumption that the normal layer is thin. In the case of topological insulators, the relevant states are confined to the interface because they are surface states. The spectrum of the above Hamiltonian is given by [47]:

$$\pm\epsilon_{\pm}(\mathbf{k}) = \sqrt{\Delta^2 + (\mu \pm \hbar v_{\mathrm{F}} k_{||})^2}, \tag{7.3}$$

with $k_{||} = |\mathbf{k}|$ and plotted in Fig. 7.2. We will use it later on to compare this model to our numerical results. Fu and Kane argued that the state characterised by this Hamiltonian is an instance of a topological superconductor. To see this, one rewrites the Hamiltonian in a basis that diagonalises $H_0(\mathbf{k})$ and finds that the pairing-term acquires the form of a $p_x + ip_y$ order parameter, the Fu-Kane Hamiltonian thus corresponds to a time-reversal invariant $p_x + ip_y$ superconductor [47]. Topological superconductors can be classified in full analogy to topological insulators if a mean-field perspective is adopted [110, 105]. According to this general classification scheme, their defining property is that they feature protected boundary modes which cannot be localised by disorder, too. However, Fu and Kane argue that their model was already the boundary of a 3D material and could therefore not have a boundary of its own [47]. Instead, they pursue a number of different proposal for creating Majorana quantum wires and bound states by manufacturing different types of junctions on the TI. Majorana fermions play an important role in topological quantum computation [93], and the Fu-Kane proposal attracted a lot of attention in this context. The question we address here, namely whether the model of the proximity effect assumed at the outset of this argument is valid, is certainly more modest but nonetheless important, as a proper understanding of the superconducting proximity effect in such surface states is a prerequisite for any ulterior proposal based on it.

Stanescu et al. [121] were the first to consider a microscopic model of this problem based on a three-dimensional tight-binding Hamiltonian of the TI-SC heterostructure. The spectrum of this Hamiltonian was then calculated with exact diagonalisation. This is obviously only possible for a finite sized system of relatively small dimensions, which implies that finite size effects cannot be avoided unless the interface states are strongly localised. The

---

[a]Note that this reflects our current understanding of this model and not necessarily that of Fu and Kane, who did not comment on that question in their original article.

localisation of these states on either side of the interface is controlled by the magnitude of the respective gap. While the band gap of topological insulators can be larger than 0.1 eV [58], the gap energy of conventional superconductors is a lot smaller than that. This implies that the interface states will extend on the scale of the coherence length into the SC. Stanescu et al. did, however, assume a superconducting gap of the order of the TI band gap, and thus avoided this problem in their calculation. They also showed that the proximity effect can indeed be understood in terms of McMillan-theory by explicitly calculating the effective self-energy of the superconductor from a Green's function formalism. A general analytical discussion of this procedure was provided at about the same time by Sau et al. [108].

A second analysis was performed by Lababidi and Zhao [74] in the BdG-framework. They used the $\mathbf{k} \cdot \mathbf{p}$-Hamiltonian of Bi_2Se_3 as a model for the TI. We shall see in the next chapter, that this is a two-orbital model. Hence, they also had to assume a second band in their superconductor model to maintain the same Hilbert-space dimensionality throughout the structure. The interface was then simply modelled by a step-function crossover from the TI to the SC. Rather than matching wave functions at the interface, they employed the numerical method of Halterman and Valls [55] to solve this model. At least the starting point of this investigation is quite similar to our approach and we will thus get back to this work when discussing our approach. Lababidi and Zhao assumed a realistic energy scale for the SC gap and also carried out a self-consistent calculation of the gap profile inside the SC. They also claim that their study was complementary to that of Stanescu et al., since the latter was restrained to the tunnelling limit. We do not quite agree with that, since a transfer-Hamiltonian approach is not necessarily a tunnelling theory. That is only true if the coupling through the transfer-Hamiltonian is treated as a perturbation, which is not the case in the work of Stanescu et al., given that they used exact diagonalisation.

The model we consider here is based on a real space discretisation of the $\mathbf{k} \cdot \mathbf{p}$-Hamiltonian of Bi_2Se_3, Bi_2Te_3 and Sb_2Te_3 [80] and the BCS mean-field Hamiltonian. Thanks to translational invariance in the contact plane, this discretisation must only be carried out in the z-direction, since $\mathbf{k}_{||} = (k_x, k_y)$ is a conserved quantum number. The coupling between the two materials is modelled by a transfer-Hamiltonian and we employ the recursive Green's function technique to solve it [54]. This is a non-perturbative approach which allows us to consider an infinite tight-binding model and hence avoid potential finite size effects. This comes at the expense of not being able to calculate the eigenstates of the tight-binding model, but only the spectral function. This is, however, sufficient to obtain the dispersion of the surface states and calculate the effective self-energy that enters the phenomenological model. In agreement with the earlier studies discussed above, we find that the Fu-Kane model is a reasonable low-energy theory if the coupling between the SC and the TI is small or intermediate and that it can be recovered from our theory if the coupling to the superconductor is approximated by the zero-energy and zero-momentum value of the superconductor self-energy. However, the phenomenological model is not valid at energies close to the superconducting bulk-gap, and we also show that if the coupling is strong, the Fu-Kane model breaks down completely. In that case, the energy and momentum dependence of the self-energy must be retained as first argued by Sau et al. [108].[a] The spatial profile of the interface states is analysed and, not surprisingly, we find that they extend on the scale of the superconducting coherence length into the SC. We also discuss how a self-consistent calculation can be carried out in this formalism.

Finally, we shortly comment on the few experimental achievements that have been reported so far in regard to superconductivity in topological insulators. Very recently, Bi_2Se_3 with intercalated Cu was found to be a superconductor with a T_c of about 3K [107, 73]. While

---

[a]If, $E_F \gg \Delta$, the momentum dependence can still be ignored.

specific heat data was interpreted to point towards a fully gapped order parameter [73], recent point-contact measurements found a zero-bias conductance peak [107], which must be taken as an indication of unconventional superconductivity and the presence of an Andreev bound state at the interface. The authors claim that this in-gap state was a signature of helical Majorana Fermions at the surface of the SC. These are exciting findings, but further investigations are necessary to understand the superconducting order in this material.

Concerning the proximity effect, Josephson currents were very recently observed at the surface of Bi_2Se_3 [106, 140]. While Sacepe et al. report a gate-tunable supercurrent through a thin Bi_2Se_3 crystal contacted with Al/Ti electrodes [106], Zhang et al. investigate Bi_2Se_3 nanoribbons with tungsten as the superconductor [140] and find a Josephson coupling over a distance of ≈ 580nm, which, they argue, points towards a supercurrent carried by ballistic surface states.

We did not investigate transport so far, but this is evidently an important question to address and we do believe that the method used here to study a microscopic model of the proximity effect in topological insulators can be of use in this regard, too.

8. The Model Hamiltonian

In this chapter, we introduce the tight-binding Hamiltonian that we use to model the superconductor-topological insulator heterostructure. The tight-binding models of the respective bulk-materials are obtained from a finite differences discretisation of the continuum models, being a $\mathbf{k} \cdot \mathbf{p}$-Hamiltonian for the topological insulator and the standard mean-field BCS-Hamiltonian for the superconductor. The interface is modelled by a transfer-Hamiltonian. The whole Hamiltonian is extended to Nambu-space, which allows us to apply the recursive Green's function technique to it in a straight-forward manner.

8.1. $k \cdot p$-Hamiltonian of Bi$_2$Se$_3$, Bi$_2$Te$_3$ and Sb$_2$Te$_3$ in Nambu-space

We consider a specific class of 3D topological insulators which are binary compounds made of Bi or Sb as the first and Te or Se as the second element. These materials were first predicted to belong to the topologically non-trivial class in [141] on the basis of first principle band structure calculations. In the same article, a $\mathbf{k} \cdot \mathbf{p}$-Hamiltonian fitted to the DFT band-structure was provided, which involves only those orbitals that are relevant for the topological surface states. In a later publication [80], this model Hamiltonian was further elaborated on, and we shall use it as the starting point for our model of the TI-SC device. We call it the Zhang-model in the following.

The Zhang-model is a low energy-theory fitted to the band structure around the Γ-point up to third order in $\mathbf{k}$. The relevant states are the hybridised p_z orbitals of Bi or Sb and Se or Te, respectively. These have definite (and opposite) parity and the basis can hence be labeled as $|+\uparrow\rangle$, $|-\uparrow\rangle$, $|+\downarrow\rangle$, $|-\downarrow\rangle$, where $\pm$ denotes the orbital and $\uparrow, \downarrow$ the spin [141]. In addition to that, including superconductivity will require to extend this Hamiltonian to Nambu space. Thus, we consider a Hamiltonian acting on a 8 dimensional vector space given by the direct product particle-hole⊗spin⊗orbital, in this order. As a basis of the 8×8 matrices above this space, we define

$$\left\{ \tau_j \otimes \sigma_k \otimes \nu_l \mid i, j, k \in \{0, 1, 2, 3\} \right\}, \tag{8.1}$$

where $i, j, k = 0$ refers to the respective 2×2 identity matrix and the other values to the corresponding Pauli-matrices. We define the Nambu-spinor as:

$$\mathcal{C}_{\mathbf{k}} = \begin{pmatrix} b_{\mathbf{k}} & b_{-\mathbf{k}}^\dagger \end{pmatrix}^T, \tag{8.2}$$

with

$$b_{\mathbf{k}} = \begin{pmatrix} c_{c+,\uparrow}(\mathbf{k}) & c_{+,\uparrow}(\mathbf{k}) & c_{-,\downarrow}(\mathbf{k}) & c_{-,\downarrow}(\mathbf{k}) \end{pmatrix}^T. \tag{8.3}$$

The Nambu-Hamiltonian $\mathcal{H}_{\mathrm{TI}}(\mathbf{k})$ is then defined by demanding:

$$\sum_{\mathbf{k}} b_{\mathbf{k}}^{\dagger} H_{\mathrm{TI}}(\mathbf{k}) b_{\mathbf{k}} = \frac{1}{2} \sum_{\mathbf{k}} \mathcal{C}_{\mathbf{k}}^{\dagger} \mathcal{H}_{\mathrm{TI}}(\mathbf{k}) \mathcal{C}_{\mathbf{k}}, \tag{8.4}$$

where $H_{\mathrm{TI}}(\mathbf{k})$ is the Zhang-Hamiltonian. It is important to understand that the $\mathbf{k} \cdot \mathbf{p}$-Hamiltonian describes only the subset of Bloch-states with momentum $\mathbf{k}$. The total Hamiltonian of the system is hence given by the left-hand side of the above equation. The right-hand side then implies that $\mathcal{H}_{\mathrm{TI}}(\mathbf{k})$ corresponds to two copies of the original Hamiltonian once the sum is taken over all $\mathbf{k}$. This is because we consider two copies of the system, one from the 'hole' and one from the 'particle' perspective. In his original proposal [91], Nambu was able to exploit the particular structure of the BCS-Hamiltonian to avoid this double counting by considering spin-up quasiparticles from the particle and spin-down quasiparticles from the 'hole'-perspective only. The structure of the Hamiltonian in particle-hole space is now straightforwardly derived from eq. (8.4):

$$\mathcal{H}_{\mathrm{TI}}(\mathbf{k}) = \begin{pmatrix} H_{\mathrm{TI}}(\mathbf{k}) & 0 \\ 0 & -H_{\mathrm{TI}}^{T}(-\mathbf{k}) \end{pmatrix}. \tag{8.5}$$

What remains is, obviously, the $\mathbf{k} \cdot \mathbf{p}$-Hamiltonian itself. In terms of the matrices:

$$\begin{aligned} \gamma_0 &= \sigma_0 \otimes \nu_0, & \gamma_1 &= \sigma_0 \otimes \nu_3, & \gamma_2 &= \sigma_3 \otimes \nu_1, \\ \gamma_3 &= \sigma_1 \otimes \nu_1, & \gamma_4 &= \sigma_2 \otimes \nu_1, & \gamma_5 &= \sigma_0 \otimes \nu_2, \end{aligned} \tag{8.6}$$

the Hamiltonian reads [80]:

$$\begin{aligned} H_{\mathrm{TI}}(\mathbf{k}) =& \epsilon_0(\mathbf{k})\gamma_0 + \mathcal{M}(\mathbf{k})\gamma_1 + \mathcal{B}(k_z)k_z\gamma_2 + \mathcal{A}(k_{||})[k_x\gamma_3 + k_y\gamma_4] \\ & - \frac{R_1(k_+^3 + k_-^3)}{2}\gamma_5 - i\frac{R_2(k_+^3 - k_-^3)}{2}\gamma_2, \end{aligned} \tag{8.7}$$

with the following parameters:

$$\begin{aligned} k_{\pm} &= k_x \pm i k_y & k_{||}^2 &= k_x^2 + k_y^2 & \epsilon_0(\mathbf{k}) &= C_0 + C_1 k_z^2 + C_2 k_{||}^2 \\ \mathcal{M}(\mathbf{k}) &= M_0 + M_1 k_z^2 + M_2 k_{||}^2 & \mathcal{A}(k_{||}) &= A_0 + A_2 k_{||}^2 & \mathcal{B}(k_z) &= B_0 + B_2 k_z^2. \end{aligned} \tag{8.8}$$

It contains terms up to third order in $\mathbf{k}$. We will mainly be interested in very small values of $\mathbf{k}$. Thus, keeping terms up to second order only will be sufficient for our purpose. The Hamiltonian can either be obtained from $\mathbf{k} \cdot \mathbf{p}$-theory or from the theory of invariants, i.e. the representation theory of the relevant crystal point group [80]. The values of the constants are given in Ref. [80], the model may be used for Bi_2Se_3, Bi_2Te_3 and Sb_2Te_3 and was shown to provide reasonable fits for small values of $\mathbf{k}$ [80]. To keep the length of this thesis within reasonable limits, we refrain from an extensive discussion of the theory and material properties behind this model Hamiltonian and refer the reader to Ref. [141, 80] for further details.

8.2. Tight-binding Discretisation

With $\mathcal{H}_{\mathrm{TI}}(\mathbf{k})$, we now dispose of a continuum model of the topological insulator which is sufficient for the energy scale that we are interested in and directly connected to real materials. However, when considering a TI-SC heterostructure, we break the translational

invariance of the crystal in at least one direction. If we assume a layered structure in the z-direction, translational invariance in the x-y-plane can be assumed to be maintained and k_x, k_y are still good quantum numbers. For k_z on the other hand, we need to make the replacement [80]:

$$k_z \mapsto -i\partial_z, \qquad (8.9)$$

which simply results from tracing back the action of the original differential operator on the plane wave ansatz e^{ik_z}. This obviously implies that $\mathcal{H}_{\mathrm{TI}}(k_x, k_y, \partial_z)$ becomes a Hermitian differential operator in the z-direction, while k_x and k_y can still be treated as parameters. We now discretise this operator on a 1-dimensional lattice following the standard procedure [27]. The Hamiltonian contains first-order and second-order derivatives with respect to z if we consider terms up to second order in $\mathbf{k}$ only. We define the action of the corresponding discretised operators on the lattice wave function by:

$$\partial_z \psi_n = \frac{\psi_{n+1} - \psi_{n-1}}{2a}, \quad \partial_z^2 \psi_n = \frac{\psi_{n+1} - 2\psi_n + \psi_{n-1}}{a^2}, \qquad (8.10)$$

where a is the lattice spacing. Note that to obtain next-neighbour couplings only, we implicitly used a lattice spacing of $a/2$ rather than a for discretising ∂_z^2. As long as a is chosen sufficiently small, this is of no relevance and only means that the approximation for ∂_z^2 is a bit better than for ∂_z.

We hence obtain the following tight-binding (TB) Hamiltonian, if terms up to second order in $\mathbf{k}$ are kept:[a]

$$\mathcal{H}_{TI}(k_x, k_y) = \sum_n \mathcal{O}_{\mathrm{TI}}(k_x, k_y)|n\rangle\langle n| + \mathcal{V}_{\mathrm{TI}}|n+1\rangle\langle n| + \mathcal{V}_{\mathrm{TI}}^\dagger|n\rangle\langle n+1|, \qquad (8.11)$$

with:

$$\begin{aligned}
\mathcal{O}_{\mathrm{TI}}(k_x, k_y) =&(C_0 + C_2 k_{||}^2)\gamma_0 + (M_0 + M_1 k_{||}^2)\gamma_1 \\
&+ A_0[k_x \gamma_3 + k_y \gamma_4] - 8t^2[M_1 \gamma_1 + C_1 \gamma_0], \\
\mathcal{V}_{\mathrm{TI}} =&tB_0 \gamma_2 + 4t^2[M_1 \gamma_1 + C_1 \gamma_0],
\end{aligned} \qquad (8.12)$$

and $t = -i/2a$. Analogously, a discretisation of the standard BCS-Hamiltonian in Nambu-space,[b]

$$\mathcal{H}_{\mathrm{SC}}(\mathbf{k}) = \begin{pmatrix} \xi(\mathbf{k}) & -\Delta i\sigma_2 \\ \Delta i\sigma_2 & -\xi(\mathbf{k}) \end{pmatrix}, \qquad (8.13)$$

with $\xi = \hbar^2 \mathbf{k}^2 / 2m$, is obtained:

$$\mathcal{H}_{SC}(k_{||}) = \sum_n \mathcal{O}_{\mathrm{SC}}(k_{||})|n\rangle\langle n| + \mathcal{V}_{\mathrm{SC}}|n+1\rangle\langle n| + \mathcal{V}_{\mathrm{SC}}^\dagger|n\rangle\langle n+1|. \qquad (8.14)$$

Here, we have:

$$\begin{aligned}
\mathcal{O}_{\mathrm{SC}}(k_{||}) =& \frac{\hbar^2}{2m}(k_{||}^2 - 8t^2)\tau_3 \otimes \sigma_0 + \Delta \tau_2 \otimes \sigma_2, \\
\mathcal{V}_{\mathrm{SC}} =& \frac{2\hbar^2 t^2}{m}\tau_3 \otimes \sigma_0.
\end{aligned} \qquad (8.15)$$

---

[a]Note that the tight-binding approach proposed here was also used by Zhao et al. [145] to obtain the spectral function and S-Matrix of a topological insulator/normal metal interface.

[b]Also called Bogoliubov-de-Gennes Hamiltonian.

The final step of our modelling now consists in coupling the two tight-binding Hamiltonians $\mathcal{H}_{\mathrm{TI}}(k_x, k_y)$ and $\mathrm{H}_{\mathrm{SC}}(k_{||})$ at the interface. This is done by specifying the hopping-elements between the final site of the TI tight-binding chain and the first site of the SC tight-binding chain. One thus obtains a Hamiltonian of the complete SC-TI heterostructure, i.e., instead of solving the two systems individually and matching the solutions by means of boundary conditions, we will solve the entire structure and such conditions are not required. Evidently, this comes at the expense of having to choose a transfer-Hamiltonian, that is, the aforementioned hopping elements.

8.3. Interface Model: Transfer-Hamiltonian Approach

So far, the individual tight-binding Hamiltonians of the respective subsystem have been derived from the corresponding continuum models, and in principle, these can be recovered when the lattice constant is tuned to zero. The standard way of describing an interface in the tight-binding framework is to introduce a tunnelling or transfer-Hamiltonian, that is to say, specify hopping elements that connect the two tight-binding Hamiltonians describing the respective bulk-systems. In this section, we introduce such a transfer-Hamiltonian for our model. The choice is in principle ad hoc, but it allows us to describe both strong and weak coupling between the TI and the SC, as we will show in the results section.

An alternative but comparable approach to this problem was considered by Lababidi and Zhao [74]. It's starting point is a continuum Hamiltonian of the SC-TI structure. It consists of the Zhang-Hamiltonian on the TI-side and a SC-model, which is obtained from the Zhang-Hamiltonian by putting $B_0 = A_0 = 0$ and assuming a singlet-pair potential in the '+'-orbital. This effectively corresponds to a two band Hamiltonian with a conduction band formed by the '+'-orbital and a split-off valence band formed by the '−'-orbital. This 'trick' is required since the TI and SC part of the structure must share the same Hilbert-space in this approach. The Fermi-energy is then chosen so that it lies deep inside the conduction band, and the valence band is essentially irrelevant. As in our case, the model is transformed to a real space coordinate in the z-direction and the transition from the TI to the SC part is simply modelled by a change of the Hamiltonian with a functional dependence proportional to $\Theta(z)$. The solution of this problem is then calculated with the method of Halterman and Valls, which relies on expanding the eigenfunctions of the Hamiltonian in a complete basis set of wave functions in a certain energy range [55]. In a sense, this corresponds to a discretisation in k-space, while we discretise in real space.

Irrespective of the specific model used to the describe the interface, there will be a spatial variation of the Hamiltonian. If this only applied to those parameters which are independent of k_z, this would not pose a problem at all, as only the on-site components of the TB-Hamiltonian acquire a z- or, equivalently, n-dependence in that case, while the hopping elements are the same everywhere.[a]

In the case we consider here, however, the switching between the two Hamiltonians requires a symmetrisation of the terms containing the derivative ∂_z to maintain the hermiticity of the Hamiltonian. We hence have to deal with symmetrised operators of the general form:

$$\chi(z)\partial_z \mapsto \frac{1}{2}\Big(\chi(z)\partial_z + \partial_z\chi(z)\Big) \tag{8.16}$$
$$\chi(z)\partial_z^2 \mapsto \partial_z\chi(z)\partial_z,$$

where χ can be assumed to be a real function. The symmetrisation of the operator containing the second derivative is only unique if $\chi(z)$ is linear in z. Otherwise, there is an infinite number of choices. Note that Lababidi and Zhao circumvent the symmetrisation

---

[a]This is, for instance, true for the model we used to describe the SC/FM interface, cf. appendix C.

of the second derivative operators by assuming that the corresponding parameters of the Zhang-Hamiltonian do not change at all (only B_0 and A_0 change).

If $\chi(z)$ is a smooth function, we can obtain a discretised Hamiltonian of the whole structure which has a proper continuum limit. In this case, the discretised operators read:

$$\frac{1}{2}(\partial_z\chi(z) + \chi(z)\partial_z) = \frac{1}{2a}\sum_n |n+1\rangle\langle n| \otimes \overline{\chi}_n + \text{h.c.}, \tag{8.17}$$

$$\partial_z\chi(z)\partial_z = \frac{1}{a^2}\sum_n \Big(|n+1\rangle\langle n| - |n\rangle\langle n| - |n+1\rangle\langle n+1| + |n\rangle\langle n+1|\Big) \otimes \overline{\chi}_n,$$

with $\overline{\chi}_n = \frac{1}{2}(\chi_{n+1} + \chi_n)$.[a] Such a continuum model can be used for studying structures where an interface region of finite size is included. However, we found that this generically yields a weak coupling and is hence less interesting. We can still use this result to propose a choice for the hopping elements between the final TI-site N and first SC-site $N+1$ within our model. Inspired by the fact that the arithmetic average $\overline{\chi}_n$ enters the hopping elements between neighbouring sites, we propose the transfer-Hamiltonian [54]:

$$\mathcal{H}_{\mathrm{T}} = \mathcal{T}|N+1\rangle\langle N| + \mathcal{T}^\dagger|N\rangle\langle N+1|, \tag{8.18}$$

with

$$\mathcal{T} = \frac{t}{2}\left(\mathcal{P}\mathcal{V}_{\mathrm{TI}} + \mathcal{V}_{\mathrm{SC}}\mathcal{P}\right). \tag{8.19}$$

Here, we introduced the projector $\mathcal{P}$, which projects the single band of our SC-model onto the '+'-orbital of the Zhang-Hamiltonian. More precisely, we have:

$$\mathcal{P} = \begin{pmatrix} 1 & 0 & 0 & 0 & 0 & 0 & 0 & 0 \\ 0 & 0 & 1 & 0 & 0 & 0 & 0 & 0 \\ 0 & 0 & 0 & 0 & 1 & 0 & 0 & 0 \\ 0 & 0 & 0 & 0 & 0 & 0 & 1 & 0 \end{pmatrix}. \tag{8.20}$$

This is required to match the different on-site Hilbert-spaces of the two semi-infinite tight-binding chains. Alternatively, one may use the same superconductor model as Lababidi and Zhao, but including a 'dummy' band is not necessary in our approach and changes the results only quantitatively. The same is true if a coupling to the second orbital is included in the choice of $\mathcal{P}$. Lababidi and Zhao argued that coupling the SC to the '+'-orbital would correspond to using Cu doped Bi_2Se_3 as a superconductor. However, the superconducting order in this compound is still under investigation and the order-parameter symmetry is not clear as of yet [107].

The dimensionless parameter t allows us to tune the coupling between the SC and TI. We will see that with this choice of $\mathcal{T}$, the system can be tuned from the weak-coupling to the strong-coupling regime as a function of t. We call $\mathcal{H}_{\mathrm{T}}$ transfer-Hamiltonian rather than tunnelling-Hamiltonian to underline that our approach is not perturbative in $\mathcal{T}$ and therefore not restrained to the weak-coupling limit. It may also be possible to derive such a transfer-Hamiltonian from the step-function switching assumed by Lababidi and Zhao. In that case, a δ-function would appear in the symmetrised operators, which one could, for instance, approximate by a box.

---

[a] Here again, a lattice spacing of $a/2$ was used to discretise the second operator. This results in $\chi_{n+1/2}$ rather than $\overline{\chi}_n$ appearing in the second equation – but the first can be approximated by the latter.
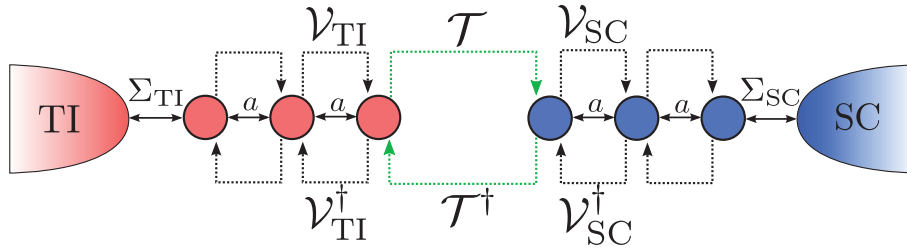
Figure 8.1. – Sketch of the tight-binding model used here to describe the SC-TI heterostructure. The two semi-infinite tight-binding chains of the TI and SC are coupled by a transfer-Hamiltonian. Eventually, we consider only a small number of sites explicitly, which are coupled through self-energies (Σ_{SC}, Σ_{TI}) to semi-infinite leads. Figure from Ref. [54].

8.4. Transformation under Rotations in the x-y-Plane

The tight-binding Hamiltonian depends parametrically on $(k_x, k_y) = \mathbf{k}_{||}$. To ease numerical effort, it is advantageous to exploit the symmetry of the Hamiltonian under rotations in the x-y-plane.[a] All terms depending on $k_{||}$ only are obviously invariant under these rotations, but terms proportional to $k_\pm$ transform non-trivially. In polar coordinates, we have $k_\pm = k_{||} e^{\pm i\varphi}$. These terms only appear in $\mathcal{O}_{\mathrm{TI}}(k_{||}, \varphi)$, and it is easy to see that:

$$\mathcal{O}_{\mathrm{TI}}(k_{||}, \varphi) = \mathcal{U}_{\mathrm{TI}} \left[\mathcal{O}_{\mathrm{TI}}(k_{||}, 0) \right] \mathcal{U}_{\mathrm{TI}}^\dagger, \tag{8.21}$$

with

$$\mathcal{U}_{\mathrm{TI}} = \nu_0 \otimes e^{-i\varphi\sigma_3} \otimes \frac{\tau_0 + \tau_3}{2} + \nu_0 \otimes e^{i\varphi\sigma_3} \otimes \frac{\tau_0 - \tau_3}{2}, \tag{8.22}$$

holds. $\mathcal{U}_{\mathrm{TI}}$ is unitary and the transformation in equation (8.21) is a similarity transformation. From this 'local' relation, we must now construct a transformation of the full tight-binding Hamiltonian. Since $\mathcal{V}_{\mathrm{TI}} = \mathcal{U}_{\mathrm{TI}} \mathcal{V}_{\mathrm{TI}} \mathcal{U}_{\mathrm{TI}}^\dagger$, the TB-Hamiltonian of a finite TI-slab abides the following transformation rule:

$$\mathcal{H}_{\mathrm{TI}}(k_{||}, \varphi) = U_{\mathrm{TI}} \mathcal{H}_{\mathrm{TI}}(k_{||}, 0) U_{\mathrm{TI}}^\dagger, \quad U_{\mathrm{TI}} = \sum_n \mathcal{U}_{\mathrm{TI}} |n\rangle \langle n|. \tag{8.23}$$

The SC-part, on the other hand, is in principle fully invariant under these rotations. Still, to obtain a global unitary transformation that leaves the transfer-Hamiltonian, which is independent of $\mathbf{k}_{||}$, invariant, we have to apply a transformation here, too. Specifically, we propose:

$$\mathcal{U}_{\mathrm{SC}} = e^{-i\varphi\sigma_3} \otimes \frac{\tau_0 + \tau_3}{2} + e^{i\varphi\sigma_3} \otimes \frac{\tau_0 - \tau_3}{2}. \tag{8.24}$$

We then have:

$$\mathcal{H}_{\mathrm{SC}}(k_{||}) = U_{\mathrm{SC}} \mathcal{H}_{\mathrm{SC}}(k_{||}) U_{\mathrm{SC}}^\dagger, \quad U_{\mathrm{SC}} = \sum_n \mathcal{U}_{\mathrm{SC}} |n\rangle \langle n|, \tag{8.25}$$

for a finite SC-slab, i.e., the transformation leaves the SC-Hamiltonian invariant as required. We now straightforwardly define:

$$U = \sum_{n=1}^{J} \mathcal{U}_{\mathrm{TI}} |n\rangle \langle n| + \sum_{n=J+1}^{N} \mathcal{U}_{\mathrm{SC}} |n\rangle \langle n|, \tag{8.26}$$

---

[a]This reasoning is inspired by Lababidi and Zhao, who applied it to their continuum model.

where J is the site of the TI next to the interface. Since $\mathcal{T} = \mathcal{U}_{\mathrm{SC}}\mathcal{T}\mathcal{U}_{\mathrm{TI}}^{\dagger}$, we then have:

$$\mathcal{H}(k_{\parallel}, \varphi) = U\mathcal{H}(k_{\parallel}, 0)U^{\dagger}. \tag{8.27}$$

A consequence of this symmetry is that the spectrum of the Hamiltonian is invariant under rotations in the x-y-plane. When calculating the dispersion of the surface states, it is thus sufficient to consider a single cut along any axis in the plane. All quantities we calculate will be obtained from the retarded Green's function of this Hamiltonian:

$$\mathcal{G}(\epsilon, k_{\parallel}, \varphi) = (\epsilon + i\eta - \mathcal{H}(k_{\parallel}, \varphi))^{-1}, \tag{8.28}$$

for which the above relation implies:

$$\mathcal{G}(\epsilon, k_{\parallel}, \varphi) = U\mathcal{G}(\epsilon, k_{\parallel}, 0)U^{\dagger}. \tag{8.29}$$

Note that this symmetry only pertains to the second order Zhang-Hamiltonian. If the third order in **k** terms are retained, the surface state dispersion will show hexagonal warping.

8.5. Choice of Parameters

For our calculations, we choose the parameters of Bi_2Se_3 for the $\mathbf{k} \cdot \mathbf{p}$-Hamiltonian. These are [80]: $C_0 = -0.2343$ eV, $C_1 = 5.74$ eVÅ^2, $C_2 = 30.4$ eVÅ^2, $M_0 = -0.28$ eV, $M_1 = 6.86$ eVÅ^2, $M_2 = 44.5$ eVÅ^2, $A_0 = 3.33$ eVÅ, $B_0 = 2.26$ eVÅ. The value of C_0 was shifted from its literature value of -0.0083 eV to move the chemical potential to the Dirac-point of the surface state. A lot of topological insulators are actually not insulators when naturally grown, i.e., their chemical potential is in the conduction band and must be tuned to lie inside the band gap by gating [20] or chemical doping [59], if one wishes to access surface state physics in transport. Our results only depend quantitatively on that choice, as long as the chemical potential lies inside the gap.[a] As we shall see, the proximity coupling will shift the surface state dispersion anyway.

For the superconductor, we choose a Fermi-energy of $E_F = 0.4$ eV, to model a metal. The effective mass of the conduction electrons is chosen to be the free electron mass, $\hbar^2/2m = 3.81$ eVÅ^2. Changing these parameters only affects our results quantitatively. In particular, the value of t in the transfer-Hamiltonian for which ideal coupling is achieved depends on these parameters.

---

[a]One may object that as long as we consider a band structure only and not its occupation, there is no point in talking about a chemical potential. However, the BCS-Hamiltonian that we couple to the TI implicitly introduces a chemical potential by specifying the position of the superconducting energy gap.

9. Recursive Green's Function Technique in the Superconducting State

9.1. A Quick Tour of the RGF-technique

The Recursive Green's Function (RGF) technique is a standard tool for transport calculations in mesoscopic physics [44]. It is based on the finite differences method for solving the Schrödinger equation [27], i.e. tight-binding discretisations as the one discussed in the previous section. We use a recent extension of this method [86, 87], that allows us to calculate the local spectral function and also adopt the notation of Metalidis [86]. The fundamental object of this formalism is the retarded Green's function of the tight-binding Hamiltonian, which can formally be defined as [86]:

$$G(E) = (E + i\eta - H)^{-1}. \tag{9.1}$$

We omit the 'R', since the retarded Green's function is the only one we need, G^{A} is simply obtained from $G^{\mathrm{A}} = [G^{\mathrm{R}}]^{\dagger}$. This definition of the Green's function is only sensible for a single-particle Hamiltonian, i.e., if interactions are ignored or described at the mean-field level, as it is the case here.

Obviously, G has the same size as the Hamiltonian H. However, for the calculation of observables like the current density or the density of states, only certain matrix-elements of G in site-space are required:

$$G_{n,m} = \langle n|G|m \rangle. \tag{9.2}$$

Specifically, these are the elements $G_{n,n}$ for the spectral function and if currents are to be calculated within the Landauer-Büttiker framework, the matrix elements between sites on the respective leads are required [86].

We now turn to the fundamental equation which makes this formalism tick. Consider

$$H = h + V, \quad g = (E + i\eta - h)^{-1}, \tag{9.3}$$

i.e., we assume that H is the sum of a Hamiltonian h, of which we know the Green's function, and some perturbation V. Some simple algebra then shows that the Green's function of the full Hamiltonian can be obtained from [44]:

$$G = g + gVG. \tag{9.4}$$
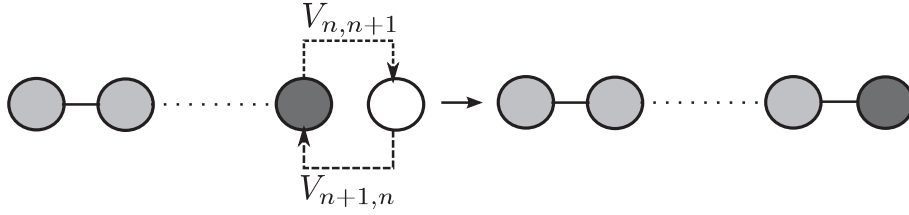
Figure 9.1. – The sketch depicts the calculation of $G^{\mathrm{L}}_{n+1,n+1}$. Grey sites are sites that have already been connected, the dark grey site is the site j of the connected subsystem of which we know $G^{\mathrm{L}}_{j,j}$. Figure adapted from Ref. [86].

This is a Dyson-type equation that one can use to successively obtain the desired elements of G by gluing together disconnected parts of the system, which is the fundamental idea behind the RGF technique [44, 86].

We are interested in spectral properties of the system and the local spectral function is obtained as usual:

$$A_n(\mathbf{k}_{||}, \epsilon) = -\frac{1}{\pi a} \mathrm{Im}\ \mathrm{Tr}[\langle n|G|n\rangle], \quad \mathbf{k}_{||} = (k_x, k_y), \tag{9.5}$$

assuming that the system is discretised in one dimension only, as it is the case here. The factor $1/a$ stems from the fact that the projection of G on the site n is not perfectly local, i.e., the site carries a spatial weight, which is exactly the lattice constant in one dimension. One can check that if the factor $1/a$ is included, $A_n(\mathbf{k}_{||}, \epsilon)$ is invariant under changes of a in an infinite system and coincides with the local spectral function of the corresponding continuum model.

Consequently, only the diagonal elements in site-space $G_{n,n}$ are of interest, and the recursive scheme for their calculation is the following. First, one calculates the Green's function of the isolated individual sites [86]:

$$G^{\mathrm{isol}}_n = (\epsilon + i\eta - O_n)^{-1}. \tag{9.6}$$

Here, O_n is the on-site part of the TB-Hamiltonian at site n.

Subsequently, Green's functions $\mathcal{G}^{\mathrm{L}}_{n,n}$ and $\mathcal{G}^{\mathrm{R}}_{n,n}$ are calculated by starting from the left or the right end of the TB-chain respectively and adding single sites successively.[a] The recursive scheme for their calculation is [86]:

$$G^{\mathrm{L}}_{n+1,n+1} = [1 - G^{\mathrm{isol}}_{n+1,n+1} V_{n+1,n} G^{\mathrm{L}}_{n,n} V_{n,n+1}]^{-1} G^{\mathrm{isol}}_{n+1,n+1}, \tag{9.7}$$

$$G^{\mathrm{R}}_{n,n} = [1 - G^{\mathrm{isol}}_{n,n} V_{n,n+1} G^{\mathrm{R}}_{n+1,n+1} V_{n+1,n}]^{-1} G^{\mathrm{isol}}_{n,n}.$$

These relations can easily be proven from equation (9.4) by projecting it on the relevant sites. A subtlety here[b] is that $G^{\mathrm{L}}_{n,n}$ always refers to the Green's function of the subsystem that has been connected so far, i.e., in $G^{\mathrm{L}}_{n,n}$ and $G^{\mathrm{L}}_{n+1,n+1}$ the G^{L} are not the same, they refer to different Hamiltonians (see Fig. 9.1). The notation is still unique in the sense that for each subsystem, we only know the Green's function at its final site.

Eventually, we obtain $G_{n,n}$ from the relation [86]:

$$G_{n,n} = [1 - G^{\mathrm{L}}_{n,n} V_{n,n+1} G^{\mathrm{R}}_{n+1,n+1} V_{n+1,n}]^{-1} G^{\mathrm{L}}_{n,n}, \tag{9.8}$$

---

[a]This obviously implies that the chain is finite. Eventually, we will couple this finite chain to semi-infinite leads via self-energy terms.

[b]One may also say: a deficiency of this notation.

which can also be derived from (9.4). The point is that for each subsystem constructed from the left, we also constructed the complementary subsystem from the right; and if we want to join them to construct the full system, we only need the respective surface Green's functions - and those were calculated in the previous step.

This scheme is easily extended to two dimensions. In that case, one adds up slices rather than single sites and the local Hilbert-space is spanned by the sites of an individual slice [44, 86]. This implies that the matrices which need to be inverted by standard means in the above relations grow with the size of the system in the second dimension. Consequently, the scheme is best suited for systems which are small in this second dimension and can only be used for rectangular lattices. Alternatively, one can devise recursive schemes based on adding single sites even in two or three dimensions. However, this involves more elaborate book-keeping.[a]

Coupling to leads

A particular advantage of the RGF technique is that it effectively allows us to consider infinite tight-binding models by coupling a finite 'device' region to semi-infinite leads via self-energy terms [86]. Again, it is eq. (9.4) which makes that work.

We illustrate this for a single, semi-infinite lead attached to a finite TB-chain. Let g be the Green's function of the Hamiltonian where the coupling V between the final site N of the central device and the first site $N + 1$ of the lead is turned off. We thus have a Hamiltonian with two independent blocks, one of them being the central device and finite dimensional. We are only interested in the central device, i.e. matrix elements $\langle i|G|j\rangle$ with $i, j \leq N$. Exploiting that $V = V_0|N + 1\rangle\langle N| + V_0^\dagger|N\rangle\langle N + 1|$, we obtain:

$$\langle i|G|j\rangle = \langle i|g|j\rangle + \langle i|g|N\rangle V_0^\dagger \langle N + 1|g|N + 1\rangle V_0 \langle N|G|j\rangle, \qquad (9.9)$$

from the Dyson-equation.

Inspecting this result shows that the only matrix element of g on the lead is the surface Green's function $\langle N + 1|g|N + 1\rangle$. If we limit G and g to the central device, we can hence write:

$$G = 1 + g\Sigma G. \qquad (9.10)$$

with $\Sigma = |N\rangle V_0^\dagger \langle N + 1|g|N + 1\rangle V_0 \langle N|$ independent of the central device Green's functions. This Dyson-equation is equivalent to defining G with respect to the renormalised Hamiltonian $\mathcal{H}_{\text{cd}} + \Sigma$, i.e. the central device Hamiltonian with the self-energy added to the on-site term at site N [86].

We now still have to calculate the surface Green's function of the lead. It turns out that due to its semi-infinity and translation invariance, this can be done very efficiently with a recursive algorithm that basically doubles the size of the lead at each step [86].[b] Since this scheme does not exploit the structure of the Hamiltonian in any kind of way – apart from the fact that it must have next-neighbour coupling only – it applies to superconductor or topological insulator leads without any limitations or extra effort.

9.2. Nambu-Gor'kov-Green's Function on a Lattice

The RGF technique is traditionally used in transport calculations for low-dimensional mesoscopic conductors like semi-conductor quantum wells [44] or graphene flakes [31], but

---

[a]Personal communication from T. Löfwander.
[b]This scheme is explained in detail in the appendix of Ref. [86].

has also been used to describe superconducting structures [122, 123, 5]. This extension is straight-forward, since – as shown in the previous section – the Nambu-notation allows us to write the mean-field Hamiltonian of BCS-theory as an operator which is quadratic in (Nambu) field-operators and therefore complies to the basic requirement of the RGF-technique, i.e., the Hamiltonian in question must be a single-particle Hamiltonian.

We denote Green's functions and Hamiltonians in Nambu-space be calligraphic letters and define the Nambu-Gor'kov Green's function by:

$$\mathcal{G} = (\epsilon + i\eta - \mathcal{H})^{-1}, \tag{9.11}$$

where $\mathcal{H}$ is a tight-binding Hamiltonian in Nambu-space. Naturally, $\mathcal{G}$ has a matrix structure in particle-hole space, and the familiar Gor'kov Green's functions are:

$$\langle n|\mathcal{G}|m\rangle = \begin{pmatrix} G_{n,m} & F_{n,m} \\ -\tilde{F}_{n,m} & -\tilde{G}_{n,m} \end{pmatrix}, \tag{9.12}$$

in this context. Let us now assume that we know all eigenfunctions ψ_λ of $\mathcal{H}$ with eigenvalues ϵ_λ. Generically, they have the structure:

$$\psi_\lambda(\mathbf{k}_{||}) = \sum_n \mathbf{u}_{n,\lambda}(\mathbf{k}_{||}) \otimes \gamma_p \otimes |n\rangle + \mathbf{v}_{n,\lambda}(-\mathbf{k}_{||}) \otimes \gamma_h \otimes |n\rangle. \tag{9.13}$$

Here, γ_p, γ_h are the canonical basis of particle-hole space, and $\mathbf{u}_{n,\lambda}(\mathbf{k}_{||})$, $\mathbf{v}_{n,\lambda}(-\mathbf{k}_{||})$ are vectors in spin- and potentially orbital-space. It is then straight-forward to show that:

$$G_{n,n} = \sum_\lambda \frac{\mathbf{u}_{n,\lambda}\mathbf{u}_{n,\lambda}^\dagger}{\epsilon + i\eta - \epsilon_\lambda}, \quad \tilde{G}_{n,n} = -\sum_\lambda \frac{\mathbf{v}_{n,\lambda}\mathbf{v}_{n,\lambda}^\dagger}{\epsilon + i\eta - \epsilon_\lambda}, \tag{9.14}$$

$$F_{n,n} = \sum_\lambda \frac{\mathbf{u}_{n,\lambda}\mathbf{v}_{n,\lambda}^\dagger}{\epsilon + i\eta - \epsilon_\lambda}, \quad \tilde{F}_{n,n} = -\sum_\lambda \frac{\mathbf{v}_{n,\lambda}\mathbf{u}_{n,\lambda}^\dagger}{\epsilon + i\eta - \epsilon_\lambda}.$$

The Green's function defined in (9.11) coincides with the usual definition of the Nambu-Gor'kov Green's function [3] in the absence of impurities or other self-energies.

Symmetry relations

As always, considering Nambu-space implies redundancy and thus a particle-hole symmetry relation. Our Green's function is defined with respect to the BdG-Hamiltonian $\mathcal{H}(\mathbf{k})$. Due to the symmetry of the operator in particle-hole space, for every eigenstate $\psi_\lambda = (u_\lambda(\mathbf{k}), v_\lambda(-\mathbf{k}))^T$ with energy ϵ_λ, $\tilde{\psi}_\lambda = (v_\lambda(-\mathbf{k}), u_\lambda(\mathbf{k}))^T$ is an eigenstate of $\mathcal{H}^*(-\mathbf{k})$ with energy $-\epsilon_\lambda$. It is then easy to show that:

$$\left[\tilde{G}(-\epsilon, -\mathbf{k})\right]^* = G(\epsilon, \mathbf{k}). \tag{9.15}$$

In our case $\mathbf{k} = \mathbf{k}_{||}$ and $\mathcal{H}(\mathbf{k}_{||})$ is a tight-binding Hamiltonian, which does not change anything about this result, since the particle-hole symmetry of $\mathcal{H}$ still holds.

Usually, the spectral function is defined as the trace over G only. From equation (9.14), we see that this corresponds to the particle-like weight of the eigenstates. To extract the full dispersion of the BdG-Hamiltonian, we will, however, consider a more unconventional definition of A, i.e., take the full trace over $\mathcal{G}$. In this case, the above symmetry relation implies:

$$A(\epsilon, \mathbf{k}) = -\frac{1}{a\pi}\text{Im}\Big[\text{Tr } G(\epsilon, \mathbf{k}) - \text{Tr } \tilde{G}(\epsilon, \mathbf{k})\Big] \tag{9.16}$$

$$= -\frac{1}{a\pi}\text{Im}\Big[\text{Tr } G(\epsilon, \mathbf{k}) + \text{Tr } G(-\epsilon, -\mathbf{k})\Big] = A(-\epsilon, -\mathbf{k}).$$

We will compare both definitions in our discussion of the results.

9.3. The Gap-equation

The gap-equation for this problem, where the z-coordinate is in real space and the x, y-coordinates in k-space, was given in Ref. [74] in terms of the BdG wave functions:

$$\Delta(z) = -g(z) \int d\mathbf{k}_{||} \sum_{\lambda}' u_{\lambda,\uparrow}(\mathbf{k}_{||}, z) v_{\lambda,\downarrow}^*(-\mathbf{k}_{||}). \tag{9.17}$$

Where the accent on the sum indicates that the sum is to be taken over eigenvectors with $0 < \epsilon_\lambda < \epsilon_c$, ϵ_c being the energy cut-off.[a] Using that:

$$\lim_{\eta \to 0} \left(\frac{1}{\epsilon + i\eta - \epsilon_\lambda} - \frac{1}{\epsilon - i\eta - \epsilon_\lambda} \right) \longrightarrow -2\pi i \delta(\epsilon - \epsilon_\lambda), \tag{9.18}$$

is is straight-forward to show that this is identical to

$$\Delta_{n,n} = g(n) \int d\mathbf{k}_{||} \int_{\epsilon > 0} \frac{d\epsilon}{2i\pi} (F_{n,n}^{(\uparrow,\downarrow)}(\epsilon, \mathbf{k}_{||}) + [\tilde{F}_{n,n}^{(\uparrow,\downarrow)}]^\dagger(\epsilon, \mathbf{k}_{||})), \tag{9.19}$$

in the context of our model, where $(\uparrow, \downarrow)$ refers to the up-down entry in the spin-matrices $F_{n,n}$, $\tilde{F}_{n,n}$. Given that $\tau_3 \mathcal{G}^{\mathrm{A}} \tau_3 = [\mathcal{G}^{\mathrm{R}}]^\dagger$ and $\mathcal{G}^{\mathrm{K}} = (\mathcal{G}^{\mathrm{R}} - \mathcal{G}^{\mathrm{A}}) \tanh(\epsilon/2k_{\mathrm{B}}T)$, this is also consistent with the usual definition of the gap-equation in terms of F^{K} at zero-temperature.

To perform the calculation of the gap-profile in the most efficient way, one must consider a SC tight-binding chain coupled to the TI-lead on the left and the SC-lead on the right. The part of the TB-chain considered to be the central device must contain the whole region of varying $\Delta(n)$, i.e., must extend over several coherence lengths. The self-energy of the TI-lead is then given by:

$$\Sigma_{\mathrm{TI}}(k_{||}, \varphi) = \mathcal{T} \langle J | g_{\mathrm{TI}}(k_{||}, \varphi) | J \rangle \mathcal{T}^\dagger | J+1 \rangle \langle J+1 |. \tag{9.20}$$

Here, $\langle J | g_{\mathrm{TI}}(k_{||}, \varphi) | J \rangle$ is the surface Green's function of the TI, and $J+1$ the site of the SC next to the interface. Exploiting the transformation rules under rotations in the x-y-plane discussed in the previous section, we obtain:

$$\Sigma_{\mathrm{TI}}(k_{||}, \varphi) = \mathcal{U}_{\mathrm{SC}} \mathcal{T} \mathcal{U}_{\mathrm{TI}}^\dagger \mathcal{U}_{\mathrm{TI}} \langle J | g_{\mathrm{TI}}(k_{||}, 0) | J \rangle \mathcal{U}_{\mathrm{TI}}^\dagger \mathcal{U}_{\mathrm{TI}} \mathcal{T}^\dagger \mathcal{U}_{\mathrm{SC}}^\dagger, \tag{9.21}$$

and thus

$$\Sigma_{\mathrm{TI}}(k_{||}, \varphi) = \mathcal{U}_{\mathrm{SC}} \Sigma_{\mathrm{TI}}(k_{||}, 0) \mathcal{U}_{\mathrm{SC}}^\dagger. \tag{9.22}$$

The same holds for the self-energy Σ_{SC} from the SC-lead and we arrive at:

$$\mathcal{G}(k_{||}, \varphi) = (\epsilon + i\eta - \mathcal{H}_{\mathrm{SC}}(k_{||}, \varphi) - \Sigma_{\mathrm{TI}}(k_{||}, \varphi) - \Sigma_{\mathrm{SC}}(k_{||}, \varphi))^{-1} = U_{\mathrm{SC}} \mathcal{G}(k_{||}, 0) U_{\mathrm{SC}}^\dagger. \tag{9.23}$$

This relation can be used to reduce the numerical effort for the calculation of the $d\mathbf{k}_{||} = k_{||} \cdot dk_{||} d\varphi$-integral, since only $\mathcal{G}(k_{||}, 0)$ must be calculated with the RGF-technique.

---

[a]In their definition of the BCS mean field Hamiltonian, Lababidi and Zhao choose the sign of the pairing terms to be positive, as opposed to us. This leads to an additional minus sign in the gap-equation stated here.

10. Results

We briefly discuss the results obtained from our model and first show that our one-dimensional TB-Hamiltonian correctly reproduces the bulk band structure of topological insulator and also the surface states by comparing our numerical results to the solutions of the continuum model. We then turn to the TI/SC heterostructure and discuss the induced superconductivity in the interface states in terms of the spectral function which provides their dispersion. Finally, we briefly comment on the spatial profile of the interface states, which, not surprisingly, extend far into the superconductor, as already noted by Lababidi and Zhao [74].

10.1. Analytical Discussion of the k·p-Model and Comparison with Numerical Results

We first provide an analytical solution of the **k·p**-model at a vacuum boundary. Specifically, we derive the surface state solutions and their dispersion. While this has been done already [141, 80], we repeat the analysis here – the purpose being to check the validity of our tight-binding model. We show that so-called hard wall boundary conditions for the TB-model, i.e., simply terminating the tight-binding chain, implement the open boundary condition ($\psi(z = 0) = 0$) of the continuum model, and that the analytical solution of the surface state dispersion and the spatial profile of these states is reproduced.

First, we need to obtain the plane wave solutions of $H_{\text{TI}}(\mathbf{k})$ for a given $\mathbf{k}_{||}$ and ϵ, i.e., we have to solve the Schrödinger equation for k_z. Since we have second order terms in k_z that is a non-linear problem, but a system of linear equations can be obtained by introducing the auxiliary vector $\Phi' = k_z \Phi$ [145] and:

$$\hat{H}_{\text{TI}} = \hat{h}_0(k_x, k_y) + \hat{h}_1 k_z + \hat{h}_2 k_z^2. \tag{10.1}$$

The Schrödinger equation $H_{\text{TI}}(\mathbf{k})\Phi = \epsilon\Phi$ then becomes [145]:

$$\begin{pmatrix} 0 & 1 \\ -\hat{h}_2^{-1}(\hat{h}_0 - \varepsilon) & -\hat{h}_2^{-1}\hat{h}_1 \end{pmatrix} \begin{pmatrix} \Phi \\ \Phi' \end{pmatrix} = k_z \begin{pmatrix} \Phi \\ \Phi' \end{pmatrix}, \tag{10.2}$$

i.e., an eigenvalue equation for k_z. The solutions for k_z and the corresponding eigenvectors are easily inferred from this equation. Analytical expression can be obtained [79], but they are cumbersome and will thus not be stated here. All we need to know at this point, is that there are four eigenvalues for k_z with $k_z = \pm k_{1,2}$. We are looking for states inside the

band-gap of $H_{\mathrm{TI}}(\mathbf{k})$. For energies ϵ inside the gap, the solutions for k_z will be complex, and a surface state solution satisfying $\psi(z=0)=0$ can be obtained from a linear superposition of the corresponding eigenvectors. Assuming a semi-infinite crystal implies that only two of the possible k_z solutions allow for normalisability of the wave function. These are both twofold degenerate, i.e., have a two dimensional eigenspace. We hence have the ansatz:[a]

$$\Psi(k_{||},z,\varepsilon) = e^{ik_1 z}\left[\alpha \cdot \Phi_1^{(1)}(k_{||},\varepsilon) + \beta \cdot \Phi_1^{(2)}\right] + e^{ik_2 z}\left[\gamma \cdot \Phi_2^{(1)}(k_{||},\varepsilon) + \delta \cdot \Phi_2^{(2)}(k_{||},\varepsilon)\right], \tag{10.3}$$

where $((\Phi'_{1,2})^{(1,2)}\ \Phi_{1,2}^{(1,2)})^T$ form a basis of the eigenspace of $k_{1,2}$ in eq. (10.2). We know that eigenspaces of different eigenvalues are necessarily orthogonal. The boundary condition can however only be fulfilled with the above ansatz, if $<\Phi_1^{(1)},\Phi_1^{(2)}>$ and $<\Phi_2^{(1)},\Phi_2^{(2)}>$ share a common subspace which is at least one-dimensional. This is not a contradiction, since they are not eigenspaces of equation (10.2).[b] This condition provides an additional constraint, resulting in the surface state dispersion $\varepsilon(k_x,k_y)$. The dispersion can hence be obtained from:

$$0 = \mathrm{Det}([\Phi_1^{(1)},\Phi_1^{(2)},\Phi_2^{(1)},\Phi_2^{(2)}]), \tag{10.4}$$

since these vectors need to be linearly dependent for the surface state to exist.

Surface state Hamiltonian

The surface state Hamiltonian can be obtained by solving the problem outlined above for $k_{||}=0$ and projecting the full Hamiltonian $H_{\mathrm{TI}}(\mathbf{k})$ on these solutions [80]. This provides a reasonable description of the surface states for small values of $k_{||}$. For $k_{||}=0$, the Hamiltonian reads:

$$\hat{H}_{\mathrm{TI}}(k_{||}=0) = (C_0 + C_1 k_z^2) \cdot 1_{4\times 4} + \tag{10.5}$$
$$+ \begin{pmatrix} M_0 + M_1 k_z^2 & B_0 k_z & 0 & 0 \\ B_0 k_z & -(M_0 + M_1 k_z^2) & 0 & 0 \\ 0 & 0 & M_0 + M_1 k_z^2 & -B_0 k_z \\ 0 & 0 & -B_0 k_z & -(M_0 + M_1 k_z^2) \end{pmatrix},$$

i.e., is block-diagonal, and we have solutions with the structure $\Psi_\uparrow = (\psi_\uparrow\ \ 0)^T$, $\Psi_\downarrow = (0\ \ \psi_\downarrow)^T$ [80]. We consider the upper block, the eigenvalue equation $\hat{H}_{\mathrm{TI}}(k_{||}=0)\Psi_\uparrow = \varepsilon\Psi_\uparrow$ can be rewritten as [80]:[c]

$$\left[(C_0 - \varepsilon + C_1 k_z^2)\nu_1 - (M_0 + M_1 k_z^2)i\nu_2\right]\psi_\uparrow = -B_0 k_z \psi_\uparrow. \tag{10.6}$$

Diagonalising the matrix yields two solutions for $\psi_\uparrow$, which we call $\varphi_\pm$, since they are the same for the lower block (note that the difference between the upper and the lower block is only a sign change on the right side of equation (10.6)). The equation then becomes:

$$\pm\left[(-\tilde\varepsilon + C_1 k_z^2)^2 - (M_0 + M_1 k_z^2)^2\right]^{1/2}\varphi_\pm = -B_0 k_z \varphi_\pm, \tag{10.7}$$

with $\tilde\varepsilon = -C_0 + \varepsilon$, which yields an equation for k_z:

$$(-\tilde\varepsilon + C_1 k_z^2)^2 - (M_0 + M_1 k_z^2)^2 = B_0^2 k_z^2, \tag{10.8}$$

---

[a]This ansatz implicitly assumes that $k_{1,2}$ are the decaying solutions. This assumption can be made without loss of generality, since the solutions come in $\pm$-pairs.
[b]Only the spaces spanned by the full eigenvectors $(\Phi',\Phi)^T$ are.
[c]Recall that $\nu_{1,2,3}$ are the Pauli-matrices in orbital-space.

that has the same solutions as above, i.e. $k_z = \pm k_\alpha$. From (10.7), we now see immediately that if k_α is a solution for φ_+, then $-k_\alpha$ is a solution for φ_-. $\varphi_\pm$ are given by:

$$\varphi_+ = c\left(\sqrt{\frac{(-\tilde{\varepsilon} + C_1 k_\alpha^2) - (M_0 + M_1 k_\alpha^2)}{(-\tilde{\varepsilon} + C_1 k_\alpha^2) + (M_0 + M_1 k_\alpha^2)}} \quad 1\right)^T, \tag{10.9}$$

$$\varphi_- = c\left(-\sqrt{\frac{(-\tilde{\varepsilon} + C_1 k_\alpha^2) - (M_0 + M_1 k_\alpha^2)}{(-\tilde{\varepsilon} + C_1 k_\alpha^2) + (M_0 + M_1 k_\alpha^2)}} \quad 1\right)^T,$$

where c is a normalisation constant. The existence condition of the surface state implies that $\varphi_\pm$ must be the same for $\alpha = 1, 2$, which gives an implicit equation for the energy of the surface state:

$$\tilde{\varepsilon} = M_0 - (C_1 + M_1)\sqrt{k_1^2 k_2^2}. \tag{10.10}$$

This equation is quadratic in ε and hence has two solutions:

$$\tilde{\varepsilon}_1 = M_0 \quad \tilde{\varepsilon}_2 = -\frac{C_1 M_0}{M_1}, \tag{10.11}$$

but there should only be one. Plugging $\tilde{\varepsilon}_1$ into (10.8), however, shows that either k_1 or k_2 is zero, which does not allow for the construction of a surface state, i.e. $\varepsilon_2 = \tilde{\varepsilon}_2 + C_0$ is the energy of the surface state. The surface state hence has the structure:

$$\psi_\uparrow = (\alpha e^{ik_1 z} + \beta e^{ik_2 z})\varphi_+ + (\gamma e^{-ik_1 z} + \delta e^{-ik_2 z})\varphi_-. \tag{10.12}$$

Due to normalisability, we have $\delta = \gamma = 0$, and consequently:

$$\psi_\uparrow = \sqrt{\frac{1}{2}}(e^{ik_1 z} - e^{ik_2 z})\varphi_+, \tag{10.13}$$

fulfils the boundary condition. This implies on the other hand:

$$\psi_\downarrow = \sqrt{\frac{1}{2}}(e^{ik_1 z} - e^{ik_2 z})\varphi_-. \tag{10.14}$$

Thus, we fully solved the edge states for $k_\parallel = 0$. One may now try to construct the solutions for finite $k_\parallel$ from these states. To this end, we separate $\hat{H}_{\text{TI}} = \hat{h}(\partial_z) + \hat{h}(k_x, k_y)$ and observe that the states constructed above solve $\hat{h}(\partial_z)$ since $\hat{h}(k_x = 0, k_y = 0) = 0$. For the states $\varphi_\pm$ we introduce the notation:

$$\varphi_+ = c\,(\chi \quad 1)^T \quad \varphi_- = c\,(-\chi \quad 1)^T, \tag{10.15}$$

Now that we know k_1, k_2 and ε, χ only depends on model parameters. Projecting the Hamiltonian $\hat{h}(k_x, k_y)$ on the states φ_+, φ_- then results in [80]:

$$(\varphi_+^\dagger \quad \varphi_-^\dagger)\hat{h}(k_x, k_y)\begin{pmatrix} \varphi_+ \\ \varphi_- \end{pmatrix} = \begin{pmatrix} \varepsilon_2 + \tilde{C}_2 k_\parallel^2 & i\tilde{A}_0 k_- \\ -i\tilde{A}_0 k_+ & \varepsilon_2 + \tilde{C}_2 k_\parallel^2 \end{pmatrix}, \tag{10.16}$$

with

$$\tilde{C}_2 = |c|^2 \cdot [(C_2 + M_2)|\chi|^2 + (C_2 - M_2)], \quad \tilde{A}_0 = -|c|^2 \cdot 2\text{Im}\chi \cdot A_0. \tag{10.17}$$

In the special case of $C_0 = C_1 = 0$, we have $\varepsilon_2 = 0$ and $\chi = i$, resulting in $\tilde{C}_1 = 0$, the surface state Hamiltonian reduces to [80]:

$$H_{\text{surface}} = -A_0(k_y \sigma_x - k_x \sigma_y), \tag{10.18}$$

which agrees with the standard model Hamiltonian that enters the Fu-Kane model after the transformation:

$$A_0(\sigma_x k_x + \sigma_y k_y) = U H_{\text{surface}} U^\dagger, \tag{10.19}$$

with $U = e^{-i\sigma_z \pi/4}$.
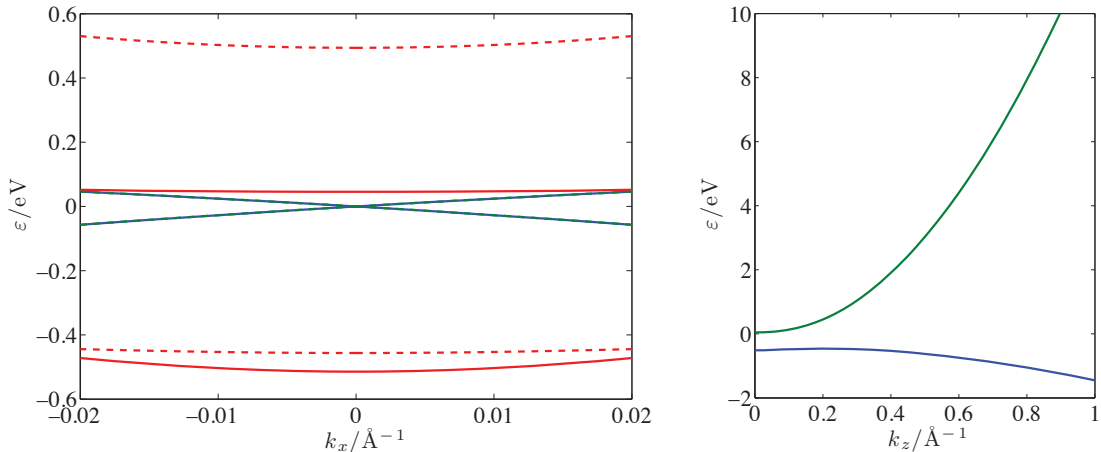
Figure 10.1. – Left: Dispersion of the surface states calculated from (10.4) (blue) and from the effective surface state Hamiltonian (10.16) (dashed-green) and the pair of bulk-bands for $k_z = 0$ (solid-red) and $k_z = 0.21\text{Å}^{-1}$ (dashed-red). The parameters of the $\mathbf{k} \cdot \mathbf{p}$-model are those of Ref. [80] for Bi$_2$Se$_3$, but C_0 has been shifted so that the crossing-point of the surface state dispersion lies as $\varepsilon = 0$. The dispersion is plotted along the cut $k_x = k_y$. Right: Dispersion of the bulk states for $k_x = k_y = 0$ as a function of k_z.

Numerical results and comparison

In Fig. 10.1, we compare the dispersion of the surface states obtained from the effective surface state Hamiltonian in equation (10.16) to that inferred from the general existence condition (10.4). The agreement is perfect, even far away from the Γ-point. This is surprising, since the solutions $k_{1,2}$ do in general depend on $\mathbf{k}_{||}$, which should imply a renormalisation of the surface state dispersion. We also plot two pairs of bulk-states. At $k_z = 0$, we have the band-minimum of the conduction band and at $k_z = 0.21\text{Å}^{-1}$ the maximum of the valence band. The dispersion of the bulk bands as a function of k_z is plotted on the right-hand side of Fig. 10.1. Note that the valence band has a very flat dispersion around the band maximum.

For comparison, we plot the numerical result obtained from the tight-binding model we introduced before in Fig. 10.3. We consider a semi-infinite topological insulator, the spectral function $A_n(\mathbf{k}_{||}, \epsilon)$ is evaluated at site n=200. We see that the dispersion of the surface states agrees exactly with the analytical model. The spectral weight of the surface states is, however, not homogenous, which implies that their spatial profile in the z-direction changes as a function of $\mathbf{k}_{||}$. The spectral density of the bulk-states also agrees well with what one would expect from the analytical solution. The band maxima and minima are consistent with the analytical solution and the enhanced spectral weight in the valence band agrees with its flat dispersion. The spectral weight of the conduction band is small in comparison and decreases for higher energies. Given the steep dispersion of this band, this is not surprising.

In Fig. 10.4, we compare the spatial profile of the surface states at $\mathbf{k}_{||} = 0$. The local spectral function is proportional to the square modulus of the wave function and must thus be compared to:

$$|\chi(z)|^2 = |e^{ik_1 z} - e^{ik_2 z}|^2, \tag{10.20}$$

with $k_1 = 0.5237i\text{Å}^{-1}$ and $k_2 = 0.0779i\text{Å}^{-1}$ for the given set of parameters. We normalise both quantities to their maximum value and find that the spatial profile agrees perfectly
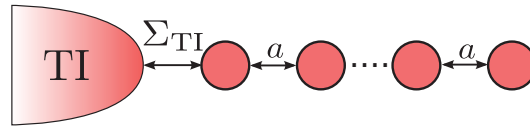
Figure 10.2. – The tight-binding model used to calculate the spectral function for a topological insulator with a single surface.
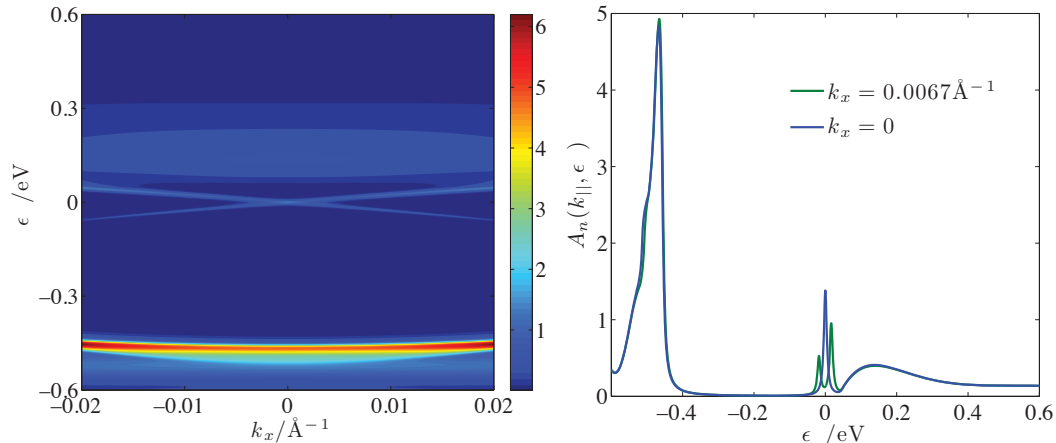
Figure 10.3. – Left: Spectral function at site n=200 for $a = 0.1$Å and $\eta = 0.005$eV. Right: cut along $k_x = 0$ and $k_x = 0.0065$Å^{-1}. $k_x = k_y$ was assumed for these calculations.

if $z = n \cdot a$ is assumed, where n is the site number and a the lattice constant of the TB-model.[a] We also checked this for finite values of $k_{||}$, using equation (10.2) to obtain the values of $k_{1,2}$. We find that the spatial profile of the states indeed changes with $\mathbf{k}_{||}$ and that the negative energy states decay faster than the positive energy ones. This can be understood from the fact that the negative branch moves deeper into the bulk-gap, while the positive branch approaches the conduction band. The agreement with the TB-model is again perfect (not shown here).

To conclude, we established that the tight-binding model we put forward reproduces material specific properties, i.e. the band structure, correctly and that terminating the tight-binding chain implements the vacuum boundary condition. Both the dispersion and the spatial profile of the surface states are found to be in perfect agreement with analytical results.

10.2. Interface State Dispersions

In the following, we discuss how the dispersion of the surface states is renormalised when the TI is coupled to the superconductor. If we are interested in the dispersion only, the most effective model to consider is a single TI-site coupled to semi-infinite leads on the left and right (see Fig. 10.5). This single site is the one sitting right next to the interface. The spectral weight is relatively small here, since the states reach their maximum amplitude deeper inside the TI. The relevant energy scale is given by the superconducting gap, this implies that compared to Fig. 10.3, we stay very close to the Γ-point. Note that the spectral function is calculated from the full trace over the Nambu-Gor'kov Green's function $\mathcal{G}$, in order to obtain the full dispersion of the BdG-Hamiltonian. Usually, the trace is taken

---

[a]This implies that the first site of the semi-infinite TB-chain does not correspond to the surface, i.e. $z = 0$, but to $z = a$.
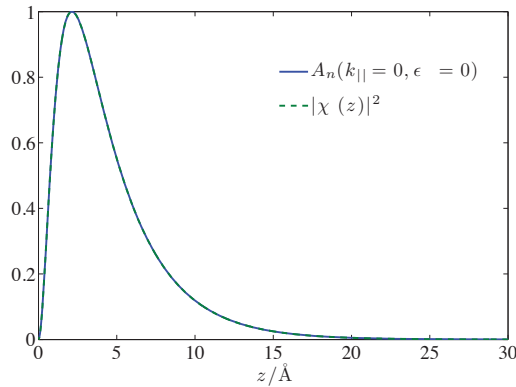
Figure 10.4. – The spectral function $A_n(\mathbf{k}_{||} = 0, \epsilon = 0)$ was calculated for $a = 0.1$Å and $\eta = 1e^{-4}$eV. Both $|\chi(z)|^2$ and A_n are normalised to their maximum value. $z = n \cdot a$. Note that $n = 1$ corresponds to $z = 0.1$Å, not to $z = 0$.
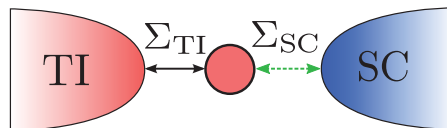
Figure 10.5. – Model used to calculate the interface state dispersion. A single TI-site is coupled to semi-infinite leads on the left and right. The green line indicates that the surface Green's function of the superconductor couples through the transfer-Hamiltonian to the site.

over G only. We will consider that case later on. The surface state dispersion is plotted in the top panel of Fig. 10.6, i.e., the coupling to the SC is turned off. In the other plots, we show the result for finite coupling ($t \neq 0$). We observe that a gap opens in the dispersion of the interface states and the spectral function is symmetric both in energy and momentum. Two pairs of dispersions appear due to the doubling of states that arises as a consequence of the Nambu-space construction. The spectral weight of the states is enhanced for energies smaller than the bulk-gap of the superconductor. This is because truly localised states exist only for these energies. For energies exceeding $|\Delta_{\mathrm{SC}}|$, the surface states of the TI hybridise with the continuum of bulk-states of the superconductor. The size of the induced gap increases with the coupling parameter t that enters the transfer-Hamiltonian (8.19) until the point of ideal coupling is reached at about $t = 0.85$ for this choice of parameters. At this point, the interface states merge fully into the DOS of the superconductor, and there are basically no states left inside the superconducting gap. As t increases further, the coupling becomes weaker again and the induced gap eventually closes. For large t, the superconductor is effectively decoupled, but the surface state dispersion is shifted in energy compared to the $t = 0$ case. The plot shown for $t = 20$ in Fig. 10.6 is a bit confusing in this respect, since a second pair of states appears that is shifted in the opposite direction. Again, this is a consequence of the fact that we trace over the whole Nambu-Gor'kov Green's function. For clarity, the spectral function calculated from the trace over G only is plotted in Fig. 10.7. Obviously, the Γ-point of the surface state dispersion is shifted to negative energies. In terms of the Fu-Kane model, this corresponds to $\mu > 0$. This shift increases with the coupling strength and is maximal for $t = 0.85$.[a]

At energies smaller than Δ_{SC} and for intermediate couplings, the dispersion looks indeed very similar to that of the Fu-Kane model, which we plotted in Fig 7.2. We shall discuss

---

[a]Note that the momentum scale is larger by a factor of 10 in the $t = 0.85$ plot.
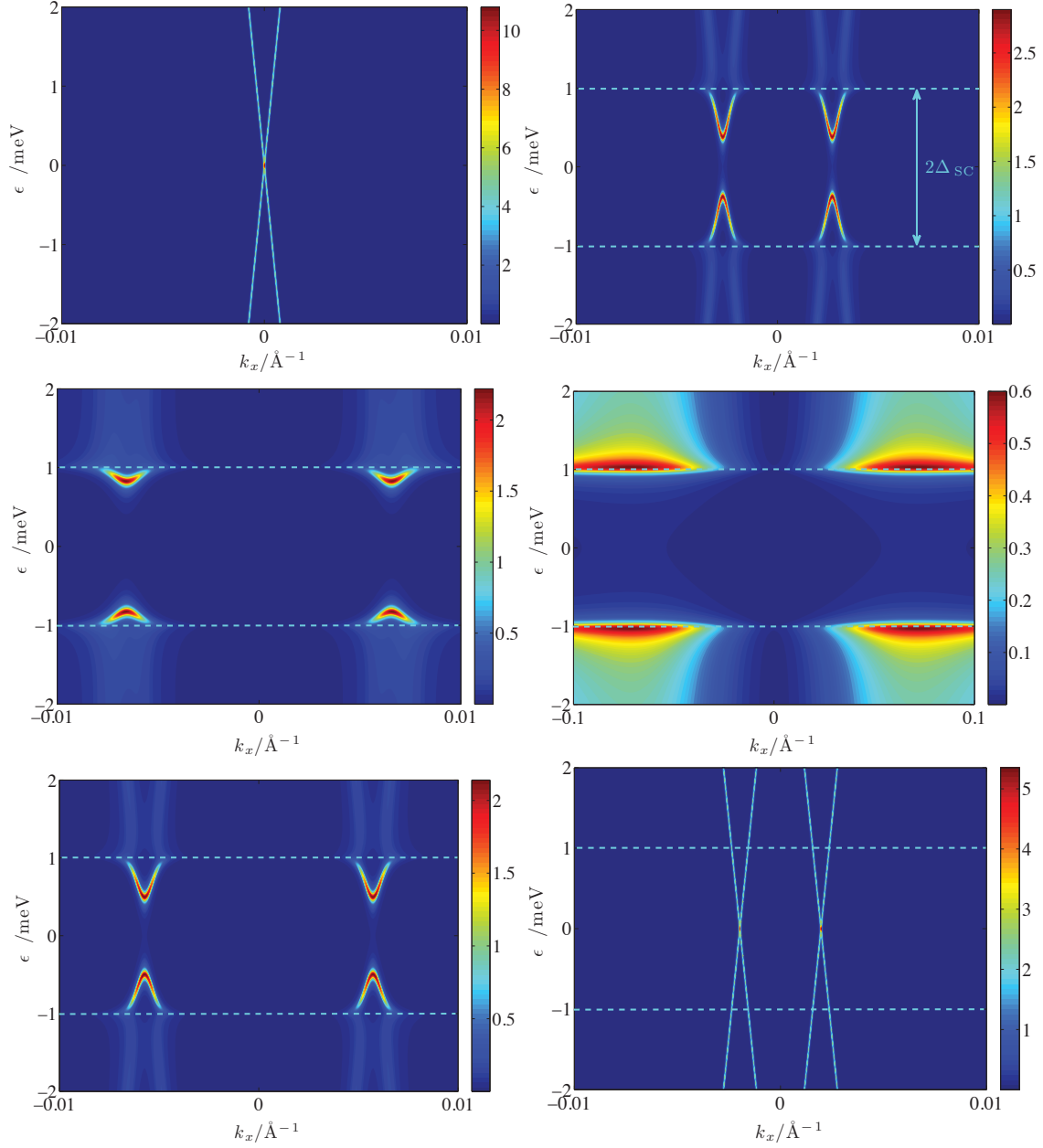
Figure 10.6. – The spectral function $A_n(\mathbf{k}_{||}, \epsilon)$ for $a = 0.1$Å and $\eta = 5\mathrm{e}^{-5}$eV. The blue dashed lines indicate the bulk-gap of the superconductor. Top-left: $t = 0$; top-right: $t = 0.65$; middle-left: $t = 0.75$; middle-right: $t = 0.85$; bottom-left: $t = 1.05$; bottom-right: $t = 20$.
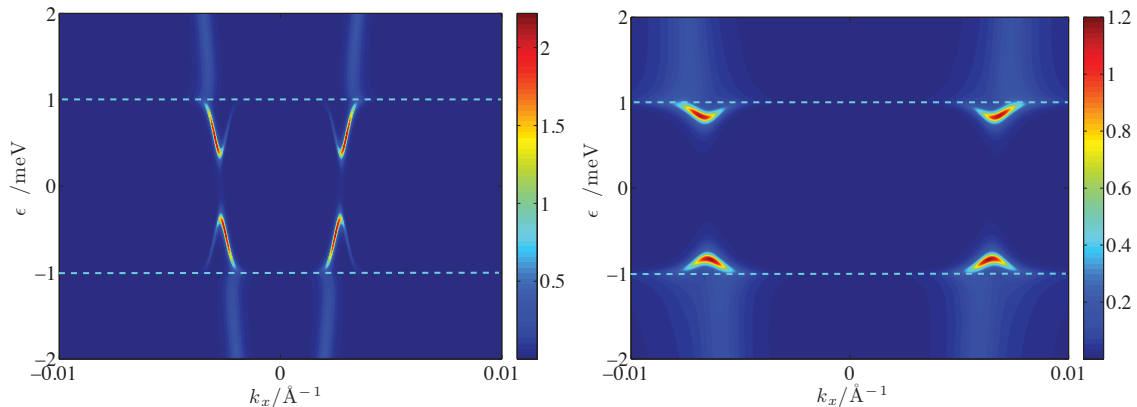
Figure 10.7. – The spectral function $A_n(\mathbf{k}_{||}, \epsilon)$ with the trace over G only for $a = 0.1\text{Å}$ and $\eta = 5\text{e}^{-5}\text{eV}$. The blue dashed lines indicate the bulk-gap of the superconductor. Left: $t = 0.65$; right: $t = 0.75$.

this in more detail in the next section.

An important question to address is the dependence of these results on the lattice parameter a. As shown in the previous section, the spectral function is invariant under changes of a and reproduces the continuum model, provided that a is small enough. This does, however, only hold if the tight-binding model has a proper continuum limit, as it is the case for the semi-infinite TI we considered before. The model we consider here does not have a continuum limit. The transfer-Hamiltonian was chosen ad-hoc and does not increase in size when a is reduced. Consequently, our results depend quantitatively on the choice of a, but the conclusions we draw from our analysis do not. For two different choices of a, we find two choices of t which give us the same coupling strength. This is illustrated in Fig. 10.8, where we plot the position of the minimum $(\varepsilon_{\min}, k_{x,\min})$ of the interface state dispersion as function of t for two values of the lattice constant. The point where the coupling is maximal is almost invariant at around $t \approx 0.845 - 0.85$, but is suppressed more quickly for $a = 0.01\text{Å}$ than for $a = 0.1\text{Å}$. In fact, for two different lattice constants $a_{1,2}$, we find that if the curves for a_2 are rescaled with the formula:

$$t' = (t - t_{\max}) \cdot \frac{a_1}{a_2} + t_{\max}, \qquad (10.21)$$

where $t_{\max}$ is the position of the maximum, they agree relatively well around the maximum, but not for large t. For $t \to \infty$, a shift of the dispersion in energy remains, which is different for different values of a. In the context of a real system, the transfer-Hamiltonian is supposed to model the interface coupling of the two materials and should in principle be calculated from overlaps of atomic orbitals. In the ad-hoc model we chose, t has does not have the meaning of a transmission coefficient as in the scattering matrix approach we considered in the context of quasiclassical theory. It rather serves to interpolate between the band dispersions of the adjacent materials. Thus, there is some ideal value of it, which depends on the material parameters. Other choices for this transfer-Hamiltonian have been considered in the literature, as, for instance, the mean-square of the hopping elements [123]. But in any case, our choice allows us to model the superconducting proximity effect in the surface states of a topological insulator both in weak and strong coupling limits, and the conclusion we draw from it for the validity of the Fu-Kane model are independent of the lattice-parameter choice.
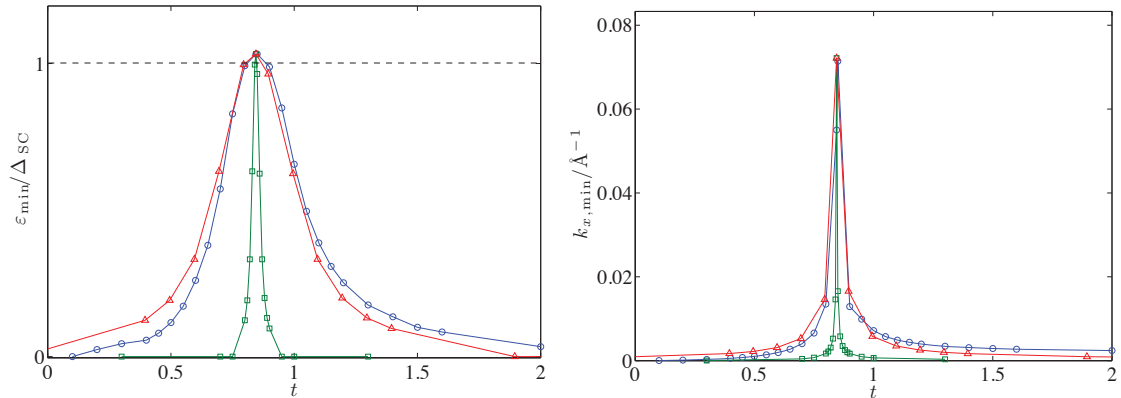
Figure 10.8. – Position of the minimum $\epsilon_{\min}, k_{x,\min}$ of the interface state dispersion as inferred from the spectral function for $\eta = 5\mathrm{e}^{-5}\mathrm{eV}$ and an energy resolution of $\Delta\epsilon = 4\mathrm{e}^{-6}\mathrm{eV}$ and a momentum resolution of $\Delta k_x = 3.33\mathrm{e}^{-5}\mathrm{\AA}^{-1}$ and $k_y = k_x$. Blue: $a = 0.1\mathrm{\AA}$; green: $a = 0.01\mathrm{\AA}$; red: $a = 0.01\mathrm{\AA}$ with t rescaled as $t = (t - 0.845) \cdot 10$. The position of the minimum was determined from the maximum of the spectral function at the bottom of the interface state dispersion, which lies slightly above the SC bulk-gap for ideal coupling. The values of $\epsilon_{\min}$ in the range of weak coupling ($\epsilon_{\min} < 0.1\Delta_{\mathrm{SC}}$) are not very accurate, as it is hard to tell in these cases, whether the gap already closed or not.

10.3. Comparison with the Fu-Kane Model

In Fig. 10.9 , we plot the spectral function for $a = 0.1\mathrm{\AA}$ and $t = 0.65$, 0.75 and fit the dispersion of the Fu-Kane Hamiltonian (7.3) to our numerical data. The fit-values are stated in table 10.1. Naturally, the Fu-Kane model does not capture the fact that apart from the gap induced in the interface states, Δ_{FK}, the bulk-gap of the superconductor does also play an important role. Thus, it is not surprising that this theory does not describe the dispersion correctly at energies comparable to Δ_{SC}. As long as the interface states do not merge completely into the bulk-DOS of the superconductor, it is, however, always possible to obtain a reasonable fit to the Fu-Kane model around the minimum of the interface state dispersion.

Fu-Kane theory assumes a singlet-gap which is independent of momentum and energy. In the context of McMillan theory, this pair-potential must be provided by the self-energy Σ_{SC} of the superconducting lead coupled through the transfer-Hamiltonian to the topological insulator. While it is easy to show that with our choice of the transfer-Hamiltonian, this self-energy does indeed have the spin-structure of a singlet pair potential in its off-diagonal terms in particle-hole space, it also depends on energy and momentum. However, this dependence is weak for small ϵ and $\mathbf{k}_{||}$, and one is thus tempted to approximate:

$$\Sigma_{\mathrm{SC}}(\mathbf{k}_{||}, \epsilon) \approx \Sigma_{\mathrm{SC}}(\mathbf{k}_{||} = 0, \epsilon = 0). \tag{10.22}$$

In the bottom row of Fig. 10.9, we show the spectral function calculated from our model with this approximation. In regard to the plot for $t = 0.65$, we observe that (a) the spectrum is in reasonable agreement with the one using the correct self-energy for small energies and (b) it can be perfectly fitted with the Fu-Kane model. In the case of stronger coupling, however, the approximation does not make any sense at all; the induced gap in the interface states would be even larger than the bulk-gap of the superconductor, as shown in the plot for $t = 0.75$.

In conclusion, one may say that the phenomenological Fu-Kane model provides a reasonable description of the proximity effect in surface states of topological insulators if the
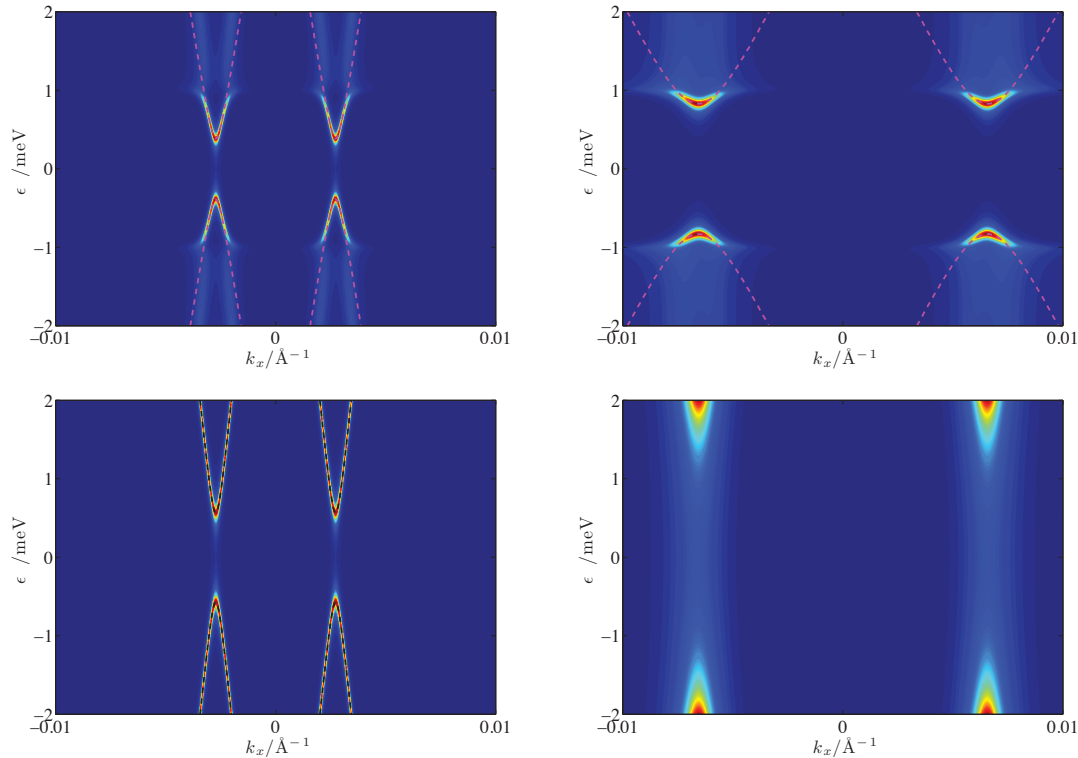
Figure 10.9. – Top row: spectral function for $t = 0.65$ (left) and $t = 0.75$ (right), $a = 0.1$Å, $\eta = 5e^{-5}$eV, with fitted dispersions of the Fu-Kane Hamiltonian. Bottom row: spectral function for the same parameters but with the approximation $\Sigma_{\text{SC}}(\mathbf{k}_{||}, \epsilon) = \Sigma_{\text{SC}}(\mathbf{k}_{||} = 0, \epsilon = 0)$.

	$\Delta_{\text{FK}}/$ meV	$\mu/$ meV	$\hbar v_{\text{F}}/$ eVÅ
$t = 0.65$	0.385	0.46	1.2
$t = 0.75$	0.83	0.37	0.4
$t = 0.65, \Sigma_{\text{SC}} = \Sigma_{\text{SC}}(\mathbf{k}_{||} = 0, \epsilon = 0)$	0.57	0.73	1.9

Table 10.1. – Fit-parameters for the fits shown in Fig 10.9.

coupling to the SC is weak to intermediate, i.e., $\Delta_{\text{FK}} \approx 0.5\Delta_{\text{SC}}$, but is not a valid approximation if the coupling is strong. In the latter case, the proximity effect is properly described if the energy and momentum dependence of the self-energy Σ_{SC} is taken into account. From the structure of the self-energy:

$$\Sigma_{\text{SC}} = \mathcal{T}^{\dagger} g_{\text{SC}}(\mathbf{k}_{||}, \epsilon)\mathcal{T}, \qquad (10.23)$$

we also see that the induced gap is not necessarily of the singlet type if $\mathcal{T}$ contains spin-flip elements.

These results are in line with the general argument of Sau et al. [108], who derived an analytical expression for this self-energy assuming a general basis of normal-state wave functions for the superconducting lead and directly included it in the surface state Hamiltonian of the TI.

10.4. Spatial Profile of the Interface States

Finally, we shortly discuss the spatial profile of the interface states shown in Fig. 10.10 for the states at the bottom of the interface state dispersion and $t = 0.65, 0.75$. We
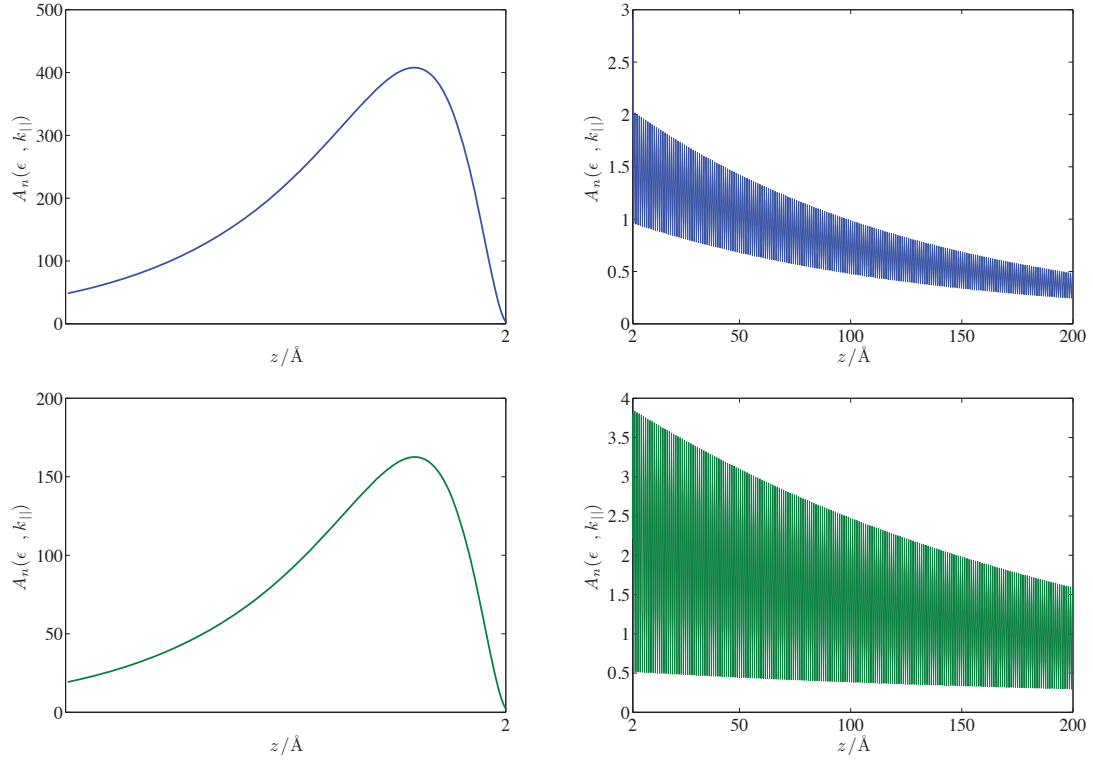
Figure 10.10. – Spatial profile of the interface states for $t = 0.65$ (blue) and $t = 0.75$ (green), $a = 0.1\text{Å}$ and $\eta = 5\mathrm{e}^{-5}\mathrm{eV}$, at the bottom of the interface state dispersion, i.e., $k_x = k_y = 0.00273\text{Å}^{-1}$(blue), $= 0.00657\text{Å}^{-1}$(green) and $\epsilon = 0.38\mathrm{meV}$ (blue), $= 0.83\mathrm{meV}$ (green). The interface is at $z = 2\text{Å}$, the left plot shows the profile inside the TI, the right plot the profile inside the SC. The oscillations on the k_{F}-scale are very fast and not properly resolved in the plots shown here.

observe that most of the spectral weight of the states still resides inside the TI, even for relatively strong coupling and that the states are well localised on the TI-side. In the superconductor, the local spectral weight is a lot smaller, the wave function oscillates on the interatomic scale and decays on the scale of the superconducting coherence length. We also observe that the decay is stronger for $t = 0.65$, which can be understood from the fact that the corresponding state lies deeper inside the gap than the state we plot for $t = 0.75$. Thus, the interface states are in fact not well localised inside the SC, which is not surprising, since the relevant energy gap, Δ_{SC}, is two orders of magnitude smaller than the band-gap of the TI.

Conclusion

In the first part of this thesis we presented a comprehensive study of the triplet proximity effect at superconductor-ferromagnet interfaces, focusing on two prominent problems: the Andreev spectra of point-contacts and the Josephson effect. This analysis was carried out with the quasiclassical Green's function method using a generalisation of its boundary conditions at interfaces and surfaces.

We derived a theory of conductance spectra that fully accounts for effects due spin-dependent scattering and Fermi-surface geometry in the ballistic limit and showed that it contains earlier theoretical models of this problem as limiting cases. In this context, we also analysed the scattering effects responsible for the creation of triplet-correlations in terms of various models for interface potentials. The theory was directly compared to experimental data on CrO_2 and $(Ga,Mn)As$. We were able to show that these cannot only be fitted with our theory, but that our model also provides new physical interpretations that we believe to be more sound than the conclusions inferred from extended BTK-theory.

In regard to the Josephson effect, the most prominent prediction resulting from our analysis is the emergence of exotic current-phase relations (CPRs) that arise from the magnetisation of the interfaces. An implication of this is the prediction of a spin Josephson effect in superconductor-ferromagnet heterostructures with only one superconducting electrode. The Fourier-analysis of the current-phase relation shows that there are two dominant processes of Cooper-pair transfer. The first is the spin-neutral crossed pair transmission, with an equal number of triplet pairs transferred in both spin-bands, and the second one are the spin-polarised contributions that depend on the first harmonics in $\Delta\varphi$.[a] This additional handle, which is provided by the relative misalignment of interface magnetisation directions, may offer interesting perspectives for controlling the CPR through magnetic fields. However, experiments on the long range triplet Josephson effect focused on critical currents so far, while current-phase relations have, to our knowledge, not yet been investigated.

We showed that the presence of anti-ferromagnetic domain structure in the interlayer implies additional backscattering of quasiparticles and hence an additional suppression of the supercurrent. We also found that this domain structure may imply a 0-π switching behaviour of the current-phase relation. We provided a comprehensive study of the critical current as a function of junction length and temperature. In particular, we investigated the temperature anomaly predicted for half metallic junctions in the ferromagnetic case and in the presence of domain walls. Additional pair-breaking at the domain boundaries, which would be provided by spin-flip scattering, was neglected here, but must be included to explain the observations of Khasawneh et al. [70], who refer to it as 'spin-memory loss'.

The idea of creating a $p_x + ip_y$ state by means of the triplet-proximity effect, where the singlet-triplet conversion is caused by spin-orbit coupling, was briefly commented on. We showed that if a ferromagnet is considered instead of half metal, two such states with

---

[a] $\Delta\varphi$ is the relative angle between the quantisation axes of the two interfaces.

opposite chirality can be induced and are stable against backscattering at a surface. We therefore conclude that such states could be engineered in thin ferromagnetic layers, if the samples are clean.

In the second part, a numerical analysis of the superconducting proximity effect in the surface states of topological insulators was presented and compared to the phenomenological model of Fu and Kane. In agreement with earlier work on this problem, we found that the phenomenological model can be understood in terms of McMillan's theory of the proximity effect in the regime of weak to intermediate coupling. If the effective self-energy of the superconductor is approximated by its zero-energy and zero-momentum value, its anomalous part has exactly the same structure as a singlet pair-potential if the interface is not spin-active. This picture breaks down if the coupling to the superconductor becomes strong and the energy and momentum dependence of the self-energy must be retained in that case. While this problem has been studied before, the numerical method that we describe and employ is very efficient and allows for material specific calculations by starting from multi-orbital tight-binding models. We believe that it can be useful in the future for transport calculations in topological insulator nanostructures.

Bibliography

[1] ABOLFATH, M., JUNGWIRTH, T., BRUM, J., AND MACDONALD, A. H. Theory of magnetic anisotropy in $III_{1-x}Mn_xV$ ferromagnets. *Physical Review B 63*, 5 (2001), 054418.

[2] ABRIKOSOV, A. A., GORKOV, L. P., AND DZYALOSHINSKI, I. E. *Methods of Quantum Field Theory in Statistical Physics*, 2nd ed. Pergamon Press Ltd., 1965.

[3] ALTLAND, A., AND SIMONS, B. *Condensed Matter Field Theory*, 2nd ed. Cambridge University Press, 2010.

[4] ANWAR, M. S., CZESCHKA, F., HESSELBERTH, M., PORCU, M., AND AARTS, J. Long-range supercurrents through half-metallic ferromagnetic CrO_2. *Physical Review B 82*, 10 (2010), 100501(R).

[5] ASANO, Y., SAWA, Y., TANAKA, Y., AND GOLUBOV, A. A. Odd-frequency pairs and Josephson current through a strong ferromagnet. *Physical Review B 76*, 22 (2007), 224525.

[6] AVRON, J. E., OSADCHY, D., AND SEILER, R. A topological look at the quantum Hall effect. *Physics today 56*, 8 (2003), 38–42.

[7] AWSCHALOM, D. D., AND FLATTE, M. E. Challenges for semiconductor spintronics. *Nature Physics 3*, 3 (2007), 153–159.

[8] BARDEEN, J., COOPER, L. N., AND SCHRIEFFER, J. R. Theory of superconductivity. *Physical Review 108*, 5 (1957), 1175.

[9] BELZIG, W., WILHELM, F. K., BRUDER, C., SCHÖN, G., AND ZAIKIN, A. D. Quasiclassical Green's function approach to mesoscopic superconductivity. *Superlattices and Microstructures 25*, 5-6 (1999), 1251 – 1288.

[10] BERGERET, F. S., VOLKOV, A. F., AND EFETOV, K. B. Long-range proximity effects in superconductor-ferromagnet structures. *Physical Review Letters 86*, 18 (2001), 4096–4099.

[11] BERGERET, F. S., VOLKOV, A. F., AND EFETOV, K. B. Odd triplet superconductivity and related phenomena in superconductor-ferromagnet structures. *Reviews of Modern Physics 77*, 4 (2005), 1321–1373.

[12] BÉRI, B., KUPFERSCHMIDT, J. N., BEENAKKER, C. W. J., AND BROUWER, P. W. Quantum limit of the triplet proximity effect in half-metal-superconductor junctions. *Physical Review B 79*, 2 (2009), 024517.

[13] BERNEVIG, B. A., HUGHES, T. L., AND ZHANG, S.-C. Quantum spin Hall effect and topological phase transition in HgTe quantum wells. *Science 314*, 5806 (2006), 1757–1761.

[14] BERNEVIG, B. A., AND ZHANG, S.-C. Quantum spin Hall effect. *Physical Review Letters 96*, 10 (2006), 106802.

[15] Blonder, G. E., Tinkham, M., and Klapwijk, T. M. Transition from metallic to tunneling regimes in superconducting microconstrictions: Excess current, charge imbalance, and supercurrent conversion. *Physical Review B 25*, 7 (1982), 4515–4532.

[16] Brydon, P. M. R., Asano, Y., and Timm, C. Spin Josephson effect with a single superconductor. *Physical Review B 83*, 18 (2011), 180504.

[17] Buzdin, A. Direct coupling between magnetism and superconducting current in the Josephson φ_0 junction. *Physical Review Letters 101*, 10 (2008), 107005.

[18] Buzdin, A. I. Proximity effects in superconductor-ferromagnet heterostructures. *Reviews of Modern Physics 77*, 3 (2005), 935–976.

[19] Campion, R. P., Edmonds, K. W., Zhao, L. X., Wang, K. Y., Foxon, C. T., Gallagher, B. L., and Staddon, C. R. The growth of GaMnAs films by molecular beam epitaxy using arsenic dimers. *Journal of Crystal Growth 251*, 1-4 (2003), 311–316.

[20] Chen, J., Qin, H. J., Yang, F., Liu, J., Guan, T., Qu, F. M., Zhang, G. H., Shi, J. R., Xie, X. C., Yang, C. L., Wu, K. H., Li, Y. Q., and Lu, L. Gate-voltage control of chemical potential and weak antilocalization in Bi_2Se_3. *Physical Review Letters 105*, 17 (2010), 176602.

[21] Chen, Y. L., Analytis, J. G., Chu, J.-H., Liu, Z. K., Mo, S.-K., Qi, X. L., Zhang, H. J., Lu, D. H., Dai, X., Fang, Z., Zhang, S. C., Fisher, I. R., Hussain, Z., and Shen, Z.-X. Experimental realization of a three-dimensional topological insulator, Bi_2Te_3. *Science 325*, 5937 (2009), 178–181.

[22] Chung, S. B., Zhang, H.-J., Qi, X.-L., and Zhang, S.-C. Topological superconducting phase and Majorana fermions in half-metal/superconductor heterostructures. *Physical Review B 84*, 6 (2011), 060510(R).

[23] Coey, J. M. D., and Venkatesan, M. Half-metallic ferromagnetism: Example of CrO2 (invited). *Journal of Applied Physics 91*, 10 (2002), 8345–8350.

[24] Coleman, P. *Introduction to Many Body Physics.* Available online at http://www.physics.rutgers.edu/∼coleman/620/mbody/pdf/bkx.pdf, 2011.

[25] Cottet, A., Huertas-Hernando, D., Belzig, W., and Nazarov, Y. V. Spin-dependent boundary conditions for isotropic superconducting Green's functions. *Physical Review B 80*, 18 (2009), 184511.

[26] Cuevas, J. C., and Fogelström, M. Quasiclassical description of transport through superconducting contacts. *Physical Review B 64*, 10 (2001), 104502.

[27] Datta, S. *Electronic Transport in Mesoscopic Systems.* Cambridge University Press, 1995.

[28] De Jong, M. J. M., and Beenakker, C. W. J. Andreev reflection in ferromagnet-superconductor junctions. *Physical Review Letters 74*, 9 (1995), 1657–1660.

[29] Deutscher, G. Andreev-Saint-James reflections: A probe of cuprate superconductors. *Reviews of Modern Physics 77*, 1 (2005), 109–135.

[30] Deutscher, G., and de Gennes, P. G. *Proximity effects.* In "Superconductivity", edited by R. D. Parks, MARCEL DEKKER, INC., New York, 1969, ch. 17.

[31] Dietl, P., Metalidis, G., Golubev, D., San-Jose, P., Prada, E., Schomerus, H., and Schön, G. Disorder-induced pseudodiffusive transport in graphene nanoribbons. *Physical Review B 79*, 19 (2009), 195413.

[32] DYNES, R. C., NARAYANAMURTI, V., AND GARNO, J. P. Direct measurement of quasiparticle-lifetime broadening in a strong-coupled superconductor. *Physical Review Letters 41*, 21 (1978), 1509–1512.

[33] EILENBERGER, G. Transformation of Gorkov's equation for type II superconductors into transport-like equations. *Zeitschrift für Physik A Hadrons and Nuclei 214* (1968), 195–213.

[34] ELIASHBERG, G. M. Inelastic electron collisions and nonequilibrium stationary states in superconductors. *Zhurnal Eksperimentalnoi I Teoreticheskoi Fiziki 61* (1971), 1254 [Sov. Phys. JETP 34, 668 (1972)].

[35] ESCHRIG, M. *Mikroskopische Theorie isolierter Wirbel in Hoch-TC-Supraleitern unter dem Einfluß eines elektromagnetischen Wechselfeldes.* PhD thesis, Universität Bayreuth, 1997.

[36] ESCHRIG, M. Distribution functions in nonequilibrium theory of superconductivity and Andreev spectroscopy in unconventional superconductors. *Physical Review B 61*, 13 (2000), 9061–9076.

[37] ESCHRIG, M. Scattering problem in nonequilibrium quasiclassical theory of metals and superconductors: General boundary conditions and applications. *Physical Review B 80*, 13 (2009), 134511.

[38] ESCHRIG, M. Spin-polarized supercurrents for spintronics. *Physics Today 64*, 1 (2011), 43–49.

[39] ESCHRIG, M., KOPU, J., CUEVAS, J. C., AND SCHÖN, G. Theory of half-metal/superconductor heterostructures. *Physical Review Letters 90*, 13 (2003), 137003.

[40] ESCHRIG, M., AND LÖFWANDER, T. Triplet supercurrents in clean and disordered half-metallic ferromagnets. *Nature Physics 4*, 2 (2008), 138–143.

[41] ESCHRIG, M., AND LÖFWANDER, T. S-matrix for an interface including strong rashba spin-orbit interaction. Internal report, 2009.

[42] ESCHRIG, M., LÖFWANDER, T., CHAMPEL, T., CUEVAS, J. C., KOPU, J., AND SCHÖN, G. Symmetries of pairing correlations in superconductor-ferromagnet nanostructures. *Journal of Low Temperature Physics 147*, 3-4 (2007), 457–476.

[43] FEOFANOV, A. K., OBOZNOV, V. A., BOL'GINOV, V. V., LISENFELD, J., POLETTO, S., RYAZANOV, V. V., ROSSOLENKO, A. N., KHABIPOV, M., BALASHOV, D., ZORIN, A. B., DMITRIEV, P. N., KOSHELETS, V. P., AND USTINOV, A. V. Implementation of superconductor/ferromagnet/superconductor π-shifters in superconducting digital and quantum circuits. *Nature Physics 6*, 8 (2010), 593–597.

[44] FERRY, D. K., GOODNICK, S. M., AND BIRD, J. *Transport in Nanostructures*, 2nd ed. Cambridge University Press, 2009.

[45] FISHER, D. S., AND LEE, P. A. Relation between conductivity and transmission matrix. *Physical Review B 23*, 12 (1981), 6851–6854.

[46] FOGELSTRÖM, M. Josephson currents through spin-active interfaces. *Physical Review B 62*, 17 (2000), 11812–11819.

[47] FU, L., AND KANE, C. L. Superconducting proximity effect and Majorana fermions at the surface of a topological insulator. *Physical Review Letters 100*, 9 (2008), 096407.

[48] Fu, L., Kane, C. L., and Mele, E. J. Topological insulators in three dimensions. *Physical Review Letters 98*, 10 (2007), 106803.

[49] Geilikman, B. T. Thermal conduction of superconductors. *Zhurnal Eksperimentalnoi I Teoreticheskoi Fiziki 34* (1958), 1042 [Sov. Phys. JETP 7, 721 (1958)].

[50] Geresdi, A., Halbritter, A., Csontos, M., Csonka, S., Mihály, G., Wojtowicz, T., Liu, X., Jankó, B., and Furdyna, J. K. Nanoscale spin polarization in the dilute magnetic semiconductor (In, Mn)Sb. *Physical Review B 77*, 23 (2008), 233304.

[51] Grein, R. Spin-activity at interfaces between superconductors and strongly polarized ferromagnets. Diploma thesis, 2008.

[52] Grein, R., Eschrig, M., Metalidis, G., and Schön, G. Spin-dependent cooper pair phase and pure spin supercurrents in strongly polarized ferromagnets. *Physical Review Letters 102*, 22 (2009), 227005.

[53] Grein, R., Löfwander, T., Metalidis, G., and Eschrig, M. Theory of superconductor-ferromagnet point-contact spectra: The case of strong spin polarization. *Physical Review B 81*, 9 (2010), 094508.

[54] Grein, R., Michelsen, J., and Eschrig, M. A numerical study of the superconducting proximity effect in topological surface states. *Arxiv preprint arXiv:1111.0445* (2011).

[55] Halterman, K., and Valls, O. T. Proximity effects at ferromagnet-superconductor interfaces. *Physical Review B 65*, 1 (2001), 014509.

[56] Hasan, M. Z., and Kane, C. L. Colloquium: Topological insulators. *Reviews of Modern Physics 82*, 4 (2010), 3045–3067.

[57] Houzet, M., and Buzdin, A. I. Long range triplet Josephson effect through a ferromagnetic trilayer. *Physical Review B 76*, 6 (2007), 060504(R).

[58] Hsieh, D., Qian, D., Wray, L., Xia, Y., Hor, Y. S., Cava, R. J., and Hasan, M. Z. A topological Dirac insulator in a quantum spin Hall phase. *Nature 452*, 7190 (2008), 970–974.

[59] Hsieh, D., Xia, Y., Qian, D., Wray, L., Dil, J. H., Meier, F., Osterwalder, J., Patthey, L., Checkelsky, J. G., Ong, N. P., Fedorov, A. V., Lin, H., Bansil, A., Grauer, D., Hor, Y. S., Cava, R. J., and Hasan, M. Z. A tunable topological insulator in the spin helical Dirac transport regime. *Nature 460*, 7259 (2009), 1101–1105.

[60] Hsieh, D., Xia, Y., Wray, L., Qian, D., Pal, A., Dil, J. H., Osterwalder, J., Meier, F., Bihlmayer, G., Kane, C. L., Hor, Y. S., Cava, R. J., and Hasan, M. Z. Observation of unconventional quantum spin textures in topological insulators. *Science 323*, 5916 (2009), 919–922.

[61] Hübler, F., Wolf, M. J., Beckmann, D., and v. Löhneysen, H. Observation of Andreev bound states at spin-active interfaces. *Arxiv preprint arXiv:1012.3867* (2010).

[62] Ji, Y., Strijkers, G. J., Yang, R. Y., and Chien, C. L. Comparison of two models for spin polarization measurements by Andreev reflection. *Physical Review B 64*, 22 (2001), 224425.

[63] Jungwirth, T., Sinova, J., Mašek, J., Kučera, J., and MacDonald, A. H. Theory of ferromagnetic (III, Mn)V semiconductors. *Reviews of Modern Physics 78*, 3 (2006), 809–864.

[64] KANE, C. L., AND MELE, E. J. Z_2 topological order and the quantum spin Hall effect. *Physical Review Letters 95*, 14 (2005), 146802.

[65] KANE, C. L., AND MELE, E. J. Quantum spin Hall effect in graphene. *Physical Review Letters 95*, 22 (2005), 226801.

[66] KATSNELSON, M. I., IRKHIN, V. Y., CHIONCEL, L., LICHTENSTEIN, A. I., AND DE GROOT, R. A. Half-metallic ferromagnets: From band structure to many-body effects. *Reviews of Modern Physics 80*, 2 (2008), 315–378.

[67] KEIZER, R. S., GOENNENWEIN, S. T. B., KLAPWIJK, T. M., MIAO, G. X., XIAO, G., AND GUPTA, A. A spin triplet supercurrent through the half-metallic ferromagnet CrO_2. *Nature 439*, 7078 (2006), 825–827.

[68] KHAIRE, T. S., KHASAWNEH, M. A., PRATT JR., W. P., AND BIRGE, N. O. Observation of spin-triplet superconductivity in Co-based Josephson junctions. *Physical Review Letters 104*, 13 (2010), 137002.

[69] KHASAWNEH, M. A., KHAIRE, T. S., KLOSE, C., PRATT JR., W. P., AND BIRGE, N. O. Spin-triplet supercurrent in Co-based Josephson junctions. *Superconductor Science & Technology 24*, 2 (2011), 024005.

[70] KHASAWNEH, M. A., KLOSE, C., PRATT JR., W. P., AND BIRGE, N. O. Spin-memory loss at Co/Ru interfaces. *Physical Review B 84*, 1 (2011), 014425.

[71] KLOSE, C., KHAIRE, T. S., WANG, Y., PRATT JR., W. P., BIRGE, N. O., MCMORRAN, B., GINLEY, T., BORCHERS, J., KIRBY, B., MARANVILLE, B., AND UNGURIS, J. Optimization of spin-triplet supercurrent in ferromagnetic Josephson junctions. *Arxiv preprint arXiv:1108.5666* (2011).

[72] KÖNIG, M., WIEDMANN, S., BRÜNE, C., ROTH, A., BUHMANN, H., MOLENKAMP, L. W., QI, X.-L., AND ZHANG, S.-C. Quantum spin Hall insulator state in HgTe quantum wells. *Science 318*, 5851 (2007), 766–770.

[73] KRIENER, M., SEGAWA, K., REN, Z., SASAKI, S., AND ANDO, Y. Bulk superconducting phase with a full energy gap in the doped topological insulator $Cu_xBi_2Se_3$. *Physical Review Letters 106*, 12 (2011), 127004.

[74] LABABIDI, M., AND ZHAO, E. Microscopic simulation of superconductor/topological insulator proximity structures. *Physical Review B 83*, 18 (2011), 184511.

[75] LANDAU, L. D. The theory of a Fermi-liquid. *Zhurnal Eksperimentalnoi I Teoreticheskoi Fiziki 30* (1956), 1058–1064 [Sov. Phys. JETP 3, 920 (1957)].

[76] LARKIN, A. I., AND OVCHINNIKOV, Y. N. Quasiclassical method in the theory of superconductivity. *Zhurnal Eksperimentalnoi I Teoreticheskoi Fiziki 55* (1968), 2262 [Sov. Phys. JETP 28, 1200 (1969)].

[77] LARKIN, A. I., AND OVCHINNIKOV, Y. N. Nonlinear conductivity of superconductors in the mixed state. *Zhurnal Eksperimentalnoi I Teoreticheskoi Fiziki 68* (1975), 1915 [Sov. Phys. JETP 41, 960 (1976)].

[78] LINDER, J., AND SUDBØ, A. Signatures of retroreflection and induced triplet electron-hole correlations in ferromagnet–*s*-wave-superconductor structures. *Physical Review B 75*, 13 (2007), 134509.

[79] LINDER, J., YOKOYAMA, T., AND SUDBØ, A. Anomalous finite size effects on surface states in the topological insulator Bi_2Se_3. *Physical Review B 80*, 20 (2009), 205401.

[80] LIU, C.-X., QI, X.-L., ZHANG, H., DAI, X., FANG, Z., AND ZHANG, S.-C. Model Hamiltonian for topological insulators. *Physical Review B 82*, 4 (2010), 045122.

[81] LÖFWANDER, T., GREIN, R., AND ESCHRIG, M. Is CrO_2 fully spin polarized? analysis of Andreev spectra and excess current. *Physical Review Letters 105*, 20 (2010), 207001.

[82] MAZIN, I. I. Superconductivity gets an iron boost. *Nature 464*, 7286 (2010), 183–186.

[83] MAZIN, I. I., GOLUBOV, A. A., AND NADGORNY, B. Probing spin polarization with Andreev reflection: A theoretical basis. *Journal of Applied Physics 89*, 11 (2001), 7576–7578.

[84] MAZIN, I. I., AND SCHMALIAN, J. Pairing symmetry and pairing state in ferropnictides: Theoretical overview. *Physica C-Superconductivity and Its Applications 469*, 9-12 (2009), 614–627.

[85] MCMILLAN, W. L. Tunneling model of the superconducting proximity effect. *Physical Review 175*, 2 (1968), 537–542.

[86] METALIDIS, G. *Electronic Transport in Mesoscopic Systems*. PhD thesis, Martin-Luther-Universität Halle-Wittenberg, 2007.

[87] METALIDIS, G., AND BRUNO, P. Green's function technique for studying electron flow in two-dimensional mesoscopic samples. *Physical Review B 72*, 23 (2005), 235304.

[88] METALIDIS, G., ESCHRIG, M., GREIN, R., AND SCHÖN, G. Nonlocal conductance via overlapping Andreev bound states in ferromagnet-superconductor heterostructures. *Physical Review B 82*, 18 (2010), 180503(R).

[89] MILLIS, A., RAINER, D., AND SAULS, J. A. Quasiclassical theory of superconductivity near magnetically active interfaces. *Physical Review B 38*, 7 (1988), 4504–4515.

[90] MOORE, J. E., AND BALENTS, L. Topological invariants of time-reversal-invariant band structures. *Physical Review B 75*, 12 (2007), 121306(R).

[91] NAMBU, Y. Quasi-particles and gauge invariance in the theory of superconductivity. *Physical Review 117*, 3 (1960), 648–663.

[92] NASH, C., AND SEN, S. *Topology and Geometry for Physicists*. Academic Press Inc., 1983.

[93] NAYAK, C., SIMON, S. H., STERN, A., FREEDMAN, M., AND DAS SARMA, S. Non-Abelian anyons and topological quantum computation. *Reviews of Modern Physics 80*, 3 (2008), 1083–1159.

[94] NOVÁK, V., OLEJNÍK, K., WUNDERLICH, J., CUKR, M., VÝBORNÝ, K., RUSHFORTH, A. W., EDMONDS, K. W., CAMPION, R. P., GALLAGHER, B. L., SINOVA, J., AND JUNGWIRTH, T. Curie point singularity in the temperature derivative of resistivity in (Ga, Mn)As. *Physical Review Letters 101*, 7 (2008), 077201.

[95] PANGULURI, R. P., KU, K. C., WOJTOWICZ, T., LIU, X., FURDYNA, J. K., LYANDA-GELLER, Y. B., SAMARTH, N., AND NADGORNY, B. Andreev reflection and pair-breaking effects at the superconductor/magnetic semiconductor interface. *Physical Review B 72*, 5 (2005), 054510.

[96] PARKER, J. S., WATTS, S. M., IVANOV, P. G., AND XIONG, P. Spin polarization of CrO_2 at and across an artificial barrier. *Physical Review Letters 88*, 19 (2002), 196601.

[97] PEREZ-WILLARD, F., CUEVAS, J. C., SÜRGERS, C., PFUNDSTEIN, P., KOPU, J., ESCHRIG, M., AND VON LÖHNEYSEN, H. Determining the current polarization in Al/Co nanostructured point contacts. *Physical Review B 69*, 14 (2004), 140502(R).

[98] PIANO, S., GREIN, R., MELLOR, C. J., VÝBORNÝ, K., CAMPION, R., WANG, M., ESCHRIG, M., AND GALLAGHER, B. L. Spin polarization of (Ga, Mn)As measured by Andreev spectroscopy: The role of spin-active scattering. *Physical Review B 83*, 8 (2011), 081305(R).

[99] QI, X.-L., HUGHES, T. L., RAGHU, S., AND ZHANG, S.-C. Time-reversal-invariant topological superconductors and superfluids in two and three dimensions. *Physical Review Letters 102*, 18 (2009), 187001.

[100] QI, X.-L., HUGHES, T. L., AND ZHANG, S.-C. Topological field theory of time-reversal invariant insulators. *Physical Review B 78*, 19 (2008), 195424.

[101] QI, X.-L., AND ZHANG, S.-C. Topological insulators and superconductors. *Reviews of Modern Physics 83*, 4 (2011), 1057–1110.

[102] RAMMER, J., AND SMITH, J. Quantum field-theoretical methods in transport theory of metals. *Reviews of Modern Physics 58*, 2 (1986), 323–359.

[103] ROBINSON, J. W. A., WITT, J. D. S., AND BLAMIRE, M. G. Controlled injection of spin-triplet supercurrents into a strong ferromagnet. *Science 329*, 5987 (2010), 59–61.

[104] RYAZANOV, V. V., OBOZNOV, V. A., RUSANOV, A. Y., VERETENNIKOV, A. V., GOLUBOV, A. A., AND AARTS, J. Coupling of two superconductors through a ferromagnet: Evidence for a π junction. *Physical Review Letters 86*, 11 (2001), 2427–2430.

[105] RYU, S., SCHNYDER, A. P., FURUSAKI, A., AND LUDWIG, A. W. W. Topological insulators and superconductors: tenfold way and dimensional hierarchy. *New Journal of Physics 12* (2010), 065010.

[106] SACÉPÉ, B., OOSTINGA, J. B., LI, J., UBALDINI, A., COUTO, N. J. G., GIANNINI, E., AND MORPURGO, A. F. Gate-tuned normal and superconducting transport at the surface of a topological insulator. *Nature Communications 2* (2011), 575.

[107] SASAKI, S., KRIENER, M., SEGAWA, K., YADA, K., TANAKA, Y., SATO, M., AND ANDO, Y. Topological superconductivity in $Cu_xBi_2Se_3$. *Physical Review Letters 107* (2011), 217001.

[108] SAU, J. D., LUTCHYN, R. M., TEWARI, S., AND DAS SARMA, S. Robustness of majorana fermions in proximity-induced superconductors. *Physical Review B 82*, 9 (2010), 094522.

[109] SCHMID, A., AND SCHÖN, G. Linearized kinetic equations and relaxation processes of a superconductor near T_c. *Journal of Low Temperature Physics 20*, 1-2 (1975), 207–227.

[110] SCHNYDER, A. P., RYU, S., FURUSAKI, A., AND LUDWIG, A. W. W. Classification of topological insulators and superconductors in three spatial dimensions. *Physical Review B 78*, 19 (2008), 195125.

[111] SCHOPOHL, N. Transformation of the eilenberger equations of superconductivity to a scalar riccati equation. *Arxiv preprint arXiv:9804.064v1* (1998).

[112] SCHOPOHL, N., AND MAKI, K. Quasiparticle spectrum around a vortex line in a d-wave superconductor. *Physical Review B 52*, 1 (1995), 490–493.

[113] SCHRIEFFER, J. R. *Theory of superconductivity.* PERSEUS BOOKS, 1964.

[114] SERENE, J. W., AND RAINER, D. The quasiclassical approach to superfluid ^{3}He. *Physics Reports-Review Section of Physics Letters 101*, 4 (1983), 221–311.

[115] SHELANKOV, A. On the derivation of quasiclassical equations for superconductors. *Journal of Low Temperature Physics 60*, 1-2 (1985), 29–44.

[116] SHELANKOV, A., AND OZANA, M. Quasiclassical theory of superconductivity: A multiple-interface geometry. *Physical Review B 61*, 10 (2000), 7077–7100.

[117] SHELANKOV, A. L. Two-particle tunnelling in normal metal-semiconductor contact. *Fizika Tverdogo Tela 26*, 6 (1984), 1615–1624 [Sov. Phys. Solid State 26, 981 (1984)].

[118] SOSNIN, I., CHO, H., PETRASHOV, V. T., AND VOLKOV, A. F. Superconducting phase coherent electron transport in proximity conical ferromagnets. *Physical Review Letters 96*, 15 (2006), 157002.

[119] SOULEN JR., R. J., BYERS, J. M., OSOFSKY, M. S., NADGORNY, B., AMBROSE, T., CHENG, S. F., BROUSSARD, P. R., TANAKA, C. T., NOWAK, J., MOODERA, J. S., BARRY, A., AND COEY, J. M. D. Measuring the spin polarization of a metal with a superconducting point contact. *Science 282*, 5386 (1998), 85–88.

[120] SPRUNGMANN, D., WESTERHOLT, K., ZABEL, H., WEIDES, M., AND KOHLSTEDT, H. Evidence for triplet superconductivity in Josephson junctions with barriers of the ferromagnetic Heusler alloy Cu_2MnAl. *Physical Review B 82*, 6 (2010), 060505(R).

[121] STANESCU, T. D., SAU, J. D., LUTCHYN, R. M., AND DAS SARMA, S. Proximity effect at the superconductor-topological insulator interface. *Physical Review B 81*, 24 (2010), 241310(R).

[122] TADDEI, F., SANVITO, S., JEFFERSON, J. H., AND LAMBERT, C. J. Suppression of giant magnetoresistance by a superconducting contact. *Physical Review Letters 82*, 24 (1999), 4938–4941.

[123] TADDEI, F., SANVITO, S., AND LAMBERT, C. J. Spin-polarized transport in F/S nanojunctions. *Journal of Low Temperature Physics 124*, 1-2 (2001), 305–320.

[124] TEO, J. C. Y., FU, L., AND KANE, C. L. Surface states and topological invariants in three-dimensional topological insulators: Application to $Bi_{1-x}Sb_x$. *Physical Review B 78*, 4 (2008), 045426.

[125] THOULESS, D. J., KOHMOTO, M., NIGHTINGALE, M. P., AND DEN NIJS, M. Quantized hall conductance in a two-dimensional periodic potential. *Physical Review Letters 49*, 6 (1982), 405–408.

[126] TOKUYASU, T., SAULS, J. A., AND RAINER, D. Proximity effect of a ferromagnetic insulator in contact with a superconductor. *Physical Review B 38*, 13 (1988), 8823–8833.

[127] UPADHYAY, S. K., PALANISAMI, A., LOUIE, R. N., AND BUHRMAN, R. A. Probing ferromagnets with Andreev reflection. *Physical Review Letters 81*, 15 (1998), 3247–3250.

[128] USADEL, K. D. Generalized diffusion equation for superconducting alloys. *Physical Review Letters 25*, 8 (1970), 507–509.

[129] VAN HARLINGEN, D. J. Phase-sensitive tests of the symmetry of the pairing state in the high-temperature superconductors - evidence for $d_{x^2-y^2}$ symmetry. *Reviews of Modern Physics 67*, 2 (1995), 515–535.

[130] VOLLHARDT, D., AND WÖLFLE, P. *The superfluid phases of helium 3*. Taylor & Francis, 1990.

[131] VON KLITZING, K., DORDA, G., AND PEPPER, M. New method for high-accuracy determination of the fine-structure constant based on quantized Hall resistance. *Physical Review Letters 45*, 6 (1980), 494–497.

[132] WANG, J., SINGH, M., TIAN, M., KUMAR, N., LIU, B., SHI, C., JAIN, J. K., SAMARTH, N., MALLOUK, T. E., AND CHAN, M. H. W. Interplay between superconductivity and ferromagnetism in crystalline nanowires. *Nature Physics 6*, 5 (2010), 389–394.

[133] WILCZEK, F. Majorana returns. *Nature Physics 5*, 9 (2009), 614–618.

[134] WOLF, S. A., AWSCHALOM, D. D., BUHRMAN, R. A., DAUGHTON, J. M., VON MOLNAR, S., ROUKES, M. L., CHTCHELKANOVA, A. Y., AND TREGER, D. M. Spintronics: A spin-based electronics vision for the future. *Science 294*, 5546 (2001), 1488–1495.

[135] WOODS, G. T., SOULEN JR., R. J., MAZIN, I., NADGORNY, B., OSOFSKY, M. S., SANDERS, J., SRIKANTH, H., EGELHOFF, W. F., AND DATLA, R. Analysis of point-contact Andreev reflection spectra in spin polarization measurements. *Physical Review B 70*, 5 (2004), 054416.

[136] XIA, K., KELLY, P. J., BAUER, G. E. W., AND TUREK, I. Spin-dependent transparency of ferromagnet/superconductor interfaces. *Physical Review Letters 89*, 16 (2002), 166603.

[137] XIA, Y., QIAN, D., HSIEH, D., WRAY, L., PAL, A., LIN, H., BANSIL, A., GRAUER, D., HOR, Y. S., CAVA, R. J., AND HASAN, M. Z. Observation of a large-gap topological-insulator class with a single Dirac cone on the surface. *Nature Physics 5*, 6 (2009), 398–402.

[138] YATES, K. A., BRANFORD, W. R., MAGNUS, F., MIYOSHI, Y., MORRIS, B., COHEN, L. F., SOUSA, P. M., CONDE, O., AND SILVESTRE, A. J. The spin polarization of CrO_2 revisited. *Applied Physics Letters 91*, 17 (2007), 172504.

[139] ZAITSEV, A. Quasiclassical equations of the theory of superconductivity for contiguous metals and the properties of constricted microcontacts. *Zhurnal Eksperimentalnoi I Teoreticheskoi Fiziki 86*, 5 (1984), 1742–1758 [Sov. Phys. JETP 59, 1015 (1984)].

[140] ZHANG, D., WANG, J., DA SILVA, A. M., LEE, J. S., GUTIERREZ, H. R., CHAN, M. H. W., JAIN, J., AND SAMARTH, N. Superconducting proximity effect and possible evidence for Pearl vortices in a candidate topological insulator. *Physical Review B 84*, 16 (2011), 165120.

[141] ZHANG, H., LIU, C.-X., QI, X.-L., DAI, X., FANG, Z., AND ZHANG, S.-C. Topological insulators in Bi_2Se_3, Bi_2Te_3 and Sb_2Te_3 with a single Dirac cone on the surface. *Nature Physics 5*, 6 (2009), 438–442.

[142] ZHAO, E., LOFWANDER, T., AND SAULS, J. A. Nonequilibrium superconductivity near spin-active interfaces. *Physical Review B 70*, 13 (2004), 134510.

[143] ZHAO, E., AND SAULS, J. A. Dynamics of spin transport in voltage-biased Josephson junctions. *Physical Review Letters 98*, 20 (2007), 206601.

[144] ZHAO, E., AND SAULS, J. A. Theory of nonequilibrium spin transport and spin-transfer torque in superconducting-ferromagnetic nanostructures. *Physical Review B 78*, 17 (2008), 174511.

[145] Zhao, E., Zhang, C., and Lababidi, M. Mott scattering at the interface between a metal and a topological insulator. *Physical Review B 82*, 20 (2010), 205331.

Appendix

A. Parameterisation of $U(4)$ matrices

The boundary conditions discussed in chapter 3 are formulated in terms of incoming Riccati amplitudes and the scattering matrix for quasiparticles in the normal state. The only fundamental symmetry of this matrix is unitarity. Other symmetries may be implied by symmetries of the physical problem under consideration. In the case we consider here, i.e. an N/I/FM interface, the only remaining symmetry is translational invariance in the x-y-plane, implying the conservation of parallel momentum. Spin-rotation symmetry is fully broken if the quantisation axes of the interface and the ferromagnet are misaligned.

A general unitary 4×4 matrix has 16 free parameters, a 3×3 matrix has 9. Thus, to facilitate the interpretation of results, it is highly desirable to find a representation of the S-matrix that supplies a set of parameters with a clear physical meaning, and, if possible, eliminate at least some of them. The latter is indeed possible, since we are free to choose the spin-quantisation in the superconductor (normal metal here), and because the region which we define to be the interface can extend into the asymptotic regions (N and FM parts) without changing physical results. Eventually, the considerations we discuss here lead to the parameterisations stated in eqs. (4.2) and (4.3).

It is a well-known result of linear algebra that any $n \times n$ matrix possesses at least one singular value decomposition (SVD):

$$A = U\Lambda V^\dagger, \tag{A.1}$$

where $\Lambda = \mathrm{diag}(\lambda_1, \lambda_2, ..., \lambda_n)$, with λ_i real and ≥ 0 and U, V unitary. Our starting point is a 'partial' singular value decomposition of the S-matrix, i.e., a SVD is computed for the transmission and reflection sub-blocks independently [40, 53]:

$$S = \begin{pmatrix} URV^\dagger & WT\tilde{Z}^\dagger \\ \tilde{W}\tilde{T}Z^\dagger & -\tilde{U}\tilde{R}\tilde{V}^\dagger \end{pmatrix}, \tag{A.2}$$

where U, V, W, $\tilde{Z}$, $\tilde{W}$, Z, $\tilde{U}$ and $\tilde{V}$ are unitary 2×2-matrices, while R, T, $\tilde{T}$, $\tilde{R}$ are diagonal, real matrices with positive entries. These singular values can be identified with generalised transmission and reflection parameters, while the outer unitary matrices contain all scattering phases and rotations in spin-space implied by the spin-activity of the interface. As explained above, the SVD is general, which means that we did not exploit the unitarity of S so far. The unitarity relation $SS^\dagger = 1$ provides us with the equations:

$$U(1 - R^2)U^\dagger = WTT^\dagger W^\dagger, \quad V(1 - R^2)V^\dagger = Z\tilde{T}^\dagger\tilde{T}Z^\dagger, \tag{A.3}$$
$$\tilde{U}(1 - \tilde{R}^2)\tilde{U}^\dagger = \tilde{W}\tilde{T}\tilde{T}^\dagger\tilde{W}^\dagger, \quad \tilde{V}(1 - \tilde{R}^2)\tilde{V}^\dagger = \tilde{Z}T^\dagger T\tilde{Z}^\dagger,$$

which are the diagonal parts of $S^\dagger S = 1$ and $SS^\dagger = 1$. The first of these equations can be written as $W^\dagger U(1 - R^2)U^\dagger W = TT^\dagger$. Obviously $(1 - R^2)$ and $TT^\dagger$ are related to

one another by what is called a similarity transformation. A similarity transformation preserves the eigenvalues of any matrix. In this case, both matrices are diagonal and one may erroneously infer that they should thus be identical. However, it is clear that while the eigenvalues are the same, a similarity transformation still allows for a permutation, so $(1 - R^2) = TT^\dagger$ does not hold in general. Then again, permuting the eigenvalues of a 2×2 diagonal matrix corresponds to the similarity transformation $\Sigma \to \sigma_x \Sigma \sigma_x$ and we may just redefine the matrices $W, Z, \tilde{W}, \tilde{Z}$ by $X \to X \sigma_x$ if needed to exclude this possibility. Note that such a redefined matrix is again unitary, which implies that this construction does not cause any contradictions to the SVD that we started with. To sum it up, we can assume without loss of generality that

$$(1 - R^2) = TT^\dagger = \tilde{T}^\dagger \tilde{T}, \tag{A.4}$$

$$(1 - \tilde{R}^2) = T^\dagger T = \tilde{T}\tilde{T}^\dagger. \tag{A.5}$$

Since both T and $\tilde{T}$ are real with positive eigenvalues, we can infer $T = \tilde{T}$ and $R = \tilde{R} = \sqrt{1 - T^2}$ from this.

To proceed, we need to assume that the matrices $\Phi = W^\dagger U$, $\Psi = Z^\dagger V$, $\tilde{\Phi} = \tilde{W}^\dagger \tilde{U}$ and $\tilde{\Psi} = \tilde{Z}^\dagger \tilde{V}$ are diagonal. This is necessarily the case if the eigenvalues of T, R are not degenerate. Since we consider a ferromagnetic interface, this is generically true. If they are degenerate, i.e., R and T are proportional to the unit matrix, the following argument holds as well. Namely, it follows from the remaining unitarity conditions

$$URV^\dagger Z\tilde{T}^\dagger \tilde{W}^\dagger = WT\tilde{Z}^\dagger \tilde{V}\tilde{R}U^\dagger, \tag{A.6}$$

$$VRU^\dagger WT\tilde{Z}^\dagger = Z\tilde{T}^\dagger \tilde{W}^\dagger \tilde{U}\tilde{R}\tilde{V}^\dagger \tag{A.7}$$

that

$$\Phi^\dagger \tilde{\Psi} = \Psi^\dagger \tilde{\Phi}. \tag{A.8}$$

This can be used to simplify the partial SVD [53]:

$$S = \begin{pmatrix} U\Phi^\dagger R\Phi V^\dagger & WT\tilde{Z}^\dagger \\ \tilde{W}\tilde{T}Z^\dagger & -\tilde{U}\tilde{\Psi}^\dagger \tilde{R}\tilde{\Psi}\tilde{V}^\dagger \end{pmatrix} = \begin{pmatrix} \mathcal{U} & 0 \\ 0 & \tilde{\mathcal{U}} \end{pmatrix} \begin{pmatrix} R & T \\ T & -R \end{pmatrix} \begin{pmatrix} \mathcal{V}^\dagger & 0 \\ 0 & \tilde{\mathcal{V}}^\dagger \end{pmatrix}, \tag{A.9}$$

with the definitions $U\Phi^\dagger \to \mathcal{U}$, $\tilde{U}\tilde{\Psi}^\dagger \to \tilde{\mathcal{U}}$, $\Phi V^\dagger \to \mathcal{V}^\dagger$ and $\tilde{\Psi}\tilde{V}^\dagger \to \tilde{\mathcal{V}}^\dagger$. This means that the partial SVD is first redefined for the diagonal blocks and the equation then follows from (A.8) and the fact that either, $\Psi, \Phi, \tilde{\Psi}, \tilde{\Phi}$ are diagonal, or R and T are proportional to the unit matrix. Thus, we arrived at a decomposition with an appealing structure. The central part is a block-diagonal scattering matrix with real entries that can be identified with generalised reflection and transmission coefficients. The outer matrices define rotations in spin-space and phase factors for incoming $(\mathcal{V}, \tilde{\mathcal{V}})$ and outgoing $(\mathcal{U}, \tilde{\mathcal{U}})$ scattering states on either side of the interface. One may continue to decompose them in matrices containing scattering phases and matrices belonging to $SU(2)$, i.e., rotations in spin-space. We do not discuss further details of this and simply state the final result [53]:

$$\begin{aligned} S = & \begin{pmatrix} Q & 0 \\ 0 & \tilde{Q} \end{pmatrix} \begin{pmatrix} \Phi^{\frac{1}{2}} & 0 \\ 0 & \tilde{\Phi}^{\frac{1}{2}} \end{pmatrix} \begin{pmatrix} Y & 0 \\ 0 & \tilde{Y} \end{pmatrix} \\ & \times \begin{pmatrix} \sqrt{1 - TT} & \Psi T \\ \Psi^\dagger T & -\sqrt{1 - TT} \end{pmatrix} \\ & \times \begin{pmatrix} Y^\dagger & 0 \\ 0 & \tilde{Y}^\dagger \end{pmatrix} \begin{pmatrix} \Phi^{\frac{1}{2}} & 0 \\ 0 & \tilde{\Phi}^{\frac{1}{2}} \end{pmatrix} \begin{pmatrix} Q^\dagger & 0 \\ 0 & \tilde{Q}^\dagger \end{pmatrix}. \end{aligned} \tag{A.10}$$

The matrices Q, $\tilde{Q}$, Y, $\tilde{Y} \in SU(2)$ are the rotations in spin-space. They can be parameterised as:

$$\text{rot}(\alpha, \varphi) \equiv \begin{pmatrix} \cos(\alpha/2) & -\sin(\alpha/2)e^{-i\varphi} \\ \sin(\alpha/2)e^{i\varphi} & \cos(\alpha/2) \end{pmatrix}. \tag{A.11}$$

The matrices $\Phi^{\frac{1}{2}}$, $\tilde{\Phi}^{\frac{1}{2}}$ and $\Psi^{\frac{1}{2}}$ contain the scattering phases ($\Psi = (\Psi^{\frac{1}{2}})^2$). They can be written as:

$$\text{phase}(\eta, \vartheta) \equiv e^{i\eta}e^{i\sigma_z \vartheta/2}. \tag{A.12}$$

For reasons that are obvious from our discussion of the spin-mixing effect, we choose a definition where η is a global phase and ϑ a relative phase [53]. Note that this decomposition has exactly 16 independent parameters and thus describes a general $U(4)$ matrix.

On the basis of this decomposition, we may now try to reduce the number of free parameters using the 'gauge' freedom that we have. To this effect, we exploit the fact that we are free to choose a spin-quantisation axis in the normal region, since the scattering states on that side of the interface are invariant under spin-rotations. We thus assume $Q = 1$ [53]. Moreover, as explained in chapter 4, we may assume that the quantisation axis rotates in the x-z-plane only, since an additional rotation in the x-y-plane can be accounted for by the transformation stated in eq. (4.4). We hence have $Y^\dagger = Y^T$, $\tilde{Y}^\dagger = \tilde{Y}^T$, $\tilde{Q}^\dagger = Q^T$ and Ψ is real [53].

The second 'gauge' freedom we have arises from the fact that the choice of an interface region is arbitrary in the sense that all physical results must be independent of how far we define the interface to extend into the asymptotic regions.[a] This results in a gauge transformation that accounts for the additional propagation of the scattered waves inside these asymptotic regions [53]:

$$S' = \eta S \eta \tag{A.13}$$

with

$$\eta = \begin{pmatrix} e^{i\eta_1} & 0 \\ 0 & e^{i(\eta_2 + \eta_3 + (\eta_2 - \eta_3)\sigma_z)/2} \end{pmatrix}. \tag{A.14}$$

By plugging the transformed S-matrix into the boundary conditions, one can show that both the outgoing coherence and the distribution functions are indeed invariant [53]. The additional phases η, η_2, η_3 can be used to obtain exactly the structure of the S-matrix shown in eq. (4.2) [53]. Finally, we discuss the relation of this decomposition to the spin-mixing phases. For reflections on the left side of the interface (superconductor side), the only complex phase that remains is the relative phase in $\Phi^{\frac{1}{2}}$, which must thus be identified with the spin-mixing angle [53]:

$$\vartheta = \vartheta_\Phi. \tag{A.15}$$

It is also clear that the rotation angle α entering the reflection block on the SC side, is due to Y, which is why we refer to it as α_Y in chapters 4 and 5. Unfortunately, there is no simple relation for the mixing phases $\vartheta_{2,3}$.

We focused on the more complicated case of ferromagnetic trajectories here. The 3×3 case relevant for the half metallic ones is fully analogous, but also simpler, as all $\sim$-matrices above are just scalar phases [40]. This also implies the important relation [53]:

$$\vartheta_2 = \vartheta_\Phi/2, \tag{A.16}$$

that we refer to in chapter 4.

---

[a]Obviously, the interface must still be a lot smaller than the coherence length.

B. Scattering Matrix of the Box-Potential

The normal-state scattering matrix entering the quasiclassical boundary conditions cannot be obtained within QC theory itself. In the case of a box-potential, we calculate it from plane wave matching in the normal state, using the model described in chapter 4.

We will consider two types of interface Hamiltonians, either containing a ferromagnetic exchange field:

$$H^{\mathrm{I}} = \sum_{\mathbf{k}\mu\nu} c_{\mathbf{k}\mu}^{\dagger} (\xi_{\mathbf{k}}^{\mathrm{I}} \delta_{\mu\nu} + \frac{\vec{J_{\mathrm{I}}}}{2} \cdot \vec{\sigma}) c_{\mathbf{k}\nu} \tag{B.1}$$

or a spin-orbit coupling term:

$$H^{\mathrm{I}} = \sum_{\mathbf{k}\mu\nu} c_{\mathbf{k}\mu}^{\dagger} (\xi_{\mathbf{k}}^{\mathrm{I}} \delta_{\mu\nu} + \alpha \vec{g}_{\mathbf{k}} \cdot \vec{\sigma}) c_{\mathbf{k}\nu}. \tag{B.2}$$

Here, the $\vec{g}$-vector is given by [41]:

$$\vec{g}_{\mathbf{k}} = \frac{\mathbf{k} \times \hat{z}}{|\mathbf{k} \times \hat{z}|} = \frac{1}{k_x^2 + k_y^2} (k_y, -k_x, 0) \tag{B.3}$$

$$= (\sin \varphi_{\mathbf{k}}, -\cos \varphi_{\mathbf{k}}, 0).$$

Accordingly, the normal state Hamiltonians of the ferromagnet and the superconductor read:

$$H^{\mathrm{FM}} = \sum_{\mathbf{k}\mu\nu} c_{\mathbf{k}\mu}^{\dagger} (\xi_{\mathbf{k}}^{\mathrm{FM}} \delta_{\mu\nu} + \frac{\vec{J}}{2} \cdot \vec{\sigma}) c_{\mathbf{k}\nu}, \tag{B.4}$$

$$H^{\mathrm{SC}} = \sum_{\mathbf{k}\mu\nu} c_{\mathbf{k}\mu}^{\dagger} (\xi_{\mathbf{k}}^{\mathrm{SC}} \delta_{\mu\nu}) c_{\mathbf{k}\nu}. \tag{B.5}$$

Obviously, H^{SC} is invariant under rotations in spin-space, while both H^{I} and H^{FM} break spin-rotation symmetry. For $\xi_{\mathbf{k}}^{\mathrm{I,SC,FM}}$, we assume a parabolic dispersion with the same effective mass in all cases. The dispersions $\xi_{\mathbf{k}}^{\mathrm{I}}$ and and $\xi_{\mathbf{k}}^{\mathrm{FM}}$ are, however, shifted by a constant energy V_{I} and V_{FM} respectively compared to $\xi_{\mathbf{k}}^{\mathrm{SC}}$. No matter whether an interface-layer with spin-orbit coupling or with a ferromagnetic exchange field is considered, for any wave vector $\mathbf{k}$, there is a unitary matrix $U_{\mathbf{k}}$ mapping the spin-eigenbasis of the interface to that of the ferromagnet:

$$U_{\mathbf{k}} = \begin{pmatrix} \cos \frac{\alpha_{\mathbf{k}}}{2} & -\sin \frac{\alpha_{\mathbf{k}}}{2} e^{-i\varphi_{\mathbf{k}}} \\ \sin \frac{\alpha_{\mathbf{k}}}{2} e^{i\varphi_{\mathbf{k}}} & \cos \frac{\alpha_{\mathbf{k}}}{2} \end{pmatrix}. \tag{B.6}$$

The k-dependence arises only in the spin-orbit case and is the crucial mechanism leading to p-wave superconductivity in the FM layer.

The scattering matrix is obtained by diagonalising the Hamiltonians and inferring the respective values of k_z at the Fermi-level for a given $k_{||}$. The corresponding wave-functions in the three layers are then matched at the SC/I and the I/FM interface, respectively, assuming that the spin-quantisation axis in the SC is aligned with that of the interface, while at the I/FM interface, the rotation $U_{\mathbf{k}}$ must be taken into account [53, 51]. Solving this problem is an exercise in elementary quantum mechanics, we presented a solution of it in Ref. [51].

As explained in chapter 3, the requirement that $k_{||}$ be conserved across the interface implies that even if the ferromagnet is not fully spin-polarised, some trajectories will have

an evanescent solution in the minority band of the FM, corresponding to the half metallic case. In the case where this minority band solution is propagating, we obtain a 4×4 scattering matrix. If it is evanescent, the matrix is 3×3.

The plane wave ansatz for the normal metal (more precisely, the superconductor in the normal state) is [53]:

$$\Psi^{\text{SC}} = \frac{e^{i\vec{k}_{||}\vec{r}_{||}}}{\sqrt{v_1}} \left[\begin{pmatrix} s_{1+} \\ s_{1-} \end{pmatrix} e^{ik_1 z} + \begin{pmatrix} A_{1+} \\ A_{1-} \end{pmatrix} e^{-ik_1 z} \right], \tag{B.7}$$

with $|\vec{k}_{||}|^2 + k_1^2 = 2mE_F/\hbar^2$. The plane waves inside the interface have imaginary wave vectors if the interface potential is larger than the Fermi-energy. We thus have [53]:

$$\Psi^{\text{I}} = e^{i\vec{k}_{||}\vec{r}_{||}} U_{\mathbf{k}} \begin{pmatrix} B_+ e^{\kappa_+ z} + C_+ e^{-\kappa_+ z} \\ B_- e^{\kappa_- z} + C_- e^{-\kappa_- z} \end{pmatrix}. \tag{B.8}$$

The values $\kappa_\pm$ depend on the interface Hamiltonian. In chapter 6, we also considered the case where some of the interface plane waves are propagating. The interface spinor must be rotated onto the quantisation axis of the FM, which is why $U_{\mathbf{k}}$ appears here.

Finally, the ansatz for the FM reads [53]:

$$\Psi^{\text{FM}} = e^{i\vec{k}_{||}\vec{r}_{||}} \left[\begin{pmatrix} \frac{s_2}{\sqrt{v_2}} e^{-ik_2(z-a)} \\ \frac{s_3}{\sqrt{v_3}} e^{-ik_3(z-a)} \end{pmatrix} + \begin{pmatrix} \frac{A_2}{\sqrt{v_2}} e^{ik_2(z-a)} \\ \frac{A_3}{\sqrt{v_3}} e^{ik_3(z-a)} \end{pmatrix} \right], \tag{B.9}$$

where $|\vec{k}_{||}|^2 + k_2^2 = 2m(E_F - V_{\text{FM}} + J/2)/\hbar^2$ and $|\vec{k}_{||}|^2 + k_3^2 = 2m(E_F - V_{\text{FM}} - J/2)/\hbar^2$ if both solutions are propagating (FM-case), and

$$\Psi^{\text{FM}} = e^{i\vec{k}_{||}\vec{r}_{||}} \left[\begin{pmatrix} \frac{s_2}{\sqrt{v_2}} e^{-ik_2(z-a)} \\ 0 \end{pmatrix} + \begin{pmatrix} \frac{A_2}{\sqrt{v_2}} e^{ik_2(z-a)} \\ D_3 e^{-\kappa_3(z-a)} \end{pmatrix} \right], \tag{B.10}$$

where $|\vec{k}_{||}|^2 + k_2^2 = 2m(E_{\text{F}} - V_{\text{FM}} + J/2)/\hbar^2$ and $|\vec{k}_{||}|^2 - \kappa_3^2 = 2m(E_{\text{F}} - V_{\text{FM}} - J/2)/\hbar^2$, in the half metallic case.

The scattering matrices are then defined by the relations [53]:

$$\begin{pmatrix} A_{1+} \\ A_{1-} \\ A_2 \\ A_3 \end{pmatrix} = S_{\text{FM}} \begin{pmatrix} s_{1+} \\ s_{1-} \\ s_2 \\ s_3 \end{pmatrix}, \quad \begin{pmatrix} A_{1+} \\ A_{1-} \\ A_2 \end{pmatrix} = S_{\text{HM}} \begin{pmatrix} s_{1+} \\ s_{1-} \\ s_2 \end{pmatrix}, \tag{B.11}$$

for these two cases.

Spin-rotation matrix

We discuss the spin-orbit coupled case first and introduce a spin-rotation mapping the quantisation axis of the interface onto the $\hat{z}$-axis [41]:

$$\mathcal{U}_{\mathbf{k}} = \frac{1}{\sqrt{2}} \begin{pmatrix} 1 & -ie^{-i\varphi_{\mathbf{k}}} \\ -ie^{i\varphi_{\mathbf{k}}} & 1 \end{pmatrix}. \tag{B.12}$$

If the quantisation axis of the FM is not aligned with the $\hat{z}$-axis, a second rotation, mapping the FM-quantisation axis onto the $\hat{z}$-axis, must be considered:

$$\mathcal{D} = \begin{pmatrix} \cos\frac{\alpha}{2} & -\sin\frac{\alpha}{2} \\ \sin\frac{\alpha}{2} & \cos\frac{\alpha}{2} \end{pmatrix}, \tag{B.13}$$
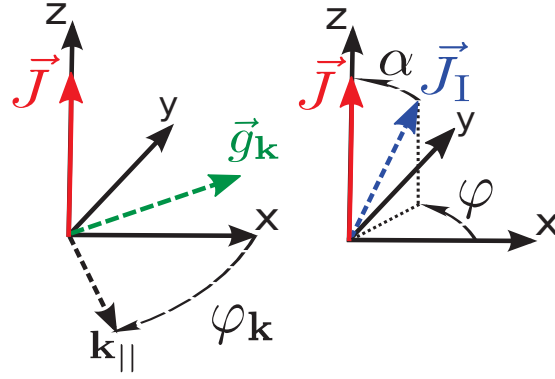
Figure B.1. – Definition of angles for the spin-orbit interface (left) and the ferromagnetic interface (right).

assuming that the rotation is in the x-z-plane. We then have $U_{\mathbf{k}} = \mathcal{D}^\dagger \mathcal{U}_{\mathbf{k}}$.

In the ferromagnetic case, $U_{\mathbf{k}}$ is independent of $\mathbf{k}$ and given by:

$$U = \begin{pmatrix} \cos\frac{\alpha}{2} & -\sin\frac{\alpha}{2}e^{-i\varphi} \\ \sin\frac{\alpha}{2}e^{i\varphi} & \cos\frac{\alpha}{2} \end{pmatrix},$$ (B.14)

where α and φ characterise the misalignment between $\vec{J}_{\mathrm{I}}$ and $\vec{J}$.

C. Scattering Matrix of the Smooth Potential

The scattering matrix for the smooth potential model is obtained numerically with the Recursive Green's Function technique. Since the effective mass is assumed to be the same throughout the structure, we do not have the problem of having to introduce a transfer-Hamiltonian, as in the case of the topological insulator-superconductor interface. Instead, the hopping elements of the tight-binding model are the same everywhere and read:

$$V = \frac{2\hbar^2 t^2}{m}\sigma_0, \tag{C.1}$$

with $t = -i/2a$. The on-site Hilbert-space only has a spin degree of freedom, since we consider a single band and the normal state of the system. The on-site term reads:

$$O(n, k_{||}) = \frac{\hbar^2}{2m}(k_{||}^2 - 8t^2)\sigma_0 + V(n), \tag{C.2}$$

where $V(n)$ is a matrix in spin-space that accounts for the interface potential whose spatial variation is stated in chapter 3. We couple a central device region, where $V(n)$ varies, to semi-infinite leads on both sides, where $V = 0$ (left lead) and $V = V_{\text{FM}} + \frac{J}{2}\sigma_3$ (right lead).

The scattering matrix is calculated from the Green's function by means of the Fisher-Lee relations:

$$S(k_{||}) = \begin{pmatrix} R_{\text{L}} & T_{\text{LR}} \\ T_{\text{RL}} & R_{\text{R}} \end{pmatrix}, \tag{C.3}$$

with:

$$R_{\text{L}} = -\sigma_0 + iv_1 G_{1,1}, \quad T_{\text{LR}} = i\sqrt{v_1}G_{1,N}\nu \tag{C.4}$$
$$T_{\text{RL}} = i\sqrt{v_1}\nu G_{N,1}, \quad R_{\text{R}} = -\sigma_0 + i\nu G_{N,N}\nu,$$

where v_1 is the Fermi-velocity of the normal metal and $\nu^2 = \text{diag}(v_2, v_3)$, with $v_{2,3}$ the Fermi-velocities of the FM-bands. 1 and N are the sites at the endpoints of the central device, and $G = G(k_{||}, \epsilon = E_{\text{F}})$. As discussed in the section on the parameterisation of the S-matrix, it is irrelevant how far the central-device region extends into the region where $V = const$.

D. Solution of the Boundary Conditions for the Josephson Geometry

Solutions at the SC/FM-interface

The solutions of the boundary conditions for FM-trajectories read:

$$\Gamma_2 = \gamma'_{22} + \Gamma_{2\leftarrow 1}\tilde{\gamma}_1\gamma'_{12} + \Gamma_{2\leftarrow 3}\tilde{\gamma}_3\gamma'_{32}, \quad \Gamma_3 = \gamma'_{33} + \Gamma_{3\leftarrow 1}\tilde{\gamma}_1\gamma'_{13} + \Gamma_{3\leftarrow 2}\tilde{\gamma}_2\gamma'_{23}, \tag{D.1}$$

with the auxiliary amplitudes:

$$\Gamma_{2\leftarrow 1} = (\gamma'_{21} + \Gamma_{2\leftarrow 3}\tilde{\gamma}_3\gamma'_{31}) \cdot N_1, \quad \Gamma_{3\leftarrow 1} = (\gamma'_{31} + \Gamma_{3\leftarrow 2}\tilde{\gamma}_2\gamma'_{21}) \cdot N_1, \tag{D.2}$$
$$\Gamma_{2\leftarrow 3} = (\gamma'_{23} + \gamma'_{21}N_1\tilde{\gamma}_1\gamma'_{13}) \cdot N_3, \quad \Gamma_{3\leftarrow 2} = (\gamma'_{32} + \gamma'_{31}N_1\tilde{\gamma}_1\gamma'_{12}) \cdot N_2,$$

and

$$N_1 = (1 - \tilde{\gamma}_1\gamma'_{11})^{-1}, \tag{D.3}$$
$$N_2 = (1 - \tilde{\gamma}_2\gamma'_{22} - \tilde{\gamma}_2\gamma'_{21}N_1\tilde{\gamma}_1\gamma'_{12})^{-1}, \quad N_3 = (1 - \tilde{\gamma}_3\gamma'_{33} - \tilde{\gamma}_3\gamma'_{31}N_1\tilde{\gamma}_1\gamma'_{13})^{-1}.$$

These solutions hold for both retarded and Matsubara amplitudes. We do not state the solution for Γ_1, as it is irrelevant here.

The diagrammatic representation of these solutions can be cast into a finite graph, as demonstrated in Fig. D.2 for Γ_2. The graph is to be understood in the following sense: The complete solution is obtained by summing over all paths that can be generated by walking through the graph, starting at one of the three 'entrance' diagrams in the topmost row and ending at on of the three 'exit' diagrams shown in the second row. Obviously, there are loops in the graph through which one can pass an arbitrary number of times, and thus the number of paths contributing to the solution is infinite.

For HM-trajectories, the solution simplifies to:

$$\Gamma_2 = \gamma'_{22} + \Gamma_{2\leftarrow 1}\tilde{\gamma}_1\gamma'_{12}, \tag{D.4}$$

with the auxiliary amplitude:

$$\Gamma_{2\leftarrow 1} = \gamma'_{21} \cdot N_1. \tag{D.5}$$

Solution at the anti-ferromagnetic domain boundary

We need to match four transport channels in this case, as we have a FM-layer on both sides of the interface. In the most general case, this would imply a very cumbersome solution. However, since we consider an anti-ferromagnetic orientation of the magnetisation, the scattering matrix, which in this simplified picture is determined by wave vector mismatches only and spin conserving, has the following structure:

$$S = \begin{pmatrix} R & T \\ T^\top & R \end{pmatrix} \tag{D.6}$$

with

$$R = \begin{pmatrix} r & 0 \\ 0 & -r \end{pmatrix}, \; T = \begin{pmatrix} 0 & t \\ -t & 0 \end{pmatrix} \tag{D.7}$$

and

$$r = \frac{k_\uparrow - k_\downarrow}{k_\uparrow + k_\downarrow}, \; t = \frac{2\sqrt{k_\uparrow k_\downarrow}}{k_\uparrow + k_\downarrow}. \tag{D.8}$$
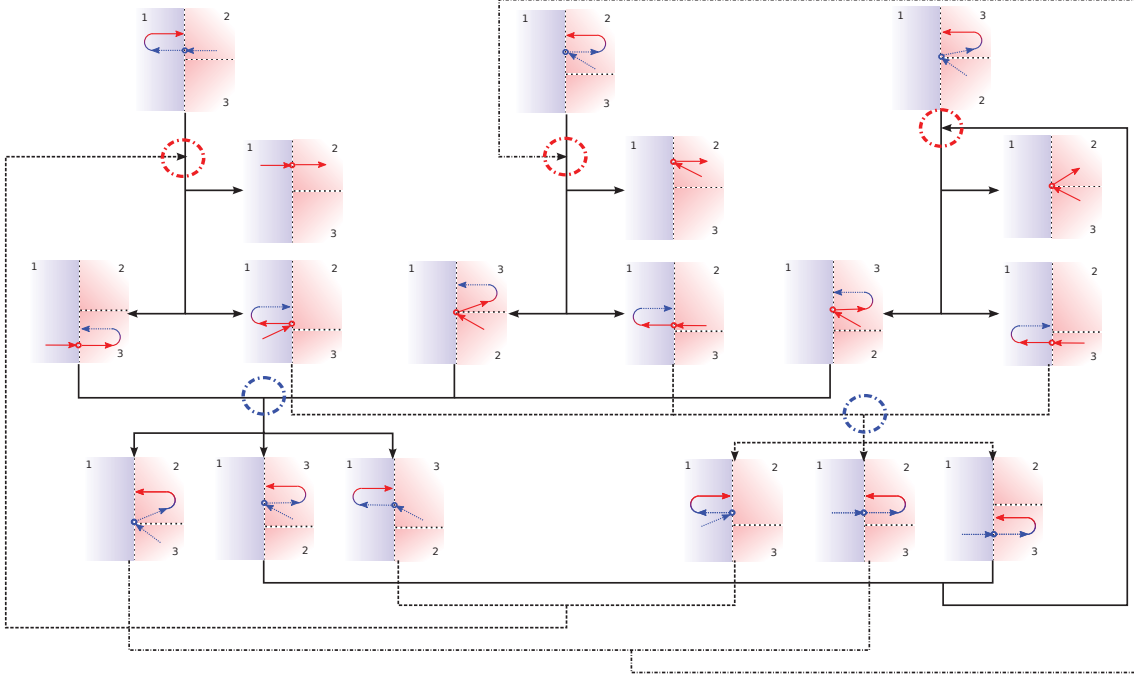
Figure D.2. – Diagrammatic solution of the boundary conditions for Γ_2. The terms corresponding to these diagrams are (always left to right): (top row) $\gamma_1 \tilde{T}_{12}$, $\gamma_2 \tilde{r}_{22}$, $\gamma_3 \tilde{r}_{32}$; (second row) T_{21}, r_{22}, r_{23}; (third row) $\tilde{\gamma}_3 T_{31}$, $\tilde{\gamma}_1 R_{11}$, $\tilde{\gamma}_3 r_{32}$, $\tilde{\gamma}_1 T_{12}$, $\tilde{\gamma}_3 r_{33}$, $\tilde{\gamma}_1 T_{13}$; (fourth row) $\gamma_2 \tilde{r}_{23}$, $\gamma_3 \tilde{r}_{33}$, $\gamma_1 \tilde{T}_{13}$, $\gamma_1 \tilde{R}_{11}$, $\gamma_2 \tilde{T}_{21}$, $\gamma_3 \tilde{T}_{31}$. Red circles indicate the endpoints of finite sub-loops.

Note the off-diagonal structure of T, which implies that quasiparticles change bands when transmitting through the boundary. The structure of the S-matrix implies that the boundary conditions decouple into two sets of independent equations, each involving two of the four channels:

$$\Gamma_{1'} = \gamma'_{1'1'} + \Gamma_{1' \leftarrow 4'} \tilde{\gamma}_{4'} \gamma'_{4'1'}, \tag{D.9}$$
$$\Gamma_{2'} = \gamma'_{2'2'} + \Gamma_{2' \leftarrow 3'} \tilde{\gamma}_{3'} \gamma'_{3'2'},$$
$$\Gamma_{3'} = \gamma'_{3'3'} + \Gamma_{3' \leftarrow 2'} \tilde{\gamma}_{2'} \gamma'_{2'3'},$$
$$\Gamma_{4'} = \gamma'_{4'4'} + \Gamma_{4' \leftarrow 1'} \tilde{\gamma}_{1'} \gamma'_{1'4'},$$

with the auxiliary amplitudes:

$$\Gamma_{1' \leftarrow 4'} = \gamma'_{1'4'} \cdot (1 - \tilde{\gamma}_{4'} \gamma'_{4'4'})^{-1}, \tag{D.10}$$
$$\Gamma_{4' \leftarrow 1'} = \gamma'_{4'1'} \cdot (1 - \tilde{\gamma}_{1'} \gamma'_{1'1'})^{-1},$$
$$\Gamma_{2' \leftarrow 3'} = \gamma'_{2'3'} \cdot (1 - \tilde{\gamma}_{3'} \gamma'_{3'3'})^{-1},$$
$$\Gamma_{3' \leftarrow 2'} = \gamma'_{3'2'} \cdot (1 - \tilde{\gamma}_{2'} \gamma'_{2'2'})^{-1}.$$

We included an accent in the channel labels to express that these labels do not correspond to the convention followed otherwise in this thesis. Specifically, we have $1' \equiv\, \uparrow$ (left), $2' \equiv\, \downarrow$ (left), $3' \equiv\, \uparrow$ (right) and $4' \equiv\, \downarrow$ (right).
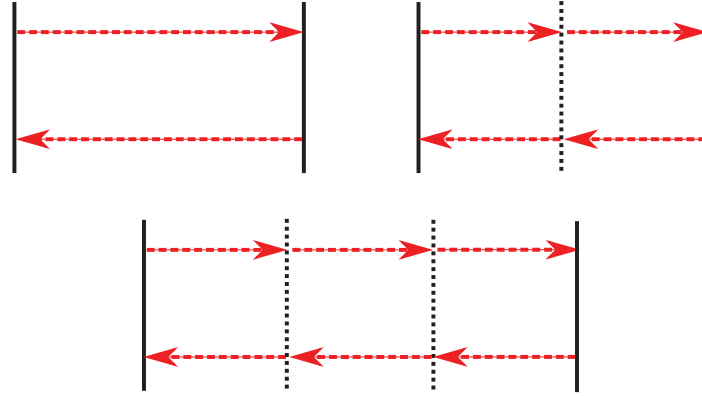
Figure E.3. – Iteration loop for the 1 domain (top left) 2 domain (top right) and 3 domain (bottom) junctions. Red arrows indicate simultaneous propagations. At the end of each propagation, the boundary conditions are solved at the respective interface or domain boundary.

E. Numerical Scheme for Multilayer Junctions

In the multilayer geometries discussed in chapter 6, we obtain the coherence function numerically by iterating the boundary conditions and propagations through the FM-layer. The iteration steps are shown in Fig. E.3. Every iteration starts by solving the boundary conditions at all interfaces and domain boundaries. We use the incoming bulk-coherence functions in the SC-electrode, while those inside the FM-layer are initialised with 0 at the beginning of the iteration. We repeat the iteration steps two times in the 1-domain and in the 2-domain case, and three times in the 3-domain case before we check the convergence condition:

$$\frac{|\gamma_2^{\mathrm{I,new}}(\epsilon_n, k_{||}=0) - \gamma_2^{\mathrm{I,old}}(\epsilon_n, k_{||}=0)|}{|\gamma_2^{\mathrm{I,new}}(\epsilon_n, k_{||}=0) + \gamma_2^{\mathrm{I,old}}(\epsilon_n, k_{||}=0)|} \leq \eta, \tag{E.1}$$

and update $\gamma_2^{\mathrm{I,old}}(\epsilon_n, k_{||}=0) = \gamma_2^{\mathrm{I,new}}(\epsilon_n, k_{||}=0)$. This is to avoid a spurious termination of the iteration caused by the initialisation of the FM-coherence functions.

Apart from η, the Matsubara sum cut-off and the number of k-points considered for the FS-average control the numerical precision of our calculation. These parameters were generally chosen so that all plots are free of perceptible imprecision.

F. Solution of the Linearised Equations

In this appendix, we briefly state the solutions of the linearised equations (eq. (6.6)) for the Josephson geometry.

We first define the quantities:

$$\tilde{\mathcal{A}}_2^{\text{II}} = \mathcal{A}_2^{\text{II}} + \rho_2^{\text{II}}\beta_2\mathcal{A}_2^{\text{I}} + \rho_{23}^{\text{II}}\beta_3\mathcal{A}_3^{\text{I}}, \quad \tilde{\mathcal{A}}_3^{\text{II}} = \mathcal{A}_3^{\text{II}} + \rho_{32}^{\text{II}}\beta_2\mathcal{A}_2^{\text{I}} + \rho_3^{\text{II}}\beta_3\mathcal{A}_3^{\text{I}}, \tag{F.1}$$

and

$$\tilde{\rho}_2^{\text{II}} = \rho_2^{\text{I}}\rho_2^{\text{II}}\beta_2^2 + \rho_{23}^{\text{II}}\rho_{32}^{\text{I}}\beta_2\beta_3, \quad \tilde{\rho}_3^{\text{II}} = \rho_3^{\text{I}}\rho_3^{\text{II}}\beta_3^2 + \rho_{32}^{\text{II}}\rho_{23}^{\text{I}}\beta_3\beta_2, \tag{F.2}$$
$$\tilde{\rho}_{23}^{\text{II}} = \rho_2^{\text{II}}\rho_{23}^{\text{I}}\beta_2\beta_3 + \rho_3^{\text{I}}\rho_{23}^{\text{II}}\beta_3^2, \quad \tilde{\rho}_{32}^{\text{II}} = \rho_3^{\text{II}}\rho_{32}^{\text{I}}\beta_3\beta_2 + \rho_{32}^{\text{II}}\rho_2^{\text{I}}\beta_2^2.$$

In the next step, we define:

$$\bar{\mathcal{A}}_3^{\text{II}} = \tilde{\mathcal{A}}_3^{\text{II}} + \tilde{\rho}_{32}^{\text{II}}(1 - \tilde{\rho}_2^{\text{II}})^{-1}\tilde{\mathcal{A}}_2^{\text{II}}, \quad \bar{\rho}_3^{\text{II}} = \tilde{\rho}_{32}^{\text{II}}(1 - \tilde{\rho}_2^{\text{II}})^{-1}\tilde{\rho}_{23}^{\text{II}} + \tilde{\rho}_3^{\text{II}}. \tag{F.3}$$

In terms of these parameters, the solutions read:

$$\Gamma_3^{\text{II}} = (1 - \bar{\rho}_3^{\text{II}})^{-1}\bar{\mathcal{A}}_3^{\text{II}}, \quad \Gamma_2^{\text{II}} = (1 - \tilde{\rho}_2^{\text{II}})^{-1}(\tilde{\mathcal{A}}_2^{\text{II}} + \tilde{\rho}_{23}^{\text{II}}\Gamma_3^{\text{II}}), \tag{F.4}$$
$$\Gamma_2^{\text{I}} = \mathcal{A}_2^{\text{I}} + \rho_2^{\text{I}}\beta_2\Gamma_2^{\text{II}} + \rho_{23}^{\text{I}}\beta_3\Gamma_3^{\text{II}}, \quad \Gamma_3^{\text{I}} = \mathcal{A}_3^{\text{I}} + \rho_{32}^{\text{I}}\beta_2\Gamma_2^{\text{II}} + \rho_3^{\text{I}}\beta_3\Gamma_3^{\text{II}}.$$

G. Invariance of the CPR under Rotations in the x-y-Plane

The Josephson-geometry is invariant under rotations in the x-y-plane. Obviously, such a rotation implies a shift of the spherical angles that characterise the interface magnetisation direction in the interface plane, $\varphi_{\mathrm{I,II}} \mapsto \varphi_{\mathrm{I,II}} + \delta$. Naturally, all observables must be invariant under such rotations and therefore independent of δ. This is true if the current-phase relations depends on $\Delta\varphi$ only. We provided a general, but not very elegant proof of this in Ref. [51]. We propose a more compact proof here and extend it to the case of multi-domain junctions. Only the ferromagnetic trajectories are discussed, it is easy to convince oneself that the simpler half metallic case follows from our proof by eliminating the minority band.

To this end, we consider the matrix notation of the boundary conditions [37]:

$$\mathbf{\Gamma} = \Gamma_{k \to k'}, \quad \overline{\mathbf{\Gamma}} = \mathbf{\Gamma} - \Gamma_k \delta_{kk'}, \tag{G.1}$$

$$\boldsymbol{\gamma} = \gamma_k \delta_{kk'}, \boldsymbol{\gamma}' = S \circ \boldsymbol{\gamma} \circ \tilde{S}, \tag{G.2}$$

where $\circ$ denotes a matrix product including 'channel'-space. The boundary conditions then read [37]:

$$\mathbf{\Gamma} = \boldsymbol{\gamma}' + \overline{\mathbf{\Gamma}} \circ \tilde{\boldsymbol{\gamma}} \circ \boldsymbol{\gamma}'. \tag{G.3}$$

As discussed in chapter 4, the scattering matrix S_φ of a trajectory with finite φ is related to the matrix of the trajectory with the same $k_\parallel$, but $\varphi = 0$ by a spin-rotation in the x-y-plane:

$$S_\varphi = \Phi S \Phi^*, \quad \Phi = \begin{pmatrix} e^{-i\sigma_z \varphi/2} & 0_{2\times 2} \\ 0_{2\times 2} & e^{-i\sigma_z \varphi/2} \end{pmatrix}. \tag{G.4}$$

We now make the following ansatz for the incoming coherence functions at the two interfaces:

$$\gamma_2^{\mathrm{I}} = b_2^{\mathrm{I}} e^{-i\varphi_{\mathrm{II}}}, \quad \gamma_3^{\mathrm{I}} = b_3^{\mathrm{I}} e^{i\varphi_{\mathrm{II}}}, \quad \tilde{\gamma}_2^{\mathrm{I}} = \tilde{b}_2^{\mathrm{I}} e^{i\varphi_{\mathrm{II}}}, \quad \tilde{\gamma}_3^{\mathrm{I}} = \tilde{b}_3^{\mathrm{I}} e^{-i\varphi_{\mathrm{II}}}, \tag{G.5}$$
$$\gamma_2^{\mathrm{II}} = b_2^{\mathrm{II}} e^{-i\varphi_{\mathrm{I}}}, \quad \gamma_3^{\mathrm{II}} = b_3^{\mathrm{II}} e^{i\varphi_{\mathrm{I}}}, \quad \tilde{\gamma}_2^{\mathrm{II}} = \tilde{b}_2^{\mathrm{II}} e^{i\varphi_{\mathrm{I}}}, \quad \tilde{\gamma}_3^{\mathrm{II}} = \tilde{b}_3^{\mathrm{II}} e^{-i\varphi_{\mathrm{I}}},$$

where all b quantities depend on $\varphi_{\mathrm{I,II}}$ through $\Delta\varphi$ only. The incoming amplitudes from the superconductor are the bulk-coherence functions, and – as such – independent of the φ-phases. We now prove that this ansatz is consistent with the solutions of the boundary conditions at both interfaces in the single domain case. Adopting the matrix notation for the incoming coherence functions, we observe that

$$[\Phi^* \circ \boldsymbol{\gamma} \circ \Phi^*]^{\mathrm{I,II}}, \quad [\Phi \circ \tilde{\boldsymbol{\gamma}} \circ \Phi]^{\mathrm{I,II}} \tag{G.6}$$

depend on $\varphi_{\mathrm{I,II}}$ through $\Delta\varphi$ only. In combination with equation (G.4) and the particle-hole symmetry of the S-matrix this implies that

$$[\Phi^* \circ \boldsymbol{\gamma}' \circ \Phi^*]^{\mathrm{I,II}}, \quad [\Phi \circ \tilde{\boldsymbol{\gamma}}' \circ \Phi]^{\mathrm{I,II}} \tag{G.7}$$

also depend on $\Delta\varphi$ only.

In what follows, all quantities refer to one of the two interfaces, which one does not matter. We thus omit the interface index in the following. In regard to the boundary conditions at this interface, we then have:

$$\mathbf{\Gamma} = \boldsymbol{\gamma}' + \overline{\mathbf{\Gamma}} \circ \tilde{\boldsymbol{\gamma}} \circ \boldsymbol{\gamma}' \tag{G.8}$$
$$= \Phi \circ \left[\Phi^* \circ \boldsymbol{\gamma}' \circ \Phi^* + \Phi^* \circ \overline{\mathbf{\Gamma}} \circ \Phi^* \circ \Phi \circ \tilde{\boldsymbol{\gamma}} \circ \Phi \circ \Phi^* \circ \boldsymbol{\gamma}' \circ \Phi^* \right] \circ \Phi,$$

and thus

$$\Phi^* \circ \boldsymbol{\Gamma} \circ \Phi^* = \Phi^* \circ \boldsymbol{\gamma}' \circ \Phi^* + \Phi^* \circ \overline{\boldsymbol{\Gamma}} \circ \Phi^* \circ \Phi \circ \tilde{\boldsymbol{\gamma}} \circ \Phi \circ \Phi^* \circ \boldsymbol{\gamma}' \circ \Phi^*. \tag{G.9}$$

This is an implicit equation for $\Phi^* \circ \boldsymbol{\Gamma} \circ \Phi^*$. It follows from the above that all parts of this equation save $\Phi^* \circ \boldsymbol{\Gamma} \circ \Phi^{*\mathrm{a}}$ depend on $\Delta\varphi$ only. However, since the latter is determined by the equation, it must depend on $\Delta\varphi$ only as well. This, in turn, implies that $\boldsymbol{\Gamma}$ itself has exactly the same structure as the ansatz we made for the incoming coherence functions. And thanks to the particle-hole symmetry relation, the same holds for $\tilde{\boldsymbol{\Gamma}}$. Since the propagation through the interlayer cannot change anything about the φ-dependence, the incoming coherence functions at the opposite interface are also consistent with the ansatz. We thus proved that our ansatz is a self-consistent solution for the coherence functions in the SC/FM/SC structure. In principle, this is only a necessary but not a sufficient condition. But obviously, the conclusion remains true if the incoming coherence functions from the FM are assumed to be zero. Since any particle-hole coherence inside the FM layer must have been induced by the superconductors, we can assume that this was indeed the case at some point in time, which completes the prove.

In the case of multi-domain junctions with the domain boundary scattering matrix that we assume, the rotational invariance of the junction in the x-y-plane is maintained and our conclusion for the φ-dependence must remain true. This is obviously true if the number of domains is odd, nothing changes in that case. There is an even number of boundaries, and the propagation through the bulk will thus not change the φ-dependence of the coherence functions. Secondly, the orientation of the bulk-magnetisation is the same at both interfaces, and the φ-angles are thus not modified compared to the single domain case. If, however, the number of domains is even, the propagation through the bulk will interchange the coherence functions and the orientation of the bulk-magnetisation will be opposite at the two interfaces.

We begin by discussing the consequences of the first modification. We propose the ansatz:

$$\gamma_2^{\mathrm{I}} = b_2^{\mathrm{I}} e^{i\varphi_{\mathrm{II}}}, \quad \gamma_3^{\mathrm{I}} = b_3^{\mathrm{I}} e^{-i\varphi_{\mathrm{II}}}, \quad \tilde{\gamma}_2^{\mathrm{I}} = \tilde{b}_2^{\mathrm{I}} e^{-i\varphi_{\mathrm{II}}}, \quad \tilde{\gamma}_3^{\mathrm{I}} = \tilde{b}_3^{\mathrm{I}} e^{i\varphi_{\mathrm{II}}}, \tag{G.10}$$
$$\gamma_2^{\mathrm{II}} = b_2^{\mathrm{II}} e^{i\varphi_{\mathrm{I}}}, \quad \gamma_3^{\mathrm{II}} = b_3^{\mathrm{II}} e^{-i\varphi_{\mathrm{I}}}, \quad \tilde{\gamma}_2^{\mathrm{II}} = \tilde{b}_2^{\mathrm{II}} e^{-i\varphi_{\mathrm{I}}}, \quad \tilde{\gamma}_3^{\mathrm{II}} = \tilde{b}_3^{\mathrm{II}} e^{i\varphi_{\mathrm{I}}},$$

where all b quantities depend on $\varphi_{\mathrm{I,II}}$ through $\varphi_{\mathrm{I}} + \varphi_{\mathrm{II}}$ only. The remainder of the prove is fully analogous to what we discussed before, just that $\Phi^* \boldsymbol{\Gamma} \Phi^*$ is now shown to be a function of $\varphi_{\mathrm{I}} + \varphi_{\mathrm{II}}$ rather than $\Delta\varphi$. The consistency of the ansatz then follows if the scattering at the domain boundary is properly taken into account.[b] To complete the prove, we now recall that φ_{II} must be replaced by $-\varphi_{\mathrm{II}}$ in the scattering matrix, due to the orientation of the bulk magnetisation at the second interface. Thus the ansatz is mapped back onto the one we had for the single domain case.

To show that the supercurrent depends on $\Delta\varphi$ only, we inspect the diagonal entries of $g^{\mathrm{M}}(p_{\mathrm{F,z}} > 0)$ at interface (I) and observe that they depend on the coherence functions through $[\boldsymbol{\Gamma}\tilde{\gamma}]^{\mathrm{I}}$. From the structure of the solutions, we then infer that this quantity depends on $\varphi_{\mathrm{I,II}}$ through $\Delta\varphi$ exclusively.

---

[a]Note that $\Phi^* \circ \overline{\boldsymbol{\Gamma}} \circ \Phi^*$ is just a part of $\Phi^* \circ \boldsymbol{\Gamma} \circ \Phi^*$.

[b]We do not discuss this in detail here. It follows from the solutions stated in the previous section and $e^{-i\varphi_{\mathrm{I,II}}} = e^{i\varphi_{\mathrm{II,I}}} \cdot e^{-i(\varphi_{\mathrm{I}}+\varphi_{\mathrm{II}})}$.